The Search for Double-Beta Decay to Excited States in ^{76}Ge using the Majorana Demonstrator

Ian Guinn

A dissertation
submitted in partial fulfillment of the
requirements for the degree of

Doctor of Philosophy

University of Washington

2019

Reading Committee:

Jason Detwiler, Chair

R.G. Hamish Robertson

Alejandro Garcia

Program Authorized to Offer Degree:
Department of Physics

University of Washington

Abstract

The Search for Double-Beta Decay to Excited States in ^{76}Ge using the Majorana Demonstrator

Ian Guinn

Chair of the Supervisory Committee:
Associate Professor Jason Detwiler
Department of Physics

The discovery of neutrino mass is the first tangible contradiction of the Standard Model of particle physics. Two neutrino double-beta decay ($2\nu\beta\beta$) is an allowed second order process in the Standard Model that has been observed with half-lives in the range of $10^{18} - 10^{24}$ y. Because it involves two neutrino vertices, double-beta decay is a useful tool for studying the properties of neutrinos. In particular, the discovery of neutrinoless double-beta decay ($0\nu\beta\beta$) would indicate that the neutrino is granted mass by the Majorana mechanism, and provide a means of measuring the mass scale of the neutrino. This would also provide a means for violating Lepton number conservation in the Standard Model, potentially enabling a mechanism for the asymmetric creation of more matter than anti-matter in the universe. $0\nu\beta\beta$ has never been observed and is the active subject of a variety of experiments, with best half-life limits in the range of $10^{25} - 10^{26}$ y. In addition, parent nuclei can double-beta decay into excited states of the daughter nucleus. Observing double-beta decay to excited states ($\beta\beta$ E.S.) is helpful in understanding the nuclear matrix elements that are required for interpretting a $0\nu\beta\beta$ result. The branching ratios to different daughter nuclear states may also provide sensitivity to additional physics beyond the Standard Model; for example, the $2\nu\beta\beta$ to 2^+ daughter states could indicate violation of the Pauli Exclusion Principle, and measurement of $0\nu\beta\beta$ to excited states would probe the exchange mechanism underlying

$0\nu\beta\beta$.

The MAJORANA DEMONSTRATOR is measuring double-beta decay in ^{76}Ge using an array of P-type Point Contact (PPC) High Purity Germanium (HPGe) detectors. The experiment contains 35 detectors totalling 29.8 kg of detector mass that are enriched to 88% in ^{76}Ge so that the detectors act as both source and detector for $\beta\beta$-decay; there are an additional 23 detectors totalling 14.4 kg of detector mass with the natural isotopic abundance. The experiment is constructed using ultra-low background materials, in a clean environment located 4850' underground at the Sanford Underground Research Facility in Lead, SD. Thanks to the granularity of the detector array and the PPC dector geometry, the DEMONSTRATOR is capable of distinguishing single- and multi-site events. The PPC detectors also have the best energy resolution of any current generation experiment, at 2.5 keV in the 2039 keV region of interest for $0\nu\beta\beta$. These properties have enabled the experiment to measure one of the lowest background rates of currently running experiments. The experiment is also engaged in searching for $\beta\beta$ E.S.. Excited state events are inherently multi-site due to the prompt emission of a γ-ray; by searching through events that hit multiple detectors, the DEMONSTRATOR is capable of performing a sensitive, low background search for these events.

This dissertation will begin by presenting the theoretical motivations for both the searches for $0\nu\beta\beta$ and $\beta\beta$-decay to excited states. Next, it will describe the MAJORANA DEMONSTRATOR, with a focus on the elements of the experiment most relevant to the search for $\beta\beta$ E.S.. The DEMONSTRATOR's simulation framework will be described, along with the simulations necessary to the search for $\beta\beta$ E.S.. The techniques used to perform an optimal search for $\beta\beta$ E.S., and the estimation of the detection efficiency and its uncertainty will then be described. A world-leading result using 22 kg-y of exposure will be presented. Finally, this result will be placed in the context of previous results and current theory, and opportunities to improve on the result will be discussed.

TABLE OF CONTENTS

LIST OF FIGURES

GLOSSARY

2$\nu\beta\beta$: Two-neutrino double-beta decay

0$\nu\beta\beta$: Neutrinoless double-beta decay

$\beta\beta$ E.S.: Double-beta decay to excited states

BSM: Beyond the Standard Model

νMSM: Minimal extension to the Standard Model for neutrino mass

LRSM: Left-Right Symmetric Model

GUT: Grand Unified Theory

RPV SUSY: R-Parity Violating Super-Symmetry

NME: Nuclear Matrix Element

LNE: Light Neutrino Exchange

QRPA: Quasi-Random Phase Approximation

SM: nuclear Shell Model

IBM: Interacting Boson Model

EDF: Energy Density Functional

EFT: Effective Field Theory

Q-VALUE: Total kinetic energy released in a β-decay

FWHM: Full Width at Half Max

HPGE: High Purity Germanium

PPC: P-type Point Contact

BEGE: Broad Energy Germanium

DS#: Data Set designation

LMFE: Low-Mass Front End

TRAPENF: Trapezoidal Filter Energy with Nonlinearity correction and Fixed-time pickoff

PSA: Pulse Shape Analysis

AVSE: Maximum current amplitude vs energy; PSA parameter for detecting multi-site events

DCR: Delayed Charge Recovery

MaGe: MAJORANA/GERDA simulation framework

ORCA: Object-oriented Real-time Control and Acquisition

GAT: Germanium Analysis Toolkit

MGDO: MAJORANA and GERDA Data Objects

MCMC: Markov Chain Monte Carlo

HMC: Hamiltonian/Hybrid Monte Carlo

LE/HE TAIL: Low/High-Energy exponentially modified gaussian tail

ACKNOWLEDGMENTS

Chapter 1

THE THEORY OF NEUTRINO MASS AND DOUBLE-BETA DECAY

1.1 A Brief History of Neutrinos

1.1.1 Discovery of Neutrinos

Nuclear radioactivity was discovered and characterized at the turn of the twentieth century by a group of physicists including Henri Becquerel, Marie Curie and Ernest Rutherford. The three main types of decay studied were:

- α-decay, in which a ^{4}He nucleus is ejected from a nucleus

- β^--decay, in which an electron is emitted from a nucleus and a neutron inside the nucleus becomes a proton

- γ-decay, in which a nucleus in an excited state decays to the ground state and emits a high energy photon in the process

In the cases of α- and γ-decays, the particles are emitted monoenergetically, with kinetic energies that can be predicted using energy conservation by the change in mass between the parent and daughter nuclei, according to

$$E = mc^2 \tag{1.1}$$

However, extensive experimental efforts by Lise Meitner, Otto Hahn, Jean Danysz, James Chadwick, Charles Drummond Ellis, and others established that β-decay has a diffuse energy spectrum that could not be explained through energy conservation; furthermore, angular momentum conservation appeared to be violated in these decays. In 1930, Wolfgang Pauli

(a) Beta Decay   (b) Fermi Decay Diagram   (c) Energy Spectrum
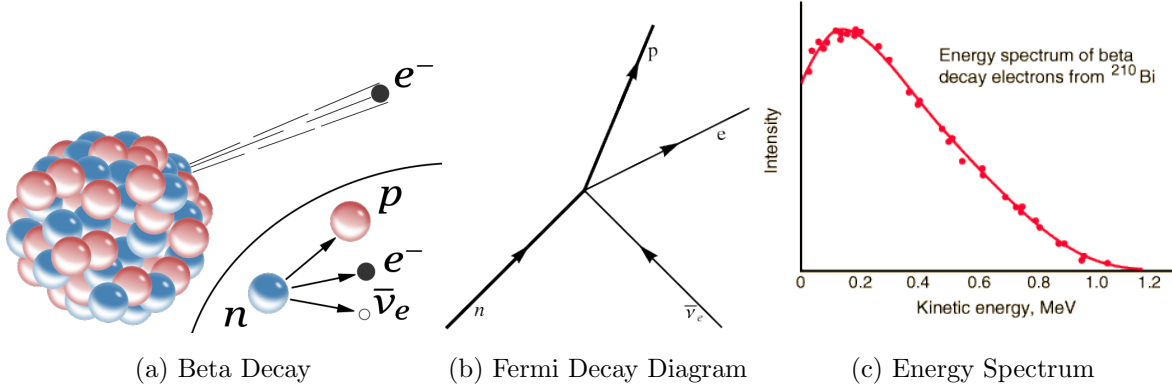
Figure 1.1: A beta decay emits an electron while transmuting a neutron into a proton. The energy spectrum of the electron is broad instead of peak-like (measured by G.J. Neary (1940), taken from `http://hyperphysics.phy-astr.gsu.edu/hbase/Nuclear/beta2.html`).

proposed that this broad spectrum could instead be explained by a small, non-interacting, spin-1/2 particle that escapes the nucleus along with the electron, and carries away undetected kinetic energy, thus conserving energy and angular momentum.

By 1934, Enrico Fermi proposed a theory of β-decay that included Pauli's neutral particle, a spin 1/2 electrically neutral particle he named the neutrino (ν)[1]. The Lagrangian for the Fermi interaction is

$$\mathcal{L}_F = \frac{G_F}{\sqrt{2}} \left(\bar{\psi}_p \gamma^\mu \psi_n \right) \left(\bar{\psi}_e \gamma_\mu \psi_\nu \right) \tag{1.2}$$

This theory was capable of describing the broad energy spectrum of β-decay, and also capable of describing nuclear β^+-decay, in which a positron is emitted and a nuclear proton becomes a neutron. Furthermore, this theory predicted the process of inverse β-decay, in which a neutrino is absorbed by a nucleus, and either an electron is produced with a proton becoming a neutron, or a positron is produced with a neutron becoming a proton. Fermi's theory, however, predicted a cross-section for inverse β-decay on the order of $\sigma \approx 10^{-44}$ cm^2, meaning that a single neutrino would have a mean free path on the order of light-years through lead. Due to the extremely low cross-section, the force mediating the interactions described by

Fermi's theory became known as the weak force. Pauli, Fermi and the Nature review board were all understandably pessimistic about the possibility of actually detecting this newly predicted process, resulting in Nature's refusal to publish Fermi's theory[2].

This pessimism, however, was unwarrented. Twenty years later, Reines and Cowan detected the inverse β-decay in a water target using liquid scintillator detectors[3]. This experiment was enabled by the high flux of neutrinos produced by the Savannah River nuclear reactor. Specifically, Reines and Cowan detected the production of positrons by inverse β^--decay of protons in the water. Other attempts to detect electrons produced by inverse β^+-decay from neutrinos produced in a reactor failed to measure anything [4]. This is explained by the existence of distinct neutrinos (ν) and anti-neutrinos ($\bar{\nu}$). Weak interactions are expected to conserve the quantity of Lepton Number (L), where electrons and neutrinos have $L = +1$ and positrons and anti-neutrinos have $L = -1$. This means that β^+- and inverse β^+-decays will involve neutrinos, and β^- and inverse β^--decays will involve anti-neutrinos. Since the Savannah River nuclear reactor produced almost entirely anti-neutrinos via β^--decays, the only interaction detected involved the production of positrons via inverse β^--decay. To date, no interaction has been observed that violates Lepton-number conservation.

1.1.2 Parity Violation in the Weak Force

The discrete parity symmetry (P) is conserved for the electromagnetic and strong forces. In 1956, Lee and Yang suggested that the discrete parity symmetry (P) could be violated by the weak force, as no experimental evidence existed to confirm or reject this[5]. Within a year, Wu and collaborators experimentally demonstrated P violation by placing ^{60}Co under a strong magnetic field at low temperature and by measuring the correlation between the directions of the deexcitation γs and of the electron emitted. If P is conserved, no correlation is expected in these directions; however, Wu found an anti-correlation, implying P-violation[6]. Shortly after, Garwin, Lederman and Weinrich confirmed this in the polarization of muons produced by decays of pions in flight[7].

In 1958, Goldhaber and collaborators observed that the weak force is maximally parity

violating, and weak interactions involve only left-handed neutrinos[8]. This result, combined with contemporary results that were consistent witha massless neutrino[9], meant that there was no experimental evidence for the existence of right-handed neutrinos. For this reason, neutrinos were presumed to be strictly left-handed, represented by massless Weyl spinors. In addition, the weak Lagrangian was modified to be

$$\mathcal{L}_W = -\frac{G_F}{\sqrt{2}} \left(\bar{\psi}_p \gamma^\mu \frac{1 - \gamma^5}{2} \psi_n \right) \left(\bar{\psi}_e \gamma_\mu \frac{1 - \gamma^5}{2} \psi_\nu \right) \tag{1.3}$$

Due to P violation, the Fermi vertex has a vector-axial vector (V-A) tensor structure.

1.1.3 Flavors of Neutrinos

In addition to the electron, additional charged elementary particles with identical properties (e.g. spin, charge) to the electron, except for mass, exist[9]. These are the muon ($m_\mu = 113$ MeV) and tau lepton ($m_\tau = 1.8$ GeV), which are unstable due to their high masses. The existence of three different particles with similar properties except for mass is mirrored in quarks (the constituents of protons and neutrons and other "baryons"), and the different types are called "flavors", with the different mass groupings called "generations". Both heavy leptons decay via the weak force, producing neutrinos in the process. The neutrinos produced in these decays can subsequently undergo processes analogous to inverse beta decay, producing either muons or tau leptons instead of electrons, and maintaining conservation of lepton number. Furthermore, over short distances, it was observed that these neutrinos produced the same particle as those which created them. This means that there are three distinct types of neutrinos corresponding to the three types of lepton; these are called the electron neutrino (ν_e), muon neutrino (ν_μ), and tau neutrino (ν_τ). The weak decay of a muon into an electron looks like:

$$\mu \to e + \nu_\mu + \bar{\nu}_e \tag{1.4}$$

The fact that the flavor of leptons appeared to be conserved was in contrast with quarks, where a weak decay could transmute quarks between different generations.

1.1.4 Electroweak Unification

During the 1930's-50's, a large number of new particles were discovered, with properties and interactions that could be described using the algebra of Lie groups. Between 1961 and 1967, Glashow, Weinberg and Salam proposed a theory of electro-weak unification, a theory which simultaneously described the electromagnetic and weak interactions with a U(1) gauge symmetry representing weak hypercharge and a SU(2) gauge symmetry representing isospin (i.e. a SU(2)×U(1) gauge symmetry)[10, 11, 12]. This theory predicted the existence of the $W^{+/-}$ boson, a heavy, electrically charged, spin 1 particle which forms interaction vertices with electrons and neutrinos or with up and down quarks, which are the components of protons and neutrons. As shown in Figure 1.2, this theory is capable of reproducing the vertex in Fermi's theory of weak interaction, with the W boson acting as a mediator for β-decay. The W boson interacts only with left-handed particles, and the effective charged-current interaction term lagrangian at energies below the electroweak symmetry breaking scale is:

$$\mathcal{L}_C = -\frac{g}{\sqrt{2}}\big(\bar{u}_i\gamma^\mu\frac{1-\gamma^5}{2}M_{ij}^{CKM}d_j + \bar{\nu}_i\gamma_\mu\frac{1-\gamma^5}{2}e_i\big)W_\mu^+ + \text{h.c.} \tag{1.5}$$

where M_{ij}^{CKM} is the Cabibbo-Kobayashi-Maskawa (CKM) matrix that describes the probability of a weak transition between different generations of quark, and i and j index over the generations.

This theory also made a number of new predictions, which have since been confirmed. The Z boson, a heavy, neutral, spin 1 boson was predicted, which would enable elastic scattering of neutrinos off other weakly interacting particles. Neutrino elastic scattering of a muon neutrino off of an electron was observed by the Gargamelle detector in 1973[13], and both the W and Z bosons were observed at the Super Proton Synchotron in 1983[14, 15]. This theory also incorporated the Higgs boson, a spin 0 boson that imparts mass to the fermions in the standard model, as will be discussed in Section 1.3.2. The Higgs boson was discovered at the ATLAS and CMS detectors using the Large Hadron Collider in 2012[16, 17].
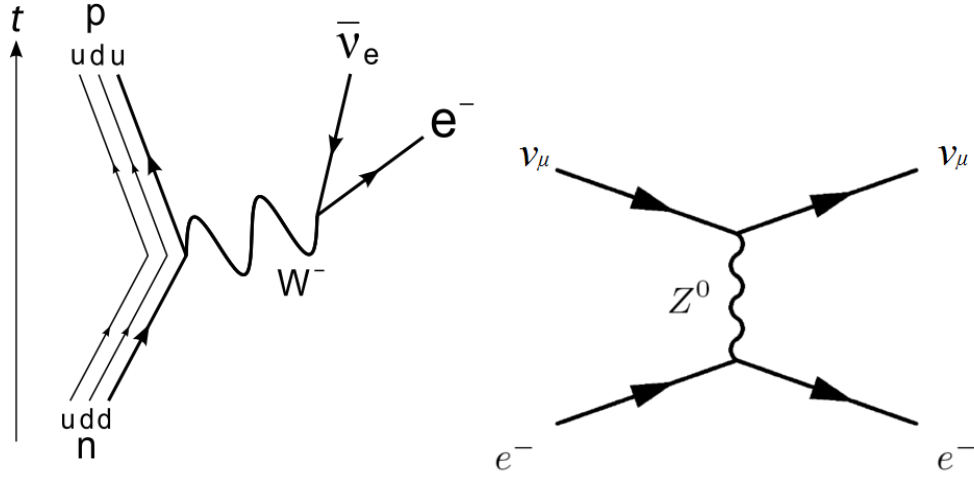
Figure 1.2: Diagrams of β-decay mediated by the W-boson and of a neutral current scatter of a neutrino off an electron, mediated by the Z-boson.

1.1.5 The Standard Model of Particle Physics

Over the course of the 1960's through 80's, this electroweak unification scheme was expanded into a theory called the Standard Model, based on a U(1)×SU(2)×SU(3) gauge symmetry, with the non-Abelian SU(3) component describing the strong force [9]. All of the fundamental particles included in this theory are summarized in Figure 1.3. This theory included five integer-spin bosons:

- The photon (γ) mediates electromagnetism, and only interacts with electrically charged particles

- The W and Z bosons mediate the weak force, and only interact with left-handed fermions

- 8 types of gluons, with different "color" charges, mediate the strong force, and only interact with quarks
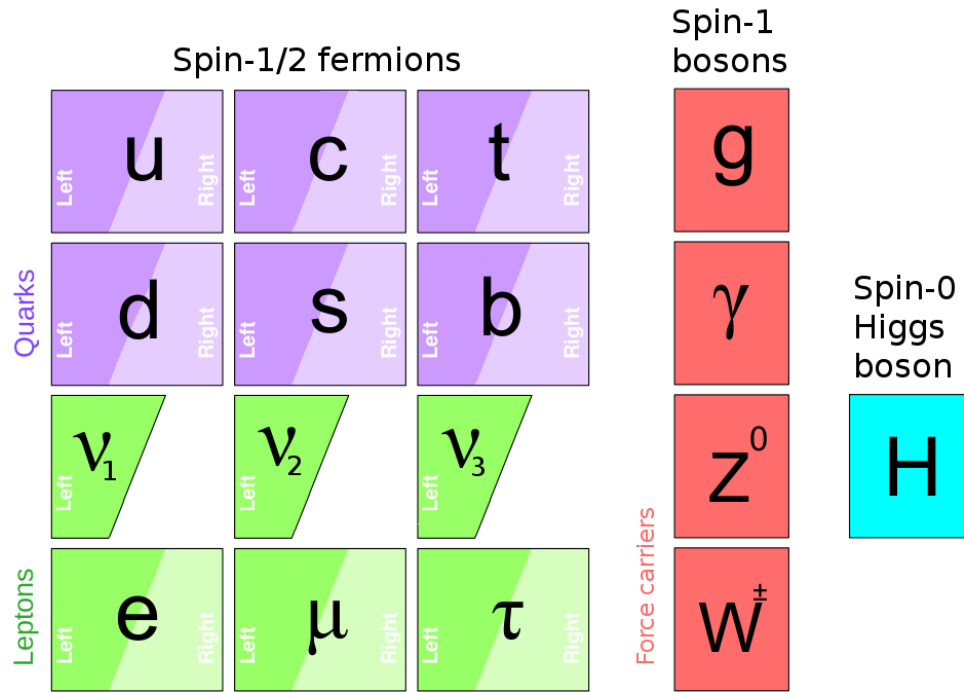
Figure 1.3: Diagram of all standard model particles.

- The Higgs boson imparts mass to all the other particles, except for the massless photons and neutrinos

The spin-1/2 fermions include the rest of the particles, and are divided into four groups, with 3 generations each:

- Up-type quarks (up (u), charm (c) and top (t)) have electrical charge $+2/3$ and interact via the EM, weak and strong forces

- Down-type quarks (down (d), strange (s) and bottom (b)) quarks have electrical charge $-1/3$ and interact via the EM, weak and strong forces

- Charged leptons (e, μ and τ) have charge -1, and interact via the EM and weak forces

- Neutrinos (ν_e, ν_μ and ν_τ) have no charge and interact only via the weak force. In addition, they are massless, and have only left-handed components

Table 1.1: Table of weak properties of the Standard Model fermions. Note the lack of right-handed neutrino singlets.

Fermion type	Electric Charge	Weak isospin		Generation 1	2	3
Quarks	$+\frac{2}{3}, -\frac{1}{3}$	doublet	$\frac{1}{2}$	$\begin{pmatrix} u \\ d \end{pmatrix}_L$	$\begin{pmatrix} c \\ s \end{pmatrix}_L$	$\begin{pmatrix} t \\ b \end{pmatrix}_L$
		singlet	0	u_R, d_R	s_R, c_R	t_R, b_R
Leptons	$-1, 0$	doublet	$\frac{1}{2}$	$\begin{pmatrix} e \\ \nu_e \end{pmatrix}_L$	$\begin{pmatrix} \mu \\ \nu_\mu \end{pmatrix}_L$	$\begin{pmatrix} \tau \\ \nu_\tau \end{pmatrix}_L$
		singlet	0	e_R	μ_R	τ_R

Because the weak force only interacts with left-handed particles, each grouping is divided into a left-handed doublet and right-handed singlets, as shown in Table 1.1. The Standard Model has been extensively tested for interactions between the particles included therein, and with few exceptions, has been verified. It is, however, incomplete, failing to describe gravity, dark matter, the accelerating expansion of the universe, the matter asymmetry of the universe, and other natural phenomena; this not-yet-described physics is referred to as Beyond the Standard Model (BSM).

Lepton number and Baryon number (B, the total number of Baryons—composites of three quarks, minus anti-Baryons) are both conserved in low energy interactions in the Standard Model, including the weak force. At energies above the electroweak unification scale (~ 1 TeV), however, the nonperturbative "sphaleron" process is capable of violating both B and L conservation. Figure 1.4 shows how a sphaleron can occur if a system is heated above the sphaleron energy and then cools into a different vaccuum state, with different Lepton-

(a) Vacuum Potential   (b) Sphaleron
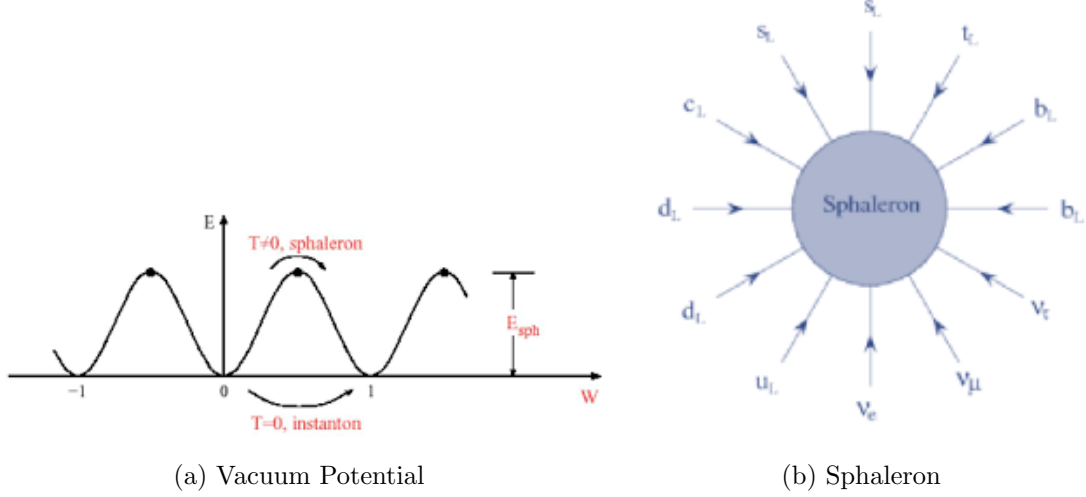
Figure 1.4: Left: The periodic vacuum potential of the Standard Model as a function of essentially $B + L$. If the temperature of a system is brought above E_{sp}, the system can re-cool into a state with different $B + L$.

Right: A sphaleron diagram generating $\Delta B = -\Delta L = 3$

and Baryon-numbers. The simplest process would increment or decrement both L and B by 3; any such process would conserve the value of $B - L$, as this is an exact, accidental symmetry of the Standard Model. Because of the extreme energies required for this process to occur with any significant probability, it has never been observed; however, this process would occur during the early universe, with consequences that will be briefly discussed in Section 1.3.4.

1.2 Discovery of Neutrino Mass

1.2.1 The Solar Neutrino Problem

The first hint of BSM physics in neutrinos came from the Solar Neutrino problem. During the various processes involved in nuclear fusion in the Sun, numerous neutrinos are produced; for example, the pp-process, which is the dominant process for producing ^{4}He from ^{1}H, pro-

(a) Illustration of the pp-fusion process

(b) Solar neutrino energy spectrum
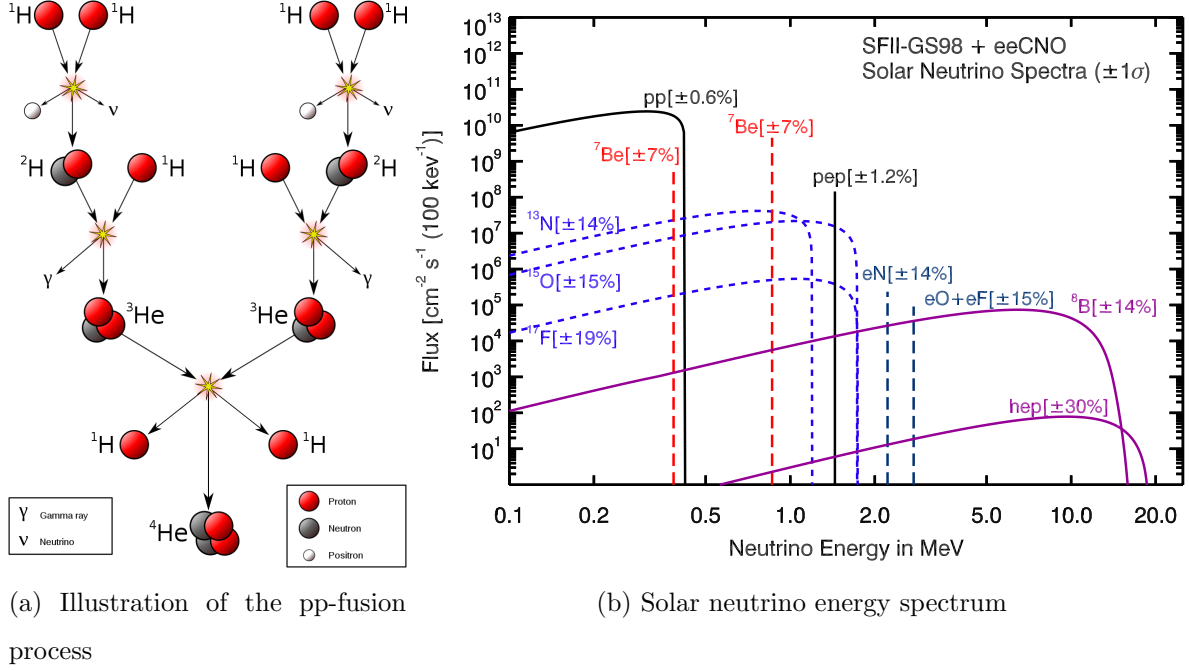
Figure 1.5: The energy spectrum of neutrinos produced by the Sun (right) can be predicted by understanding the fusion processes that occur (such as the pp-process, left). Taken from [9].

duces two neutrinos per ^{4}He nucleus (see Figure 1.5). Solar models can predict the number and energy spectrum of neutrinos emitted by various production channels in the Sun[18]. In 1962, Davis began to directly measure the flux of solar neutrinos in the Homestake mine in South Dakota by counting inverse β-decays of ^{37}Cl into ^{37}Ar. Over multiple decades of measurement, Davis consistently measured one third as many neutrinos as expected[19]. Additional experiments observed similar deficits, including SAGE and GALLEX, which measured inverse β-decays with a lower energy threshold than the Homestake experiment using ^{71}Ga[20].

1.2.2 Neutrino Mass Mixing

One (among many) explanation for this deficit is neutrino mixing, which was predicted by Pontecorvo in 1957[21], and further developed by Maki, Nakagawa and Sakata in 1962[22]. Under this model, neutrinos are described by mass eigenstates, ν_1, ν_2 and ν_3, which describe how the neutrinos move freely through space. The neutrinos of the Standard Model, now called flavor eigenstates, are coherent quantum admixtures of the mass eigenstates, and describe how neutrinos interact weakly with other particles. In 1969, Pontecorvo proposed neutrino oscillation as an explanation for the observed deficit of Solar neutrinos[23].

Mathematically, mixing is described by the Pontecorvo-Maki-Nakagawa-Sakata (PMNS) matrix (U^{PMNS}), which is unitary. In the example of a β-decay, the electron anti-neutrino emitted is the following superposition:

$$|\bar{\nu}_e\rangle = U_{1e}^* |\bar{\nu}_1\rangle + U_{2e}^* |\bar{\nu}_2\rangle + U_{13}^* |\bar{\nu}_3\rangle \tag{1.6}$$

The PMNS matrix can be written as

$$\begin{pmatrix} U_{e1} & U_{e2} & U_{e3} \\ U_{\mu1} & U_{\mu2} & U_{\mu3} \\ U_{\tau1} & U_{\tau2} & U_{\tau3} \end{pmatrix} = \begin{pmatrix} 1 & 0 & 0 \\ 0 & c_{23} & s_{23} \\ 0 & -s_{23} & c_{23} \end{pmatrix} \cdot \begin{pmatrix} c_{13} & 0 & s_{13}e^{-i\delta} \\ 0 & 1 & 0 \\ -s_{13}e^{i\delta} & 0 & c_{13} \end{pmatrix} \cdot \begin{pmatrix} c_{12} & s_{12} & 0 \\ -s_{12} & c_{12} & 0 \\ 0 & 0 & 1 \end{pmatrix} \tag{1.7}$$

where s/c_{ij} are the sines and cosines of the mixing angles θ_{ij} and δ is a CP-violating term known as the CP-phase. During neutrino oscillation, the probability of measuring a neutrino in a weak eigenstate changes according to (in the approximation of only two neutrinos):

$$P_{\alpha \to \beta} = \sin^2(2\theta_{ij}) \sin^2\left(\frac{(\Delta m^2)_{ij} c^3}{4\hbar E} L\right) \tag{1.8}$$

where $(\Delta m^2)_{ij}$ is the difference in the squares of the masses of the neutrino mass eigenstates i and j, L is the distance from the neutrino source, and E is the energy of the neutrino. The neutrinos oscillate as a function of L/E, with a frequency proportional to Δm^2. This mixing in the Lepton sector is similar to mixing of quarks via the CKM matrix, which enables flavor changing weak decays in mesons and baryons.

(a) SuperK ν Oscillation Sig-
nal

(b) SNO ν Mass Mixing Signal

(c) KamLAND ν Oscillation Signal
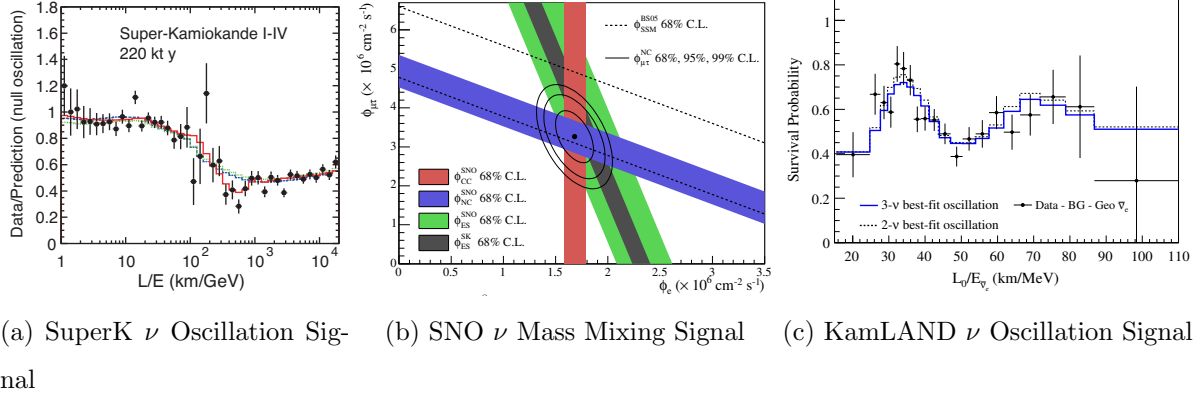
Figure 1.6: The signals of neutrino mixing from disappearence of atmospheric ν_μs in Su-
perKamiokande, difference in total solar-ν flux and solar-ν_e flux from SNO, and disappearence
of reactor ν_es in KamLAND. Taken from [9]

1.2.3 Discovery of Neutrino Oscillation

In 1998, SuperKamiokande, observed a deficit of atmospheric muon neutrinos dependant
on the zenith angle, consistent with neutrino oscillation[24]. In 2000, the SNO experiment
observed neutrino flavor mixing in solar neutrinos. Since solar ν_es are produced amid an
extremely high electron density, as they escape the Sun, they will adiabatically transform into
the ν_2 eigenstate due to the MSW effect. By observing solar neutrinos via different interaction
mechanisms, SNO had sensitivity to both the total number of neutrinos, regardless of flavor,
via neutral current interactions, and to the number of electron neutrinos via charged current
interactions. SNO observed the expected total number of neutrinos according to the Standard
Solar Model[18], while observing a deficit in electron neutrinos, definitively solving the Solar
Neutrino Problem[25]. Finally, in 2003 KamLAND observed a deficit of electron neutrinos
from nuclear reactors consistent with oscillation[26]. Figure 1.6 shows the results of all
three experiments. Between these three measurements, a deficit has been observed in Solar,
atmospheric, and reactor neutrinos, and this deficit has been explained in a simple and

Parameter	best-fit	3σ
Δm^2_{21} $[10^{-5}$ eV $^2]$	7.37	$6.93 - 7.96$
$\Delta m^2_{31(23)}$ $[10^{-3}$ eV $^2]$	2.56 (2.54)	$2.45 - 2.69$ $(2.42 - 2.66)$
$\sin^2\theta_{12}$	0.297	$0.250 - 0.354$
$\sin^2\theta_{23}$, $\Delta m^2_{31(32)} > 0$	0.425	$0.381 - 0.615$
$\sin^2\theta_{23}$, $\Delta m^2_{32(31)} < 0$	0.589	$0.384 - 0.636$
$\sin^2\theta_{13}$, $\Delta m^2_{31(32)} > 0$	0.0215	$0.0190 - 0.0240$
$\sin^2\theta_{13}$, $\Delta m^2_{32(31)} < 0$	0.0216	$0.0190 - 0.0242$
δ/π	1.38 (1.31)	2σ: (1.0 - 1.9)
		(2σ: (0.92-1.88))

(a) Neutrino Oscillation Parameters
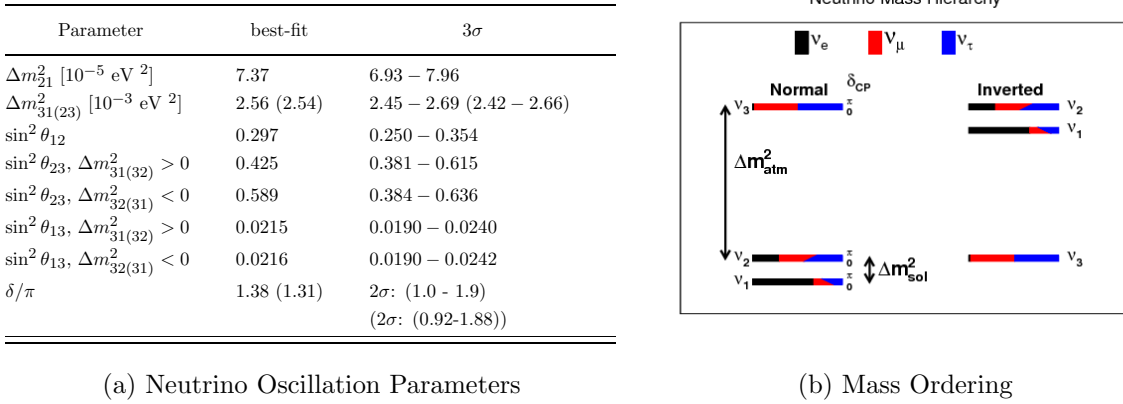
(b) Mass Ordering

Figure 1.7: Left: Table of measured neutrino parameters from oscillation experiments, taken from [9].

Right: Solutions of neutrino mass ordering that are consistant with oscillation results.

consistent way using the PMNS mass mixing model.

An extensive experimental program of oscillation experiments has since measured all of the mixing angles in the PMNS matrix, and the Δm^2 parameters, as shown in Figure 1.7. Even so, many questions remain. First, the absolute masses of the neutrinos are unknown. Second, the sign of Δm^2_{32} is unknown, resulting in two possible orderings for the neutrino masses. These are referred to as the "Normal" ordering, in which $m_3 > m_2 > m_1$, and the "Inverted" ordering, in which $m_2 > m_1 > m_3$, as shown in Figure 1.7. Third, the CP-phase of the PMNS-matrix, δ, has not been measured. Fourth, the possibility for additional, heavier neutrinos that do not interact via the weak force, but do mix with the other neutrinos, exists. Finally, and of greatest interest to this document, the mechanism for granting mass to neutrinos is currently unknown. As will be discussed in Section 1.3, the Standard Model does not allow for neutrino mass, and multiple possible mechanisms exist for granting it.

1.3 Theory of Neutrino Mass

The Standard Model of Particle Physics includes only left-handed neutrinos. The Lagrangian represents neutrinos as left-handed Weyl spinors, representing a left-handed (LH) particle and a right-handed (RH) anti-particle. A CPT transformation, flips between a LH particle and RH anti-particle; due to CPT invariance, these must have identical properties except for helicity and charge, meaning this is the simplest possible representation of a spin-$\frac{1}{2}$ particle. However, we now understand that neutrinos are massive, which cannot be explained without extending the Standard Model. This section will discuss possible mechanisms for generating neutrino mass and why extension of the Standard Model is required for each. For a more detailed and complete discussion, see C. Giunti and C.W. Kim, Chapter 6 [27].

1.3.1 A Brief Discussion of Helicity and Chirality

So far, this document has been loose in its description of handedness, which can refer to either helicity or chirality. The helicity operator (h) is defined as

$$h = \frac{\mathbf{s} \cdot \mathbf{p}}{|\mathbf{p}|} = \frac{p_1[\gamma^2, \gamma^3] + p_2[\gamma^3 \, \gamma^1] + p_3[\gamma^1 \, \gamma^2]}{2|\mathbf{p}|} \tag{1.9}$$

where $\mathbf{s}$ is spin, $\mathbf{p}$ is particle momentum, and γ^i are Dirac matrices. Helicity can be equivalently described as the particle spin projected onto its momentum. The chirality operator (γ^5) is defined as

$$\gamma^5 = i\gamma^0\gamma^1\gamma^2\gamma^3 \tag{1.10}$$

Furthermore, for massless particles (and in the ultra-relativistic limit for massive particles), helicity and chirality eigenstates are identical, with equal eigenvalues for particles and opposite eigenvalues for anti-particles.

For massive particles, helicity is not Lorentz invariant, while chirality is. This can be intuitively seen by imagining a massive, classical fermion moving through free space from frames of reference moving slower and faster than it. When switching between these frames, the spin direction will appear the same, while the direction of momentum will flip, meaning

that the helicity will flip as well. For this reason, the helicity operator cannot appear as a part of the Standard Model Lagrangian while chirality can. This means that Fermion spinors are eigenstates of chirality, and the weak force interacts directly with left-chiral states rather than left-helicity states. On the other hand, for massive particles, helicity is a constant of motion since momentum and angular momentum are both conserved, while chirality is not.

1.3.2 Dirac Mass

All other Standard Model fermions gain mass via the Dirac mechanism, and are called Dirac fermions[28]. A Dirac fermion is represented by a Dirac spinor, which consists of a left-handed Weyl spinor paired with a right-handed one. Dirac spinors represent the states used to solve the Dirac equation which describes the wavefunction for a free, relativistic, spin-1/2 particle:

$$i\gamma^\mu \partial_\mu \psi - m\psi = 0 \tag{1.11}$$

In the standard model lagrangian, a Dirac mass term appears as:

$$\mathcal{L}_{Dirac} = -m\bar{\nu}\nu = m(\bar{\psi}_L\psi_R + \bar{\psi}_R\psi_L) \tag{1.12}$$

This represents a coupling between a left- and right-handed fermion.

In the Standard Model, a bare mass term is forbidden because the fermions are not invariant under SU(2) gauge transformations, due to the doublet structure of the left-handed fermions. A mass term is introduced by the Higgs field, which is a spin-0 doublet $\Phi = \begin{pmatrix} \phi^+ \\ \phi_0 \end{pmatrix}$. The ϕ^+ field is charged and the ϕ_0 field is neutral, and therefore able to take on a vacuum expectation value:

$$\Phi(x) = \frac{1}{\sqrt{2}} \begin{pmatrix} 0 \\ v + H(x) \end{pmatrix} \tag{1.13}$$

where v is the vacuum expectation and $H(x)$ is the field that produces the Higgs Boson. Through the Higgs, then, we can introduce mass to a Standard Model fermion in the doublet

$\begin{pmatrix} f' \\ f \end{pmatrix}_L$ and singlet f_R:

$$\mathcal{L}_Y = -g \begin{pmatrix} \bar{f}' & \bar{f} \end{pmatrix}_L \cdot \frac{1}{\sqrt{2}} \begin{pmatrix} 0 \\ v + H(x) \end{pmatrix} f_R = -\frac{gv}{\sqrt{2}} \bar{f}_L f_R \qquad (1.14)$$

where g is the coupling of the fermion to the Higgs field. To introduce Dirac mass to the neutrino, we would have to add a right-handed neutrino singlet to the standard model with a non-zero Higgs coupling.

1.3.3   Majorana Mass

A second mechanism for granting mass to neutral fermions exists, called the Majorana mechanism[29]. In this case, fermions are the solutions to the Majorana equation:

$$i\gamma^\mu \partial_\mu \psi - m\psi^C = 0 \qquad (1.15)$$

where ψ^C is the charge-conjugated field:

$$\psi^C = \mathcal{C}\bar{\psi}^T \qquad (1.16)$$

The Majorana equation is solved by a two-component Majorana spinor consisting of a single left-chiral spinor or right-chiral spinor:

$$\psi = \psi_{L/R} + \psi^C_{L/R} \qquad (1.17)$$

where $\psi_{L/R}$ are left/right-handed Weyl spinors. For a Majorana fermion, the mass term in the Lagrangian is:

$$\mathcal{L}_{Majorana} = -m\bar{\psi}^C\psi = -m(\bar{\psi}^C{}_L\psi_L + \bar{\psi}_L\psi^C_L) \qquad (1.18)$$

This represents a coupling between a left-handed particle and a right-handed anti-particle. Because of this mass coupling, the electric charge of the fermion is no longer a constant of motion; this means that only a neutral fermion can possibly have Majorana mass, making

the neutrino the only Standard Model particle that could possibly be a Majorana fermion. Similarly, lepton number is no longer a constant of motion, which would enable lepton-number violating processes. For this reason, we often say that a Majorana particle is its own anti-particle.

The Standard Model, however, forbids a bare Majorana mass term, once again due to the SU(2) doublet structure of the left-handed leptons. Such a term would appear as:

$$\mathcal{L}_{Majorana} = -m \left(\begin{pmatrix} \bar{e} & \bar{\nu} \end{pmatrix}_L \begin{pmatrix} e^C \\ \nu^C \end{pmatrix}_L + h.c. \right) \tag{1.19}$$

which would violate electric charge conservation due to the electron term. If the Standard Model is an effective field theory for a more complete model with BSM physics at higher energy scales, a dimension five term could be introduced to the Lagrangian that generates Majorana mass:

$$\mathcal{L}_5 = -\frac{g}{\Lambda}(L_L^T \tau_2 \Phi)C^\dagger(\Phi^T \tau_2 L_L) + h.c. = -\frac{gv^2}{2\Lambda}\bar{\nu}^C_L \nu_L + h.c. \tag{1.20}$$

where L_L is a lepton doublet and Φ is the Higgs doublet, and Λ is the energy scale of the BSM physics involved. Several possible BSM diagrams that generate this dimension five term are shown in Figure 1.9.

If neutrinos are Majorana, the PMNS matrix is allowed to have additional CP phases as follows:

$$U_{MJ}^{\text{PMNS}} = U_D^{\text{PMNS}} \cdot \begin{pmatrix} e^{i\alpha_1/2} & 0 & 0 \\ 0 & e^{i\alpha_2/2} & 0 \\ 0 & 0 & 1 \end{pmatrix} \tag{1.21}$$

where U_D^{PMNS} is the PMNS matrix as described in equation 1.7, U_{MJ}^{PMNS} is the PMNS matrix modified for Majorana neutrinos, and α_1 and α_2 are the Majorana CP phases.

1.3.4   Why are Majorana Neutrinos Compelling?

If neutrinos are Majorana particles, it would potentially help to answer additional questions about the universe. One such question is why neutrinos are so much lighter than all the other
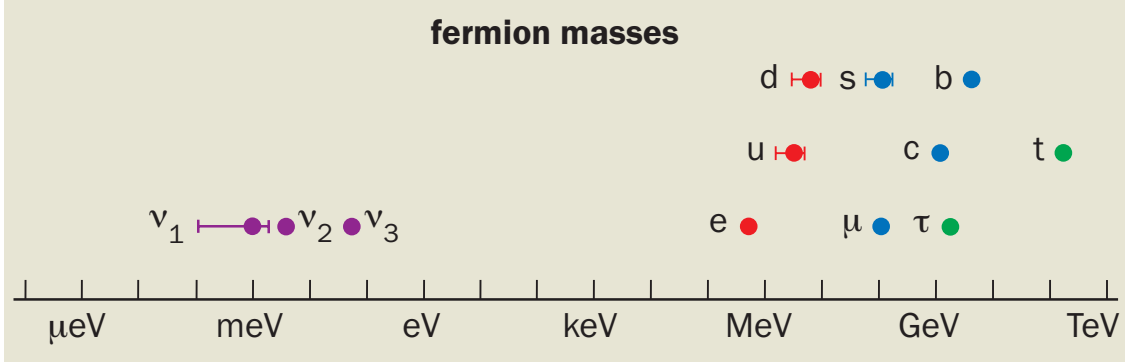
Figure 1.8: Comparison of the masses of fermions in the standard model. Current limits place six orders of magnitude between the heaviest neutrino and the electron. Taken from H. Murayama, Physics World (2002).

Standard Model fermions. Current upper limits on neutrino mass are $\sqrt{\sum_{i=0}^{3}|U_{ei}|^2 m_i^2} < 2$ eV from direct mass measurements and $\sum_{i=0}^{3} m_i < (0.3 - 1.3)$ eV from cosmological measurements, depending on model assumptions[9]. As shown in Figure 1.8, these limits place nearly six orders of magnitude difference in mass between the heaviest neutrino and the lightest charged fermion, which is larger than the log-scale difference between the lightest and heaviest charged fermion! While this doesn't strictly require explanation, it is an unusual feature of the Standard Model if neutrinos gain their mass via the same mechanism as the other fermions. Because the dimension five operator generates neutrino mass of $\frac{gv^2}{\Lambda}$, and where gv^2 is the square of a mass term generated by coupling a fermion to the Higgs field, and Λ is expected to be at an energy scale beyond the electroweak unifcation scale, the mass generated would likely be very small. Since this dimension five operator produces very light neutrino masses from the addition of heavy particles, the mechanisms for producing mass are often referred to as see-saw mechanisms.

Another mystery is why the universe consists of a significant amount of Baryonic matter (i.e. "normal" matter). Under the Standard Model and the big bang theories, one would expect in the early universe to create large amounts of matter and anti-matter, which would

annihilate leaving almost no matter in the universe. Sakharov proposed three conditions necessary to generate the matter that we see[30]:

- Baryon number violation

- C and CP violation

- B-, C-, and CP-violating process must happen out of thermal equilibrium

Since the Sphaleron process described in Section 1.1.5 is capable of converting lepton number into baryon number, Lepton number conservation would similarly suffice to generate a baryon number asymmetry. A process that generates Majorana neutrino mass would also violate lepton number conservation and generate additional CP violation, potentially solving this mystery.

1.3.5   Mechanisms for Generating Majorana Mass

This section will briefly discuss an incomplete list of BSM theories that could generate the dimension five operator that creates Majorana neutrino mass. For more detailed descriptions of these theories, see [32, 33].

- **Minimal Extention of the Standard Model (νMSM)**: The simplest extention of the Standard Model that would produce Majorana neutrino mass is to simply add a right-handed neutrino singlet, N. This neutrino would be sterile, meaning it would not interact with any of the force carrying Bosons of the Standard Model. A right-handed neutrino would enable the addition of a Dirac mass term m_D, and since it would be an SU(2) singlet, also a Majorana mass term M_R. In this case, the mass term of the Lagrangian would appear as:

$$\mathcal{L}_{\nu\text{SM}} = \begin{pmatrix} \bar{\nu}^C_L & \bar{N}^C_R \end{pmatrix} \begin{pmatrix} 0 & m_D \\ m_D & M_R \end{pmatrix} \begin{pmatrix} \nu_L \\ N_R \end{pmatrix} \tag{1.22}$$

Canonical seesaw models
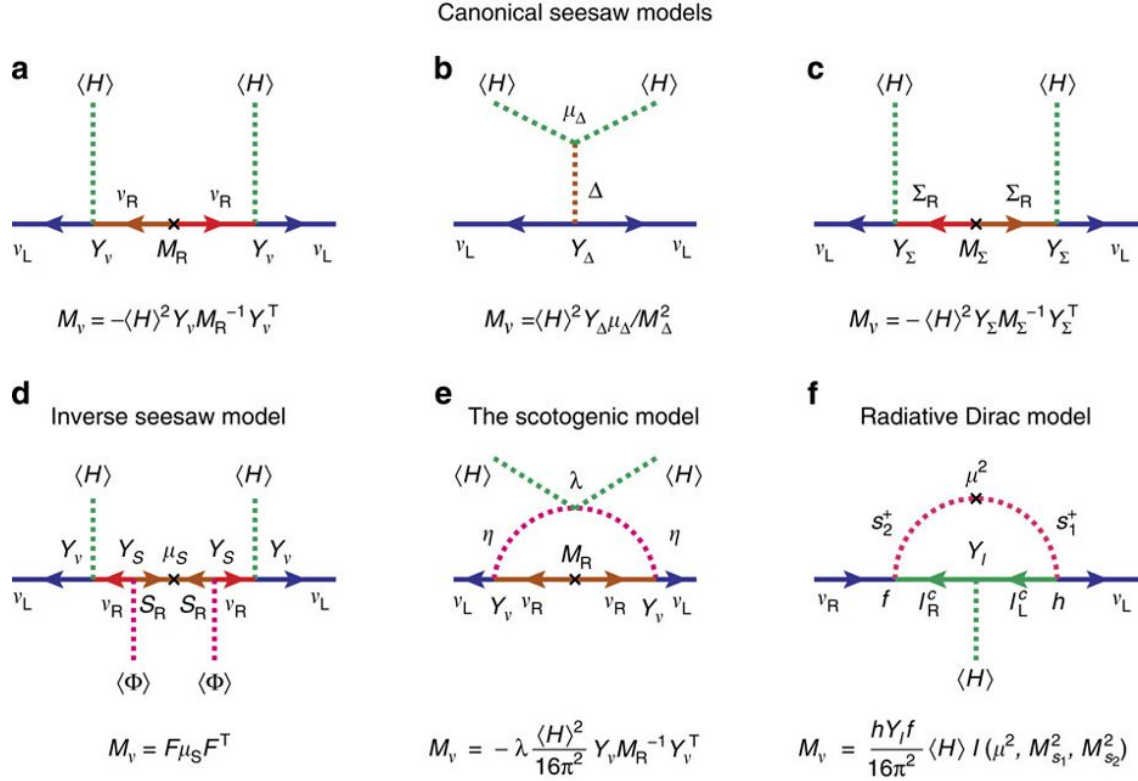
Figure 1.9: Examples of BSM mass generating mechanisms. Mechanisms a-e all reduce to the dimension five operator in equation 1.20 in a low energy effective theory. See referece [31].

The mass matrix can be diagonalized, resulting in a left-chiral eigenstate with mass $\frac{m_D^2}{M_R}$ and a heavy, right-chiral eigenstate with mass $\approx M_R$. This process of generating a light, left-handed Majorana mass from a heavy right-handed neutrino is called the Type I see-saw mechanism (letter a in Figure 1.9). If the Dirac masses are at a similar energy scale to the other Standard Model fermions, and the right-handed mass is between the electro-weak and GUT energy scales, it is possible to generate neutrinos with masses similar to what we see.

- **Left-Right Symmetric Model (LRSM)**: This model adds an additional SU(2) gauge symmetry that results in a second weak force that acts only on right-chiral

particles. The right-handed symmetry breaking scale is at higher energies than the left-handed one, with the result that the right-chiral weak force interacts even less strongly than the left-chiral weak force. Under this model, the right-handed Fermions gain a doublet structure, requiring the addition of a right-handed neutrino. Additional Higgs fields are also required, resulting in a pair of Higgs triplets. This term would interact with both the right- and left-handed lepton doublets, generating Dirac and Majorana mass terms. Because the right-handed electroweak symmetry breaking scale is much higher than the left-handed one, this model would produce a light left-handed Majorana neutrino and a heavy right-handed Majorana neutrino. This is an example of a type II mixed with a type I see-saw mechanism (b and a in Figure 1.9).

- **SU(5) or SO(10) Grand Unified Theory (GUT)** SU(5) and SO(10) are the two smallest simple Lie groups that contain SU(3)×SU(2)×U(1) as a subgroup, making them popular groups for Grand Unified Theories. These GUTs violate lepton and baryon number, introducing particles called Leptoquarks. They also predict proton decay with a half-life that could be feasibly detected[34]. SU(5) GUTs are disfavored by such measurements, while SO(10) GUTs will be investigated in future experiments. GUTs often add an additional fermion triplet that would induce a Majorana mass in the neutrino via a type III and type I see-saw mechanism (c and a in Figure 1.9).

- **R-Parity Violating Super-Symmetry (RPV SUSY)**: SUSY models add bosonic super-symmetric partners for each Standard Model fermion and vice-versa. R-parity is a discrete symmetry within SUSY; an R-parity transformation switches between a particle and its super-symmetric partner. Versions of SUSY that violate R-Parity symmetry enable Baryon and Lepton number violation, and in particular can add a Majorana neutrino mass.

The νMSM, as the minimal extension (only one particle added) needed to generate neutrino mass, is the typical model used when discussing Majorana neutrinos. The other models
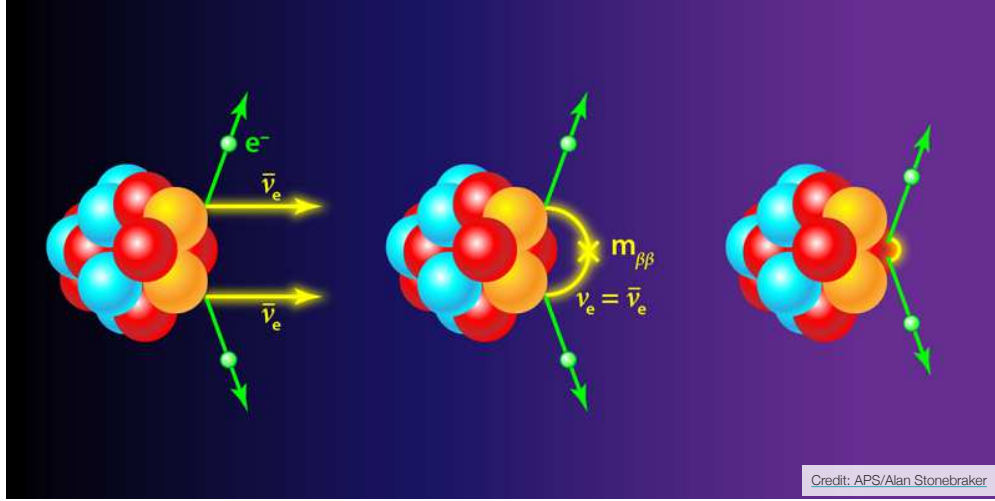
Figure 1.10: A drawing of three possible modes of double-beta decay. Left: $2\nu\beta\beta$; Center: $0\nu\beta\beta$ via light neutrino exchange; Right: $0\nu\beta\beta$ via a short range mechanism

mentioned, while more complex, may also solve other problems in physics for which the Standard Model is insufficient. Due to their complexity, these other models will likely be observable through channels other than neutrino mass, such as scattering events at high energy colliders.

1.4 Double-Beta Decay

The only feasible way to determine whether or not the neutrino is a Majorana particle is to search for neutrinoless double-beta decay. Two-neutrino double-beta ($2\nu\beta\beta$) decay is an allowed second-order process in the standard model. Neutrinoless double-beta ($0\nu\beta\beta$) decay is a hypothetical process that depends on the Majorana nature of the neutrino. This section will describe both two-neutrino- and neutrinoless- double-beta decay, and discuss the theory for calculating the half-lives of each.
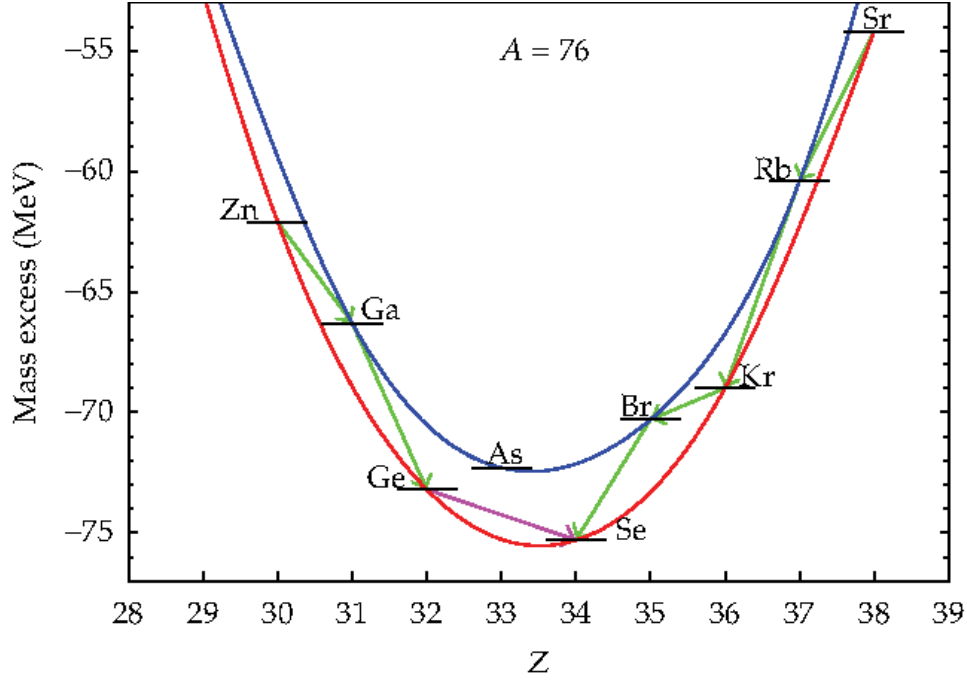
Figure 1.11: Energy levels of isotopes along the $Z = 76$ isobar. The splitting of the even-even (red) and odd-odd (blue) nuclei is due to pairing interactions. In this case, ^{76}Ge $\beta\beta$-decay into ^{76}Se is observable because the single β-decay into ^{76}As is energetically forbidden. Taken from J. Menendez's dissertation.

1.4.1 Two-neutrino Double-Beta Decay

During $2\nu\beta\beta$ decay, two neutrons inside a single nucleus become two protons, two electrons and two electron anti-neutrinos, equivalent to two simultaneous single β-decays. $\beta\beta$-decay is only observable in cases where single β-decay is energetically forbidden (with the exception of ^{48}Ca, whose single *beta*-decay has a half-life $> 10^{19}$ y). As shown in Figure 1.11, this situation occurs in nuclei with even numbers of nucleons: due to pairing interactions among protons and neutrons, odd-odd nuclei have higher masses than even-even nuclei, which can lead to single β-decay being forbidden while $\beta\beta$-decay is allowed. Because of the two neutrinos, which will carry kinetic energy out of any detectors, $2\nu\beta\beta$ has a broad energy spectrum as
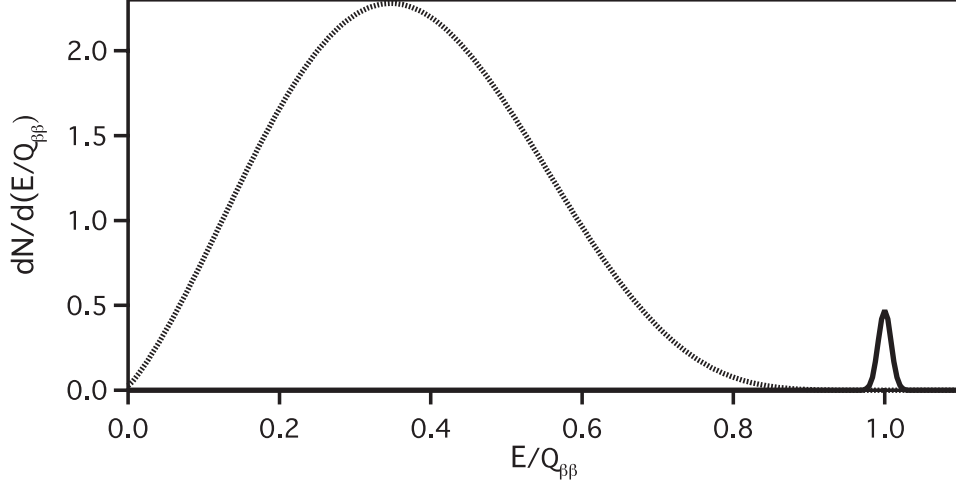
Figure 1.12:   Spectrum of electron energies in double-beta decay. The broad spectrum is due to $2\nu\beta\beta$, while the peak at the Q-value is due to $0\nu\beta\beta$ and, in the spectrum shown, has an amplitude of 1% that of the $2\nu\beta\beta$ spectrum. Taken from [35].

shown in Figure 1.12, similar to single β-decay. $\beta\beta$-decay was predicted in 1935 by Goeppert-Mayer[36], and was first measured using geochemical techniques in ^{130}Te in 1950[37], and directly in ^{82}Se in 1987[38]. $2\nu\beta\beta$ is possible in 35 naturally occuring isotopes, and has been detected in 11, with half-lives ranging from 10^{18} y to 10^{24} y[39].

1.4.2   Calculating Half-life for $2\nu\beta\beta$

The half-life for $2\nu\beta\beta$ can be expressed, per Fermi's Golden Rule, as:

$$\frac{1}{T_{1/2}^{2\nu}} = G_{2\nu}(Q, Z)(g_A^{eff})^4|M_{2\nu}|^2 \tag{1.23}$$

This equation is discussed in greater detail in [39, 40]. The three components of this equation are:

- $G_{2\nu}(Q, Z)$ is the phase space factor, an integral over the final state density for $2\nu\beta\beta$, which depends primarily on the Q-value of the decay. The phase space factor is dis-

cussed and precisely calculated in [41, 42, 43], using exact Dirac wavefunctions for the electrons and neutrinos, and accounting for the finite size of the nucleus and Coulomb screening by electrons. The differential phase space factor is also used to compute the electron energy spectrum and electron angular correlations.

- $|M_{2\nu}|$ is the nuclear matrix element (NME), which quantify information about the nuclear states involved in the decay. The NME can be expressed as:

$$M_{2\nu} = M_{GT}^{2\nu} - \frac{g_V^2}{g_A^2} M_F^{2\nu} \tag{1.24}$$

where $M_F^{2\nu}$ is the Fermi component which is produced by the Vector component of the β decay, $M_{GT}^{2\nu}$ is the Gamow-Teller component which is produced by the Axial Vector component, and $\frac{g_V^2}{g_A^2}$ is the ratio of the Vector and Axial Vector strengths. The Fermi component does not change the spin of nucleons, and due to isospin invariance, the decay must fall into the isobaric analog state of the daughter nucleus; as a result, it is highly suppressed compared to the Gamow-Teller component, so we will focus on that. The Gamow-Teller component of the NME can be expressed as:

$$M_{GT}^{2\nu} = \sum_n \frac{\langle f | \sigma_{\mathbf{a}} \sum_a \tau_a^+ | n \rangle \langle n | \sum_b \sigma_{\mathbf{b}} \tau_b^+ | i \rangle}{E_n - (M_i + M_f)/2} \tag{1.25}$$

where n are the intermediate nuclear states, and a and b are the individual nucleons that can decay. The Gamow-Teller decay requires spin flips in nucleons, and will therefore primarily involve decays through the intermediate 1^+ states. NMEs depend entirely on the nuclear structure, meaning that analogous transitions caused by different physical processes will have the same NME; in addition, the terms involving the intermediate nuclear states are related to the NME for these single transitions. As a result, the NMEs can be independantly studied through charge-exchange interactions, in which a proton from a proton beam replaces a neutron in the parent, producing an intermediate state, or vice-versa.

- g_A^{eff} is the axial vector coupling strength. For calculations of β-decay rates, the half-lives are systematically underestimated by a factor of ~ 0.74 when using the value of

(a) β-Decay Quenching

(b) $2\nu\beta\beta$ Quenching
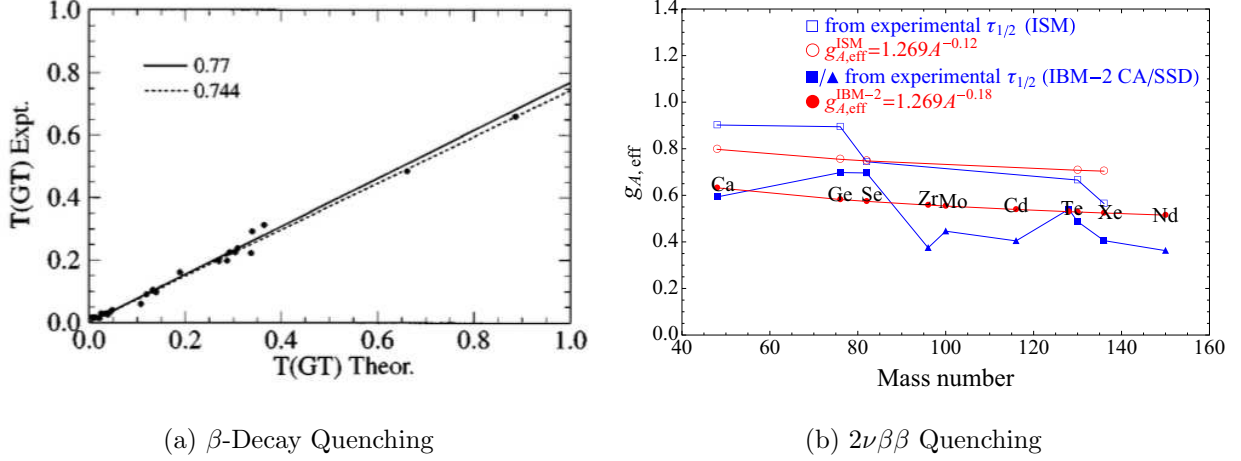
Figure 1.13: Measurements of single- and double-beta decay Gamow-Teller matrix elements consistently observe smaller values than predicted by theory. This is solved by using an effective g_A that is smaller than the value measured for a free neutron. Taken from [40].

g_A measured for the decay of a free neutron. This suppression of the rate is referred to as the quenching problem, and was only solved for singe-beta decay in 2019[44]. Applying a similar quenching factor is similarly necessary to calculate $2\nu\beta\beta$ half-lives. Figure 1.13 shows the necessity of this factor in comparisons between experimental and theoretical measurements of Gamow-Teller transitions.

1.4.3 Neutrinoless Double-Beta Decay

$0\nu\beta\beta$ is a hypothetical process in which two neutrons become two protons and two electrons, with no accompanying neutrinos. Because of the lack of neutrinos, all kinetic energy will be carried by electromagnetically interacting particles; if all of the energy is captured in a detector, it will result in a single sharp energy peak at the end-point of the $2\nu\beta\beta$ spectrum (see Figure 1.12). This decay violates lepton number by $\Delta L = 2$, requiring BSM physics. If the neutrino is a Majorana particle, it will induce $0\nu\beta\beta$ via the neutrino exchange diagram
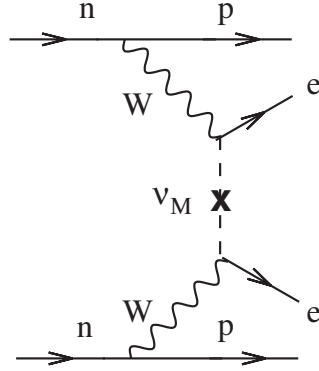
Figure 1.14: A Feynman diagram for $0\nu\beta\beta$ involving the exchange of a light neutrino.

shown in Figure 1.14. $0\nu\beta\beta$ was first suggested as a test of the Majorana nature of neutrinos by Furry in 1939[45]. Searches have been performed in ten different isotopes, with no positive results yet. The most sensitive experiments have half-life limits in the range of $10^{25}-10^{26}$ yrs, in ^{136}Xe[46], ^{76}Ge[47] and ^{130}Te[48].

If $0\nu\beta\beta$ is observed, it will unambiguously mean that the neutrino is a Majorana particle. This is true thanks to the Schechter-Valle theorem (AKA the Black Box theorem), which demonstrates that the $0\nu\beta\beta$ diagram itself induces a Majorana mass term as in Figure 1.15[49]. It should be noted that this diagram is a four loop diagram, meaning that the mass induced would be extremely small. As a result, the discovery of $0\nu\beta\beta$ does not necessarily explain fully the origin of neutrino mass.

1.4.4 Calculating Half-life for $0\nu\beta\beta$ with Light Neutrino Exchange

Assuming that light neutrino exchange (LNE), as shown in Figure 1.14, is the dominant mechanism causing $0\nu\beta\beta$, the half-life for $0\nu\beta\beta$ can be expressed as:

$$\frac{1}{T_{1/2}^{0\nu}} = G_{0\nu}(Q,Z)(g_A^{eff,0\nu})^4|M_{0\nu}|^2|m_{\beta\beta}|^2 \tag{1.26}$$

This equation is derived and discussed in detail in [35, 40]. The components of this equation, which will mostly be familiar from equation 1.23, are as follows:
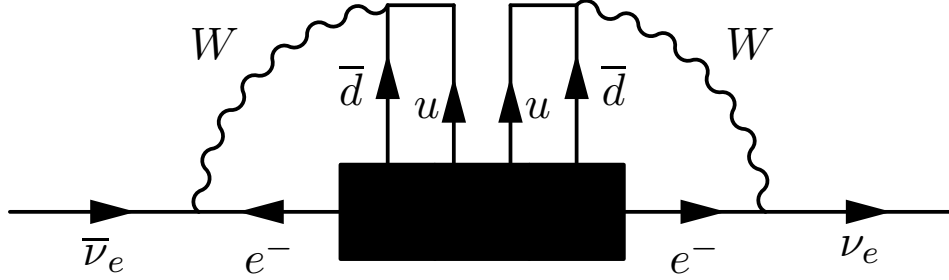
Figure 1.15: The "black box" diagram inducing Majorana neutrino mass from $0\nu\beta\beta$

- $G_{0\nu}(Q,Z)$ is the phase space factor. While the neutrinoless phase space factor differs numerically from the two-neutrino factor, it can be accurately calculated using the same techniques.

- $|M_{0\nu}|$ is the NME. This NME accounts for LNE with a long range, fermion propagator. This NME differs significantly from the $2\nu\beta\beta$ NME:

$$M_{0\nu} = M_{GT}^{0\nu} - \frac{g_V^2}{g_A^2} M_F^{0\nu} + M_T^{0\nu} \qquad (1.27)$$

where $M_T^{0\nu}$ is a the Tensor term of the NME. Recent work by Cirigliano, *et. al.* suggests that an additional contact term to the NME is also required and may have a value near to leading order[50]. The neutrino exchange operator increases the contribution of terms forbidden in the $2\nu\beta\beta$ NMEs, including the Fermi and Tensor terms and intermediate nuclear states beyond the 1^+ states. As a result, the $0\nu\beta\beta$ matrix element is very challenging to calculate; as Figure 1.19 shows, different choices of model result in a factor of ~ 3 difference in LNE NMEs. Section 1.4.6 will describe the differences between these models.

- $m_{\beta\beta}$ is the effective neutrino mass, expressed as:

$$m_{\beta\beta} = \sum_i m_i U_{ei}^2 = m_1 |U_{e1}|^2 + m_2 |U_{e2}|^2 e^{i(\alpha_2 - \alpha_1)} + m_2 |U_{e2}|^2 e^{-i(\alpha_1 + 2\delta)} \qquad (1.28)$$
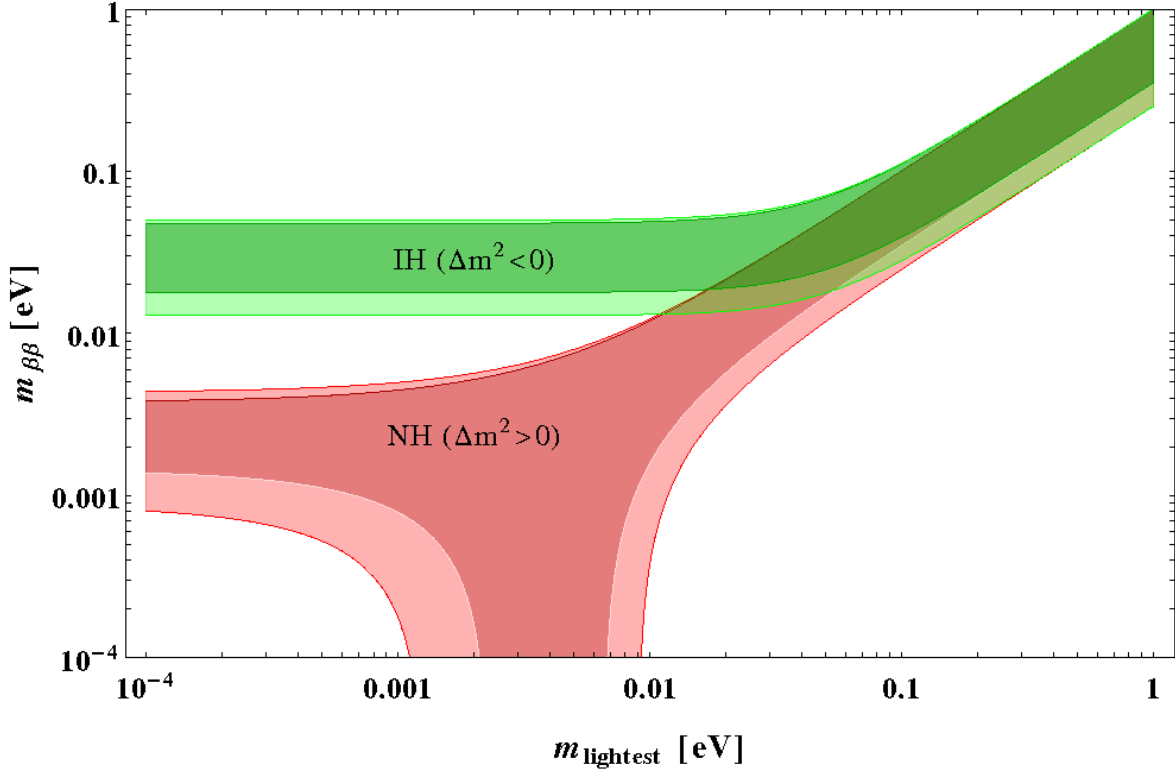
Figure 1.16: The allowed values of $m_{\beta\beta}$ based on equation 1.28 and current experimental constraints from oscillation experiments. $m_{lightest}$ is the mass of the lightest neutrino and can be determined by direct mass measurements or cosmological measurements. The allowed regions can be divided based on the mass ordering into the normal hierarchy (NH) band, the inverted hierarchy (IH) band. The light shaded regions at the boundaries of each band represent the propagation 3-σ uncertainties of oscillation parameters[51].

where m_i are the neutrino masses, U_{ei} are the PMNS matrix elements, $\alpha_{1/2}$ and δ are the CP phases. Strictly speaking, this term is included in the NME; however, since the neutrino mass is much smaller than the nuclear scale ($\sim$100 MeV), it can be separated from the NME. This term will be common between all $0\nu\beta\beta$ isotopes, and it contains interesting information about both the neutrino mass and leptonic CP violation. As a result, $m_{\beta\beta}$ is the target parameter for searches for $0\nu\beta\beta$, and is how the sensitivity and limits of experiments are compared. Figure 1.16 shows the allowed values of $m_{\beta\beta}$ based on the mass of the lightest neutrino using constraints from oscillation experiments. In order to compute a value or limit for $m_{\beta\beta}$ based on a half-life measurement, it is critical to have accurate knowledge of the NME; for this reason, reducing uncertainties and understanding the differences between different NME models is a top priority. The current best limit of $m_{\beta\beta} < 61 - 165$ meV has been set by the KamLAND-Zen experiment[46]; the factor of three range reflects the uncertainty in the NME.

- g_A^{eff} is the quenched g_A coupling. While the quenching factor for $2\nu\beta\beta$ has been verified to be similar, its effect on $0\nu\beta\beta$ is currently unknown. There are good reasons to believe it could be either larger or smaller than the traditional quenching factor, and this adds another factor of $\sim$3 uncertainty to the NMEs for all isotopes beyond what is shown in Figure 1.19[40]. The solution to single-beta g_A quenching suggests an optimistic scenario for $0\nu\beta\beta$ and should reduce this uncertainty in the future.

1.4.5   *Calculating Half-life for $0\nu\beta\beta$ with Other Physics Mechanisms*

The previous section assumed that LNE is the dominant mode for $0\nu\beta\beta$; however, with many models for generating Majorana neutrino mass, exchanges of other, heavier particles may be the primary decay mode. In such cases, $0\nu\beta\beta$ is not primarily generated by the aforementioned dimension-5 effective Standard Model Lagrangian term, but instead through dimension 6, 7 and 9 terms[52]. Figure 1.17 shows a sampling of different BSM particle

(a) $0\nu\beta\beta$ Diagrams from LRSM

(b) $0\nu\beta\beta$ Diagrams from RPV-SUSY
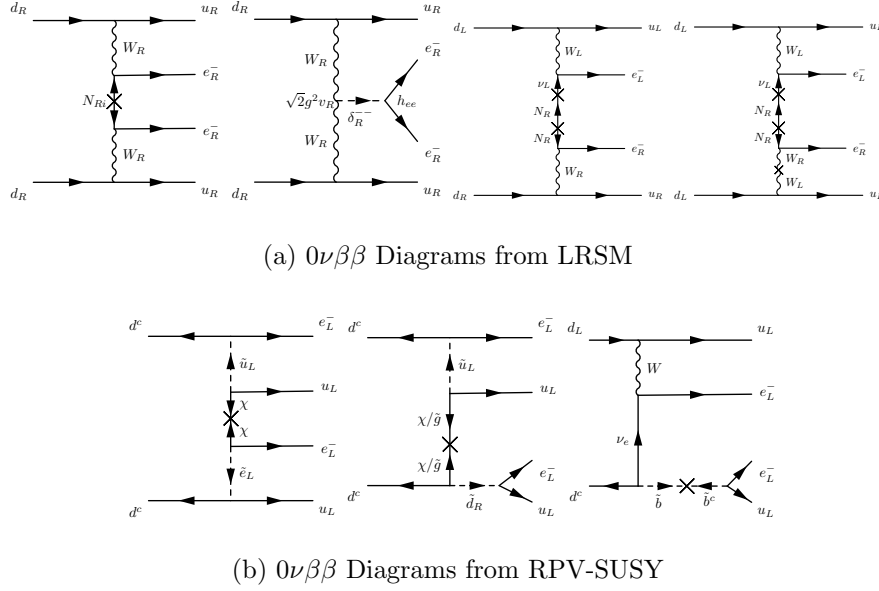
Figure 1.17: A sampling of Feynman diagrams for $0\nu\beta\beta$, assuming exchange of heavy BSM particles. Taken from [32].

exchanges that could potentially cause $0\nu\beta\beta$. A generic equation for the half-life is:

$$\frac{1}{T_{1/2}^{0\nu}} = \sum_i G_{0\nu}^i(Q,Z)(g_A^{eff,0\nu})^4 |M_{0\nu}^i|^2 \eta_i^2 \tag{1.29}$$

where i indexes over each mode of $0\nu\beta\beta$, $G_{0\nu}^i(Q,Z)$ and $M_{0\nu}^i$ are the independant phase space factors and NMEs, and η_i includes the new physics parameters. Because the particles exchanged tend to be heavier than the nuclear scale, the interactions will be short-range or point-like inside the nucleus. Most heavy-particle exchange interactions will be dominated in an effective theory by the three diagrams in Figure 1.18. The variety of mechanisms that could lead to $0\nu\beta\beta$ means that additional measurements will be required in order to understand the NMEs involved and to measure the physics parameters of interest. Furthermore, this removes many of the constraints on the half-life that exist with LNE; even so, any of these mechanisms will involve a LNE component as a result of the Schechter-Valle theorem. This means that, absent fine-tuned destructive interference, these new mechanisms would
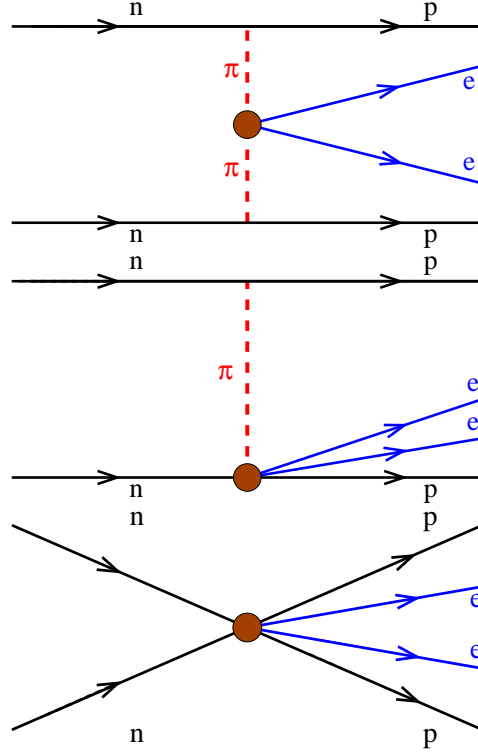
Figure 1.18: Effective short range operators for generating $0\nu\beta\beta$. The top two involve pion exchange; the bottom one is the contact operator. These operators are expected to dominate in most BSM $0\nu\beta\beta$ mechanisms involving heavy particle exchange. Taken from [40].

result in half-lives higher than those predicted for LNE.

1.4.6 Nuclear Matrix Elements

As previously mentioned, accurate NMEs are critical for interpreting the results of a $0\nu\beta\beta$ search. There is a high degree of uncertainty in the NMEs due to several factors. First, the mechanism for $0\nu\beta\beta$ is unknown; most NMEs are calculated assuming LNE, which will be the focus here. Second, different models used for calculating NMEs produce results that differ by a factor of ~ 3. Finally, without understanding the mechanism behind g_A quenching, there is another factor of ~ 3 uncertainty. This section will discuss many of the models used

to produce NMEs; for more complete discussions, see [35, 40]. These techniques can be used for $2\nu\beta\beta$ LNE $0\nu\beta\beta$ or $0\nu\beta\beta$ by some other mechanism. Figure 1.19 shows the LNE $0\nu\beta\beta$ NMEs calculated by several different theory groups.

The most commonly used NME models are:

- **Quasi Random Phase Approximation (QRPA)**: proton-neutron (pn)QRPA is a mean-field based model that uses effective particle-particle and particle-hole operators to model proton and neutron transitions near the Fermi surface. QRPA is capable of exploring a large set of valence states, but has trouble accounting fully for nucleon-nucleon correlations. Many variants of QRPA exist, incuding renormalized (R)QRPA and multiple commutator model (MCM)-QRPA.

- **Shell Model (SM)**: The nuclear shell model attempts to compute Slater determinates using a limited configuration space including nucleon states near the Fermi surface. SM is capable of including complex nucleon-nucleon correlations, but the computational complexity grows rapidly with the number of states considered, meaning only a small number of valence states can be included.

- **Energy Density Functional (EDF)**: EDF theory attempts to minimize an energy functional with respect to local densities such as the number density ρ, spin density s, current density j, etc. The Hamiltonian is minimized, with constraints, over these quantities to obain the energy density functional, which can be used to compute exact nuclear properties. EDF theories are not close enough to the exact functionals to accurately compute all quantities in all nuclei and require the explicit inclusion of correlations.

- **Interacting Boson Model (IBM)**: IBM utilizes the pairing of nucleons into Bosonic quasi-particles. IBM is capable of treating a larger valence space than SM, but loses some degrees of freedom.
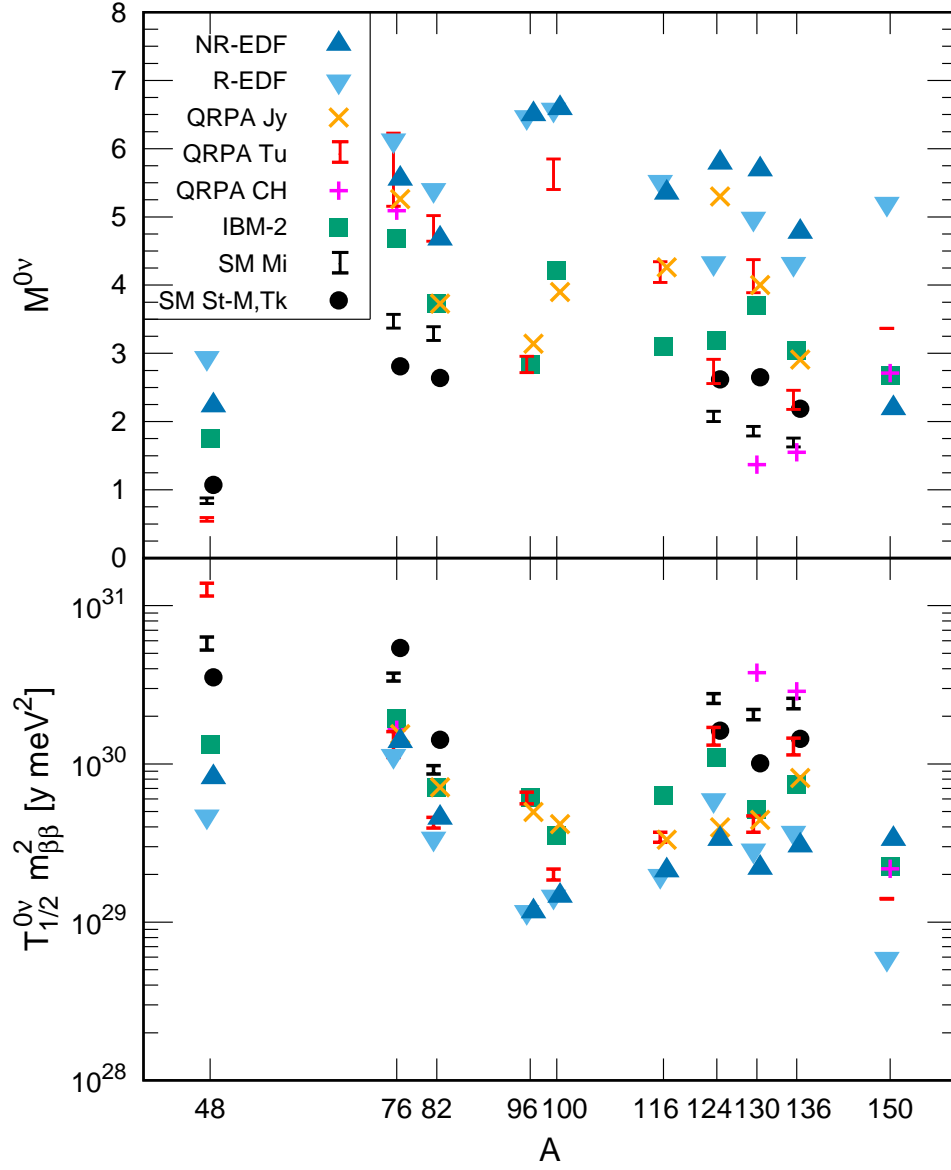
Figure 1.19: Values of LNE NMEs for all $0\nu\beta\beta$ isotopes being explored by experiments, using a variety of models. Taken from [40].

- **Effective Field Theory (EFT)**: A set of low energy effective many-body operators can be derived and incorporated into many-body calculations using any of the previously mentioned methods. Chiral (χ)EFT involves the use of up-to-four body operators, which can be calculated using lattice-QCD. One further advantage of this approach is that it is capable of computing errors, unlike the other approaches. This method cannot yet be used for $0\nu\beta\beta$ NMEs, but there are active attempts to develop this capability.

Broadly speaking, there is a tradeoff between the number of valence states that can be included in a calculation and the complexity of correlations that can be included; these differences appear to be responsible for the disagreement between different models. Ideally, improvements in these different models will eventually lead to greater agreement. These models are currently incapable of predicting the effect of g_A quenching in $0\nu\beta\beta$.

1.5 Double-Beta Decay to Excited States

Most $\beta\beta$ isotopes can decay into multiple excited states of the daughter nucleus. Because these are even-even nuclei, these decays will go from a 0^+ ground state of the parent nucleus to either a 0^+ or 2^+ excited state of the daughter. Because of the higher mass of the excited daughter state, the Q-value of an excited state decay is reduced compared to the ground state decay. In addition, the daughter will promptly deexcite into the ground state, releasing one or more gamma-rays in the process. These additional γs provide a unique detection signature that can help in searching for $\beta\beta$-decays to excited states. Figure 1.20 shows a generic $\beta\beta$ decay scheme with three excited states.

Compared to decays to ground states, the rate of excited state decays is suppressed. To first order, the phase space factor scales with the Q-value E as E^{11} for $2\nu\beta\beta$ and E^5 for $0\nu\beta\beta$; this can suppress the excited state decay rate by many orders of magnitude relative to the ground state decay rates. Furthermore, for decays to 2^+ excited states, the change in angular momentum further suppresses the decay rate.
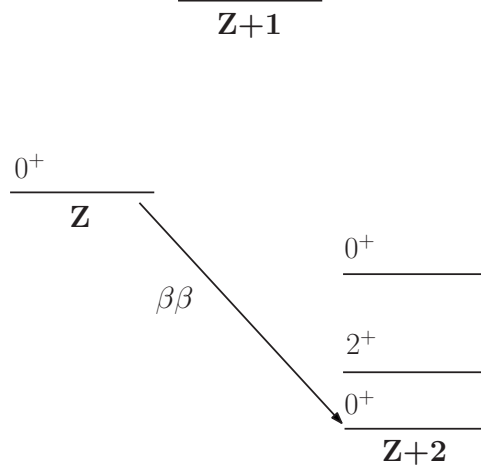
Figure 1.20: A generic level diagram for $\beta\beta$-decay, showing multiple excited nuclear daughter states that could result from the decay. This diagram has two excited states (one 0^+ and one 2^+).

So far, $2\nu\beta\beta$ to first excited 0^+ states have been observed in ^{100}Mo and ^{150}Nd, but not in any other isotope. The NME calculations vary significantly depending on what model is used for their calculation. This means that measurement of $\beta\beta$-decay to excited states can act as a test for these different models. So far, observed half-lives have differed significantly from predictions, offering an opportunity to understand sources of error in these calculations. Because of differences between the $2\nu\beta\beta$ and $0\nu\beta\beta$ decay modes previously discussed, such a comparison cannot act as a silver bullet for understanding $0\nu\beta\beta$ NMEs. For a detailed discussion of current experiments and calculations, see [53]. Decay to excited states half-lives are also sensitive to additional BSM physics.

1.5.1 $2\nu\beta\beta$ NMEs in ^{76}Ge

Table 1.2 contains a list of theoretical predictions of the half-life of each $2\nu\beta\beta$ excited state decay mode for ^{76}Ge. The models presented use the same techniques and acronyms defined

in Section 1.4.6. For some references included in Table 1.2, half-lives were not provided (the IBM[54, 55] and EFT[56]); in these cases, the half-life provided was calculated using:

$$T_{1/2}^{2\nu \; E.S.} = T_{1/2}^{2\nu \; G.S.} \cdot \frac{G_{2\nu}^{G.S.} |M_{2\nu}^{G.S.}|^2}{G_{2\nu}^{E.S.} |M_{2\nu}^{E.S.}|^2} \tag{1.30}$$

where $T_{1/2}^{2\nu \; g.s.} = 1.926 \pm 0.094 \cdot 10^{21}$ y is the ground state decay half-life measured by GERDA Phase I. $G_{2\nu}$ are the phase space factors from Mirea, *et al.*[42], and $|M_{2\nu}|$ are the matrix elements reported by the given source. The EFT calculations[56] also provided error estimates, which tend to be $40 - 80\%$ for excited state decays and are not shown here. The half-life predictions for each decay mode of ^{76}Ge span many orders of magnitude; this uncertainty is found in all $\beta\beta$-isotopes[53]. This wide range using different techniques is related to a variety of factors, including the nuclear spectroscopy of the the intermediate and final nuclear states, and the physics underlying g_A quenching. A half-life measurement may prove helpful in understanding some errors of the NME models; optimistically, it may enable improvements in the $0\nu\beta\beta$ NME predictions as well.

1.5.2 $0\nu\beta\beta$ to Excited States

If the neutrino is Majorana, then $0\nu\beta\beta$ to excited states can occur. The NMEs for $0\nu\beta\beta$ to excited states vary significantly based on the underlying physics. It has been further shown that the ratio of the half-lives for $0\nu\beta\beta$ to the first 0^+ excited state and to the ground state varies based on the physics mechanism, as shown in Figure 1.21[67, 68]. This means that a measurement of both the excited- and ground-state decays could shed light on what BSM physics is causing $0\nu\beta\beta$.

1.5.3   Bosonic Component of Neutrinos

If we violate fundamental physical assumptions, including the Pauli exclusion principle and CPT theorems, the neutrino wavefunction could have a bosonic component[69]. Because of their neutrality and small mass, neutrinos are a strong probe of such physics. In $2\nu\beta\beta$ to 2^+ excited states, a bosonic component has been shown to increase the decay rate by

Table 1.2: Table of best half-life predictions and experimental limits for each ^{76}Ge $2\nu\beta\beta$ decay mode.

$2\nu\beta\beta$ Decay Mode	$T_{1/2}^{2\nu\beta\beta}$ (yr)	Experiment/Model	ref.	year
$0^+_{g.s.} \xrightarrow{2\nu\beta\beta} 0^+_1$ $Q_{\beta\beta}$= 916.8 keV $559.1 + 563.2$ keV γ	$> 3.7 \times 10^{23}$	GERDA	[57]	2019
	4.0×10^{22}	QRPA	[58]	1994
	4.5×10^{22}	QRPA	[59]	1996
	7.5×10^{21}	MCM-QRPA	[60]	1996
	$(1.0 - 3.1) \times 10^{23}$	RQRPA	[61]	1997
	$(1.2 - 5.8) \times 10^{23}$	RQRPA	[57]	2014
	7.1×10^{24}	IBM-2	[55]	2014
	$(2.3 - 6.7) \times 10^{24}$	SM	[57]	2014
	1.7×10^{24}	EFT	[56]	2018
$0^+_{g.s.} \xrightarrow{2\nu\beta\beta} 2^+_1$ $Q_{\beta\beta}$= 1480.0 keV 559.1 keV γ	$> 1.6 \times 10^{23}$	GERDA	[57]	2019
	1.2×10^{30}	SM	[62]	1984
	5.8×10^{23}	HFB	[63]	1994
	5.0×10^{26}	QRPA	[58]	1994
	2.4×10^{24}	QRPA	[59]	1996
	7.8×10^{25}	MCM-QRPA	[60]	1996
	1.0×10^{26}	RQRPA	[61]	1997
	$(2.4 - 4.3) \times 10^{26}$	RQRPA	[64]	1998
	5.75×10^{28}	pnQRPA	[65]	2007
	2.0×10^{27}	RQRPA	[66]	2014
	1.0×10^{27}	EFT	[56]	2018
$0^+_{g.s.} \xrightarrow{2\nu\beta\beta} 2^+_2$ $Q_{\beta\beta}$= 822.0 keV $64\% : 657.0 + 559.1$ keV γ $36\% : 1216.1$ keV γ	$> 2.3 \times 10^{23}$	GERDA	[57]	2019
	1.0×10^{29}	QRPA	[58]	1994
	1.3×10^{29}	MCM-QRPA	[60]	1996
	$(0.7 - 2.2) \times 10^{28}$	RQRPA	[61]	1997

approximately an order of magnitude[70, 71]. No search for decays to excited states has yet probed 2^+ decay half-lives high enough to test this prediction, but in many isotopes, experimental capabilities are improving to the point where this may be feasible.

1.6 Summary

Double-beta decay provides a powerful probe of neutrino physics beyond the Standard Model. Detection of $0\nu\beta\beta$ would indicate that neutrinos are Majorana fermions and provide violation of lepton number. However, due to the difficulty of computing the nuclear matrix elements, interpretting experimental results becomes difficult. Detection of $\beta\beta$-decay to excited states would provide additional data to help improve NME models, and would also potentially open windows to additional BSM physics. This dissertation will describe the search for $\beta\beta$-decay to excited states in ^{76}Ge using the MAJORANA DEMONSTRATOR.
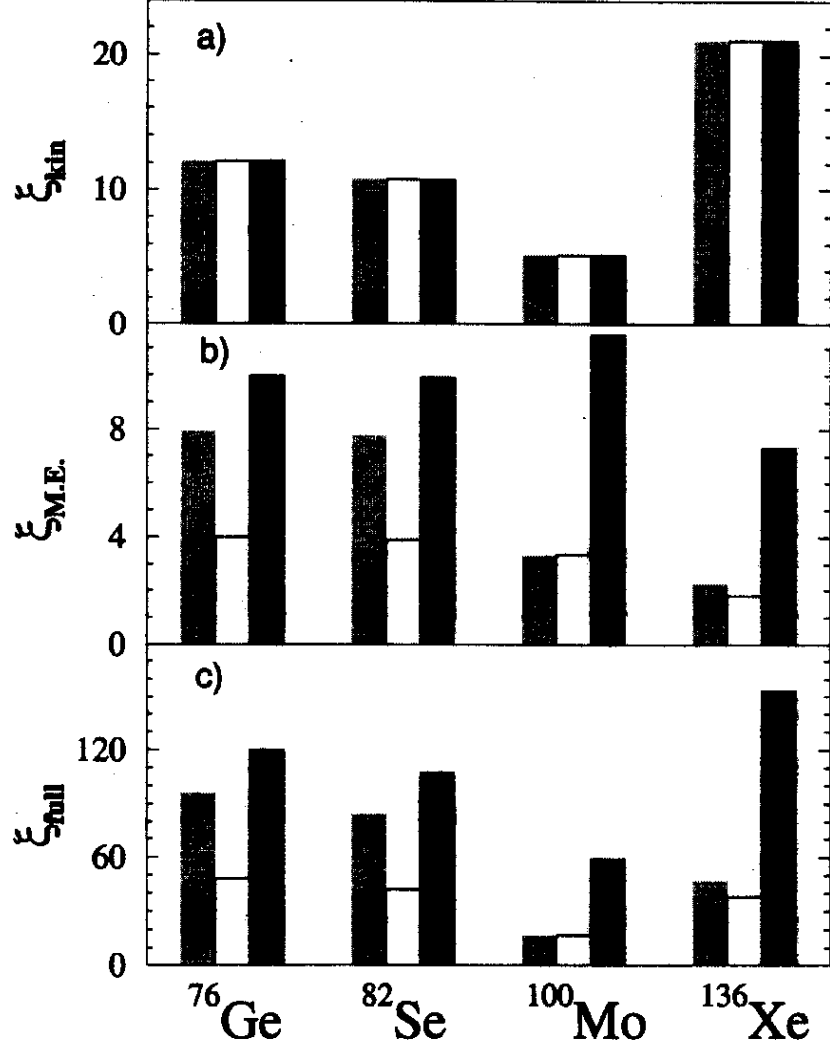
Figure 1.21: ξ_{full} (bottom) is the ratio of the half-life for the $\beta\beta$-decay to the first 0^+ excited state to the ground state. ξ_{kin} (top) and $\xi_{M.E.}$ (middle) are the ratios of the phase space integrals and squared NMEs. This shows a comparison of the rates of $0\nu\beta\beta$ to the daughter ground states and first 0^+ excited states for four different isotopes, using three different mechanisms for producing $0\nu\beta\beta$. The mechanisms shown are light neutrino exchange (left, textured black), LRSM heavy neutrino exchange (middle, white) and R-parity violating SUSY (right, solid black). Taken from [67].

Chapter 2

OVERVIEW OF THE Majorana Demonstrator

The Majorana Collaboration is studying $\beta\beta$-decay in ^{76}Ge and is currently operating an array of High Purity Germanium (HPGe) detectors called the MAJORANA DEMONSTRAT-OR[72]. The goal of the next generation of $0\nu\beta\beta$ searches is a sensitivity to $m_{\beta\beta}$ of $\sim$15 meV, which corresponds to a half-life sensitivity in ^{76}Ge of $\sim$10^{28} y. To reach this goal, an exposure on the order of several tonne-years will be required, with background levels in the region of interest of the decay of $<$ 0.1 cts/FWHM-t-y, as shown in Figure 2.1. With these future needs in mind, the MAJORANA DEMONSTRATOR was built with the following primary goals:

- Demonstrate backgrounds low enough to justify building $\beta\beta$-decay experiment involving $\sim$1 tonne of ^{76}Ge. The goal for the MAJORANA DEMONSTRATOR is a background rate of $<$ 3 background counts per tonne-year of isotopic exposure in a 4 keV region of interest around the 2039 keV Q-value of $0\nu\beta\beta$ in ^{76}Ge.

- Demonstrate the scalability of the design and techniques of the MAJORANA DEMON-STRATOR towards a tonne-scale experiment.

- Set competitive limits on the half-life of $0\nu\beta\beta$ and on $m_{\beta\beta}$ with other leading searches such as KamLAND-Zen and GERDA[46, 73].

- Search for additional physics beyond the Standard Model. This includes searches for bosonic dark matter, solar axions, Pauli exclusion principle violation, electron decay, lightly ionizing particles, and trinucleon decay[74, 75, 76]. As discussed in Section 1.5, the search for $\beta\beta$ E.S. has implications for some models beyond the standard model physics.

^{76}Ge (88% enr.)
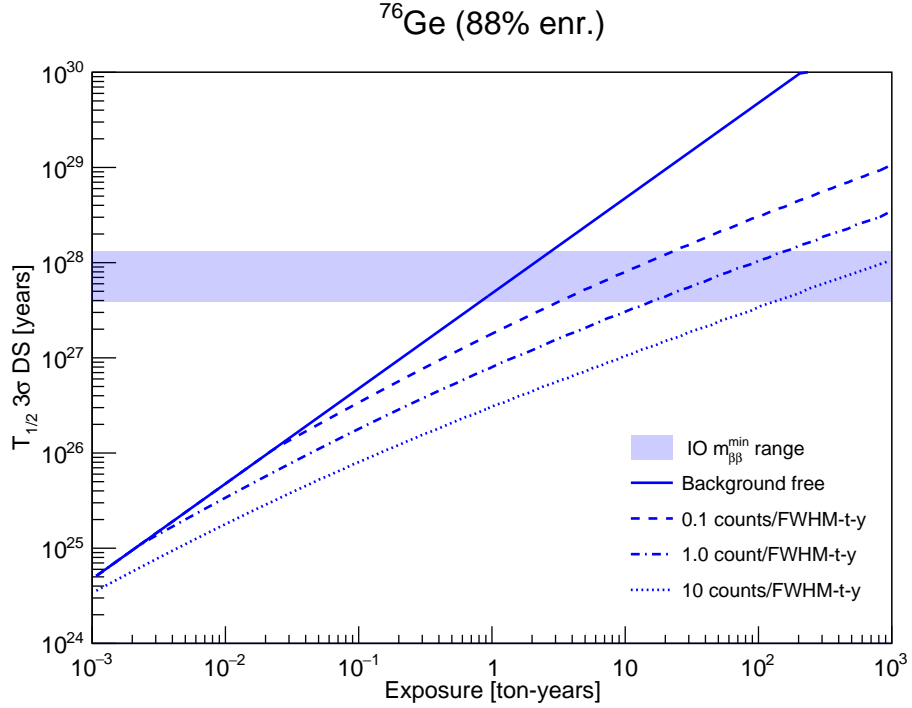
Figure 2.1: Detection sensitivity of a $0\nu\beta\beta$ search in ^{76}Ge as a function of isotopic exposure and the level of backgrounds in the region of interest. A blue band is drawn showing the next generation sensitivity goal. Image courtesy of Jason Detwiler.

This chapter will describe the design of the MAJORANA DEMONSTRATOR and progress towards meeting these goals, with a focus on the most relevant elements of the experiment to the search for $\beta\beta$ E.S..

2.1 Experimental Design

The MAJORANA DEMONSTRATOR is using P-type Point Contact (PPC)[77, 78] HPGe detectors to search for $0\nu\beta\beta$. PPC HPGe detectors are cylindrical semiconductor detectors that collect the positively charged electron holes at a small point-like contact with a diameter of a few mm. This differs from the more common coaxial detector geometry, where both the electrons and holes are collected along much larger electrodes that extend coaxially along

the detector. The PPC geometry offers several advantages in performing a low background search for $0\nu\beta\beta$. First, PPC HPGe detectors have intrisically low electronic noise due to a much lower capacitance than coaxial detectors. This results in an improved energy resolution and lower energy thresholds. Additionally, the PPC geometry enables pulse shape analysis (PSA) techniques to discriminate between single- and multi-site events.

(a) Natural Detector　　　　　　　　　　　(b) Enriched Detector
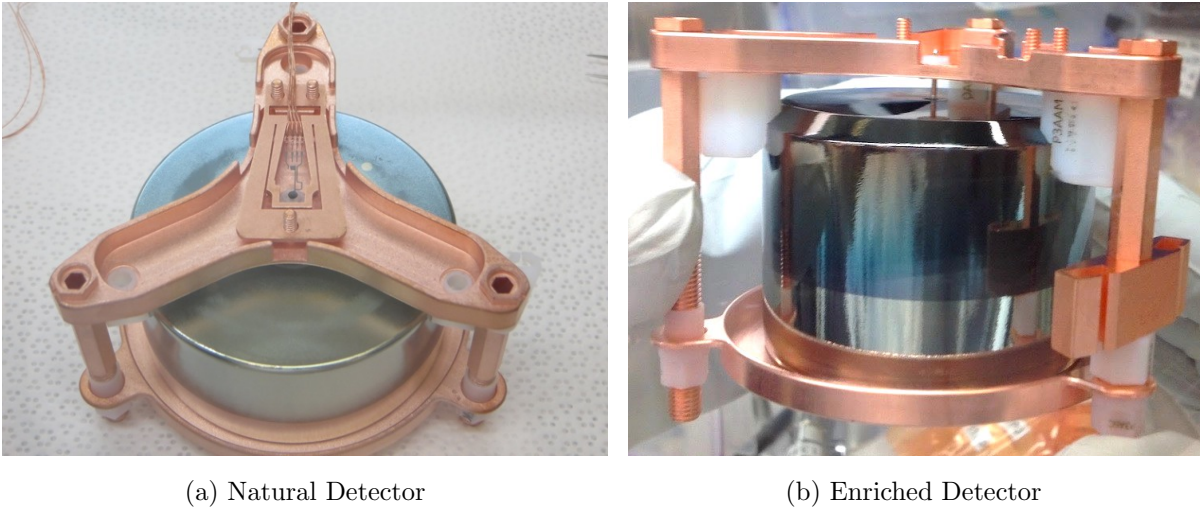
Figure 2.2: A photo of a natural detector with the BEGe geometry and an enriched detector. Note the LMFE electronics on top of the natural detector. The point contact, with copper pin inserted, is visible at the top of the enriched detector.

Two types of PPC detectors are used for the MAJORANA DEMONSTRATOR. Many of the detectors use germanium with the natural isotopic abundance (7.8% ^{76}Ge), manufactured by CANBERRA using the Broad Energy Germanium (BEGe^{TM}) detector geometry, and referred to as natural detectors. The remaining detectors use Germanium that has been isotopically enriched to $88.1 \pm 0.7\%$ in ^{76}Ge[79], manufactured by AMETEK/Ortec using a detector geometry with greater volume to surface area ratio than the BEGe detectors, and are referred to as enriched detectors. Photographs of both an enriched and natural detector are shown in Figure 2.2. By isotopically enriching the germanium used to manufacture the

detectors, they act as both the source and the detector of $0\nu\beta\beta$, with the result that all kinetic energy from a $0\nu\beta\beta$ is detected, which ensures a high detection efficiency. Furthermore, the manufacturing processes for HPGe detectors require a high material purity, which ensures intrisically low backgrounds inside of the detectors.

| PPC HPGe Detector | Low-Mass Mount | String | 7-String Array | Cryostat | Shield |

Figure 2.3: Each stage in the staged design of the MAJORANA DEMONSTRATOR, from a detector to a module. Photos taken by Matt Kapust (SURF).

Because a single HPGe detector has a mass of $\sim 0.5 - 1.1$ kg, in order to collect a high exposure, we build an array of detectors. This has the further advantage that the detectors in the array help shield one another, resulting in lower backgrounds as the size of the array increases. The MAJORANA DEMONSTRATOR used a staged, modular construction approach that is designed to be scalable towards a tonne-scale $0\nu\beta\beta$ search. Each detector is placed in interchangable detector mounts, to which the first stage preamplifier and signal and high voltage electronics cables are attached. These mounts are stacked into strings of 3-5 detectors, which are arranged into arrays of 7 strings, and the arrays are placed into cryostats. The detectors, electronics, cooling and vacuum hardware are operated independantly for each cryostat, and the combination of this hardware and the detector array is refered to as a module. Figure 2.3 shows the various stages of module assembly.

The MAJORANA DEMONSTRATOR has been constructed with two modules, shown in Figure 2.4. Module 1 contains 20 enriched detectors, totalling 16.9 kg in mass, and 9 natural

Module 1:   **16.9 kg (20) ^{enr}Ge**
                  5.6 kg (9) ^{nat}Ge

Module 2:   **12.9 kg (15) ^{enr}Ge**
                  8.8 kg (14) ^{nat}Ge

Figure 2.4:   Layout of all strings in both modules. The center string for each module is furthest to the left, and the other strings are on the outside. Enriched detectors are colored green, and natural detectors are colored blue.

detectors, totalling 5.6 kg. Module 2 contains 15 enriched detectors, totalling 12.9 kg, and 14 natural detectors, totalling 8.8 kg. The total mass of ^{76}Ge is 27.4 kg, 26.3 kg of which is contained in the enriched detectors.

To meet the stringent background requirements of the MAJORANA DEMONSTRATOR, the detector and cryostat components are built out of extra clean materials. The cryostat and detector mount structures are built out of copper that has been electroformed underground[80]. Insulating components consist of NXT-85, a low background Teflon. The first stage preamplifier electronics, called Low Mass Front End (LMFE) boards, are mounted directly on top of the detector mounts, and are specially designed to minimize the amount of material required. The high voltage and signal cables are manufactured by Axon' to minimize the component mass, and both use specially designed low mass, low background electrical connectors[81, 82]. Exposure to the surface, where a high cosmic ray flux can cosmogenically activate radioactive isotopes such as ^{60}Co, is minimized and tracked for all components, particularly the detectors and copper components[83]. Components are machined underground in a class 1000 clean room environment, and kept in nitrogen purged environments as much as possible in order to avoid exposure to Radon. An extensive radioassay campaign was carried out to

Background Rate (c/FWHM-t-y)
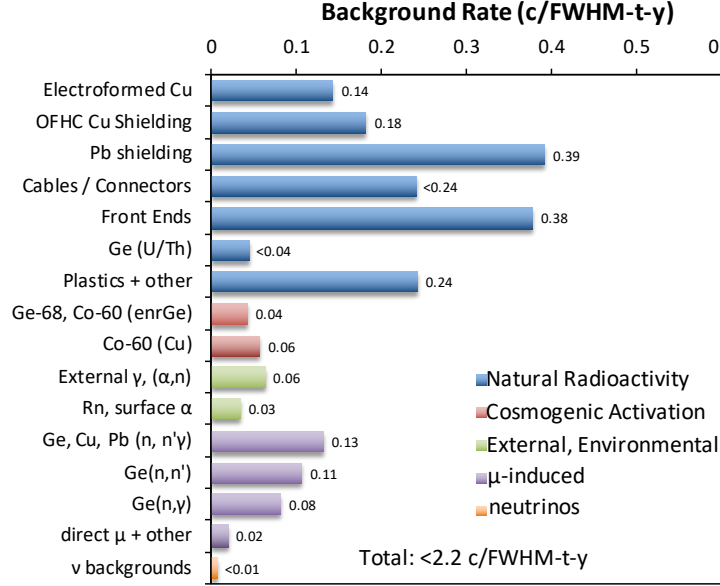
Figure 2.5: Prediction of contribution to backgrounds in the ROI around 2039 keV from different sources, based on component assays and simulations.

verify the low backgrounds of the components and the manufacturing procedures[84]. The results of this assay campaign are shown in Figure 2.5, and predict a background index of < 2.2 cts/FWHM-t-y, with primordial isotopes in the LMFE boards and the lead shield as the dominant background contributions.

Each cryostat is placed inside of a graded shield in order to further reduce backgrounds. Each layer of the shield is constructed from successiveley cleaner materials in order, consisting from outer- to inner-most layer of:

- High density polyethylene panels that reduce the energy of incoming environmental neutrons, and borated polyethylene to capture the neutrons

- Scintillating acrylic veto panels that act as an active muon veto, to be described in greater detail in Section 2.1.1

- A sealed aluminum box that is continuously purged with scrubbed nitrogen gas in order to purge the interior of radon gas

- A 45 cm thick lead shield

- A 5 cm thick shield manufactured from commercially available Oxygen-Free High thermal Conductivity (OHFC) copper

- A 5 cm thick shield manufactured from underground electroformed copper that has not been exposed to surface cosmic ray flux

Figure 2.6 contains a drawing of the shield and module hardware. In addition to this shielding, the entire experiment is hosted at the Davis Campus of the Sanford Underground Research Facility (SURF) in Lead, South Dakota, 4850', with an overburden of ∼4300 m.w.e[85].

2.1.1 Muon Veto

The muon veto consists of 32 scintillating acryllic panels instrumented with wavelength-shifting fibers and photo-multiplier tubes [86]. The panels are arranged to completely cover each face of the shielding, including the top and bottom, forming a completely enclosed surface. As a result, any muon that passes through the MAJORANA DEMONSTRATOR shield system must cross at least 2 veto panels on at least 2 different surfaces of the shield, depositing on the order of several MeV in each one. Furthermore, each surface has two orthogonal layers of panels, enabling a more precise reconstruction of the muon direction. Figure 2.7 shows a diagram of the panel layout. The muon veto is read out by two CAEN QDC digitizers, with a separate CAEN trigger card that acts as a 100 MHz clock and facilitates the trigger logic for the veto system. All channels on all three cards are simultaneously recorded if any two panels simultaneously record energies greater than a threshold set at the hardware level. LED pulsers are used to monitor the stability of each channel.

Each muon event is analyzed to identify candidate muons. LED pulsers, which affect all panels simultaneously, γ-rays, which will have lower energies and different hit patterns,
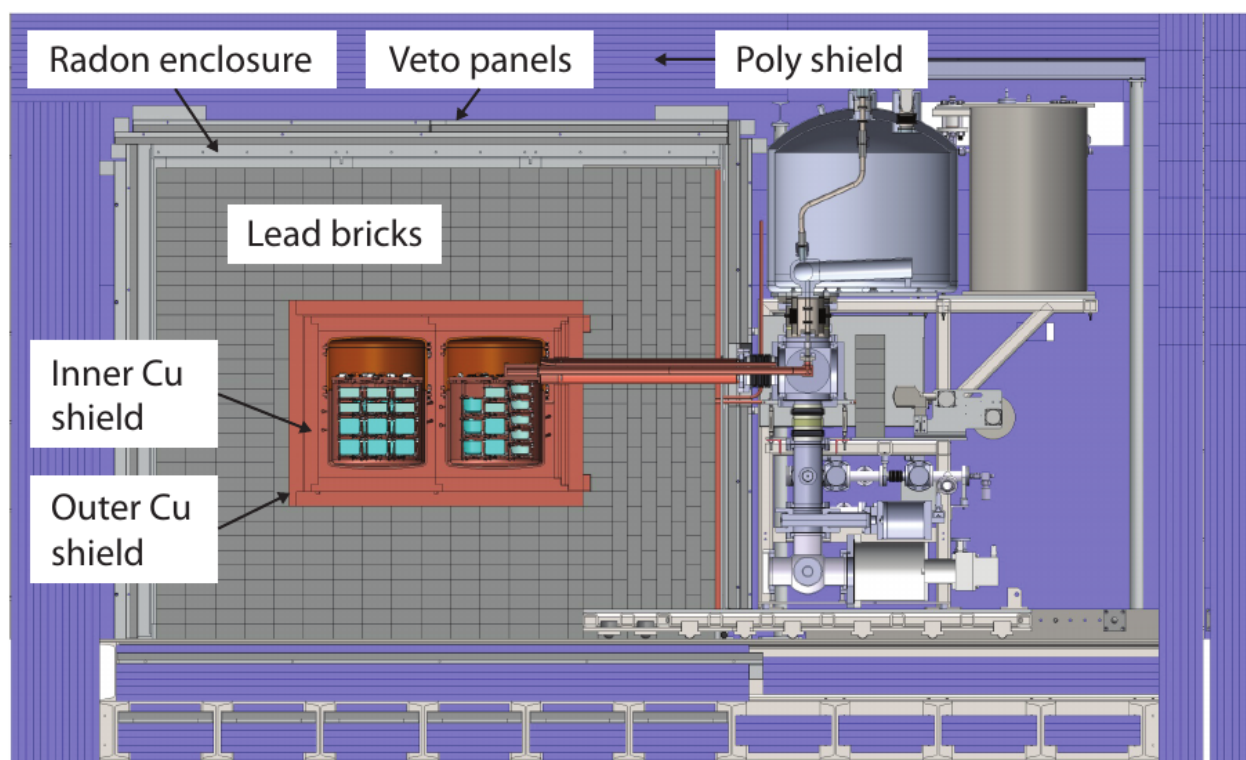
(a) Crossectional Diagram

(b) Lead Shield

(c) Overfloor

Figure 2.6: Top: A crossectional diagram showing the different layers of the shield. Bottom left: The lead shield and outer copper shield, prior to installation of other shield layers. Bottom right: The overfloor, atop which the shield is installed. The polyethylene and veto panels are visible.
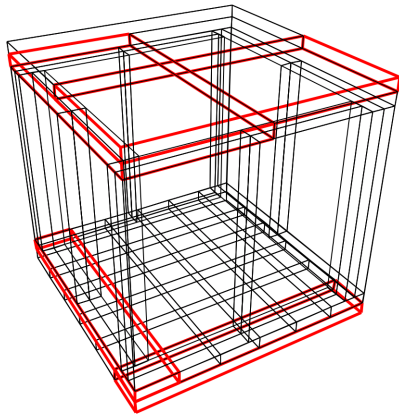
(a) Muon veto panel configuration
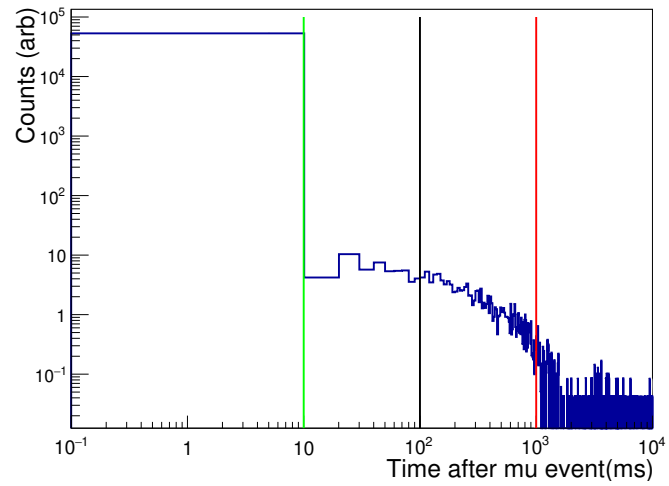
(b) Muon induced events

Figure 2.7: Left: the muon veto panel configuration. An example of a muon hit pattern is shown using the red-highlighted panels.

Right: a simulation of the timing distribution of HPGe events induced by muons, relative to the muon timing. The timing cutoff is shown using the red line.

(a) Circuit Diagram (b) LMFE Board
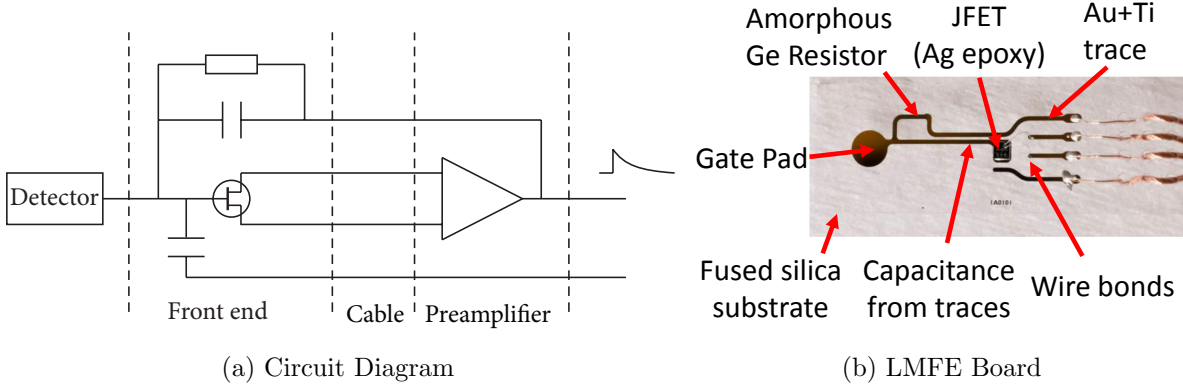
Figure 2.8: A circuit diagram and labelled photo of an LMFE board. The stray capacitance due to the proximity of the traces on the board acts as a charge-integrating capacitor.

and events caused by hardware errors can be easily identified and removed. This analysis is expected to tag $> 99\%$ of muon events that pass through the shield, with exceptions during DS0 and DS1, prior to the completion and complete debugging of the veto system. Once muon events have been analyzed, any HPGe detector events in a range of 0.2 ms before and 1 s after the muon event are cut. As shown in Figure 2.7, this cut is expected to remove $> 99.9\%$ of events induced by through-going muons, with exceptions during DS0 and DS1 when the muon and HPGe detector clocks were desynchronized. In addition to acting as a veto, this system can produce analyses of the muon flux measured at SURF's Davis Campus[87].

2.2 HPGe Detector Signal Processing

This section will describe how a signal from one of the MAJORANA DEMONSTRATOR's detectors is read out, starting with the detector electronics, through the digital waveform processing techniques that are used.

2.2.1   Charge Signal Collection

When an event occurs inside of a PPC HPGe detector, a cloud of free conduction band electrons and positively charged valance band vacancies (holes) is produced. Under the influence of a high voltage applied across the detector (1-5 kV), the electrons drift towards the n^+ contact and the holes towards the p^+ contact, inducing an electric current at each contact. By integrating the current at the p^+ contact, an induced charge signal can be measured, which is proportional to the energy of the event, with one electron-hole pair produced for every 0.7 eV of energy deposited. The induced charge signal is measured by the LMFE board, which is a charge sensitive preamplifier that is resistively coupled to ground[88]. The LMFE is mounted directly on each detector mount, offset by < 1 cm, in order to minimize electronics noise and crosstalk between electronics channels. The LMFE is connected by electronic cables to a second stage amplifier outside of the lead shield. The second stage amplifier produces two separate signals, with differing gains. The high gain channel has better noise characteristics at lower energies but saturates for a 3-4 MeV signal; the low gain channel saturates at higher energies, around 10 MeV. For the analysis presented here, events from the high gain channel will be primarily used. This circuit results in a typical peakshape that is an exponential impulse, with a decay time of $\sim$72 μs. The LMFE board additionally has a capacitively-coupled pulser line that can produce artificial pulses of a fixed energy that can be used to monitor the stability of the electronics. A circuit diagram and photo of the LMFE board is shown in Figure 2.8. A waveform shaped by these electronics can be seen in Figure 2.9.

For each detector, the signal from both channels is digitized using GRETINA digitizer cards, developed by the GRETINA experiment[89]. The MAJORANA DEMONSTRATOR signals are digitized at a freqency of 100 MHz, with 14 bits of precision. A built-in field-programmable gate array applies a pole-zero correction and trapezoidal filter independantly to each channel (these will be discussed in the next section). Each channel is independantly triggered using an energy threshold on the trap-filtered waveform, and records 2020 samples

(a) Raw Waveform   (b) Pole-zero Correction   (c) Trapezoidal Filter
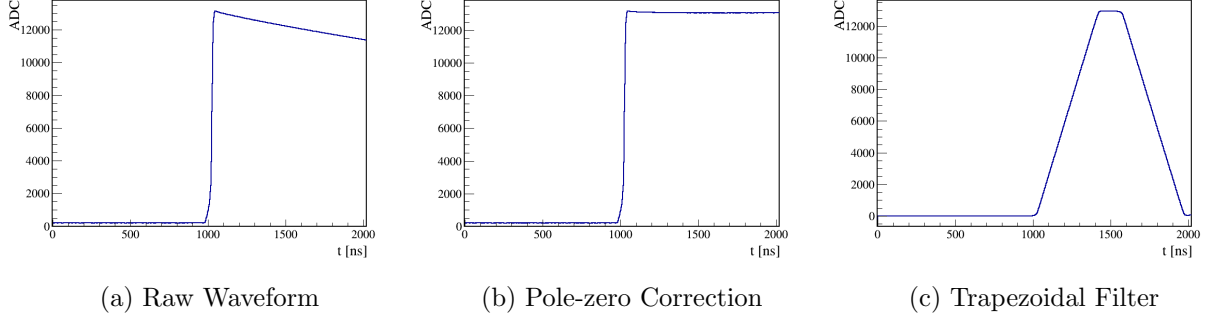
Figure 2.9: Left: A raw waveform as shaped by the signal electronics, with a time constant of ∼72 μs

Center: the same waveform after pole-zero correction, with a (nearly) flat top Right: the same waveform after application of a trapezoidal filter

per waveform. The digitizers are further capable of presumming samples by factors of 2, 4, 8 or 16, enabling variable length traces. Furthermore, the digitizers can multi-sample, using a different presumming factor for different portions of the waveform. Multi-sampling enables a high sampling frequency for the rising edge of the waveform, which aids the PSA techniques that depend on the waveform risetime, and a low sampling frequency for the falling tail and baseline of the waveforms, which improves baseline measurement, energy estimation, and PSA techniques that utilize the exponential tail of the waveform. For Majorana Demonstrator data, for different datasets, multi-sampling is either disabled, resulting in ∼20 μs waveforms with a single sampling frequency of 100 MHz, or enabled with the falling tail sampled at 25 MHz, resulting in ∼40 μs waveforms. Each digitized pulse is recorded and reanalyzed offline, using the software described in Section 2.3.

2.2.2 Energy Estimation

The energy of a waveform is estimated using a trapezoidal filter implemented in software. Trapezoidal filters are nearly optimal filters for energy estimation, enabling low noise mea-
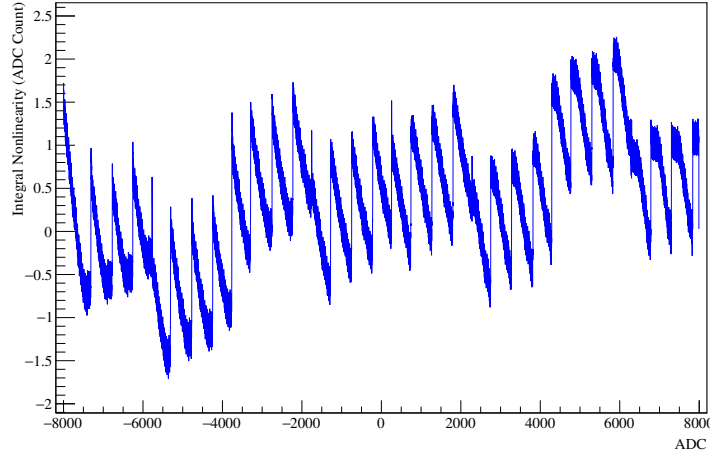
Figure 2.10: The shift in the value of each ADC bin that is applied in order to achieve a linear digitizer response with respect to voltage. This is measured by integrating over the width of each ADC bin, and is referred to as Integral nonlinearity.

surements while avoiding ballistic deficit[90, 91]. The trapezoidal filter has a flat top length of 2 μs and a ramp-time of 4 μs. The pole-zero constant is optimized independantly for each detector in order to produce a flat-top for the trapezoids, and the maximum value of the trapezoid is selected as the energy estimator. An example of a pole-zero correction and trapezoidal filter application is shown in Figure 2.9. The energy measured in this fashion is named `trapENM`.

2.2.3 Additional Energy Corrections

A second energy estimator has been implemented that corrects for several systematic errors in the `trapENM` estimator[92]. First, nonlinearities in the digitizer response are corrected for. The GRETINA digitizers have a nonlinearity, which manifests as a periodic sawtooth-shaped error, as shown in Figure 2.10. The size of this nonlinearity is measured by applying external, ramping signals from waveform generators in order to measure the voltage width of each ADC bin. The resulting size of this nonlinearity before correction can shift measured

energies by as much as 0.8 keV in the high gain readout. Before applying a trapezoidal filter, each waveform sample is corrected by the measured integral nonlinearity value, reducing the size of the ADC nonlinearity to < 0.1 keV.

A second correction is applied to correct for charge trapping. Charge trapping is a phenomenon in which local impurities in a HPGe detector capture electrons or holes as they drift to the n^+ and p^+ contacts, respectively. This results in a loss of charge collection that is dependant on the origin location of the charge cloud within the detector. This charge loss distorts the detector response, producing a low-energy tail in the peak shape, and degrades the energy resolution. The resolution degradation increases linearly as a function of hit energy, and at energies near the Q-value, this is a dominant contribution to the peak width. Charge trapping can be modelled as an exponential loss of charge with respect to the drift time of the charge inside of the HPGe crystal. To correct for this, we modify the pole-zero time constant so that the flat-top of the trapezoidal filter decays with the same time-constant as the charge trapping. As a result of this change, the measured waveform response after full charge collection will be identical, with respect to the origin time of the charge cloud, as shown in Figure 2.11. The resulting pole-zero time τ is described by:

$$\frac{1}{\tau} = \frac{1}{\tau_{PZ}} + \frac{1}{\tau_{CT}} \qquad (2.1)$$

where τ_{PZ} is the flat-top pole-zero time constant, and τ_{CT} is the charge trapping time constant. The value of τ is chosen to optimize the FWHM measured for a 2614 keV peak from a ^{228}Th calibration spectrum, using the energy estimator described here. This optimization is shown in Figure 2.11.

However, because the trapezoid no longer has a flat top, the maximum value is no longer useful as an energy estimator; instead, the amplitude of the trapezoid at a fixed time relative to the origin time of the trapezoid is used. This technique is referred to as a "fixed-time pickoff." A short trapezoidal filter with a rise-time of 1 μs and a flat-top of 1.5 μs is used, with the final crossing of a fixed threshold value used to estimate the origin time. After applying both of these corrections, the resulting energy estimator is called `trapENF`.

(a) Modified Pole-Zero

(b) FWHM Optimization
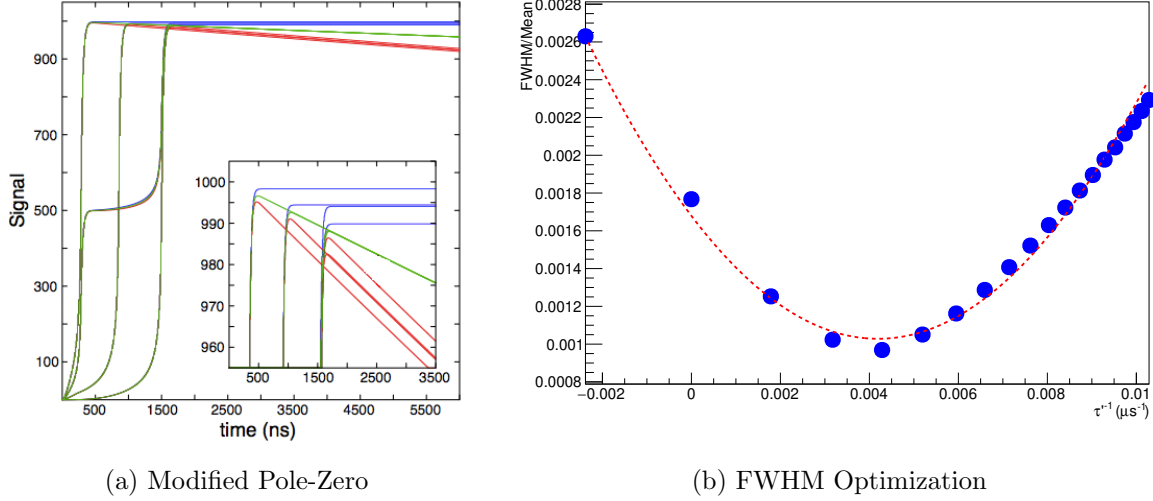
Figure 2.11: On the left, three simulated waveforms are shown with the same energy, with different loss of charge due to charge trapping. The red waveforms represent the waveforms prior to a pole-zero correction. The blue waveform uses the flat-top pole-zero constant; the tops are misalligned due to a loss of charge from charge trapping. The green waveforms apply the optimally charge-trapping corrected pole-zero constant; the tops are no longer flat, but they align perfectly. By applying a fixed-time pickoff of the ADC-value as an energy estimator, this results in improved energy resolution. On the right, we see the FWHM of a 2614 keV γ peak as a function of the pole-zero constant. By optimizing the FWHM, we can identify the optimal time constant to use for the charge trapping correction.
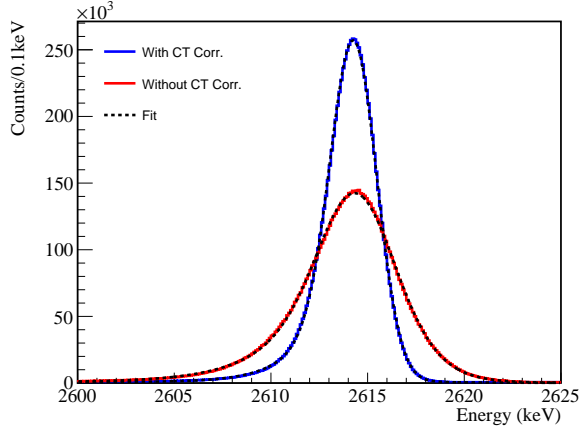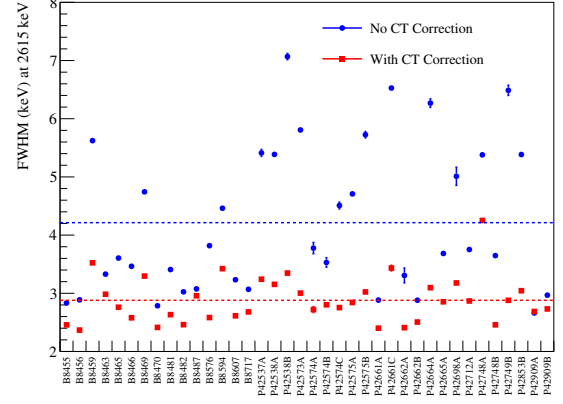
(a) `trapE` vs `trapENF`   (b) Improvement in Energy Resolution

Figure 2.12: The energy resolution is improved after applying the charge trapping and digitizer nonlinearity corrections. This results in a ∼31% improvement in energy resolution on average.

The `trapENF` estimator improves the energy resolution of the MAJORANA DEMONSTRAT-OR detectors at 2614 keV by ∼31%, as shown in Figure 2.12. Using the `trapENF` energy estimator, the MAJORANA DEMONSTRATOR has achieved the best energy resolution of any current generation $0\nu\beta\beta$ experiment. There is, however, still room for improvement by correcting for global nonlinearities that arise from an energy dependant, systematic drift in the start time estimator and a small quadratic nonlinearity in the detector response.

2.2.4 Energy Calibration

Energy calibration of detectors is performed using a ^{228}Th source[93]. ^{228}Th has a large number of prominent γ-rays in its decay chain between 238 keV and 2614 keV which can be used to calibrate and characterize the detectors. For each module, a 4.7 m long line source, consisting of ^{228}Th doped epoxy, is used to perform calibrations, with an activity of ∼10 kBq along the last 2 m of the source. The line source is inserted into guide tubes that

(a) Calibration track drawing

(b) Calibration track photo
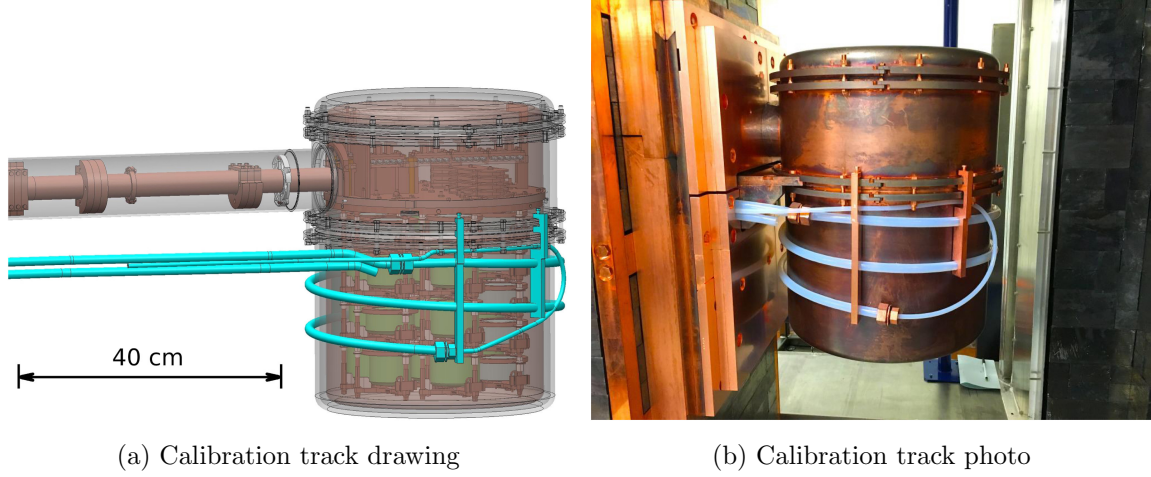
Figure 2.13: A drawing and photo of the teflon calibration track wrapping around a cryostat.

wrap around the cryostat and reach outside of the shield structure. The source is pushed by a motor located outside of the shielding, and a set of magnets and magnetic sensors are used to ensure that the source is placed in the correct position. For each module, a separate 90 minute calibration run is performed once per week, with one source inserted at a time. In addition to the ^{228}Th line source, a ^{60}Co line source with activity 6.3 kBq over the last 2 m of length and a ^{56}Co line source with activity 6 kBq over the last 2 m of length were manufactured for use inside of the calibration track. Figure 2.13 shows a drawing and photograph of the calibration track.

The γ peaks from the ^{228}Th spectrum are simultaneously fit to an analytic peakshape function, as described in Appendix A. The results of this fit are used to extract the gain, energy offset, and energy resolution of each HPGe detector, and of the combined detector array. This fit is performed on 8 calibration peaks for each 90 minute calibration run, and a gain matching of the 238- and 2614-keV peaks is used to calibrate the detectors. At the end of a major dataset, a more detailed fit of ~30 peaks is performed, which is used to measure the detailed energy characteristics. Figure 2.14 shows a ^{228}Th calibration spectrum, with the energy resolution extracted from a simultaneous peak fit.
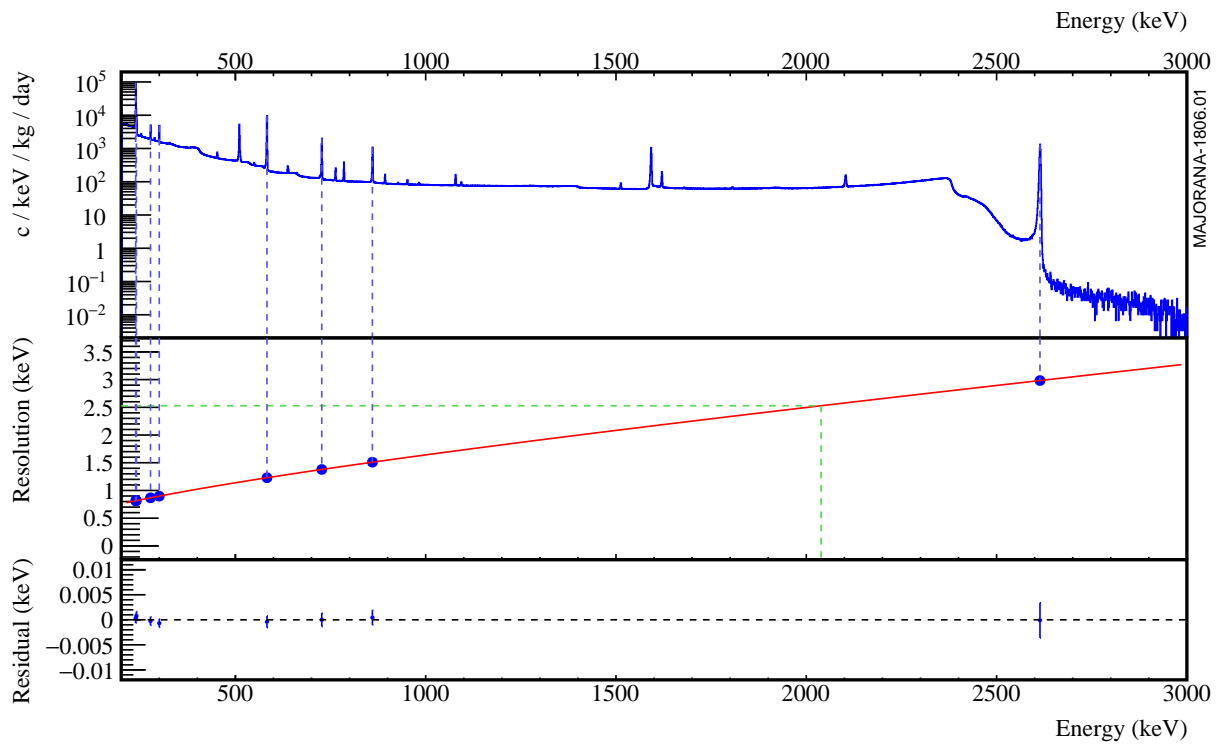
Figure 2.14: A combined detector spectrum from a ^{228}Th calibration run, with the FWHM extracted from a simultaneous fit of many peaks.

2.2.5 Multi-site Events

(a) PPC Field Map

(b) PPC Weighting Potential
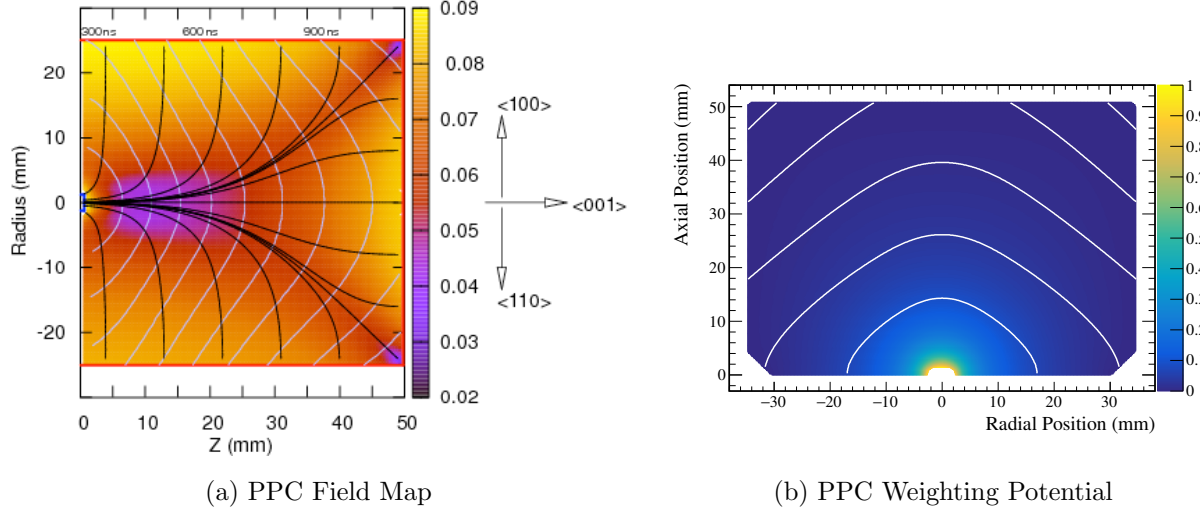
Figure 2.15: Left: a color map of the electric field strength in a PPC detector, with electron-hole drift paths (black) and surfaces of constant hole-drift time (grey).

Right: a color map of the weighting potential in a PPC detector, which is highly localized near the point contact.

PPC HPGe detectors enable several PSA techniques that can differentiate between different types of events, which can aid in reducing backgrounds. The PPC detector geometry results in low drift velocity in the bulk of the detector and a weighting potential that is highly locallized near the point contact, meaning that most of the charge signal is induced in a short period of time, as shown in Figure 2.15. The result is a sharp current signal whose timing depends heavily on the position of charge deposition inside of the detector. This enabled the discrimination of single-site events from multi-site events. All charge in a single-site event is localized within $\sim 1 - 2$ mm inside of the crystal. $\beta\beta$-decay is an inherently single-site event because both electrons from the decay are fully absorbed within ~ 1 mm of the decay site. In multi-site events, multiple localized clusters of charge are simultaneously created in the crystal, separated by more than a few mm. γ-rays that Compton scatter inside of the

(a) Single- and Multi-site waveforms

(b) Calibration track photo
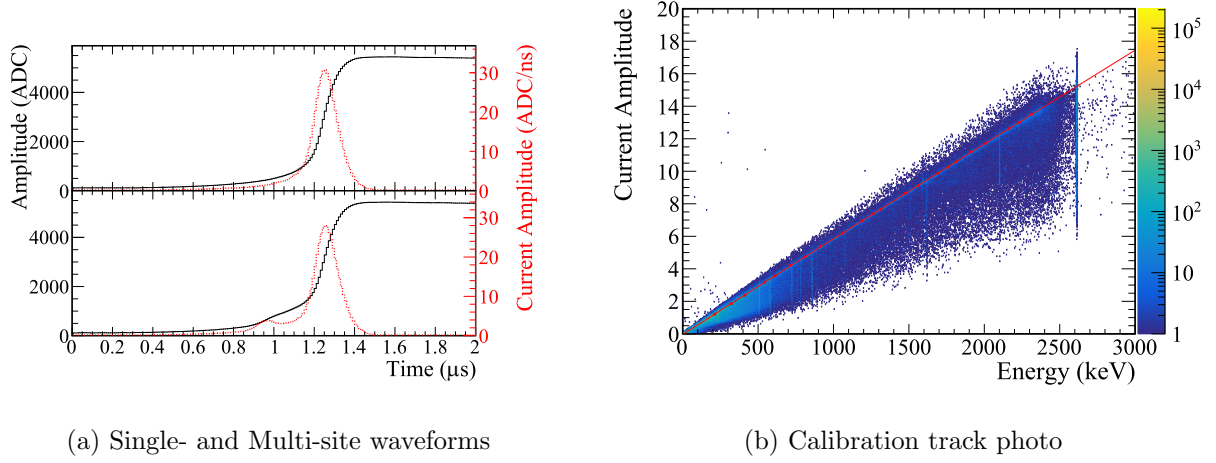
Figure 2.16: Left: A single-site event (top) and multi-site event (bottom). Note the multiple current pulses in the multi-site event, which results in a lower ratio of current amplitude to energy.

Right: Comparison of current amplitude to energy. The red line represents the expected value for single-site waveforms. Waveforms that fall below the red line will mostly be multi-site waveforms. The AvsE parameter is calculated based on a comparison between the measured current amplitude, and the expected current amplitude for a singli-site event at that energy.

crystal and then deposit their remaining energy elsewhere in the crystal are an example of a multi-site event that could potentially be a background in searching for $0\nu\beta\beta$. The charge drift times inside of PPC detectors is long enough that the drift time of each localized charge cloud in the detector will differ by potentially hundreds of ns, which is long enough to be visible to the GRETINA digitizers. Figure 2.16 shows the difference between a single- and multi-site waveform.

In order to distinguish between single- and multi-site waveforms, we compare the maximum current amplitude in the waveform to the total energy of the waveform[94]. Due to the PPC detector geometry, for a single localized charge cloud the maximum current amplitude is approximately proportional to the energy deposited in the local area. This means that
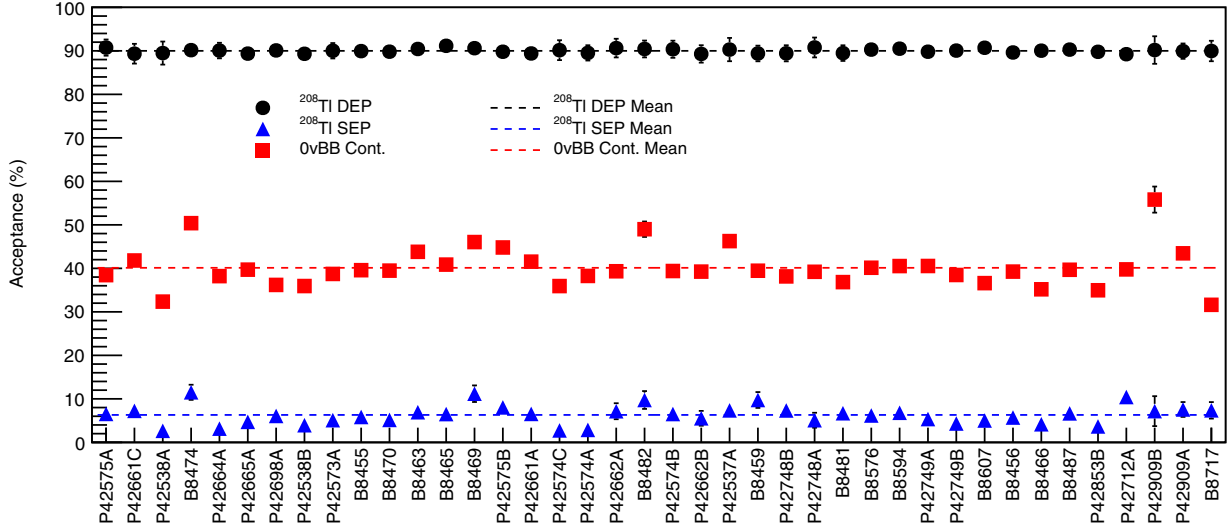
Figure 2.17: A measurement of the cut efficiency of the AvsE cut for single escape (SEP) events, which are inherently multi-site, double-escape (DEP) events, which are inherently single-site, and Compton continuum events.

single-site events will typically have a fixed ratio between these values. In a multi-site event, on the other hand, the maximum charge amplitude will be proportional to the energy of the largest local site rather than the full energy of the waveform, so this ratio will be less than that for single-site events. In Figure 2.16, the relationship between the maximum current amplitude and the energy is shown. The analysis parameter AvsE performs a comparison between these values and has been shown to cut ∼95% of multi-site events while keeping ∼90% of single-site events. A measurement of these efficiencies is shown in figure2.17 Near the $0\nu\beta\beta$ region of interest, this cut removes ∼60% of Compton continuum backgrounds, which are expected to be the primary background in the ROI.

(a) DCR and Bulk Waveform
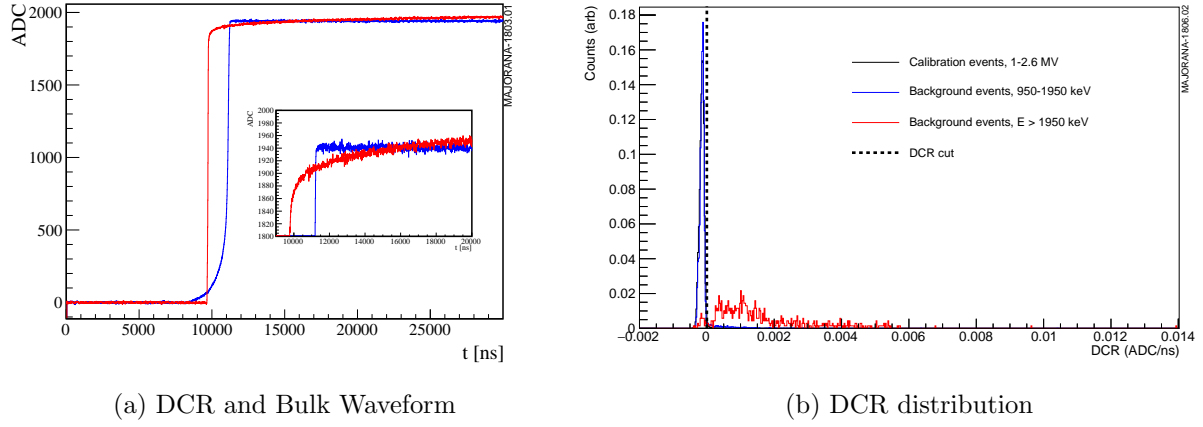
(b) DCR distribution

Figure 2.18: Left: A bulk event (black) compared with a DCR event (red) after pole-zero correction. The slope of the DCR event is used to tag it as a surface event.

Right: The distribution of the DCR parameter, which measures the slope of the falling tail of waveforms. The high energy background events (red) are mostly αs incident on the passivated surface. The calibration (black) and lower energy background events (blue) are mostly γs or $2\nu\beta\beta$s in the bulk of the detector. Surface α events can be cut based on their larger DCR values.

2.2.6 Surface Events

Additional backgrounds in the MAJORANA DEMONSTRATOR can potentially come from β- and α particles incident on the surface of the HPGe detectors. Because these are charged particles, they will be absorbed within ~ 1 mm (βs) or 10s of μm (αs) of the detector surface. The n^+ detector surfaces have a ~ 1.1 mm thick lithiated layer that is inactive (i.e. virtually no charge is collected from events in this layer), meaning that these surfaces are insensitive to incident charged particles. The p^+ contact is made by implantation of boron ions, creating another inactive layer with a depth of about 0.5 μm. A passivation layer between these contacts, however, has a thickness of $\sim 0.1 \mu$m, and holes created near this surface are strongly trapped. These holes are rereleased on a time scale much longer than the trapezoidal filter time, with the result that a highly degraded energy is measured As a result, α particles with energies of 3-9 MeV can be read with energies at or near the 2.039 MeV Q-value of $\beta\beta$-decay. Some of these rereleased holes, however, are collectected within the $20 - 40$ μs window recorded by the GRETINA cards, a phenomenon referred to as Delayed Charge Recovery (DCR). DCR can be measured by checking for a reduction in the slope of the falling tail of a waveform (or, equivalently, we would see a slow rise in the pole-zero corrected waveform instead of a flat top). Figure 2.18 shows a comparison between a DCR waveform and a bulk waveform, and the values of the DCR parameter for surface α events and bulk γ events. This cut rejects most α particles while keeping $\sim 99\%$ of $0\nu\beta\beta$events.

2.3 MAJORANA DEMONSTRATOR Software

The MAJORANA collaboration uses a suite of software, developed either independantly or in conjunction with other physics collaborations. This section will give a brief overview of the software packages in use, their purpose, and their hierarchy. The primary language for this software is C++, unless noted otherwise. Aspects of this software depend on the ROOT object oriented data storage and analysis framework[95], fftw3, a fast fourier transform package
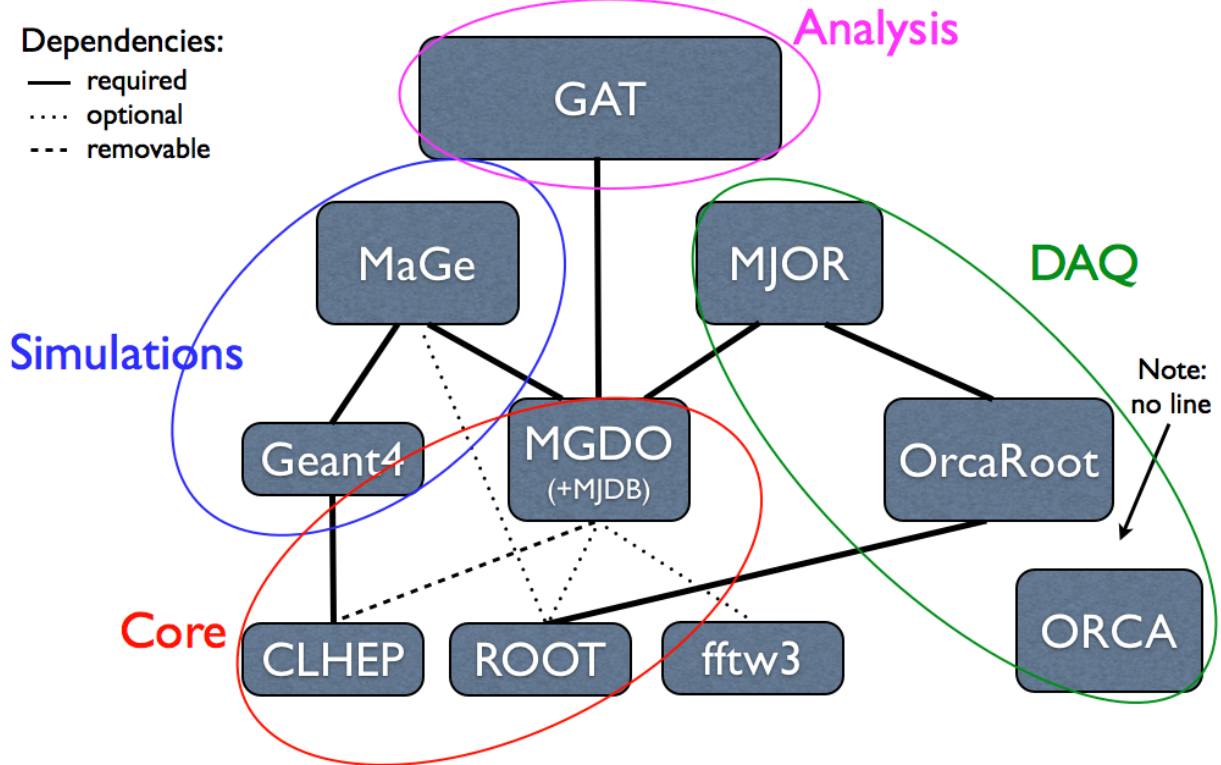
Figure 2.19:   A diagram of the dependancies between the software libraries used for the MAJORANA DEMONSTRATOR.

[96], the CLHEP high energy physics library[97], and Geant4, a simulation toolkit[98]. Figure 2.19 shows the dependancies and hierarchy of the MAJORANA DEMONSTRATOR software.

2.3.1   DAQ

The DAQ hardware is managed and read out by the Object-oriented Real-time Control and Acquisition (ORCA) software, an object oriented DAQ framework written in Objective-

C[99]. ORCA supports a wide variety of digitizers, including the GRETINA cards and CAEN QDC and scaler cards used by the MAJORANA DEMONSTRATOR. A single computer runs an instance of ORCA that collects data from all of these cards (with the exception of Summer 2016, when two computers ran separate instances of ORCA, one for each module). ORCA writes data packets written by the various cards to binary files, which are uploaded to various MAJORANA DEMONSTRATOR computing systems. Data is divided into runs, which typically last an hour in length for background runs and ∼5 minutes for calibration runs. The various cards are read asynchronously by ORCA. Between data runs, cards are not reinitialized and continue to record data; as a result, 100% livetime is achieved during normal operations. ORCA also supports readout of a variety of other devices that are used for environmental monitoring of the Davis Campus, and is capable of pushing these readings to an online database for access outside of the laboratory.

2.3.2 MGDO

The Majorana-Gerda Data Objects (MGDO) package is a software library that is maintained by both the MAJORANA and GERDA collaborations[100]. MGDO contains C++ objects for storing waveforms, data from various digitizer cards, and run information that are compatible with ROOT's `TTree`, a data storage structure. MGDO also contains objects to perform various waveform transformations that are used in digitital signal processing.

2.3.3 The Event Builder

The MJOR library contains the MAJORANA Event Builder, which converts the binary ORCA files into MGDO data storage objects and writes those objects to a ROOT `TTree`. Because the ORCA readout is asynchronous, the event builder is also responsible for sorting events in time order and combining simultaneous waveforms into events. Waveforms within a 4 μs window are combined; this is a rolling window, meaning that if a waveform is within 4 μs of any other waveform in the event, it will be added. Events containing multiple detectors can be rejected for the $0\nu\beta\beta$ analysis since $0\nu\beta\beta$ is an inherently single-site event. The event

builder also performs some basic data quality checks, known colloquially as "Garbage checks," and removes any unphysical events or events with some unreadable or incorrect data. The event builder records events from both the HPGe detectors, read by the GRETINA cards, and from the muon veto system, read by the CAEN QDC and Scaler cards. The ROOT files produced by the event builder are known as built files. Appendix C contains an in depth description of the event builder.

2.3.4   GAT

The Germanium Analysis Toolkit (GAT) is a software framework for performing various analyses on the MAJORANA DEMONSTRATOR. GAT performs the various digital waveform transformations necessary to compute the signal processing parameters described in Section 2.2. GAT records these parameters in a separate file, called a gatified file, which is used for data analysis. In addition, GAT produces skim files, which contain only events that pass additional data quality checks and only a single channel (between high and low gain) from each detector for each event. One example of events that are removed by data quality checks are events that occur during liquid nitrogen dewar fills, which last ∼15 minutes and cause periods of high electronic noise. Another example is events that are cut by the muon veto system, as described in Section 2.1.1. Finally, skim files are produced to include only runs and detectors that are determined to be high quality. GAT also contains software suites to perform other analyses for the MAJORANA DEMONSTRATOR, including the $0\nu\beta\beta$ analysis, the excited state decay analysis described in this document, and energy calibrations.

2.3.5   MaGe

The Majorana Gerda (MaGe) simulation package is used to perform simulations of the MAJORANA DEMONSTRATOR[101]. It is described in detail in Chapter 3.

2.4 Recent Results

Based on the analysis described in this chapter, the MAJORANA DEMONSTRATOR has pro-
duced a limit on the half-life of $0\nu\beta\beta$ in ^{76}Ge. So far, two results have been published: one
with $\sim$10 kg-y of data[102], and one with $\sim$26 kg-y of data[103], which will be discussed
in this section. Further data releases will be performed roughly once per year until the
decommissioning of the MAJORANA DEMONSTRATOR, expected in 2020.

2.4.1 Data Taking and Blinding

Module 1 began recording data on June 26, 2015 and has been in continuous operation since
December 31, 2015. Module 2 began recording data on August 25, 2016. The data is divided
into 6 numbered datasets (abbreviated DS#) based on the configuration of the detectors
and the DAQ system. DS5 is further subdivided into DS5a, DS5b and DS5c. The main
differences between the datasets are as follows:

- DS0: Data taken with module 1 only, prior to the installation of the inner copper
  shield. This dataset has elevated backgrounds.

- DS1: Data taken with module 1 after installation of the inner copper shield, and repairs
  to electronic components that resulted in a greater number of active detectors.

- DS2: Data taken with module 1 using the digitizer multi-sampling described in Sec-
  tion 2.2.1.

- DS3: Data taken with module 1 after installation of module 2. Multi-sampling was
  disabled for DS3.

- DS4: Data taken with module 2, simultaneously to DS3. Separate instances of ORCA
  were run for DS3 and DS4.

- DS5a: Data taken with modules 1 and 2 using a single instance of ORCA. Data taken during this period had elevated noise due to poor detector grounding. As a result, the energy resolution and cut performance is worse for this DS than others.

- DS5b: Data taken with both modules after improving detector grounding. This dataset ended when the Majorana Demonstrator had finished taking ∼10 kg-y of unblinded data for the initial data release.

- DS5c: Continuation of DS5b, after the 10 kg-y cutoff.

- DS6a: Data taken with both modules, with multi-sampling enabled. This dataset ended with the second data release of ∼26 kg-y of data.

The Majorana Demonstrator has continued recording data since the end of DS6a.

The Majorana Demonstrator follows a statistical blinding scheme, in which 75% of background data is administratively blinded and inaccessible to analysts in the Majorana collaboration. The remaining 25% of background data and all calibration data is accessible and is used to test the analysis tools and parameters. Implementation of this scheme is accomplished by alternating between 31 hours of background runs that are unblinded and 93 hours that are blinded. Unblinding is performed in several stages. First, only background events that are not candidates for use in various physics searches are unblinded; this excludes the 1950-2350 keV background index region, low energy events and multi-detector events. The data unblinded in this first stage is used to perform run and detector selection, verify the data cleaning cuts, and investigate backgrounds. After verification, further data is unblinded individually for various analyses after a collaboration-wide review of the techniques.

2.4.2 Analysis

An independant analysis is performed of each dataset. Table 2.1 contains a summary of the configuration, exposure, and detection efficiencies for each dataset. For each detector, the

Table 2.1: Summary of key parameters for each dataset.

Data Set	Start Date	Active Enr Mass (kg)	Exposure (kg-y)	ϵ_{AE} (%)	ϵ_{DCR} (%)	ϵ_{cont} (%)	ϵ_{tot} (%)	$NT\epsilon_{tot}\epsilon_{res}$ 10^{24} atom-y
DS0	6/26/15	10.69(16)	1.26(02)	$90.1^{+3.2}_{-3.5}$	$98.9^{+0.9}_{-0.2}$	90.8(11)	$80.8^{+3.1}_{-3.3}$	$6.34^{+0.25}_{-0.27}$
DS1	12/31/15	11.90(17)	2.32(04)	$90.1^{+3.6}_{-4.0}$	$99.1^{+1.0}_{-0.5}$	90.9(11)	$81.1^{+3.5}_{-3.8}$	$11.82^{+0.53}_{-0.58}$
DS2	5/24/16	11.31(16)	1.22(02)	$90.3^{+3.5}_{-3.7}$	$98.6^{+1.1}_{-0.5}$	90.9(11)	$80.9^{+3.4}_{-3.5}$	$6.24^{+0.28}_{-0.29}$
DS3	8/25/16	12.63(19)	1.01(01)	$90.0^{+3.0}_{-3.1}$	$99.0^{+1.0}_{-0.3}$	90.9(11)	$80.9^{+3.0}_{-3.0}$	$5.18^{+0.20}_{-0.20}$
DS4	8/25/16	5.47(08)	0.28(00)	$90.0^{+3.1}_{-3.4}$	$99.2^{+1.1}_{-0.2}$	90.8(10)	$80.9^{+3.0}_{-3.2}$	$1.47^{+0.06}_{-0.06}$
DS5a	10/13/16	17.48(25)	3.45(05)	$90.0^{+3.4}_{-3.6}$	$96.9^{+1.3}_{-1.3}$	90.9(13)	$79.2^{+3.4}_{-3.5}$	$17.17^{+0.76}_{-0.79}$
DS5b	1/27/17	18.44(26)	1.85(03)	$90.0^{+3.1}_{-3.3}$	$98.5^{+1.4}_{-0.5}$	90.9(13)	$80.5^{+3.2}_{-3.2}$	$9.46^{+0.39}_{-0.39}$
DS5c	3/17/17	18.44(26)	1.97(03)	$90.0^{+3.1}_{-3.3}$	$98.5^{+1.2}_{-0.3}$	90.8(11)	$80.6^{+3.1}_{-3.1}$	$10.31^{+0.47}_{-0.47}$
DS6a	5/11/17	18.44(26)	12.67(19)	$90.1^{+3.2}_{-3.2}$	$99.0^{+0.8}_{-0.2}$	90.8(11)	$81.1^{+3.0}_{-3.0}$	$65.10^{+2.92}_{-2.92}$
Total (DS0-6)			26.02(53)					133.1±6.3
Total (DS1-4,5b-6)			21.31(41)					110.0±5.1

active isotopic mass is computed, which is the mass of ^{76}Ge that is in the bulk region of a detector, excluding dead layers (see Section 2.2.6). The dead layer volume is computed based on simulations, following the procedure to be outlined in Section 3.1.3. The total exposure for each dataset is computed by totalling the product of the active mass of each detector and the total livetime of each detector. The detector livetime excludes runs for which that detector was disabled, time periods cut by the LN fill cut or muon veto cut, and detector deadtime, which is estimated as described in Section 4.2.3. The detection efficiency for this analysis is defined as the fraction of $0\nu\beta\beta$ events originating in the active region of an active detector that is contained in the region of interest selected for the peak search. The region of interest is selected by optimizing the detection efficiency with respect to the background acceptance, following a similar procedure to that described in Section 4.3.1, and results in an ROI efficiency of $\epsilon_{res} \sim 0.900 \pm 0.007$, with slight variations between DSs. The cut efficiencies of AvsE (ϵ_{AE}) and DCR (ϵ_{DCR}) are calculated using the techniques described

(a) Full background spectrum

(b) ROI background spectrum
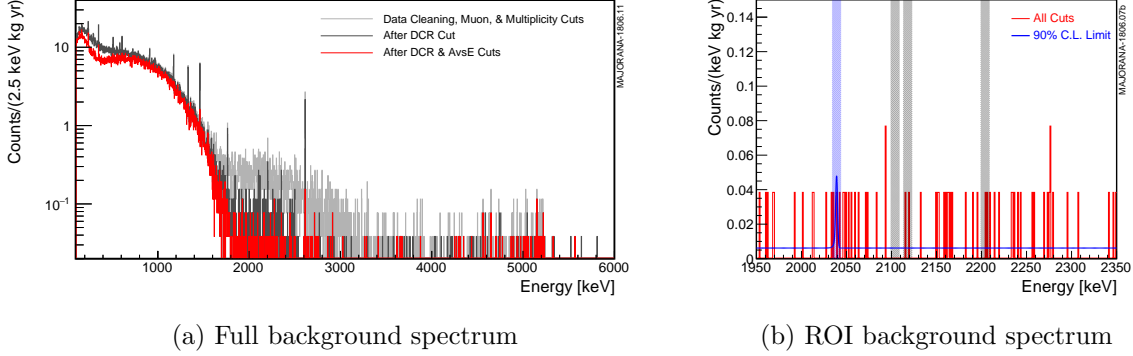
Figure 2.20: The MAJORANA DEMONSTRATOR background spectrum for datasets 0-6a. Left: the full energy range, with cuts applied sequentially. Right: the 1950-2350 keV bacgkround region of interest spectrum after applying all cuts. The blue band is the signal ROI, and the blue curve represents the flat background with a peak with amplitude equal to the 90% confidence limit.

in Sections 2.2.5 and 2.2.6. The containment efficiency (ϵ_{cont}) accounts for events that occur in the transition region between the dead layer and the bulk of the detector, where there is partial energy loss that pulls the event out of the ROI.

After applying all cuts, we measure the background spectrum shown in Figure 2.20. The background index is estimated assuming a flat background in the 1950-2350 keV range, excluding regions around the 2103 keV, 2117 keV and 2204 keV γ peaks, which are expected to be visible above the continuum background. The measured background index across all datasets is $6.1 \pm 0.8 \cdot 10^{-3}$ cts/(keV-kg-y). This corresponds to 15.4 ± 2.0 cts/(FWHM-t-y). If we exclude high background datasets (DS0 due to the lack of inner copper shield, and DS5a due to the high noise), we measure a reduced background index of 11.9 ± 2.0 cts/(FWHM-t-y). Table 2.2 lists the background indexes broken down by dataset. This background index falls short of the 3 ct/(FWHM-t-y) goal set for the MAJORANA DEMONSTRATOR, most likely due to ^{232}Th chain contamination in excess of the predicted activity based on material

assays.

Table 2.2: Background index and optimized ROI width for each dataset.

Dataset	Window Counts	BG Index (10^{-3} cts)	ROI (keV)	ROI BG (cts)
DS0	11	$24.3^{+8.4}_{-7.0}$	3.93	0.120
DS1	5	$6.0^{+3.4}_{-2.7}$	4.21	0.058
DS2	2	$4.6^{+5.1}_{-2.9}$	4.34	0.024
DS3	0	<3.6	4.39	0.000
DS4	0	<12.7	4.25	0.000
DS5a	10	$8.0^{+3.1}_{-2.6}$	4.49	0.125
DS5b	0	<1.9	4.33	0.000
DS5c	5	$7.0^{+4.0}_{-3.2}$	4.37	0.061
DS6a	24	$5.3^{+1.2}_{-1.0}$	3.93	0.262
Total	57	6.1 ± 0.8	4.13	0.653
DS1-4,5b-6	36	4.7 ± 0.8	4.14	0.529

A Poisson counting sideband analysis is performed, with 1 event in the 4.13 keV optimized ROI and 57 events in the $\sim$350 keV wide background ROI. The half-life limit is determined using

$$T_{1/2}^{0\nu} > \frac{\ln(2)NT\epsilon_{tot}\epsilon_{res}}{\hat{S}(n_{ROI}, \langle B \rangle)} \tag{2.2}$$

where $NT\epsilon_{tot}\epsilon_{res}$ is shown in Table 2.1, and $\hat{S}(n_{ROI}, \langle B \rangle, CL)$ is an estimator for the upper limit on the number of observed counts at confidence limit CL with n_{ROI} counts and $\langle B \rangle$ expected backgrounds in the ROI. For this result, the Feldman-Cousins estimator[104] is used with confidence level of 90%, yielding a half-life lower limit for ^{76}Ge $0\nu\beta\beta$ of $2.5 \cdot 10^{25}$ y. Other estimators have also been used and are quoted in reference [103]. Monto Carlo simulations were performed to measure the median sensitivity at 90% CL at $> 4.8 \cdot 10^{25}$ y. This half-life limit corresponds to a range of upper limits on $\langle m_{\beta\beta} \rangle$ of $(200 - 433)$ meV.

2.5 Future Searches for ^{76}Ge $0\nu\beta\beta$

The MAJORANA DEMONSTRATOR and GERDA experiments are the two most sensitive searches for $0\nu\beta\beta$ in ^{76}Ge to date. GERDA has achieved a leading half-life limit of $9 \cdot 10^{25}$ y (90% CL) from 82.4 kg-y of exposure[73]. The MAJORANA DEMONSTRATOR and GERDA have achieved the two lowest background indexes of any $0\nu\beta\beta$ searches, at 11.9 cts/(FWHM-t-y) for the MAJORANA DEMONSTRATOR and 2.1 cts/(FWHM-t-y) for GERDA. These low backgrounds have been achieved using differing, but complementary techniques. GERDA has achieved its low background rate largely by submerging an array of enriched HPGe detectors in liquid Argon (lAr) (see Figure 2.21). This lAr veto acts as both passive and active shielding, since it is instrumented with photo-multiplier tubes and can detect scintillation light when a background event interacts inside the lAr. The MAJORANA DEMONSTRATOR has achieved low backgrounds thanks to its ultra-clean materials, particularly the electroformed copper, superior energy resolution and improved PSA techniques. The energy resolution and PSA improvements are enabled by the low noise LMFE electronics, which are mounted directly next to the detectors.

The MAJORANA and GERDA collaborations have combined to form the LEGEND collaboration, with the plan of building a tonne-scale array of enriched PPC HPGe detectors[105]. LEGEND will combine the background techniques demonstrated by the MAJORANA DEMONSTRATOR and GERDA experiments and is currently undergoing active R&D efforts to further reduce backgrounds. Currently, two stages are planned for LEGEND. LEGEND-200 is a 200 kg array of detectors that will utilize the existing GERDA infrastructure at Gran Sasso National Laboratory (LNGS) in Italy, shown in Figure 2.21, with construction expected to begin in 2020. In addition to the existing enriched HPGe detectors in use for both expirements, new detectors will be deployed, using an inverted-coaxial geometry which will have similar performance to the MAJORANA DEMONSTRATOR Ortec detectors, but even higher mass. Low mass electronics based on the MAJORANA DEMONSTRATOR's LMFE design will be implemented, offering improved noise performance over what was achieved by GERDA.
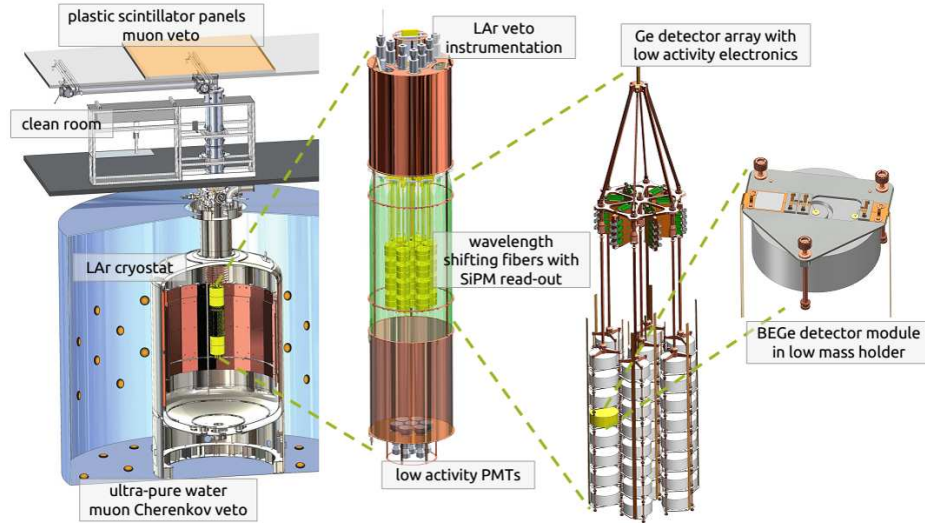
Figure 2.21: The components of the GERDA experiment. These components will be reused for LEGEND-200, with additional HPGe detectors. Image from Gusev talk.

The background goal for LEGEND-200 is < 0.6 cts/(ROI-t-y), which is expected to be feasible based on simulations of the array with the previously mentioned improvements in the GERDA lAr shield. After collecting ~ 1 t-y of exposure, LEGEND-200 is expected to have a sensitivity to ^{76}Ge $0\nu\beta\beta$ of $> 10^{27}$ y at 90% CL.

LEGEND-1000 is a planned 1 tonne experiment that is currently undergoing active R&D. A baseline design for LEGEND-1000, based on the GERDA MAJORANA DEMONSTRATOR, and LEGEND-200 designs, is shown in Figure 2.22. In addition to the improvements implemented for LEGEND-200, LEGEND-1000 will use underground electroformed copper, clean materials, and additional background rejection techniques that are under development. LEGEND-1000 may be housed in a laboratory with greater overburden than LNGS, reducing muon induced backgrounds. Low background lAr from underground sources will also be used, reducing backgrounds from cosmogenically activated isotopes such as the ^{42}Ar–^{42}K–^{42}Ca chain. Based on these improvements, a background index of < 0.1 cts/(FWHM-t-y) is expected, enabling a sensitivity to ^{76}Ge $0\nu\beta\beta$ of $> 10^{27}$ y at 90% CL with 10 t-y of exposure.
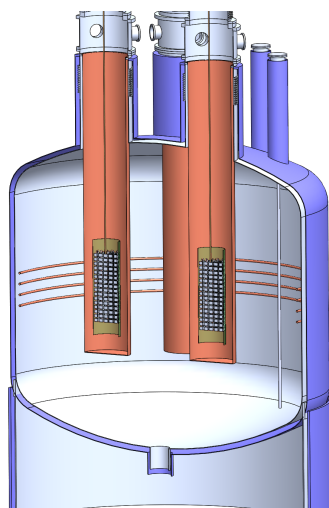
Figure 2.22: A baseline conceptual design for the LEGEND-1000 experiment.

Chapter 3

SIMULATING THE Majorana Demonstrator

3.1 Simulation Software

3.1.1 MaGe

MaGe (Majorana/ GERDA) [101] is a Monte Carlo software package developed jointly by the Majorana and GERDA collaborations for the purpose of simulating low-background experiments involving HPGe detectors. MaGe is written primarily in C++ and is based on the Geant4 physics simulation framework[98]. A Geant4 simulation requires the following inputs:

- **Experiment Geometry:** A description of the physical dimensions, location, and materials must be provided. These should be included for both the detectors and the experimental structure surrounding the detectors.

- **Event Generator:** A generator creates the initial conditions for an event, including the initial particles generated, and the intitial positions and momenta of each initial particle. Typically, the initial parameters are described by an incoming beam of particles. For the Majorana Demonstrator and other experiments that wish to model background radiation, the initial positions will typically be sampled from a particular subset of the full experimental geometry, such as the volume defined by a particular component. The initial momenta will be sampled from the allowed phase space of the process, conserving energy and momentum and sampling the angular correlation distribution. Many processes will generate multiple events; for example, a ^{228}Th decay will generate a set of particles for each decay in the chain, including γs generated by nuclear deexcitations.

- **Physics Lists:** The physics lists describe the physical processes to be simulated as the generated particles propagate through the experimental geometry. Examples of such processes include Compton scattering of γ-rays in matter and energy deposition of electrons as they propagate through matter. A physics list will describe the probability of a process happening in a given material, any changes to the tracked particle, and any new particles produced by the process.

MaGe contains geometries describing various detector configurations for the Majorana Demonstrator. MaGe also includes event generators that are used to describe $\beta\beta$-decay from inside the detectors, backgrounds generated from various experimental components from prominent radioactive isotopes, the line sources used in detector calibration, and for cosmic ray muons. Finally, MaGe includes the relevant physics lists for simulating the nuclear processes observed by the Majorana Demonstrator. MaGe enables a user to select a geometry and event generator by writing a simple macro and running the `MaGe` executable on that macro. All simulations described in this chapter will use the full as-built Majorana Demonstrator geometry, which is shown in Figure 3.1.

A Monte Carlo run by Geant4 will generate a large number of event primaries. A Monte Carlo event primary begins with the set of particles created by the input event generator. Each particle will then be given a particle track, describing the path it takes through the experiment geometry. If the particle undergoes an interaction with the experiment as described in a physics list, a Monte Carlo step will occur. A Monte Carlo step describes the particle before and after an interaction, any additional particles generated in the interaction, and the amount of energy imparted into the matter along the step. For each Monte Carlo event primary, MaGe will record an event with the details of each Monte Carlo step that occurs inside of a detector, including the position of the step, the incoming particle, the outgoing particles, the physics process that caused the step, and the amount of energy deposited. If no interactions occur inside a detector, the event will not be recorded, but recorded events are enumerated according to the event primaries to ensure that the detection efficiency can
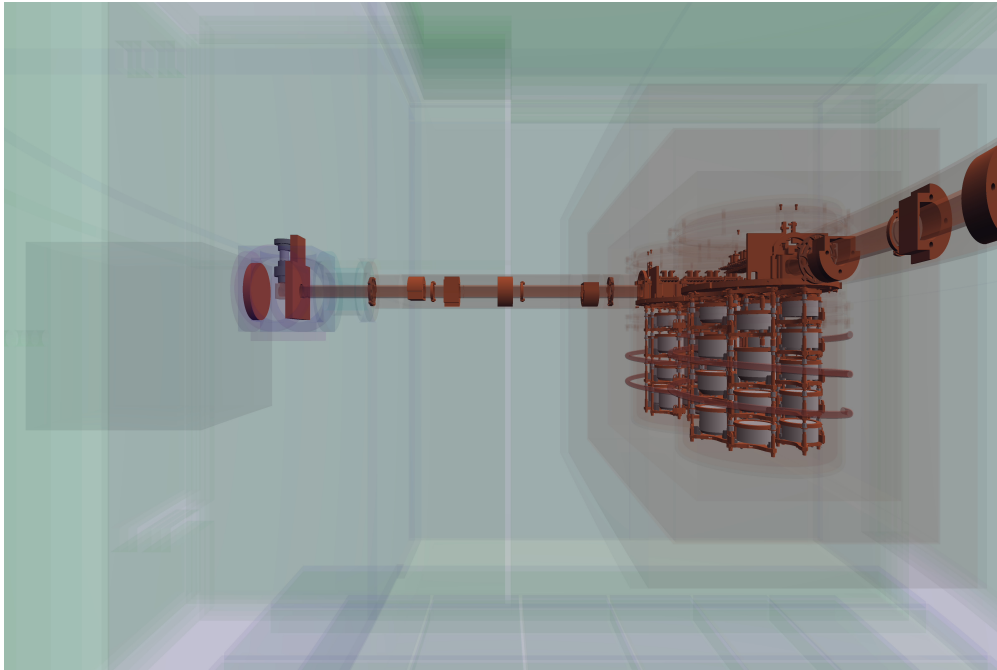
Figure 3.1: The as-built MAJORANA DEMONSTRATOR geometry as programmed in MaGe.

be accurately counted.

The simulation events are stored in a `TTree` containing the following branches:

- `fMCRun`: Contains meta-information about the simulation run, including the run number, number of events, and settings for the run.

- `eventHeader`: Contains meta-information about the event such as the event ID.

- `eventSteps`: Contains data from each event step that deposits energy in a HPGe detector volume, including the location, process and energy deposition.

- `eventPrimaries`: Contains data from the first step in an event, which generated the event.

3.1.2   Simulation Post-Processing

Once a MAGE simulation is run, the data generated must be post-processed to look like MAJORANA DEMONSTRATOR data. Post-processing is performed by the GAT executable `process_MJD_as_built_mage_results`. The post-processor requires the input of individual detector characteristics such as energy resolution and dead layer parameters, which are provided via a JSON file. The relevant steps of the post-processor will be described in the next few paragraphs.

First, steps within 0.1 mm and 5 ns of each other are grouped into clusters. A typical cluster will contain the initial physics process that generated the cluster, such as a Compton scatter or β decay which generate a high energy electron in the detector, and many electron scatters as the electron comes to rest inside of the detector, generating a cloud of electron-hole pairs. For each cluster, the total energy and energy-weighted average position of the cluster are computed.

3.1.3   Dead Layers

A region with a thickness of ~1 mm of the n^+-type surface of an HPGe detector is "dead," i.e. does not contribute any charge to the detector response. Any event inside of this dead layer will not be recorded. Furthermore, charge clouds at the boundary of the dead layer (called the transition region) will have a degraded charge response. Both dead layer and transition region events impact the detection efficiency of the MAJORANA DEMONSTRATOR for all types of events, so modelling and simulating it properly is critical to obtaining an accurate result.

The effect of the detector dead layers are computed for each step individually. The fraction of total charge collected is modelled as a function of depth beneath the detector

surface by the piecewise function

$$A(x) = \begin{cases} 0 & z < 0 \\ g(x) = Ae^{Bx} + C & 0 \leq z < t \\ h(x) = Mx + D & t \leq z < 1 \\ 1 & t \geq 1 \end{cases} \quad \text{Constrained to:} \quad \begin{cases} g(0) \equiv 0 \\ g(t) \equiv h(t) \equiv f \\ g'(t) \equiv h'(t) \\ h(1) \equiv 1 \end{cases} \quad (3.1)$$

where x is the depth of the event as a fraction of the dead layer thickness, t is the transition depth, f is the transition fraction, and all other parameters are uniquely determined by t and f [106][107]. For each cluster, the uncollected charge is summed and used to compute the deadness fraction for the cluster. The total measured energy within a detector is computed by summing the energy of each cluster and degrading by a factor of the local dead fraction. The deadness model parameters are measured by performing a fit of a simulated ^{228}Th calibration hit spectrum to calibration data, floating the dead layer parameters for each detector. The most sensitive parts of the calibration spectrum in this fit are the low energy portion of the spectrum, where the transition layer events with degraded energy accumulate, and in the peak amplitudes and steps. The parameters for this model are provided individually for each detector in a JSON file input to `process_MJD_as_built_mage_results`. Figure 3.2 shows the best fit of a ^{228}Th calibration simulation to data with and without this dead layer model applied.

Finally, the post-processor smears energies by the response function measured during ^{228}Th calibration runs. The post-processor uses the peakshape functions described in Appendix A. Only the gaussian and low energy tail parameters are used. The post-processor samples an energy from the probability distribution described by the peak-shape function centered at the energy calculated for the event. The peak-shape parameters are provided individually for each detector using the input JSON file.

(a) Flat dead layer model   (b) Full dead layer model
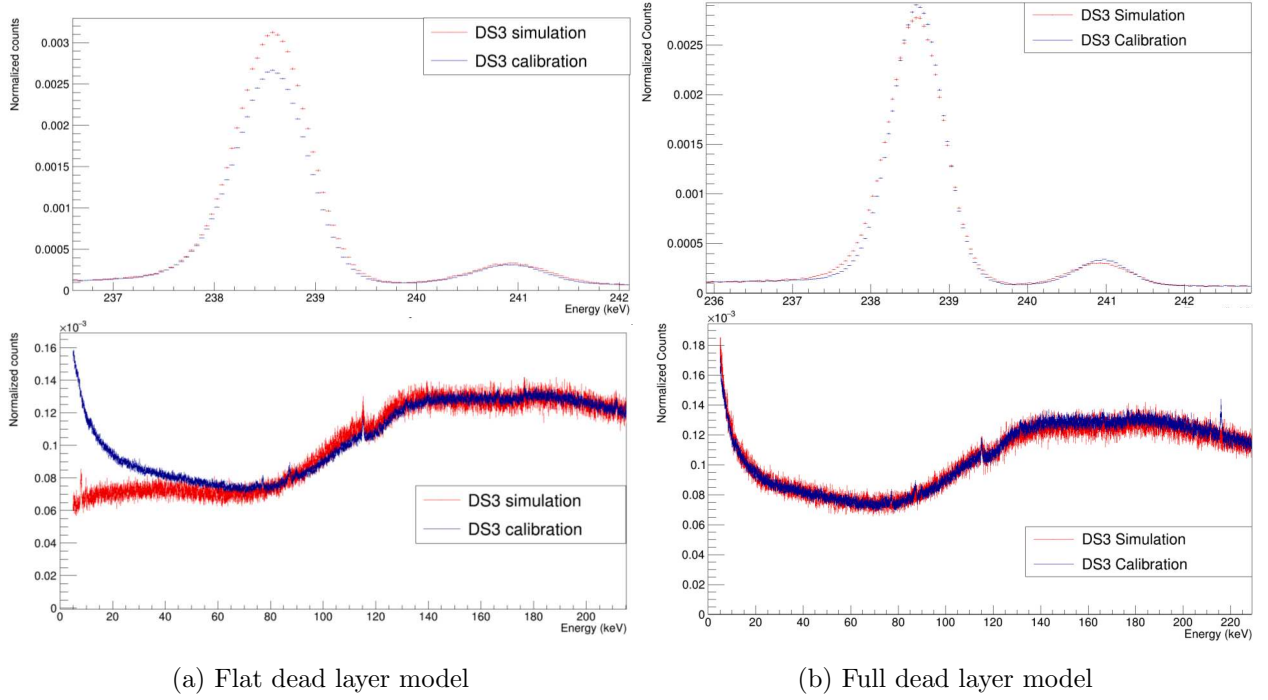
Figure 3.2: Comparison of the best fit of a ^{228}Th calibration simulation spectrum to calibration data. On the left, a flat, step-like dead layer model is used, and on the right the dead layer model described by equation 3.1 is used. The effect of the dead layer model can be seen the most strongly in the relative peak amplitude and step-heights, and in the low energy portion of the spectrum. This model fit is used to measure the dead layer thickness and the uncertainty in the thickness.

3.1.4 Simulation Skimming

Finally, skim files are produced containing parameters of interest from the post-processed files using the software `es_skimsims`. Skim files can also mix postprocessed files from multiple sources in ratios corresponding to the various activities of the sources. `es_skimsims` accepts as input a JSON file listing the simulated sources, the desired activity of each source, and the number of available event primaries. From this, it calculates the number of primaries to accept from each source by maximizing the total number of events used while maintaining the correct ratio according to the activities. Once this is done, it goes through each source sequentially and saves parameters of interest, including energy and detector position, to a `TTree`. As will be discussed in future chapters, single detector events are of little interest to this analysis, so only multi-detector events are recorded in order to maintain a small file size. Multiplicity 1 events are recorded separately to a histogram according only to energy. The skimming process also accounts for which sets of detectors are enabled. Another input of `es_skimsims` is a JSON file containing a list of detector configurations, containing a bitmask describing which detectors are and are not enabled. The detector configurations will be discussed further in Section 4.2.1. When the skimmer encounters a disabled detector in an event, it ignores that detector, and does not count it towards the event multiplicity.

Each detector spends some portion of operating time dead, due to the finite rate at which the digitizers can retrigger, which typically cause $< 0.1\%$ of HPGe hits to fail to read. However, during early datasets, some detector channels were effected by a bug in the Gretina cards that caused a high rate of triggers on negative-energy noise pulses, resulting in much higher dead time fractions. This effect is assumed to be random and uncorrelated between detectors. The dead time of each detector is measured by counting the number of pulser events in each detector for each run. Because the pulses occur at a fixed rate, we can predict the number of pulser events that should occur in any given run; the fraction of pulser events missed is assumed to represent the dead time fraction. The JSON detector configuration file contains the dead time fraction and the statistical uncertainty (assuming

binomial statistics with respect to the total number of expected pulser events) on that fraction for each active detector. For each simulated detector hit, the data skimmer randomly throws out hits according to the probability represented by the dead fraction, treating that detector as inactive for that event.

3.2 Simulation of Excited State Decays

Simulations of the ^{76}Ge decay to excited states of ^{76}Se are used to evaluate the detection efficiency of the analysis presented in this thesis. Two different event generators are used to generate ^{76}Ge $\beta\beta$-decay within MaGe. The first generator uses calculations of the phase space factors from J. Kotila and F. Iachello[41]. It is implemented in the mage class `MGGeneratorDoubleBeta` using data tables with the distribution of both electron energies and anglular correlations. These data tables are provided for the $2\nu\beta\beta$ and $0\nu\beta\beta$ decays to the ground state of ^{76}Se, but not for the decays to any excited state of ^{76}Se. This calculation is an improvement over other phase space calculations thanks to an exact evalutaion of the Dirac wave functions of the electrons involving a finite nuclear size and electron screening.

A second event generator packaged with MaGe is `DECAY0`[108], a FORTRAN program that generates a wide variety of $\beta\beta$- and β-decays. `DECAY0` is capable of generating $2\nu\beta\beta$ and $0\nu\beta\beta$ for ^{76}Ge to ^{76}Se 0^+ and 2^+ excited states using a variety of physics mechanisms. For the excited state decays, the deexcitation γs and conversion electrons are also generated. Several modifications were made to `decay0` for this analysis. First, the precision of the excited state deexcitation energies was increased from 1 keV to 0.001 keV (The γ energies changed from 559 to 559.101 keV, from 563 to 563.178 keV, from 657 to 657.041 keV, and from 1216 to 1216.104 keV). Second, angular correlations were added for the 2_2^+-2_1^+-$0_{g.s.}^+$ deexcitation γ cascade which involves a 657 keV γ with multipolarity E2+M1 and mixing ratio of +5.2 followed by a 559 keV γ with multipolarity E2[109]. The angular distribution between the γs is

$$P(\theta) \propto 1 - 0.372 \cdot \cos^2(\theta) + 0.0439 \cdot \cos^4(\theta) [110] \tag{3.2}$$

The angular correlation for the 0_1^+-2_1^+-$0_{g.s.}^+$ deexcitation was already correctly included in

`DECAY0`, and is represented by the angular distribution

$$P(\theta) \propto 1 - 3 \cdot \cos^2(\theta) + 4 \cdot \cos^4(\theta) [109,\ 110] \qquad (3.3)$$

Running `DECAY0` produces data files with the initial momenta of the generated particles. The MaGe class `MGGeneratorDecay0` reads these datafiles and generates initial positions for these events.
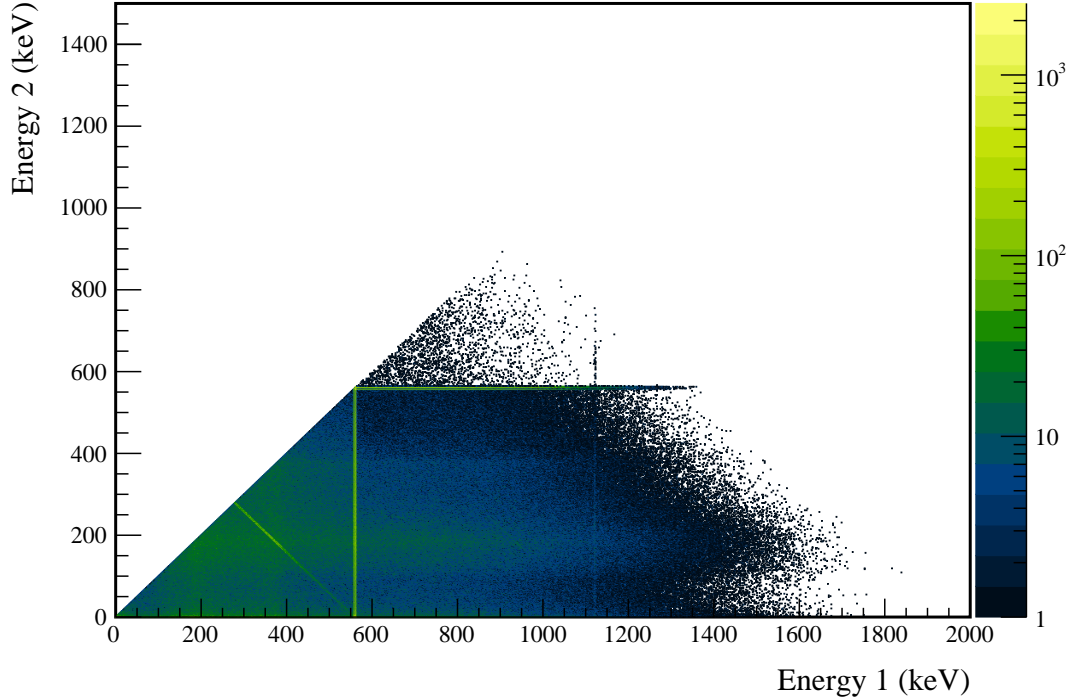
Figure 3.3: Multiplicity 2 energy spectrum produced by a `DECAY0` simulation of $2\nu\beta\beta$ of ^{76}Ge to the 0_1^+ state of ^{76}Se.

Simulations were run for ^{76}Ge $2\nu\beta\beta$ and $0\nu\beta\beta$ to the ^{76}Se 0_1^+, 2_1^+ and 2_2^+ excited states using the `DECAY0` generator. For each decay mode, 5000000 event primaries were generated in the bulk of the enriched detectors and 500000 primaries were generated in the bulk of the

(a) `decay0` $2\nu\beta\beta$ to g.s.
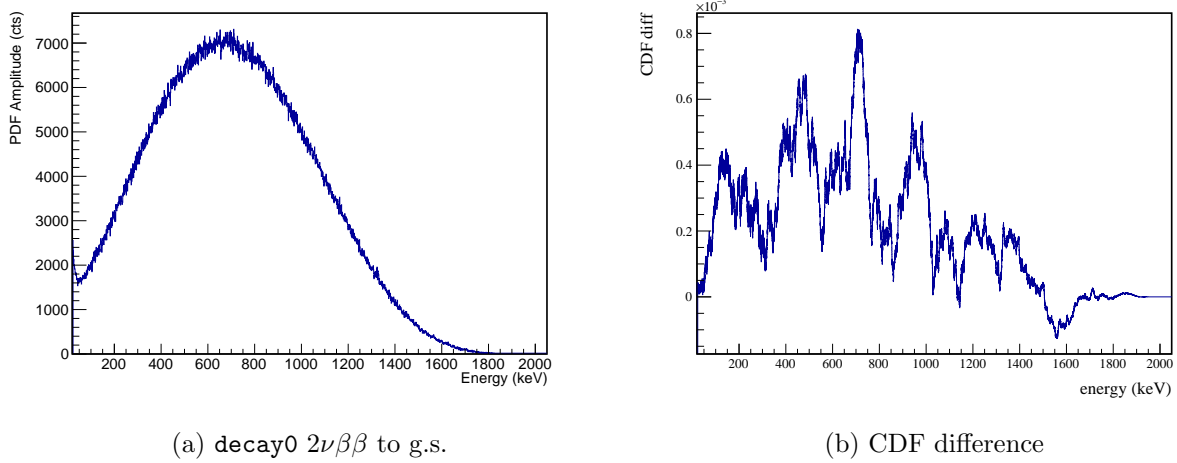
(b) CDF difference

Figure 3.4: A KS test is performed comparing the `DECAY0` $2\nu\beta\beta$ to the ground state energy spectrum to that of Kotila and Iachello. The `decay0` spectrum is shown, along with the difference between the CDF of each spectrum.

natural detectors. These events were skimmed with the relative activities set equal to the total isotopic mass in each set of detectors: 26.2538 kg in enriched detectors, and 1.1232 kg in natural detectors. These simulations were additionally post-processed and skim files were produced both with and without a dead layer, and with and without dead times. Figure 3.3 shows an energy spectrum of multiplicity 2 events produced by the simulation of the ^{76}Ge decay to the 0_1^+ excited state of ^{76}Se.

3.2.1 Comparing *DECAY0* to the Kotila and Iachello generator

The Kotila and Iachello generator performs a more accurate calculation of phase space than `DECAY0` and is used for the MAJORANA DEMONSTRATOR's measurement of $2\nu\beta\beta$ and $0\nu\beta\beta$ to the ground state. Because Kotila and Iachello present only the phase space integral for the excited state decays, and do not include the energy and angular distributions, `DECAY0` is used for this analysis. To evaluate the accuracy of `DECAY0`, we can compare the spectrum

of the $2\nu\beta\beta$ to the ground state it generates to that of Kotila and Iachello; this comparison will reflect the error with respect to the true value if we assume that the errors corrected by Kotila and Iachello are the dominant errors in `DECAY0`. This comparison is performed using a Kolmogorov-Smirnov (KS) test. The KS test statistic is the maximum difference between the CDF of each normalized energy spectrum. As we will see in Section 4.4.2, this test is useful in evaluating the uncertainties in the measurement presented in this thesis. The CDF difference is shown in Figure 3.4, with a KS statistic of 0.00081. While this error is statistically significant at a level of 97%, we will see that the systematic error generated is subdominant.

3.3   *Background Model Simulation*

A simulation of the background spectrum measured by the MAJORANA DEMONSTRATOR will be used to optimize the search for $\beta\beta$ E.S.. MAGE simulations of a variety of decay chains, including ^{232}Th, ^{238}U, ^{40}K, ^{60}Co, ^{222}Rn and ^{68}Ge, have been run using event generators internal to Geant4. A large number of component groups have been defined, encompassing one or more physical components of the experiment (e.g. all signal electronic connectors are a single component group). The event generators use the combined geometries of these groups to generate start positions, which can be in either the bulk of a component group, or on the surface. The activity of each isotope from each component group is determined by fitting a linear combination of the simulated energy spectra to the measured background spectrum. An incomplete version of this fit is used for this thesis, producing the spectra in Figures 3.5 and 3.6[111]. ^{68}Ge decays with a half-life of 271 days, so its activity is scaled to represent the exposure-weighted activity of each major dataset. ^{210}Pb in the lead shield is simulated using a special generator that samples bremsstrahlung x-rays emitted from the surface of a thick lead shield [112].

The background model used for this analysis is known to be inaccurate. Since it is only used for optimizing the search for $\beta\beta$ E.S. and is not important for the detection efficiency calculation, this does not affect the accuracy of the result presented. For future versions of
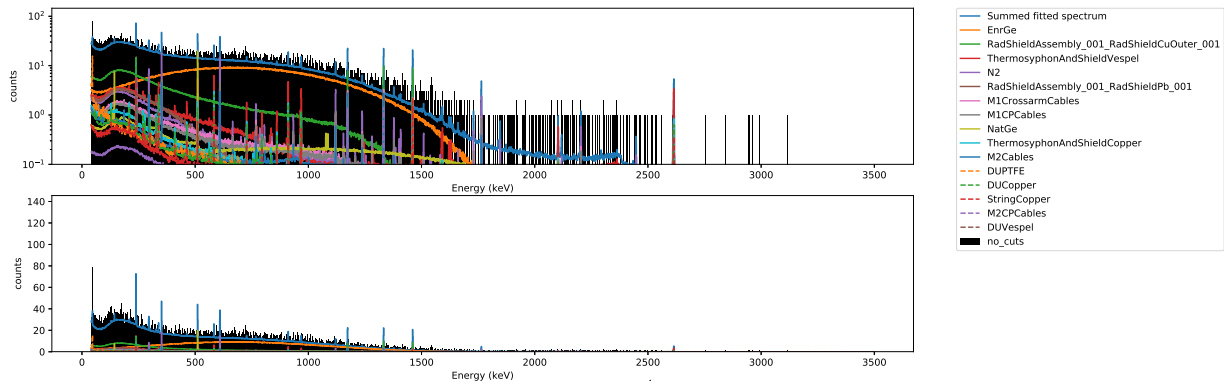
Figure 3.5: Energy spectrum of observed multiplicity 1 events produced from a simulation of the preliminary background model, with the highest contributing components labelled.
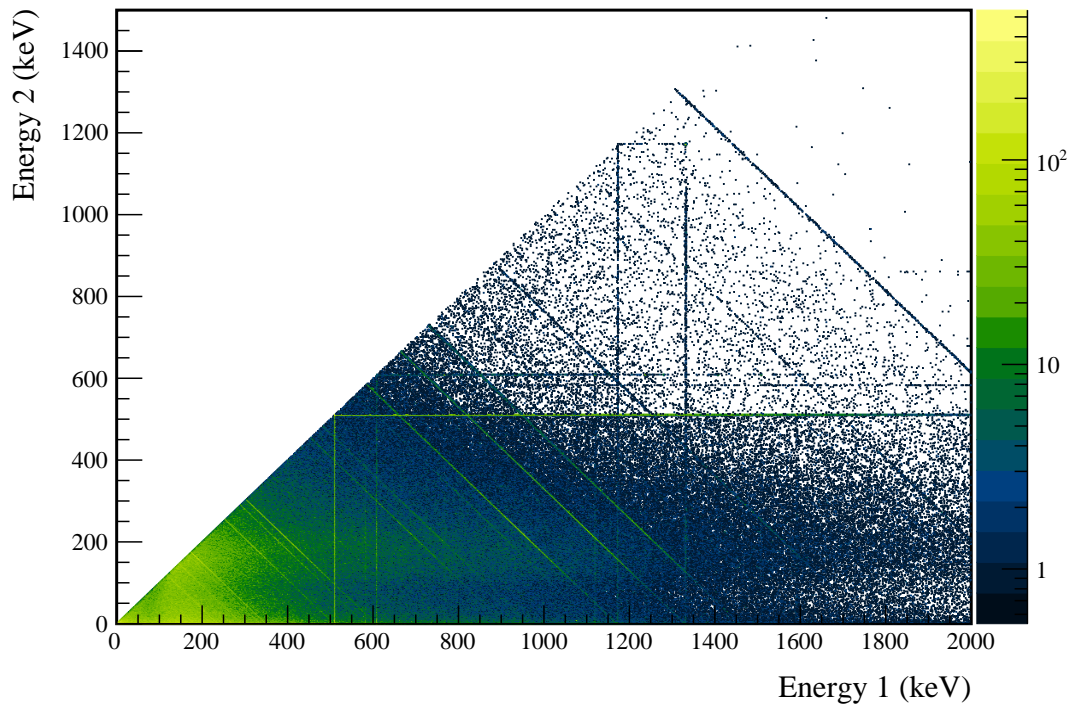
Figure 3.6: Multiplicity 2 energy spectrum produced by a simulation of a preliminary version of the MAJORANA DEMONSTRATOR background model.

this analysis, a complete and more accurate background model will be used, which should result in small improvements to the cut optimization.

3.4   *Calibration Source Simulation*

Calibration of the Majorana Demonstrator is performed for each module using a line source that is injected by motor into a spiral track that winds around the module. Both ^{228}Th and ^{56}Co line sources are used. Simulations of each of these calibration sources are performed using the Geant4 generators for these isotopes, and a spiral position sampler written in MaGe. These simulations are used to test various aspects of the MaGe simulations and to calibrate several observables. Figure 3.7 shows a comparison between a simulated and measured ^{228}Th calibration spectrum. For example, the dead layer thickness measurement described in Section 3.1.2 relies on the ^{228}Th source simulation, and the detection efficiency test described in Section 4.2.4 uses the ^{56}Co source simulation. The simulated spectra for the ^{56}Co source can be seen in Figures 3.8 and 3.9
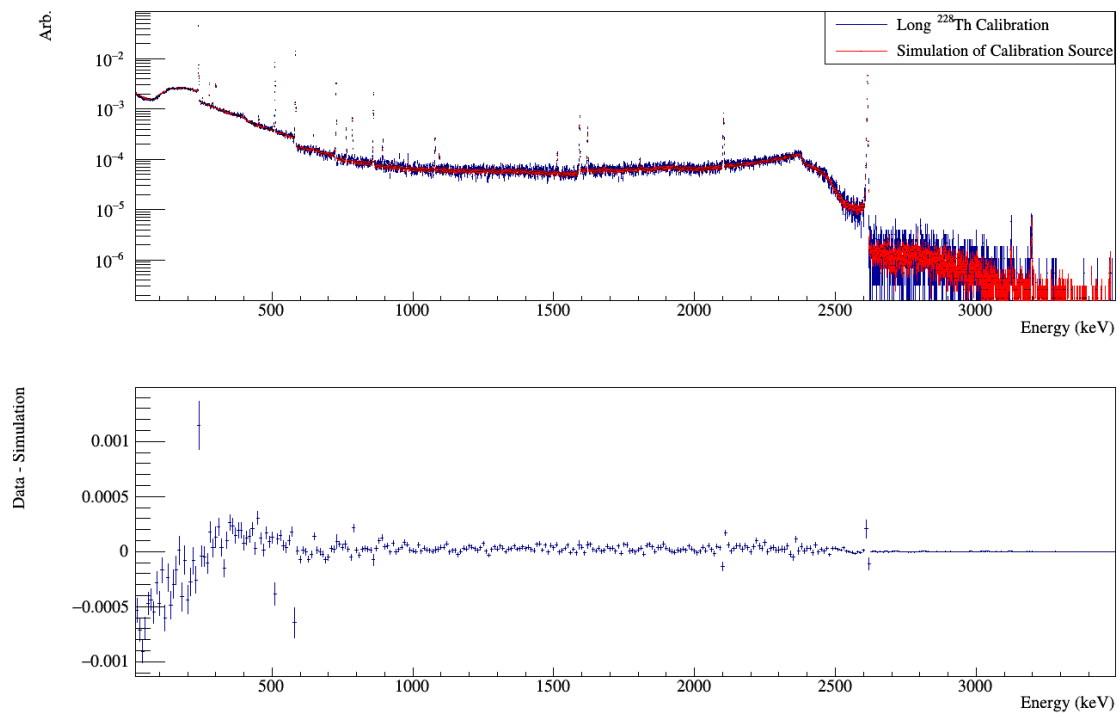
Figure 3.7: A comparison of the simulated and measured energy spectrum from the ^{228}Th line source, with residuals.
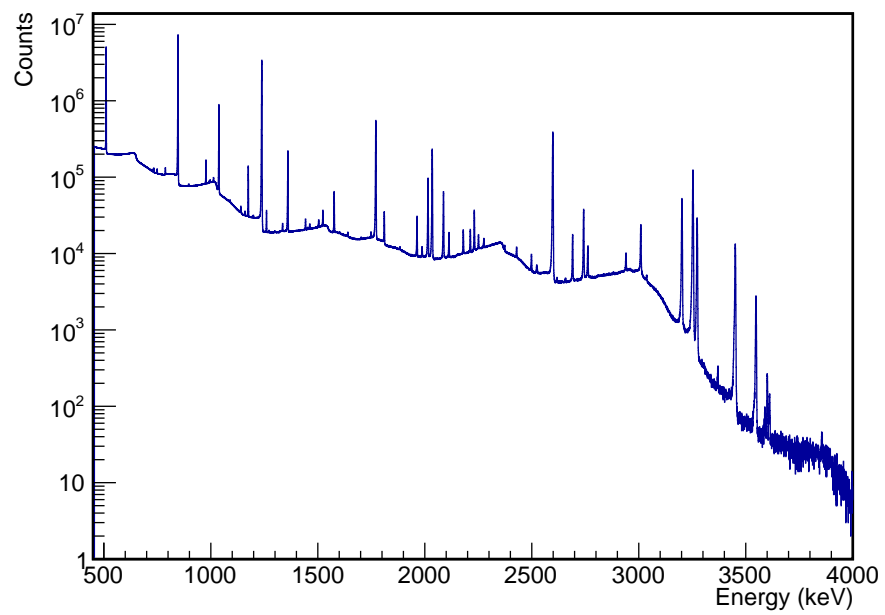
Figure 3.8: Energy spectrum of multiplicity 1 events produced from a simulation of the ^{56}Co line source inserted into the module 1 calibration track.
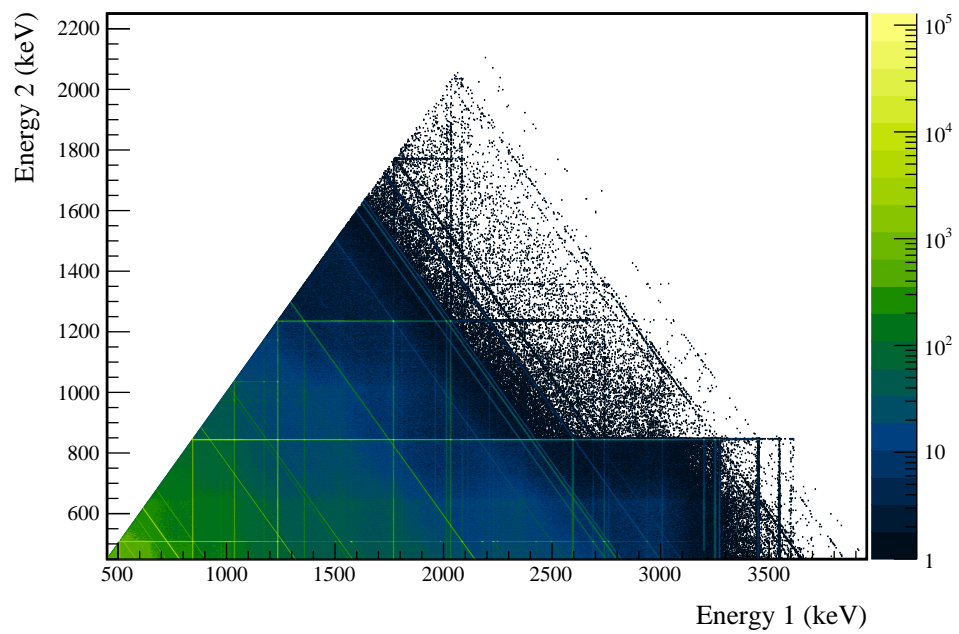
Figure 3.9: Multiplicity 2 energy spectrum produced by a simulation of the ^{56}Co line source inserted into the module 1 calibration track.

Chapter 4

SEARCHING FOR DOUBLE BETA DECAY TO EXCITED STATES

4.1 Introduction
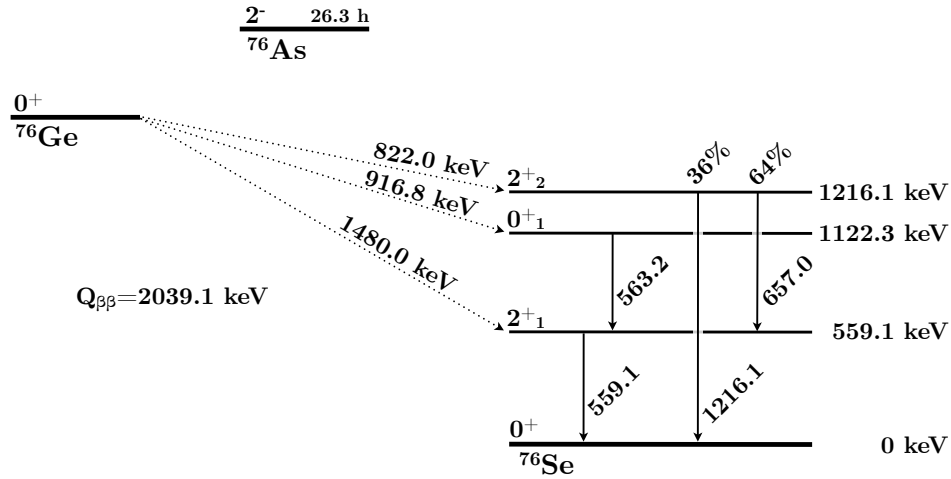
Figure 4.1: Energy level diagram for $\beta\beta$-decay of ^{76}Ge to ^{76}Se, including excited states. The Q-values for each decay branch and the energies and branching ratios for the deexcitation γs are shown next to their corresponding lines.

^{76}Se has 3 excited states that ^{76}Ge can decay into in addition to the ground state, as shown in Figure 4.9. While the ground state decay has been observed, none of the decays to excited states have been yet; current experimental limits and theoretical estimates for the half-life of each decay are listed in Table 1.2. Each excited state decay will have a $\beta\beta$-decay with a reduced Q-value compared to the ground state decay. The excited state decays will also promptly produce one or two γ-rays at known energies. These γs will typically

travel several cm before absorption and will often hit a different detector from the $\beta\beta$-decay site, meaning that we can search for peaks at these energies. Furthermore, since these γ events must hit a separate detector from the site of the $\beta\beta$-decay, the events containing this peak are inherently multi-detector. As shown in Figure 4.2, by searching for the peak only in events with high hit multiplicity, i.e. events that involve 2 or more detectors hit, $\sim$85% of backgrounds can be cut, while only sacrificing $\sim$25% of the signal. Additionally, the coincident detector hit(s) can provide additional observables that can be used to further discriminate excited state signals from multi-site backgrounds. This chapter will describe the various background reduction data cuts and how they are implemented. It will also evaluate the detection efficiency and systematic error associated with each cut based on simulations of the MAJORANA DEMONSTRATOR. The analysis presented in this chapter applies to the $2\nu\beta\beta$-decay to the 0_1^+ state of ^{76}Se, which has $Q_{\beta\beta} = 916.8$ keV and emits two γs at 559.1 keV and 563.2 keV. The same analysis is applied to all other excited states in both the $0\nu\beta\beta$ and $2\nu\beta\beta$ decay modes, and the results are presented in Appendix D.

4.2 Selection of Multi-Detector Events

Simultaneous detector hits are combined into events by the event builder (see Section 2.3.3 and Appendix C). Events are combined in a 4 μs rolling window. This window is expected to accept virtually all true coincidence events (see Figure 4.3). In a small number of runs, clocks between different Gretina cards were desynchronized. For these runs, the clocks were resynchronized by applying a timing offset during event building that is measured by seeking the time offset that aligns pulser events. With a typical overall rate between both modules of < 1 Hz, $< 0.4\%$ of all multi-site events are expected to originate from accidental coincidences, making this a negligible background. Once all the data has gone through the processing chain described in Section 2.3, the skim files from all good open runs in datasets 16a are collected into a single skim file containing a `TTree` with only multi-site events by the program `es_skimdata`.
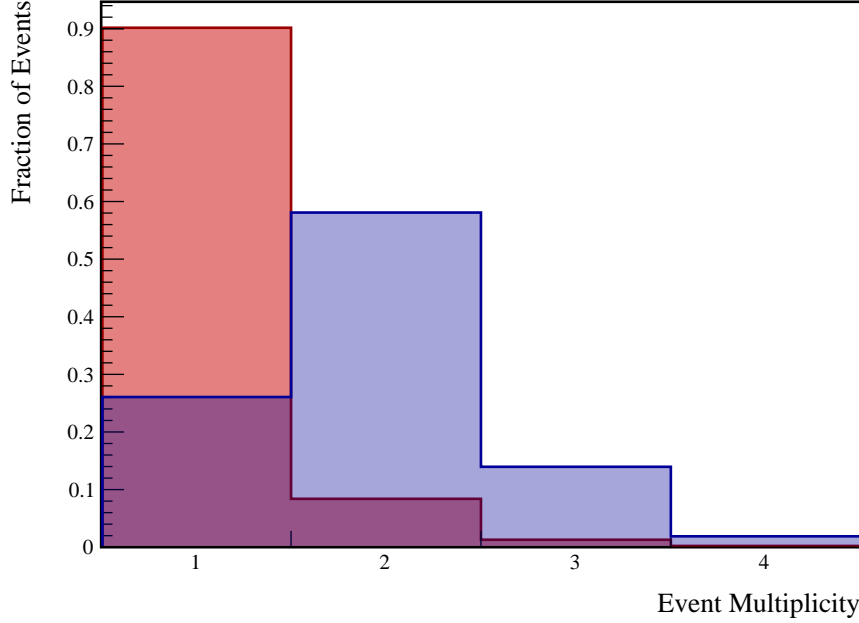
Figure 4.2: The simulated distribution of ROI event multiplicities in the background model and $\beta\beta$ E.S.to 0_1^+ decay in DS6.

4.2.1 Variation in Detector Configuration

Throughout the runtime of the MAJORANA DEMONSTRATOR, not all detectors were simultaneously active, and within each dataset, the set of active detectors varied signficantly. Because we are looking at multi-site event events, the detection efficiency for $\beta\beta$ E.S. events in any detector depends on which other detectors are enabled. For this reason, detection efficiency is computed for each module in its entirety rather than for individual detectors. To account for changes in detector configuration, each dataset is divided into subdatasets based on which detectors are active. The subdatasets are described by a pair of 64-bit masks, one for each module, with each bit representing a single detector's state. To decode the bitmask,
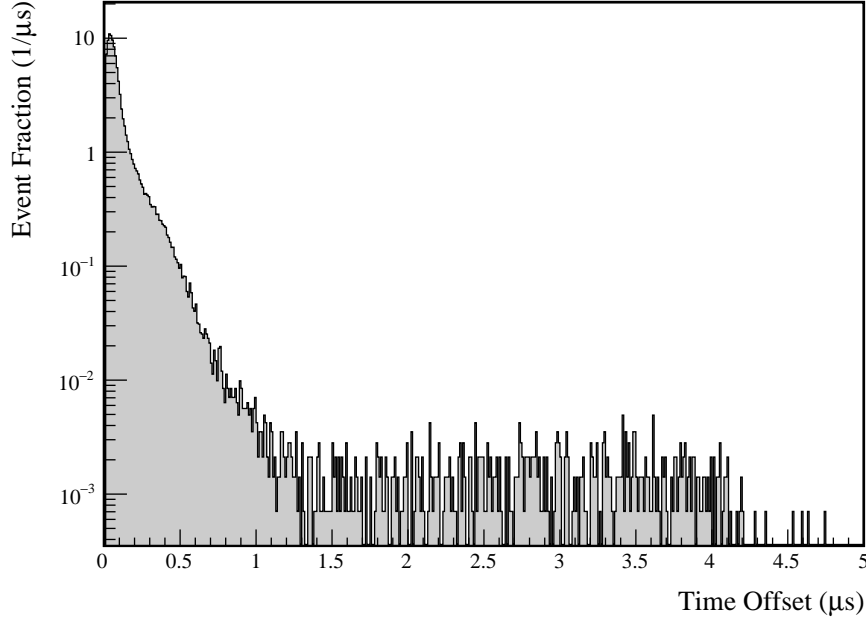
Figure 4.3: Distribution of time interval between individual hits within a multi-detector event during a ^{228}Th calibration run. Offsets of greater than $\sim$1.5 μs are due to pileup, which is significant due to the high data rate of calibration runs. Offsets greater than $\sim$4 μs must involve events with more than two hits, due to the event builder time window.

the b'th least significant bit represents string position P, detector position D if

$$b = 8 \cdot P + D \tag{4.1}$$

The set of runs and active channels for each run were determined by the run selection and data cleaning committee, and the procedures are outlined in [113]. The program `es_getdatasets` uses these selections to sort each run into a subdataset.

The detection efficiency is defined as the probability of a signal event in any detector, including inactive detectors. Detection efficiency is calculated individually for each sub-dataset and for each module by creating a separate skim file for each subdataset as outlined in Section 3.1.4. The final efficiency is then computed as an isotopic exposure weighted

average of the efficiency within each subdataset. Any efficiency uncertainties are assumed to be totally correlated between subdatasets. The livetime of each subdataset is calculated by the program `es_livetimes` by totalling the run time in each run, and subtracting any deadtime that affects the entire module, including deadtime caused by the muon veto system and by liquid nitrogen fills. Additional sources of deadtime that affect individual detectors are calculated as inefficiencies rather than being subtracted from the livetime, as discussed in Section 3.1.4. This is done because deadtime in any individual detector affects the detection efficiency of all other detectors. The isotopic exposure is computed by multiplying the livetime of each module by the total isotopic mass in each module. Since this includes mass in inactive detectors and dead layers, the isotopic exposure for this analysis will differ from that presented in the $0\nu\beta\beta$ analysis. Table 4.1 lists each subdataset along with its livetime and exposure.

DS	M1 Detector Mask	M2 Detector Mask	Run Time (days)	M1 L.T. (days)	M1 Eff.	M2 L.T. (days)	M2 Eff.	Exposure (kg·y)
DS1	061a08001e0e1c00	0000000000000000	2.64	2.60	1.693%	0.00	0.000%	0.109
DS1	161a08341e0e1c00	0000000000000000	0.02	0.02	1.978%	0.00	0.000%	0.001
DS1	161a0c341e0e1c00	0000000000000000	4.51	4.48	1.915%	0.00	0.000%	0.188
DS1	161a0c361e0e1c00	0000000000000000	3.49	3.48	1.449%	0.00	0.000%	0.146
DS1	1e1a00001e0e1c00	0000000000000000	7.82	7.73	2.015%	0.00	0.000%	0.324
DS1	1e1a08001e0e1c00	0000000000000000	25.49	25.19	2.202%	0.00	0.000%	1.057
DS1	1e1a08041e0e1c00	0000000000000000	2.95	2.93	2.277%	0.00	0.000%	0.123
DS1	1e1a08141e0e1c00	0000000000000000	0.26	0.25	2.297%	0.00	0.000%	0.011
DS1	1e1a08301e0e1c00	0000000000000000	1.40	1.37	2.305%	0.00	0.000%	0.057
DS1	1e1a08341e0e1c00	0000000000000000	7.58	7.50	2.095%	0.00	0.000%	0.315
DS1	1e1a0c001e0e1c00	0000000000000000	1.96	1.93	2.226%	0.00	0.000%	0.081
DS1	1e1a0c341e0e1c00	0000000000000000	0.67	0.67	2.296%	0.00	0.000%	0.028
DS2	1e1a08001e0e1c00	0000000000000000	9.58	9.51	2.248%	0.00	0.000%	0.399
DS3	1e1a0c3e1e0e1c00	0000000000000000	29.88	29.67	2.566%	0.00	0.000%	1.245
DS4	0000000000000000	1c061a16060e1e00	19.15	0.00	0.000%	18.85	1.811%	0.622
DS5a	08000020040e1c00	18060a02040e1e00	1.49	1.48	0.703%	1.46	1.111%	0.110
DS5a	08080020040e1c00	18060a16060e1e00	2.51	2.49	0.842%	2.47	1.484%	0.186
DS5a	08080030040e1c00	18060a02040e1e00	0.01	0.01	0.888%	0.01	1.094%	0.001
DS5a	0e1a04321e0e1c00	08020a16060e1e00	2.69	2.71	2.265%	2.66	1.165%	0.201
DS5a	0e1a0c321e0e1c00	0000000000000000	0.65	0.63	2.522%	0.00	0.000%	0.026

<div align="right">Continued on the next page</div>

Table 4.1: List of subdatasets

DS	M1 Detector Mask	M2 Detector Mask	Run Time (days)	M1 L.T. (days)	M1 Eff.	M2 L.T. (days)	M2 Eff.	Exposure (kg·y)
DS5a	0e1a0c321e0e1c00	08060a16060e1e00	1.24	1.24	2.513%	1.21	1.451%	0.092
DS5a	0e1a0c321e0e1c00	18060a02040e1e00	2.94	2.92	2.288%	2.89	1.098%	0.218
DS5a	0e1a0c321e0e1c00	18060a1406061600	0.04	0.04	2.487%	0.04	0.906%	0.003
DS5a	0e1a0c321e0e1c00	18060a1606060600	3.19	3.15	2.452%	3.16	0.774%	0.237
DS5a	0e1a0c321e0e1c00	18060a16060e0600	3.30	3.28	2.458%	3.29	0.793%	0.246
DS5a	0e1a0c3e1e0e1c00	1806020606081800	1.75	1.73	2.703%	1.73	0.726%	0.129
DS5a	0e1a0c3e1e0e1c00	18060216060c1c00	6.84	6.77	2.698%	6.74	1.068%	0.507
DS5a	0e1a0c3e1e0e1c00	18060216060e1e00	13.48	13.30	2.677%	13.27	1.189%	0.996
DS5a	0e1a0c3e1e0e1c00	18060816060e1c00	0.05	0.05	2.502%	0.05	1.247%	0.004
DS5a	0e1a0c3e1e0e1c00	18060a0606060c00	2.16	2.12	2.670%	2.12	0.982%	0.159
DS5a	0e1a0c3e1e0e1c00	18060a16040e1e00	0.76	0.76	2.668%	0.74	1.222%	0.056
DS5a	0e1a0c3e1e0e1c00	18060a1606060c00	0.25	0.25	2.682%	0.25	1.060%	0.019
DS5a	0e1a0c3e1e0e1c00	18060a1606061800	1.88	1.86	2.686%	1.86	0.998%	0.140
DS5a	0e1a0c3e1e0e1c00	18060a1606061c00	9.20	9.13	2.657%	9.06	1.353%	0.682
DS5a	0e1a0c3e1e0e1c00	18060a16060c1c00	7.89	7.79	2.688%	7.79	1.350%	0.584
DS5a	0e1a0c3e1e0e1c00	18060a16060e1c00	11.68	11.53	2.340%	11.51	1.357%	0.864
DS5a	0e1a0c3e1e0e1c00	18060a16060e1e00	5.21	5.15	2.665%	5.13	1.486%	0.386
DS5a	0e1a0c3e1e0e1c00	18061216060e1e00	2.39	2.37	2.676%	2.37	1.266%	0.178
DS5b	1e1a0c3e1e0c1c00	18061216060e1e00	24.46	24.09	2.672%	24.06	1.268%	1.805
DS5b	1e1a0c3e1e0c1c00	18061a16060e1e00	0.75	0.75	2.670%	0.75	1.654%	0.056
DS5b	1e1a0c3e1e0e1c00	18061216060e1e00	14.28	14.12	2.766%	14.07	1.169%	1.057
DS5c	1e1a0c3e1e0c1c00	00060216060e0e00	0.00	0.00	2.567%	0.00	0.787%	0.000
DS5c	1e1a0c3e1e0c1c00	00060a16060e0e00	0.91	0.89	2.664%	0.91	1.016%	0.067
DS5c	1e1a0c3e1e0c1c00	00061216060e0e00	10.22	10.15	2.645%	10.03	0.857%	0.757
DS6a	12000000000c0800	1002020006040600	1.33	1.31	0.160%	1.31	0.230%	0.099
DS6a	12000c20000c1c00	18061216060c1600	6.93	6.84	0.756%	6.86	0.679%	0.514
DS6a	12020000040c0800	1802020006040600	1.30	1.28	0.284%	1.28	0.275%	0.096
DS6a	12020c00040c1800	1802020006040600	2.37	2.33	0.676%	2.33	0.275%	0.175
DS6a	12080c20000c1c00	18061216060c1600	3.38	3.34	0.931%	3.34	0.677%	0.251
DS6a	12120c3e1c0c1c00	18061216060c1600	0.56	0.54	1.847%	0.56	0.676%	0.041
DS6a	16020c10040c1800	1806020006060600	3.23	3.20	0.883%	3.19	0.416%	0.239
DS6a	160a0c321c0c1c00	1806021006061600	1.98	1.95	2.022%	1.97	0.521%	0.147
DS6a	1e0a0c321c0c1c00	1806020006040200	2.62	2.59	2.275%	2.59	0.260%	0.194
DS6a	1e0a0c321c0c1c00	1806020006040600	1.31	1.29	2.275%	1.29	0.390%	0.097
DS6a	1e0a0c321c0c1c00	1806020006041600	1.30	1.28	2.275%	1.26	0.459%	0.096
DS6a	1e0a0c321c0c1c00	1806021006061600	1.61	1.59	2.275%	1.59	0.521%	0.119
DS6a	1e120c3e1c0c1c00	18061216060c1600	0.95	0.93	2.284%	0.93	0.676%	0.070
DS6a	1e1a0c321c0c1c00	1806020006060600	1.30	1.28	2.457%	1.28	0.416%	0.096

Continued on the next page

Table 4.1: List of subdatasets

DS	M1 Detector Mask	M2 Detector Mask	Run Time (days)	M1 L.T. (days)	M1 Eff.	M2 L.T. (days)	M2 Eff.	Exposure (kg·y)
DS6a	1e1a0c321c0c1c00	1806021006040600	3.91	3.88	2.457%	3.87	0.415%	0.291
DS6a	1e1a0c321c0c1c00	1806021006041600	2.92	2.90	2.457%	2.90	0.495%	0.217
DS6a	1e1a0c321c0c1c00	1806021006060600	1.31	1.30	2.455%	1.30	0.436%	0.097
DS6a	1e1a0c3a1c0c1c00	1806020006040600	2.32	2.31	2.553%	2.32	0.390%	0.174
DS6a	1e1a0c3a1c0c1c00	1806021006040600	1.77	1.77	2.552%	1.75	0.415%	0.132
DS6a	1e1a0c3a1c0c1c00	1806021006041600	0.67	0.67	2.553%	0.67	0.494%	0.050
DS6a	1e1a0c3e1c0c1c00	1806000006040600	2.22	2.18	2.631%	2.16	0.360%	0.163
DS6a	1e1a0c3e1c0c1c00	1806020006041600	1.32	1.30	2.630%	1.30	0.458%	0.097
DS6a	1e1a0c3e1c0c1c00	1806021006041600	1.30	1.28	2.630%	1.28	0.494%	0.096
DS6a	1e1a0c3e1c0c1c00	18060210060c1600	4.63	4.58	2.629%	4.55	0.533%	0.342
DS6a	1e1a0c3e1c0c1c00	1806021206041600	2.61	2.56	2.628%	2.57	0.515%	0.192
DS6a	1e1a0c3e1c0c1c00	18060214060c0600	1.70	1.70	2.628%	1.68	0.492%	0.127
DS6a	1e1a0c3e1c0c1c00	18060214060c1600	1.38	1.36	2.627%	1.36	0.576%	0.102
DS6a	1e1a0c3e1c0c1c00	18060214060e1600	23.42	23.19	2.601%	23.12	0.555%	1.736
DS6a	1e1a0c3e1c0c1c00	18061212060c1600	2.93	2.89	2.628%	2.90	0.644%	0.217
DS6a	1e1a0c3e1c0c1c00	18061216060c1600	6.59	6.51	2.628%	6.51	0.690%	0.488
DSTotal	–	–	321.60	318.26	2.354%	238.53	0.987%	21.228

Table 4.1: List of each subdataset with its livetime, detection efficiency measured for the $\beta\beta$ E.S.to 0_1^+ decay, and total isotopic exposure. Note the large variance in the detection efficiency.

4.2.2   Dead Layer Effects

For multi-detector events, each individual hit may be degraded by the deadlayer, so the loss of sensitivity from deadlayers is larger for this search than for searches for single-site events. For this reason, dead layer effects are treated as a loss of detection efficiency instead of a loss of exposure (as in the $0\nu\beta\beta$ analysis). Dead layers are included in the simulations as a part of post-processing as described in Section 3.1.2. To account for uncertainty in the thickness of the deadlayer, two separate simulations are run, with and without deadlayers. By comparing the efficiency measurement from each simulation, we measure the size of the dead layer effect. The percent uncertainty in the efficiency loss from dead layers is assumed to be the same as the percent uncertainty in the dead layer thickness. Typical loss of efficiency
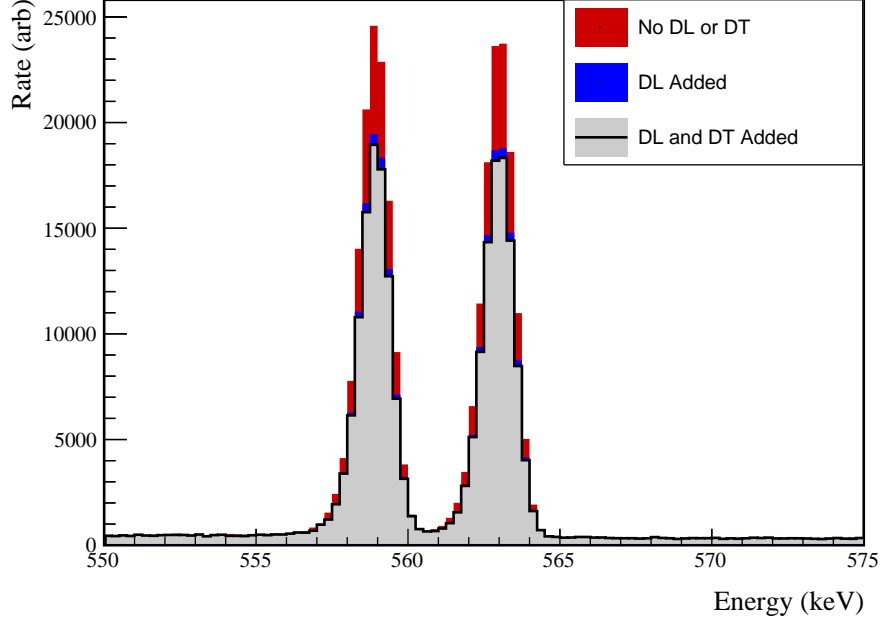
Figure 4.4: Effect of dead layers and dead times on peak amplitudes for $2\nu\beta\beta$ to the 0_1^+ peaks in multi-site event events.

for multi-site peaks is 25-35%; for the $2\nu\beta\beta$ to the 0_1^+ decay, the losses are 26% for module 1 and 34% for module 2. The uncertainty in the dead layer tends to be one of the dominant uncertainties in measuring the detection efficiency. This is much larger than the $\sim$10% loss seen in the $0\nu\beta\beta$ analysis for two reasons. First, for multi-detector events, there are multiple hits that could possibly be lost to the dead layer. Second, γ hits will be more concentrated at the surface of the detectors, near the dead layers, than $\beta\beta$ sites. The effect of dead layers on detection efficiency can be seen in Figure 4.4.

4.2.3   Dead Time Effects

Detector deadtimes, which affect only a single detector at a time, reduce the detection efficiency for events that occur in all detectors in the module. For this reason, instead

of subtracting these deadtimes from the livetime, the deadtimes are incorperated into the detection efficiency. Detector deadtimes are measured individually for each run by counting pulser events and comparing to the number of expected pulser events for each detector. The program `es_livetime` collects the detector deadtimes that are measured in this way and finds the average detector deadtime for each subdataset. These dead times are then applied to the simulation skimming process as described in Section 3.1.4. Similar to the dead layers, simulation files are produced with and without deadtimes in order to measure the size of the effect. Uncertainties in the detector deadtimes are measured as the statistical uncertainties from pulser counts. The percent uncertainty in efficiency loss from detector dead times is assumed to be the same as the average percent uncertainty in the detector dead time. Typical loss of efficiency from detector deadtimes range from 1-3%. For the $2\nu\beta\beta$ to the 0_1^+ decay, the losses are 2.5% for module 1 and 1.9% for module 2. The effects of detector deadtimes can be seen in Figure 4.4.

4.2.4   Simulation Validation and Errors

In addition to dead layer and dead time effects that can be explicitly accounted for, other possible sources of systematic uncertainty from the simulation exist, such as inaccuracies in the simulation geometry. To account for these, we use pair production events from calibration runs as a proxy for $\beta\beta$ E.S. events. In pair production events, an electron-positron pair is produced in the bulk of a detector, followed promptly by two 511 keV γs from the annihilation of the positron. Because these events involve a single pair production site and the prompt emission of gamma rays which may be absorbed in a separate detector, they make a good proxy for $\beta\beta$ E.S. events. In single-escape peak (SEP) events, one gamma is absorbed in the detector containing the pair-production, while the other escapes, resulting in a source detector hit with energy equal to the γ energy minus 511 keV. In double-escape peak (DEP) events, both gammas escape the detector, resulting in a source detector hit with energy equal to the γ energy minus 1022 keV. Both both SEP and DEP events present the possibility for a second 511 keV detector hit. By comparing the rate of multiplicity-1 events in the SEPs and
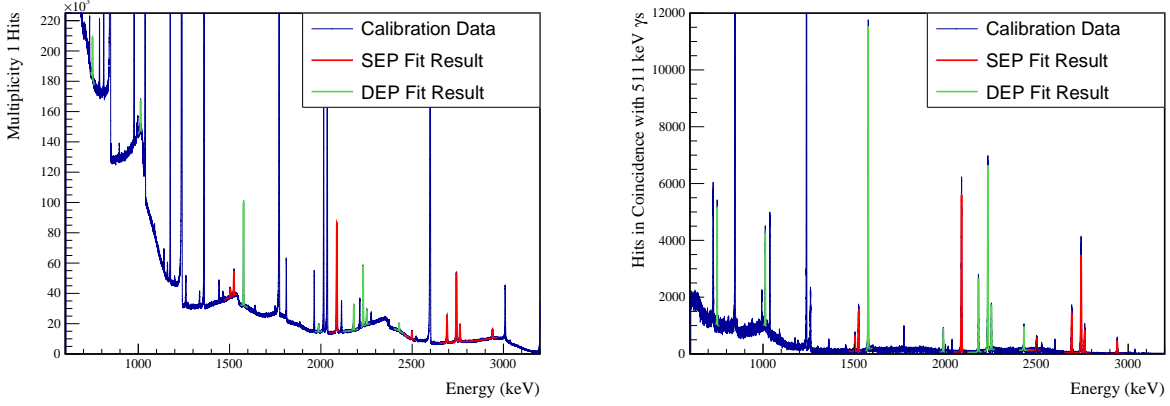
Figure 4.5: Spectra of multiplicity 1 ^{56}Co events (left) and multiplicity 2 ^{56}Co events in coincidence with an annihilation gamma. The results of the simultaneous peak fits are drawn in red (SEP fit) and green (DEP fit).

DEPs to the rate of multiplicity-2 events in which one hit falls into one of these peaks and the other falls into the 511 keV peak, we can measure a proxy for the detection efficiency of our multi-site event signature. By comparing this measurement to simulation, we can estimate the size of any unknown uncertainties in our simulation-based efficiency estimate.

To achieve this, we will use a ^{56}Co calibration source. ^{56}Co presents the advantage of a large number of γs at energies high enough to cause pair production, which allows for a comparison of many peaks to our simulation. A ^{56}Co line source was inserted into the module 1 calibration track on January 15, 2019 and 168.1 hrs of data were recorded, until January 22, 2019. Immediately after this, the source was inserted into the module 2 calibration track and 167.1 hrs of data were recorded until January 29, 2019. The source had a nominal activity of 6 kHz, resulting in a high enough data rate that the energy threshold for each channel was raised to ~400 keV. As discussed in Section 3.4, 3 billion event primaries were simulated for the ^{56}Co source in each module's source track in order to achieve similar events statistics for both the simulations and data. Simulations were run with and without

dead-layers.

8 SEPs and 7 DEPs were selected as proxies for the $\beta\beta$ E.S. signal; these peaks were selected because of their prominence above the Compton continuum and the absense of nearby peaks that would interfere with a peak-height measurement. A simultaneous fit, as described in Appendix A, of all SEPs as single-detector events and as two-detector events in coincidence with a 511 keV peak event was performed in the calibration data and in the simulations both with and without dead layers. SEPs and DEPs have abnormal peakshapes due to in-flight annihilation of the positrons, which results in Doppler broadening of the peak shapes. For this reason, a high energy tail is added to the typical peak shape function. The peak height ratios and uncertainties for peak k are determined as follows:

$$\epsilon_k = \frac{A_{k,m2}}{A_{k,m1}} \tag{4.2}$$

$$\sigma_{stat,k} = \epsilon_k \sqrt{\frac{\Sigma_{A,k,m1;A,k,m1}}{A_{k,m1}^2} - 2\frac{\Sigma_{A,k,m1;A,k,m2}}{A_{k,m1}A_{k,m2}} + \frac{\Sigma_{A,k,m2;A,k,m2}}{A_{k,m2}^2}} \tag{4.3}$$

where $A_{k,m1/2}$ are the fitted amplitudes of peak k with multiplicity 1 and multiplicity 2 respectively, and $\Sigma_{A,k,m1/2;A,k,m1/2}$ is the fitter covariance matrix element for these amplitudes. The same process of simultaneously fitting DEPs is followed to extract the DEP peak-height ratios. The measured data spectra and fit results are shown in Figure 4.5.

Figure 4.6 shows an overall offsete that cannot be explained by statistical errors; this discrepancy is measured and treated as a systematic error which will be applied to the $\beta\beta$ E.S. measurement. Since some of this discrepancy can be explained by the dead layer uncertainty, the difference between the simulated peak-height ratios with and without the dead layer is multiplied by the percent uncertainty in the dead layer thickness in order to measure the systematic error caused by the dead layer. Finally, a χ^2 value is computed for the comparison between the simulated and measured peak-heights using the statistical and dead-layer uncertainties.

$$\chi^2(\mu, \delta_{DL}) = \sum_{k=1}^{N} \frac{(\epsilon_{k,meas} - \epsilon_{k,sim} - \delta_{DL} \cdot \sigma_{DL,k} - \mu)^2}{\sigma_{stat,dat,k}^2 + \sigma_{stat,sim,k}^2} + \delta_{DL}^2 \tag{4.4}$$
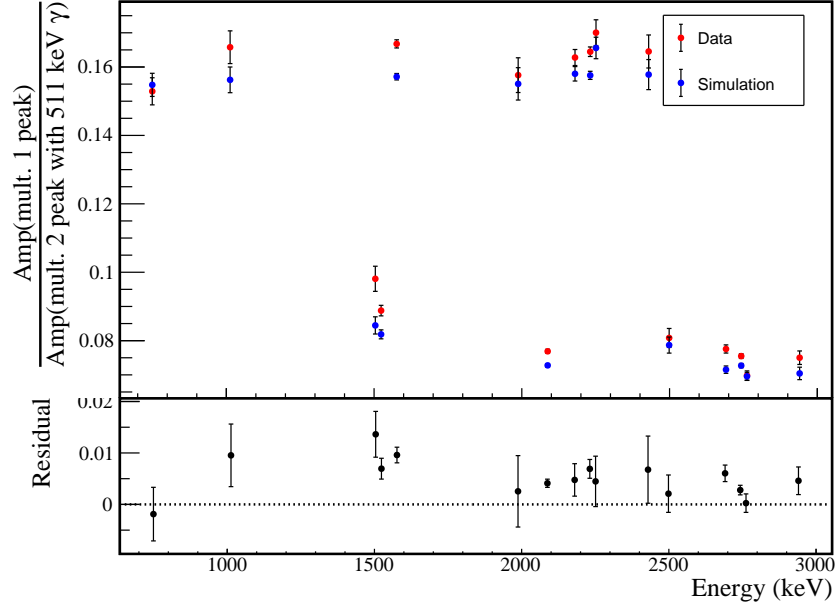
(a) Module 1
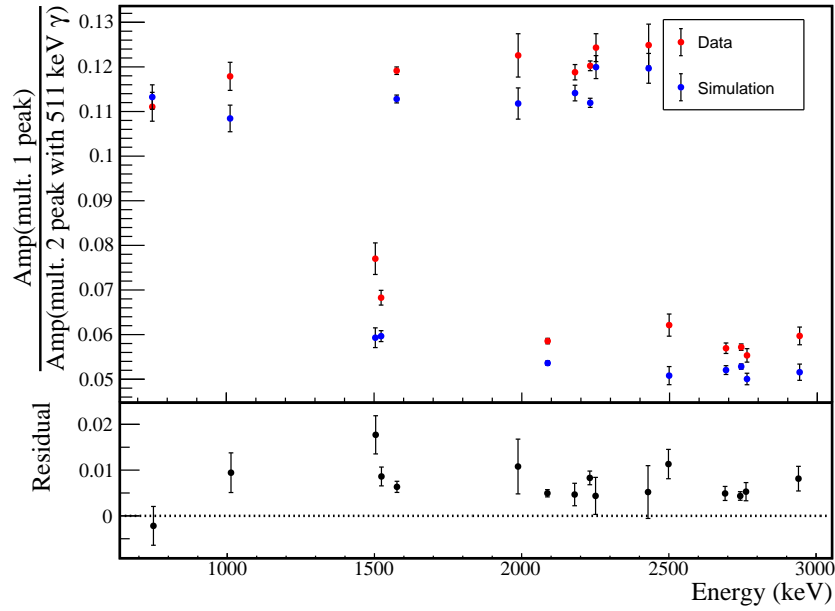
(b) Module 2

Figure 4.6: Measurement of peak height ratios between multiplicity 1 events and multiplicity 2 events containing a 511 keV annihalation γ for both simulated and measured ^{56}Co spectra. Only statistical error bars are drawn. These ratios are listed in tables 4.2 and 4.3.

where $\sigma_{DL,k}$ is the uncertainty from dead layers, δ_{DL} is the measured error from deadlayers (correlated across all peaks with a prior of 1 σ), and μ is the mean error that remains. This χ^2 function is minimized with respect to μ and δ_{DL} and the profile likelihood is used to compute the uncertainty on μ, using MINUIT[114]. The systematic error is taken to be

$$\sigma_{sim}^2 = \mu^2 + \sigma_\mu^2 \tag{4.5}$$

Tables 4.2 and 4.3 list the peak height ratios and uncertainties for each peak for module 1 and module 2, respectively. The final fractional uncertainties measured are $\sigma_{sim,M1} = 0.0020$ and $\sigma_{sim,M2} = 0.0047$. This uncertainty is applied directly to the detection efficiency measured before applying any other effects such as dead layers, dead times and cuts, without any scaling. This uncertainty is one of the dominant uncertainties on the detection efficiency along with the dead layer uncertainty; while the absolute uncertainty is small, because it is applied to the detection efficiency, which tends to be $\sim 5\%$, directly rather than to the loss from an individual effect, the fractional uncertainty is on the order of 10%. In cases where the detection efficiency is very low, such as the 1216 keV peak in module 2 from decays to the 2_2^+ state, this uncertainty can completely overwhelm the detection efficiency. Figure 4.6 plots the peak height ratios for simulated and measured data for both modules 1 and 2.

4.3 Region of Interest Selection

Once the multisite events have been collected, we want to search for detector hits with the energies of the γs emitted in each $\beta\beta$ E.S. decay mode. To do this, a signal region of interest (ROI) must be identified. To estimate the number of background events in the signal ROI, a background ROI must also be selected near the signal ROI. This section will describe the selection of the signal and background ROIs and the calculation of the efficiency and uncertainties on the efficiency due to the ROI selection.

The peakshape function and parameters are described in Appendix A. For each dataset, a simultaneous fit of many peaks is performed to a combined spectrum of all detectors and all calibration runs, ensuring that any variation in gain or energy nonlinearity between detectors

Table 4.2: Table of measured peak height ratios between multiplicity 1 events and multiplicity 2 events containing a 511 keV annihalation γ in module 1 for both simulated and measured ^{56}Co spectra, with uncertainties. A plot of these numbers is shown in Figure 4.6

Peak	$\frac{A_{m2,dat}}{A_{m1,dat}}$	$\frac{A_{m2,sim}}{A_{m1,sim}}$	$\frac{A_{m2,noDL}}{A_{m1,noDL}}$	$\sigma_{dat,stat}$	$\sigma_{sim,stat}$	$\sigma_{sim,DL}$	Residual	σ_{resid}
1504 keV (SEP)	0.098	0.084	0.110	0.004	0.003	0.004	0.014	0.004
1524 keV (SEP)	0.089	0.082	0.109	0.002	0.001	0.005	0.007	0.002
2088 keV (SEP)	0.077	0.073	0.098	0.001	0.001	0.004	0.004	0.001
2499 keV (SEP)	0.081	0.079	0.108	0.003	0.002	0.005	0.002	0.004
2691 keV (SEP)	0.078	0.072	0.099	0.001	0.001	0.005	0.006	0.002
2743 keV (SEP)	0.075	0.073	0.101	0.001	0.001	0.005	0.003	0.001
2762 keV (SEP)	0.070	0.070	0.096	0.001	0.001	0.004	0.000	0.002
2940 keV (SEP)	0.075	0.070	0.100	0.002	0.002	0.005	0.005	0.003
749 keV (DEP)	0.153	0.155	0.225	0.004	0.003	0.012	-0.002	0.005
1013 keV (DEP)	0.166	0.156	0.229	0.005	0.004	0.012	0.010	0.006
1577 keV (DEP)	0.167	0.157	0.224	0.001	0.001	0.011	0.010	0.002
1988 keV (DEP)	0.158	0.155	0.222	0.005	0.005	0.011	0.003	0.007
2180 keV (DEP)	0.163	0.158	0.225	0.002	0.002	0.011	0.005	0.003
2232 keV (DEP)	0.164	0.158	0.225	0.001	0.001	0.012	0.007	0.002
2251 keV (DEP)	0.170	0.166	0.233	0.004	0.003	0.011	0.004	0.005
2429 keV (DEP)	0.165	0.158	0.230	0.005	0.004	0.012	0.007	0.007

Table 4.3: Table of measured peak height ratios between multiplicity 1 events and multiplicity 2 events containing a 511 keV annihalation γ in module 2 for both simulated and measured ^{56}Co spectra, with uncertainties. A plot of these numbers is shown in Figure 4.6

Peak	$\frac{A_{m2,dat}}{A_{m1,dat}}$	$\frac{A_{m2,sim}}{A_{m1,sim}}$	$\frac{A_{m2,noDL}}{A_{m1,noDL}}$	$\sigma_{dat,stat}$	$\sigma_{sim,stat}$	$\sigma_{sim,DL}$	Residual	σ_{resid}
1504 keV (SEP)	0.077	0.059	0.082	0.004	0.002	0.004	0.018	0.004
1524 keV (SEP)	0.068	0.060	0.081	0.002	0.001	0.004	0.009	0.002
2088 keV (SEP)	0.059	0.054	0.074	0.001	0.000	0.003	0.005	0.001
2499 keV (SEP)	0.062	0.051	0.073	0.002	0.002	0.004	0.011	0.003
2691 keV (SEP)	0.057	0.052	0.074	0.001	0.001	0.004	0.005	0.002
2743 keV (SEP)	0.057	0.053	0.075	0.001	0.001	0.004	0.004	0.001
2762 keV (SEP)	0.055	0.050	0.071	0.002	0.001	0.004	0.005	0.002
2940 keV (SEP)	0.060	0.052	0.072	0.002	0.002	0.003	0.008	0.003
749 keV (DEP)	0.111	0.113	0.155	0.003	0.003	0.007	-0.002	0.004
1013 keV (DEP)	0.118	0.108	0.156	0.003	0.003	0.008	0.009	0.004
1577 keV (DEP)	0.119	0.113	0.161	0.001	0.001	0.008	0.006	0.001
1988 keV (DEP)	0.123	0.112	0.153	0.005	0.003	0.007	0.011	0.006
2180 keV (DEP)	0.119	0.114	0.164	0.002	0.002	0.008	0.005	0.002
2232 keV (DEP)	0.120	0.112	0.160	0.001	0.001	0.008	0.008	0.001
2251 keV (DEP)	0.124	0.120	0.170	0.003	0.003	0.008	0.004	0.004
2429 keV (DEP)	0.125	0.120	0.159	0.005	0.003	0.007	0.005	0.006

is accounted for. From each fit result, a set of parameters describing a single peak shape at the energy of the signal ROI can be extracted, along with a covariance matrix for those parameters. From these fit results, we can compute the optimal ROI, detection efficiency and uncertainty for each data set. An example of a calibration spectrum with the FWHM curve fit to it is shown in Figure 4.7.
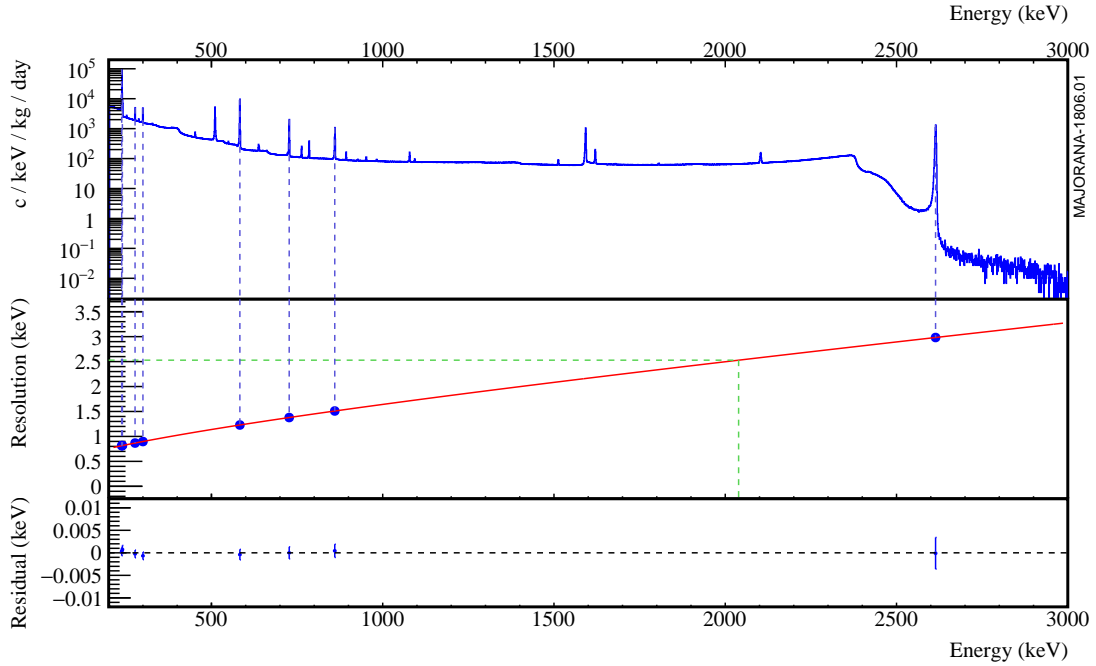
Figure 4.7: A ^{228}Th calibration run with the FWHM fit curve and individual uncertainties at several peaks. This curve is used to compute the FWHM for a peak at a given energy. The statistical uncertainties are extracted from the fit result. An additional systematic uncertainty is added to account for the residuals.

4.3.1 Signal ROI Optimization

The signal region of interest around each peak is optimized based on the peak shape functions as fit for each data set. The optimization follows the procedure laid out in Appendix B and maximizes the rate sensitivity with respect to the region of interest upper and lower

boundaries, E_{low} and E_{high} respectively:

$$\hat{\Gamma}(E_{low}, E_{high}, \overline{B}) \propto \frac{\mathrm{DP}\big(\overline{B}(E_{high} - E_{low})\big)}{\epsilon_{ROI}(E_{low}, E_{high})} \tag{4.6}$$

where DP is the discovery potential as defined in Appendix B, and a flat background with background index $\overline{B}$ measured from data is assumed. The efficiency is defined by the CDF of the Gaussian and LE tail components

$$\begin{aligned}\epsilon_{ROI}(E_{low}, E_{high}; \mu, \sigma, f_{tail}, \tau) = \frac{1}{2}\big(\mathrm{erfc}\left(\frac{E_{low} - \mu}{\sqrt{2}\sigma}\right) - \mathrm{erfc}\left(\frac{E_{high} - \mu}{\sqrt{2}\sigma}\right)\big) \\ + f_{tail}\tau\big(\mathrm{ExGaus}(E_{high}; \mu, \sigma, \tau) - \mathrm{ExGaus}(E_{low}; \mu, \sigma, \tau)\big)\end{aligned} \tag{4.7}$$

The optimal ROI is numerically calculated by minimizing $\frac{1}{\hat{\Gamma}(E_{low}, E_{high}, \overline{B})}$ with respect to E_{low} and E_{high} using MINUIT[114].

4.3.2 Background ROI Selection

For each peak, a background ROI of width $50 - 100$ keV surrounding the peak is selected. The ROI is selected to avoid any known background peaks and exclude them with at least 99.9% efficiency. A 99.9% exclusion region calculated from the peakshape function is selected around the peak and removed from the background ROI.

4.3.3 ROI Detection Efficiency and Uncertainty

The ROI detection efficiency is calculated from the CDF defined in Equation 4.7. The covariance matrix of the peak shape parameters obtained from the fit result is used to calculate the statistical uncertainty of the efficiency. Several additional systematic effects must also be accounted for:

- **Gain drift:** ^{228}Th energy calibrations are taken once per week, for 90 minutes each. In between these calibration runs, the energy calibration parameters undergo small adjustments that result in energy inaccuracies for background runs taken in between. This gain drift results in an increase in the width of the peak, which is accounted

for by adding in quadrature σ_{drift} to the value of σ obtained from the fit. This also results in the dominant systematic uncertainty on the peak width, $\delta_{fwhm,drift}$. The gain drift also results in a small systematic error in the measured energy of the peak $\delta_{\mu,drift}$. A detailed description of the measurement of this systematic effect is contained in Reference [115].

- **Energy nonlinearity:** While the energy response for HPGe detectors is ostensibly linear, several factors result in small nonlinearities. Local nonlinearities that are correlated over small energy scales of arise from the response of the Gretina digitizers. While these nonlinearities are corrected for, a residual nonlinearity of $\sim$0.1 keV with a period of $\sim$300 keV remains. Global nonlinearities result from systematic uncertainties in the energy estimation. One source of global nonlinearity arises from uncertainty in the start time of the waveform, which is energy dependant. Another is a small quadratic term resulting from charge recombination. Because calibrations are performed on peaks with energies ranging from 238 keV to 2614 keV, energy shifts due to global nonlinearities are very small in this range and local energy nonlinearities dominate. At smaller and larger energies, the shifts can be as large as $\sim$0.5 keV in some detectors. In addition to this bias, energy nonlinearities result in an increase in σ as a result of the combining of peaks from different detectors with different shifts; however, since the energy calibrations include all detectors, this shift is already included in the fit result, so no action is required. Energy nonlinearities also have a significant affect on the uncertainty in the measured peak energy, $\delta_{\mu,NL}$, which is a dominant uncertainty. A detailed description of the measurement of each of these systematic effects is contained in Reference [115].

- **Detector Crosstalk:** Because we are searching for peaks in coincidence events, the possibility for a distortion in the energy measurement due to crosstalk between the involved events exists. This effect is measured in Section 4.3.4 to be small enough that no energy correction or peakshape correction is required. However, this effect does contribute to small uncertainties in the peak position, $\delta_{\mu,xtalk}$ and peak width,

$\delta_{fwhm,xtalk}$.

Once these uncertainties have been measured, they must be propagated into the detection efficiency. The statistical and systematic uncertainties on μ and the FWHM are added in quadrature to obtain δ_μ and δ_{fwhm}. The uncertainty on the FWHM is used to calculate a width scale uncertainty, δ_α, which is simply the fractional uncertainty on the FWHM. To compute the uncertainty on the efficiency, the efficiency is computed after modifying the peakshape parameters by one-sigma in either direction. For the uncertainty from the width, we take:

$$
\begin{aligned}
\sigma_{\epsilon_{ROI},fwhm} = \frac{1}{2}\big(\epsilon_{ROI}(E_{low}, E_{high}; \mu, \sigma(1 + \delta_\alpha), f_{LE}, \tau(1 + \delta_\alpha)) \\
- \epsilon_{ROI}(E_{low}, E_{high}; \mu, \sigma(1 - \delta_\alpha), f_{LE}, \tau(1 - \delta_\alpha)))
\end{aligned}
\tag{4.8}
$$

Because the ROI is optimized around μ, shifts in the peak in either direction will cause a reduction in efficiency. For this reason, we must perform a second order propagation of uncertainties with respect to δ_μ. The result is a slight degradation in the efficiency, so that

$$
\epsilon_{ROI} = \frac{\epsilon_{ROI}(E_{low}, E_{high}; \mu + \delta_\mu, \sigma, f_{LE}, \tau) + \epsilon_{ROI}(E_{low}, E_{high}; \mu - \delta_\mu, \sigma, f_{LE}, \tau)}{2}
\tag{4.9}
$$

and

$$
\sigma_{\epsilon_{ROI},\mu} = \epsilon_{ROI}(E_{low}, E_{high}; \mu, \sigma, f_{LE}, \tau)) - \epsilon_{ROI}
\tag{4.10}
$$

These uncertainties are taken to be uncorrelated and added in quadrature to obtain the final uncertainty on the ROI efficiency. Table D.19 contains a full summary of all of the energy uncertainties, the ROIs, and the ROI efficiencies and uncertainties.

4.3.4 Detector Crosstalk

Detector crosstalk is caused when a true signal in one detector channel induces a small signal in another channel. This is not a large enough effect to trigger events in a separate channel, meaning that it does not effect single-detector events. However, it could produce an energy estimation error in multi-detector events since coincident pulses could induce signals that interfere either constructively or destructively, shifting the measured energies. In practice,

Table 4.4: Table of energy estimation uncertainties, regions of interest, and efficiencies

DS	E_{peak} (keV)	σ_{fit} (keV)	σ_{drift} (keV)	σ (keV)	$f_{t,fit}$	τ_{fit} (keV)	$\delta_{\mu,fit}$ (keV)	$\delta_{\mu,NL}$ (keV)	$\delta_{\mu,drift}$ (keV)	$\delta_{\mu,xtalk}$ (keV)	$\delta_{\mu,peak}$ (keV)	δ_{μ} (keV)	FWHM (keV)	$\delta_{fwhm,fit}$ (keV)	$\delta_{fwhm,drift}$ (keV)	$\delta_{fwhm,xtalk}$ (keV)	δ_{FWHM} (keV)	δ_{α}	$E_{ROI,1}$ (keV)	$E_{ROI,2}$ (keV)	ϵ_{ROI}	$\sigma_{\epsilon_{ROI}}$
DS1	559.101	0.460	0.063	0.464	0.230	0.515	0.001	0.104	0.002	0.012	0.005	0.105	1.152	0.001	0.039	0.011	0.040	0.035	558.199	559.847	0.871	0.015
DS2	559.101	0.461	0.055	0.464	0.249	0.515	0.002	0.067	0.004	0.012	0.005	0.068	1.158	0.001	0.107	0.011	0.108	0.093	558.186	559.845	0.874	0.031
DS3	559.101	0.470	0.066	0.474	0.224	0.505	0.001	0.026	0.024	0.012	0.005	0.038	1.174	0.001	0.073	0.011	0.074	0.063	558.187	559.863	0.879	0.021
DS4	559.101	0.455	0.077	0.461	0.108	0.445	0.002	0.076	0.010	0.012	0.005	0.078	1.111	0.001	0.106	0.011	0.107	0.096	558.283	559.856	0.888	0.032
DS5a	559.101	0.560	0.085	0.567	0.106	0.855	0.002	0.079	0.005	0.012	0.005	0.080	1.367	0.002	0.055	0.011	0.056	0.041	558.098	560.022	0.875	0.014
DS5b	559.101	0.469	0.074	0.475	0.158	0.491	0.001	0.020	0.011	0.012	0.005	0.026	1.157	0.001	0.125	0.011	0.125	0.108	558.229	559.872	0.885	0.036
DS5c	559.101	0.460	0.085	0.468	0.174	0.489	0.001	0.037	0.030	0.012	0.005	0.050	1.145	0.001	0.162	0.011	0.162	0.142	558.231	559.860	0.883	0.046
DS6a	559.101	0.456	0.044	0.458	0.191	0.463	0.001	0.069	0.025	0.012	0.005	0.075	1.123	0.000	0.041	0.011	0.042	0.038	558.241	559.841	0.881	0.014
DS1	563.178	0.461	0.064	0.466	0.230	0.518	0.001	0.104	0.002	0.012	0.005	0.105	1.156	0.001	0.039	0.011	0.040	0.035	562.273	563.927	0.871	0.015
DS2	563.178	0.463	0.055	0.466	0.249	0.517	0.002	0.067	0.004	0.012	0.005	0.068	1.162	0.001	0.107	0.011	0.108	0.093	562.259	563.924	0.874	0.030
DS3	563.178	0.471	0.066	0.476	0.224	0.508	0.001	0.026	0.024	0.012	0.005	0.038	1.179	0.001	0.073	0.011	0.074	0.063	562.261	563.943	0.879	0.021
DS4	563.178	0.457	0.077	0.463	0.108	0.447	0.002	0.076	0.010	0.012	0.005	0.078	1.115	0.001	0.106	0.011	0.107	0.096	562.357	563.935	0.888	0.032
DS5a	563.178	0.562	0.086	0.569	0.106	0.858	0.002	0.079	0.006	0.012	0.005	0.080	1.372	0.002	0.055	0.011	0.056	0.041	562.172	564.103	0.875	0.014
DS5b	563.178	0.471	0.074	0.477	0.158	0.494	0.001	0.020	0.011	0.012	0.005	0.026	1.162	0.001	0.125	0.011	0.125	0.108	562.303	563.952	0.885	0.035
DS5c	563.178	0.462	0.086	0.470	0.174	0.492	0.001	0.037	0.030	0.012	0.005	0.050	1.149	0.001	0.162	0.011	0.162	0.141	562.305	563.939	0.883	0.046
DS6a	563.178	0.457	0.044	0.459	0.191	0.465	0.001	0.069	0.026	0.012	0.005	0.075	1.127	0.000	0.041	0.011	0.042	0.038	562.315	563.921	0.881	0.013

this could produce both a shift and additional uncertainty in both the measured energy of the peak and in the width of the peak. To check for this effect, we can look at multi-detector events in ^{228}Th calibration data. In particular, we will compare the centroid and FWHM for several peaks in both single-detector events and multi-detector events.

5 peaks were selected from the ^{208}Tl γ cascade, at 277, 583, 763, 860 and 2614 keV, and one additional peak was selected from the ^{212}Bi cascade, at 785 keV. These peaks were selected based on their prominence in the high multiplicity hit spectrum. The combined calibration spectra from dataset 6 were used to perform this analysis. These peaks were fit individually, and the centroid and FWHM were computed for multiplicity 1 and multiplicity 2 events. Figure 4.8 shows the results of these measurements. While a very small reduction in peak centroid and increase in peak width are observed, the shifts are small compared to the existing uncertainties in these parameters. As a result, we will ignore this shift and instead compute an uncertainty in each parameter caused by crosstalk. We will treat the systematic error as uncorrelated between the peaks and compute the necessary error needed to make the combined statistical and systematic errors large enough to make the χ^2 value computed by comparing these peaks equal to 1:

$$\chi^2 = \sum_{k=0}^{N} \frac{(\text{cen}_{k,m1} - \text{cen}_{k,m2})^2}{\sigma^2_{cen,k,m1} + \sigma^2_{cen,k,m2} + \delta^2_{\mu,xtalk}} \tag{4.11}$$

$$\chi^2 = \sum_{k=0}^{N} \frac{(\text{FWHM}_{k,m1} - \text{FWHM}_{k,m2})^2}{\sigma^2_{fwhm,k,m1} + \sigma^2_{fwhm,k,m2} + \delta^2_{fwhm,xtalk}} \tag{4.12}$$

Both systematic errors are numerically computed using a Brent minimization algorithm. The results are $\delta_{\mu,xtalk} = 0.012$ keV and $\delta_{fwhm,xtalk} = 0.011$ keV, both of which are subdominant uncertainties.

4.4 Background Cuts

By making use of known properties of background events, data cleaning cuts can be designed to selectively reduce backgrounds while minimizing sacrifice of excited state events. Because
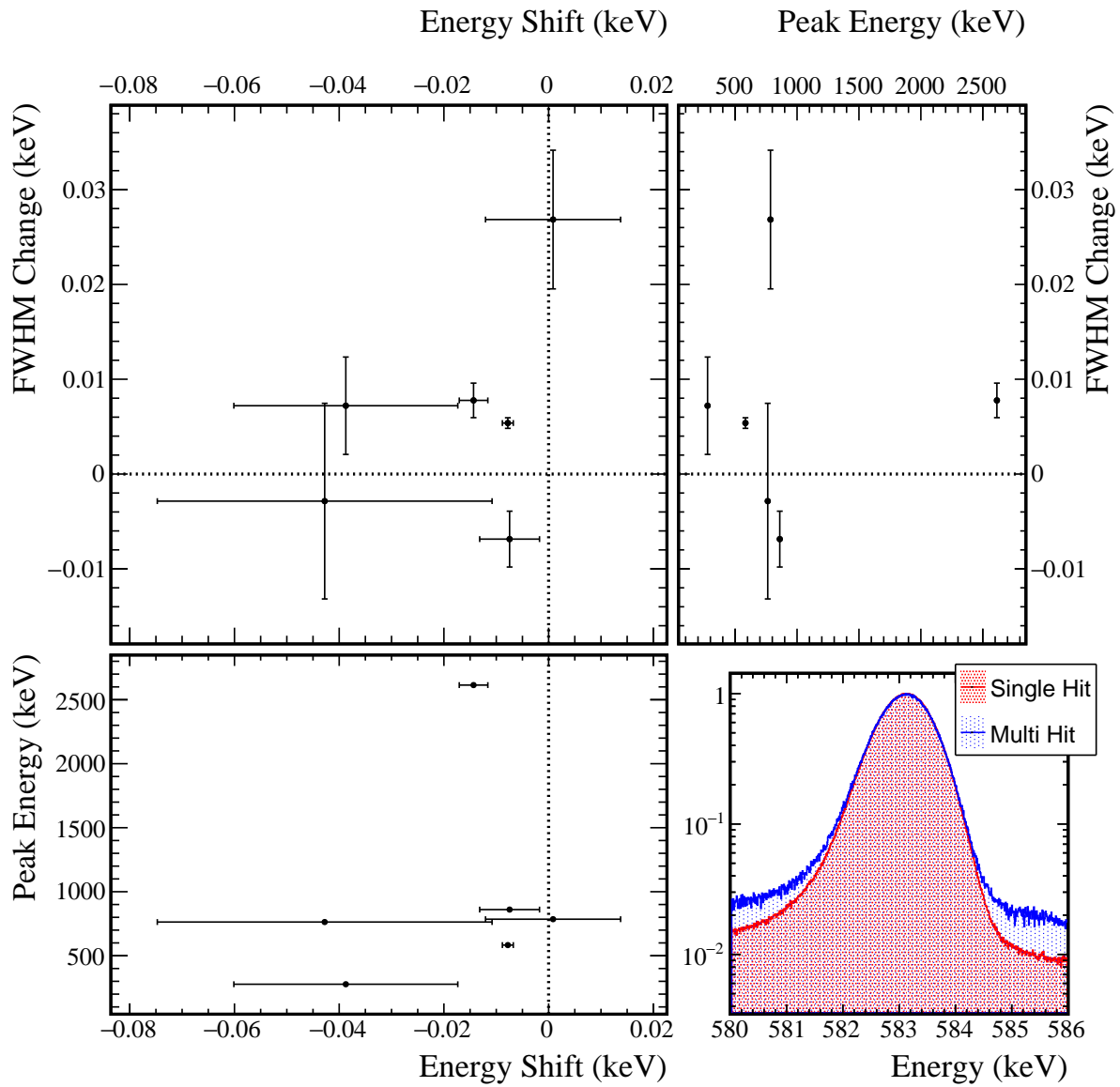
(a) Module 1

Figure 4.8: Difference of the measured centroid and FWHM of several ^{228}Th calibration peaks. Error bars represent the fit errors. Notice on the bottom right, that any difference is not visible to the naked eye.

of the multi-detector event nature of the event selection, many of these background cuts are designed to make use of observables from the detector hits in coincidence with candidate hits.

4.4.1 Enriched Source Detector Cut

Since the $\beta\beta$ E.S. events must originate in ^{76}Ge, events are far likelier to originate in enriched HPGe detectors than those with natural germanium isotopic abundances. There are 29.8 kg of enriched detectors, with $88.1 \pm 0.7\%$ abundance of ^{76}Ge and 14.4 kg of natural detectors, with $7.83 \pm 0.07\%$ abundance of ^{76}Ge. This means that $95.8 \pm 0.1\%$ of $\beta\beta$ E.S. events will originate in enriched detectors. If we assume that background events will hit all detector mass at the same rate, then we would expect only 67% of hits from background events involving two detectors to be in coincidence with a hit in an enriched detector. This means that a significant gain in sensitivity can be acheived by cutting hits that are not in coincidence with an enriched detector hit. While the detection efficiency of this cut is expected to be close to 95.8%, the actual efficiency is measured from simulations, and tends to be greater, since a greater proportion of enriched detectors are active compared to natural detectors.

Figure 4.9: Diagram showing each detector in each module, arranged by which string and position they are in. Enriched detectors are colored green and natural detectors are colored blue. 95% of ^{76}Ge in the array is contained in the enriched detectors.

4.4.2   Coincident and Sum Energy Cuts

The greatest source of background events is expected to be γ-rays from a handful of known primordial and cosmogenic isotopes. Because γ-rays are monoenergetic, they will often present a clear detection signature that can be targeted. γ-rays will often Compton scatter from one detector into another, depositing their entire energy between the two. For this reason, events whose total energy is equal to the energy of a known γ can be cut. β-decays will often result in a cascade of multiple γs, at least one of which may be fully absorbed in a single detector. These events can be cut by searching for a coincident detector with energy equal to that of a known γ. Finally, whereas the $\beta\beta$ decay spectrum approaches zero amplitude at low energies and at $Q_{\beta\beta}$, the Compton continuum of γs has a large amplitude at low energies. This means that sensitivity can be gained by setting low- and high-energy thresholds on hits in coincidence with a candidate event. These combined backgrounds can be reduced by cutting events with either sum energies or coincident hit energies that fall in a set of energy ranges. For $\beta\beta$ E.S. modes with multiple γs, the optimal energy ranges will differ between natural and enriched detectors, since natural detectors will mostly include hits from one of the γs, while enriched events will include $\beta\beta$ hits, γ hits, and pileup events including both of these, allowing a much wider energy range. For this reason, a separate set of coincident cut energy ranges are used for natural and enriched detectors.

The energy ranges that are cut can be determined by comparing the background model simulation to simulations of each $\beta\beta$ E.S. decay mode. An algorithm was written that simultaneously selects a set of both sum and coincident energy ranges to cut that optimizes discovery potential, as defined in Appendix B. The algorithm begins by identifying events in the $\beta\beta$ E.S. simulation that include at least one hit consisting of the full absorption of a γ photon and events in the background model simulation that include at least one hit in the background region of interest. These events are then sorted into energy bins for each coincident hit and for the sum energy of the event (a single event will be in multiple bins). For each bin, the algorithm checks the change in discovery potential if the bin was toggled to

be either cut or included. Following Equation B.10, the discovery potential will be improved by toggling bin k if:

$$\text{DP}'(s \cdot N_{BG}) \frac{s \cdot n_{k,BG}}{\text{DP}(s \cdot N_{BG})} < \frac{n_{k,ES}}{N_{ES}} \qquad (4.13)$$

where N_{ES} and N_{BG} are the total number of events remaining in the simulated $\beta\beta$ E.S. and background spectra, respectively; s is a scaling to estimate the number of background events in the data from the number in the simulation; and $n_{k,ES}$ and $n_{k,BG}$ are the number of simulated $\beta\beta$ E.S. and background events contained in the bin. A χ value is computed representing the normal quantile of the probability that cutting or including the bin will improve the discovery potential. This is done by assuming that the uncertainty on the number of events in the bin is Gaussian distributed, with standard deviations $\sqrt{n_{k,ES}}$ and $\sqrt{n_{k,BG}}$, respectively. In this case, we get:

$$\chi_k = \frac{\frac{n_{k,ES}}{N_{ES}} - \text{DP}'(s \cdot N_{BG}) \frac{s \cdot n_{k,BG}}{\text{DP}(s \cdot N_{BG})}}{\sqrt{\left(\text{DP}'(s \cdot N_{BG}) \frac{s}{\text{DP}(s \cdot N_{BG})}\right)^2 n_{k,BG} + \frac{n_{k,ES}}{N_{ES}^2}}} \qquad (4.14)$$

All events in the bin with highest probability of improving the discovery potential are then either cut or included, and must be cut or included to all other bins that they fall into. Note that a included event will only be included if it is not cut by any other bin. This process is repeated until toggling any bin will have $\chi_k < 0$, meaning there is a $< 50\%$ chance of improving the discovery potential. At this point, the bins are then combined in order to determine the ranges of energies to be cut in sum energy and coincident energies.

Because of limited statistics in the simulations, this cut will be biased to cut events in bins with a downward fluctuation in $\beta\beta$ E.S. rate and accept bins with an upward fluctuation, and vice-versa for the simulated background model. In order to minimize this bias and ensure that energy ranges are selected based on real backgrounds rather than statistical fluctuations, a penalty is applied to the probability calculations if a new range would be added. If a cutting or reading a bin would increase the number of energy ranges, a penalty of 3 is added to the χ value, and if it would reduce the number of ranges, a penalty of -3 is added. This corresponds to requiring a 99.8% chance that adding a new energy range will

represent an improvement before we conclude that it is not a statistical fluctuation. This is inspired by the Akaike Information Criterion (AIC)[116], which adds a penalty of 1 to a likelihood for each parameter added to a model. In this case, adding an energy range adds two parameters to our cut, so the equivalent penalty is 1.5 per parameter, which is a larger penalty than AIC. This difference can be explained by the fact that the AIC penalty of 1 requires 97.7% that toggling a bin represents an improvement; however, it has been observed that ~100 bins exist close enough to the threshold for inclusion or exclusion to accidentally toggle the bin. As a result, using a penalty of 1 will result in multiple accidentally excluded energy regions, on average, while a penalty of 1.5 will not.

To further control limited simulation statistics, a variety of bin widths is used to determine the optimal energy ranges. This is necessary because with a narrow binning, bins do not have enough statistics to overcome the penalty described above, but wider bins produce very imprecise energy ranges. The algorithm starts by optimizing the cut ranges with a bin width of 6.4 keV starting from a prior of cutting no energy ranges. Once this optimization is complete, the bin width is split in half and the algorithm re-optimizes the energy ranges, using the previous ranges as a prior. This halving of bin width is repeated until a final bin width of 0.2 keV is reached. The results of this cut optimization procedure are shown in figures 4.10 and 4.11.

The efficiency of each of the sum and coincident energy cuts can be evaluated by computing the ratio of simulated $\beta\beta$ E.S. events that pass the cut to the total number of simulated events. The primary source of uncertainty arises from imperfections in the simulated $\beta\beta$ E.S. spectra produced by DECAY0 (see Section 3.2). Additionaly uncertainty in the spectral shape arises from energy nonlinearity. Since the efficiency is calculated by integrating over portions of the coincidence spectrum, an upper limit on the systematic error can be found using the KS statistic of a comparison between the simulated spectrum and the true spectrum. As discussed in Section 3.2.1, we can perform this comparison by using the Kotila and Iachello spectrum as a proxy. This relies on the assumption that the Kotila and Iachello spectrum has corrected the dominant errors in the DECAY0 spectrum; if any
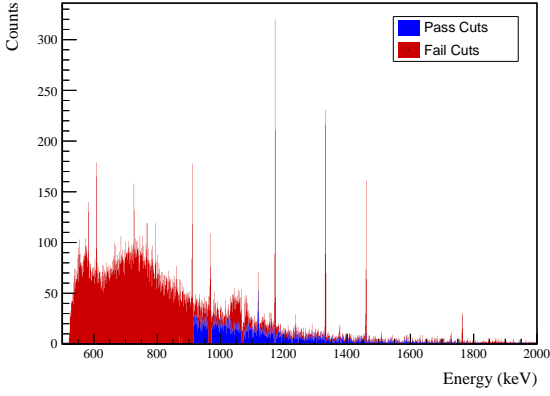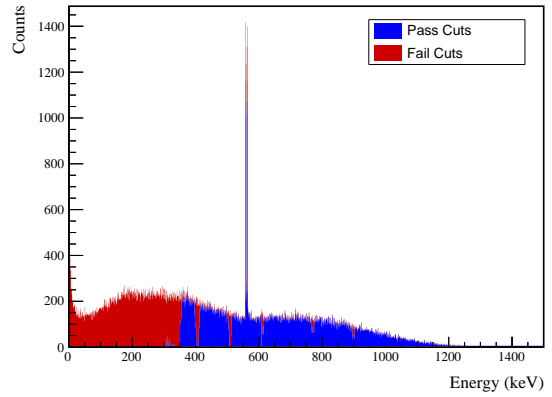
(a) Simulated BG Sum Energy Spectrum
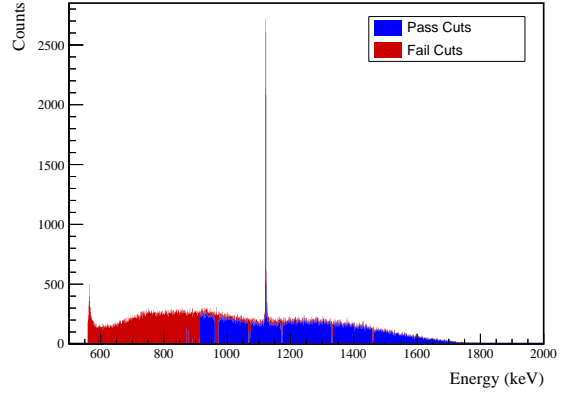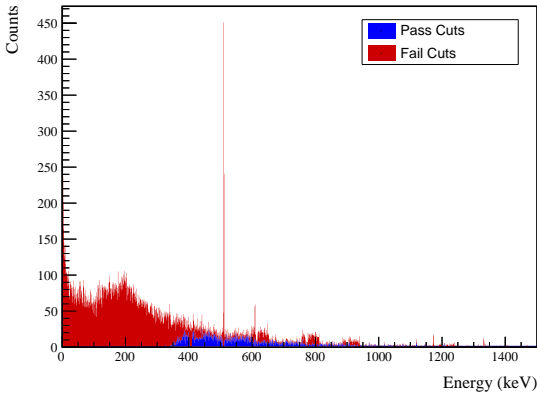
(b) Simulated ES Sum Energy Spectrum

(c) Simulated BG Coincident Energy Spectrum

(d) Simulated ES Coincident Energy Spectrum

Figure 4.10:   Top: Simulated sum energy spectra of simulated ES and BG events.   The events in red are cut by the sum- or coincident-energy cut. Note that regions around many peaks are cut, as intended.

Bottom: Simulated energy spectrum of events in coincidence with events in the ROI. Excesses in red are cut by the sum- or coincident-energy cut. Once again, regions around prominent peaks are cut out as intended.
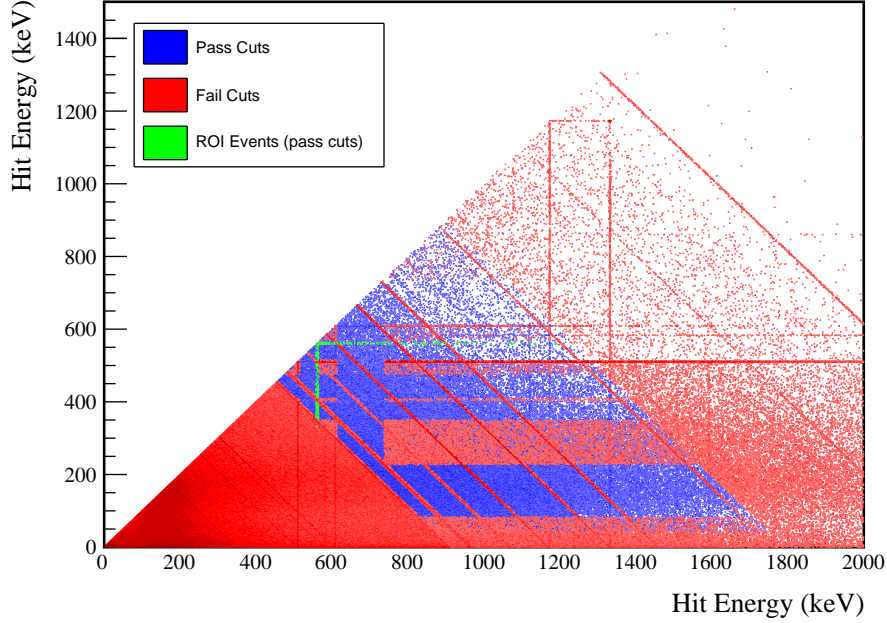
Figure 4.11: 2D energy spectrum of simulated BG events. Blue bins have at least one hit that passes both the sum- or coincident-energy cuts. For red bins, both hits have failed at least one of these cuts. Green bins have at least one hit in the BG or ES ROI that passes these cuts.

errors coexist in both spectra that have a similar order of magnitude, then this approach will underestimate the uncertainty. To account for energy nonlinearity, each simulated energy is shifted to represent the effects of digitizer nonlinearity and energy drift. Digitizer nonlinearity originates from the fact that some digitizer energy bins are slightly wider than others and has an approximately sawtooth dependency on energy with a period of ∼600 keV. A correction is applied that reduces the size of this nonlinearity to ∼0.1 keV in magnitude and smooths it out significantly, as shown in Figure 4.12. Digitizer nonlinearity is included in the simulation by shifting each energy according to a sawtooth function with rms 0.1 keV
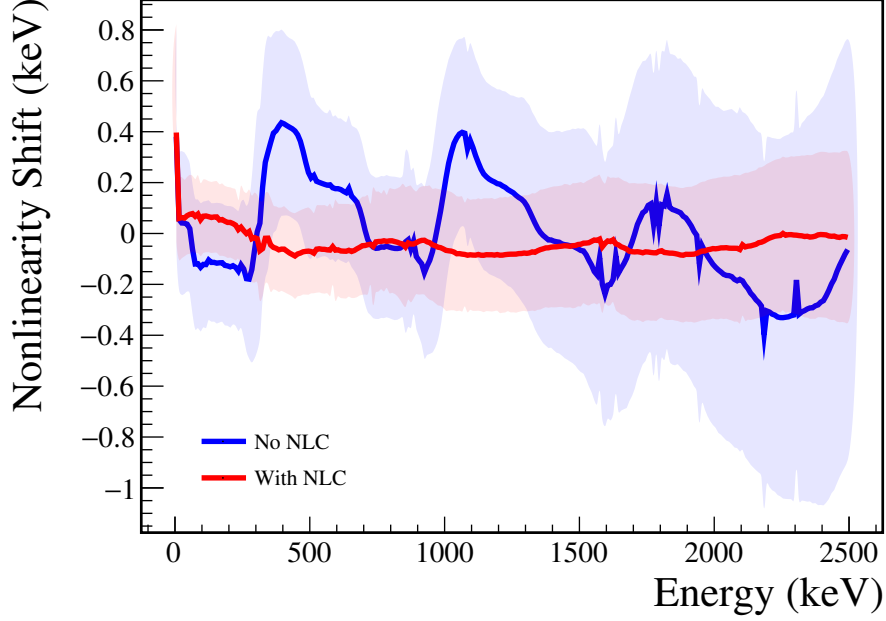
Figure 4.12: Digitizer nonlinearity before (red) and after (blue) being corrected. This nonlinearity is measured by comparing the energy measured in the high gain channel to that of the low gain channel.

and period 600 keV:

$$\Delta(E) = \sqrt{3} \cdot (0.1 \text{ keV}) \left(\text{rem}\left(\frac{E - 150 \text{ keV}}{600 \text{ keV}} \right) \right) \tag{4.15}$$

where rem is the remainder function as defined in the C++standard library. An additional shift that is randomly sampled from a Gaussian distribution with standard deviation $0.00015 \cdot E$ is applied to simulate the effect of gain drift, based on the drift observed during DS5. After applying both of these alterations to the decay0 spectrum, a KS test is performed against the Kotila and Iachello spectrum, and a maximum CDF difference of 0.08% is observed, as shown in Figure 4.13. This difference is used as an upper limit on the uncertainty from the energy range cuts for $2\nu\beta\beta$ modes.
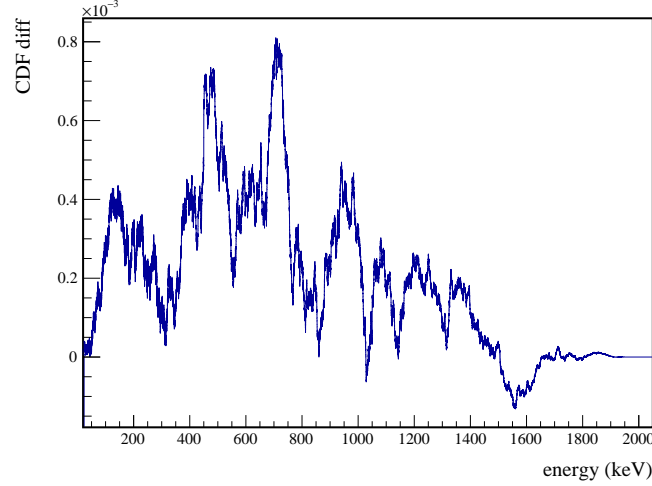
Figure 4.13: KS test comparing the CDFs of the simulated DECAY0 $2\nu\beta\beta$ ground state decay with energy nonlinearity modifications applied to the Kotila and Iachello simulated spectrum.

For $0\nu\beta\beta$, the energy ranges selected by this cut surround peaks corresponding to the $Q_{\beta\beta}$s of the decay modes or sum peaks of the $Q_{\beta\beta}$ with a deexcitation γ. In this case, since we are no longer integrating over a $\beta\beta$-spectrum, the uncertainty in the efficiency will depend on shifts in the peak, similar to the ROI-efficiency. Since the energy regions selected keep at least 99.9% of these peaks in all cases, we can set an upper limit on the uncertainty by checking the ROI efficiency uncertainty around the 2039 keV $Q_{\beta\beta}$, assuming an ROI tuned to select 99.9% of the peak. The uncertainty observed in this case is 0.325%, which is applied to the energy range cuts for $0\nu\beta\beta$ modes. For both $0\nu\beta\beta$ and $2\nu\beta\beta$ modes, this efficiency uncertainty is sub-dominant, so these highly conservative uncertainty estimates will suffice.

4.4.3 Muon Veto Cut

Cosmic ray muons have the potential to produce partical showers in the MAJORANA DEMON-STRATOR that can produce multi-site event events and can activate short-lived isotopes that
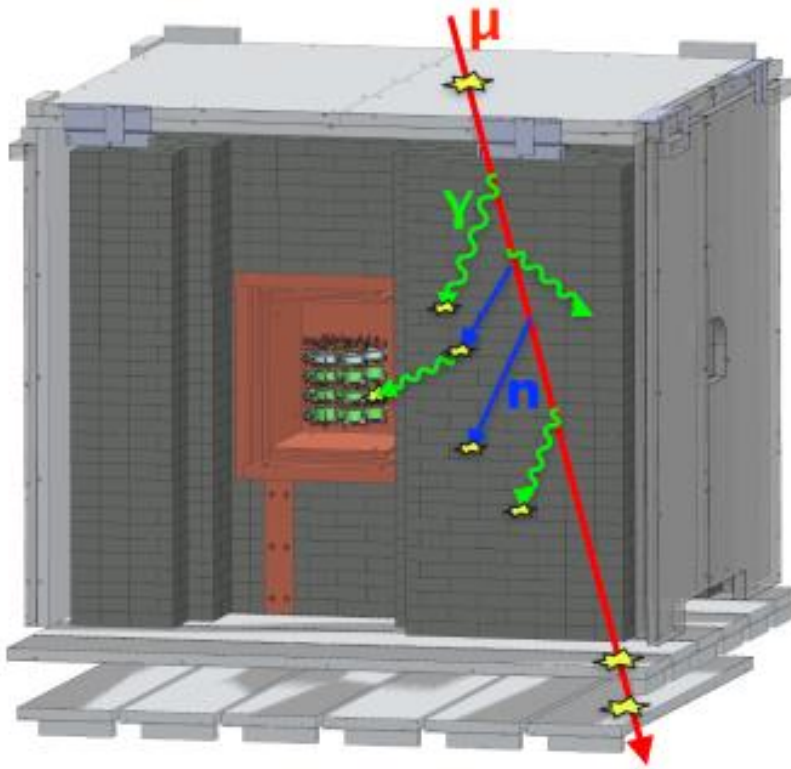
Figure 4.14: A cartoon of a particle shower created by a muon event. The particles produced in such a shower can hit multiple detectors, producing multi-detector events.

in turn may decay, producing delayed multi-site event events. Background events caused by muons can be cut using the muon veto system described in Section 2.1.1. This analysis follows the standard MAJORANA DEMONSTRATOR muon cut procedure, for which any HPGe detector events occurring 20 ms before and 1 s after a tagged muon event are cut. This cut will remove $> 99.9\%$ of events induced by the muon shower, based on simulations[86]. In reality, the cut efficiency is slightly lower due to periods of time where the muon veto system clock became desynchronized with the Germanium detector clock. The impact of this cut is to reduce the total livetime in each module by < 40 s per day[86].

4.5 Combined Detection Efficiency for $\beta\beta$ E.S.

The final efficiency measurement combining all of the effects described in this chapter for each $\beta\beta$ E.S. mode is measured directly from the simulations by computing the ratio of events that survive all cuts and effects to the total number of generated events. The efficiency used is the exposure-weighted average of the simulated efficiency for each subdataset. Because each module is an independent measurement, separate efficiencies are measured for modules 1 and 2. Because of correlations causing the probability of certain effects causing sacrifice of a $\beta\beta$ E.S. event to be conditional on other effects, the combined efficiency will differ from simply being the product of the individual efficiencies. This means that the combined efficiency ϵ_{comb} for each effect k is:

$$\epsilon_{comb} = \prod_{k=0}^{N} P(\text{event is cut}|\text{cuts } 0 \ldots k-1 \text{ are applied}) \tag{4.16}$$

In spite of this, we will assume that the sources of error are uncorrelated and the fractional uncertainty is independant of what other effects have been applied. The effect of this assumption will be discussed below. This implies that the uncertainty on the combined efficiency, $\sigma_{\epsilon,comb}$ can be expressed as:

$$\sigma_{\epsilon,comb} = \epsilon_{comb} \sqrt{\sum_{k=0} N \left(\frac{\sigma_{\epsilon,k}}{\epsilon_k}\right)^2} \tag{4.17}$$

The values ϵ_k represent the probability of cutting an event assuming no other analysis cuts are applied. Because of correlations among the cuts (particularly between the sum and coincident energy cuts), this results in a double-counting of uncertainty, making this a conservative estimate.

Table 4.5 shows the efficiency for each effect described in this chapter and uncertainty on each efficiency, and the combined efficiency and uncertainty. Similar tables for each other

Source	Module 1 efficiency	Module 2 efficiency
Multi-Detector with Full Energy γ	$5.9 \pm 0.2\%$	$3.2 \pm 0.5\%$
Region of Interest	$87.9 \pm 1.4\%$	$87.9 \pm 1.4\%$
Dead Layer	$74.5 \pm 4.3\%$	$65.7 \pm 6.0\%$
Detector Dead Times	$97.5 \pm 1.2\%$	$98.1 \pm 0.9\%$
Enriched Source Detector Cut	$96.8 \pm\ <0.1\%$	$89.4 \pm\ <0.1\%$
Coincident Energy Cut	$88.5 \pm 0.5\%$	$84.4 \pm 0.5\%$
Sum Energy Cut	$60.2 \pm 0.5\%$	$54.0 \pm 0.5\%$
Final Efficiency	$2.29 \pm 0.16\%$	$0.97 \pm 0.17\%$

Table 4.5: Table of detection efficiencies and uncertainties for $2\nu\beta\beta$ of ^{76}Ge to the 0_1^+ state of ^{76}Se. Efficiencies of individual effects are calculated without applying other cuts; because of correlations between cuts (especially the sum and coincident energy cuts), simply multiplying these efficiencies together will underestimate the efficiency. The final efficiency calculated here correctly accounts for such correlations. Note that the efficiencies are the combined efficiency for the 559 and 563 keV peaks.

$\beta\beta$ E.S. peak are shown in Appendix D. In all cases the dominant uncertainties come from either the dead layer thickness or the simulation uncertainty. Figure 4.15 shows the effect of

each cut as it is applied sequantially to the $2\nu\beta\beta$ to 0_1^+ peaks.
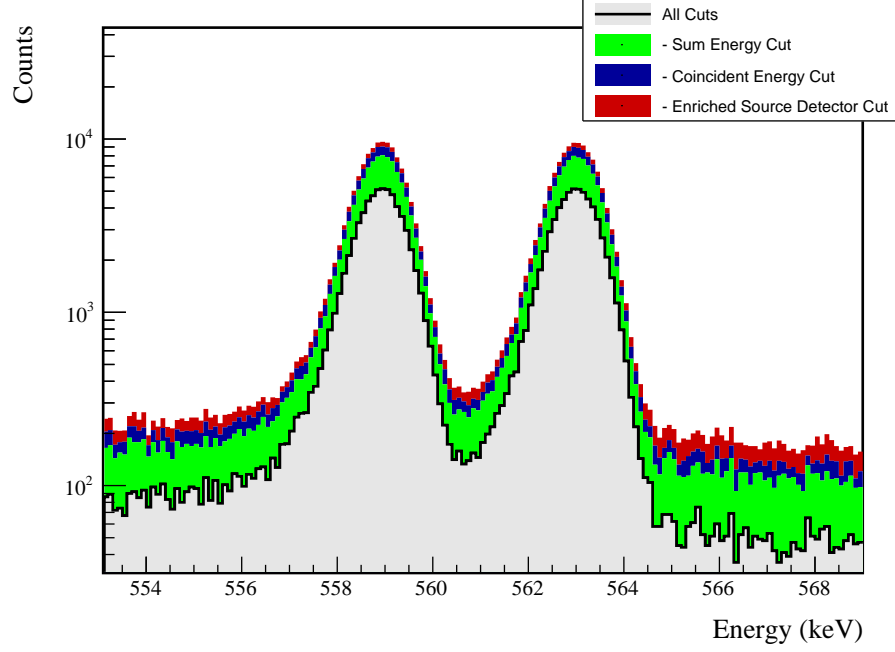

Figure 4.15: The 559 and 563 keV peaks from the $2\nu\beta\beta$ decay to the 0_1^+ decay mode, with the effect of all cuts applied sequentially to simulated ES events. The cuts are applied from top to bottom (i.e. red, blue, then green). Many events will be cut by more than one of these; in that case it will be colored by whichever cut is applied first.

Chapter 5

RESULTS OF THE Majorana Demonstrator'S SEARCH FOR DOUBLE BETA DECAY TO EXCITED STATES

Now that we have found and characterized a specific detection signature for each decay mode, we can apply this search to data. This result will look at open runs from datasets 1 through 6a that were designated silver or gold in run quality. The duty cycle and changes that define each data set are shown in Figure 5.1. These were taken from January 12, 2016 to April 18, 2018, and contain a total of 13.4 kg y of isotopic exposure for module 1 and 7.9 kg y for module 2. Approximately half the data in these datasets is blinded, and is not included in this analysis. The MAJORANA DEMONSTRATOR uses a statistical blinding scheme in which 3/4 of runs are blinded administratively (i.e. through file access) in cycles of 31 hrs of unblinded runs followed by 93 hrs of blinded runs. Unblinding data proceeds in a staged fashion, where first single-site events, not including any interesting physics regions are unblinded (i.e. no background ROI, $0\nu\beta\beta$ to the ground state ROI, low energy or multi-site data). This data is used for a variety of data validation checks prior to unblinding of any other data. The remaining data are separately unblinded after a collaboration review for individual analyses and users. For this analysis, the multi-site events have been left blinded.

In the open multi-site data, 5558 multi-detector events were observed. A histogram of the event multiplicities is shown in Figure 5.2, and a spectrum of all multiplicity 2 event energies is shown in Figure 5.3.

5.1 Validation

In addition to the basic run selection and data cleaning validation checks that are run on all multiplicity 1 data, we perform some additional checks on high multiplicity data. As
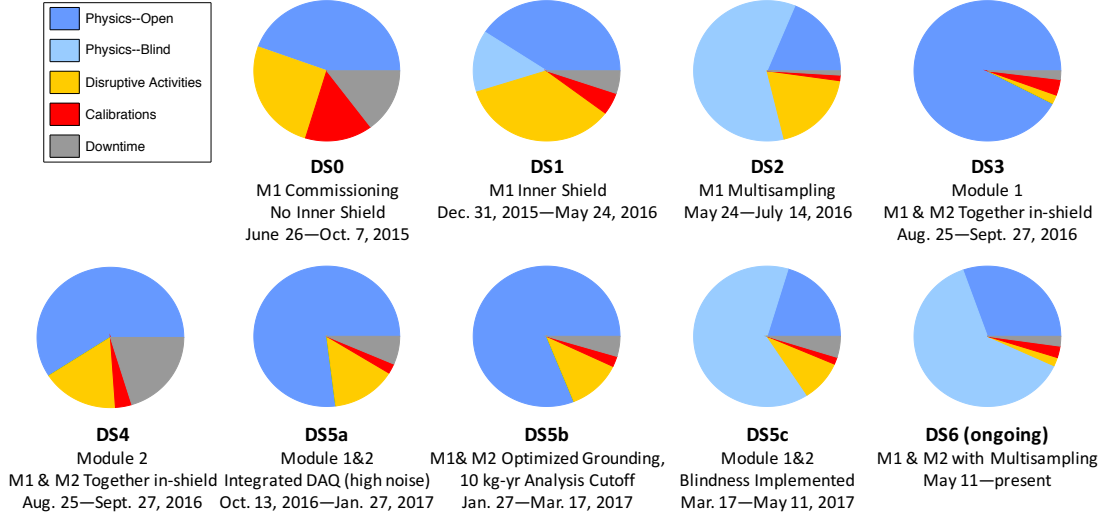
Figure 5.1: The duty cycles for each major dataset used in this analysis, and a brief description of the major changes in configuration that define each data set.

previously, this section will describe these checks applied to the $2\nu\beta\beta$ to the 0_1^+ state of ^{76}Se. Similar checks are performed on other decay modes in Appendix D.

5.1.1 Data Rate

Any spikes in the rate of multisite events would potentially indicate problems with run selection or data cleaning. Significant variation in the data rate is expected due to changes in which detectors are active. For this reason, the rate of multisite events with respect to the sensitive exposure, defined as the exposure times the detection efficiency of $\beta\beta$ E.S. events, is used instead. This quantity is interesting because the rate of observed $\beta\beta$ E.S. events should be constant with respect to it. The changes in detection efficiency from one subdataset to another for both backgrounds and $\beta\beta$ E.S. are highly correlated and driven by which detectors are enabled. For this reason, we can reasonably expect that the backgrounds should also have a nearly constant rate with respect to sensitive exposure, although differences between background source positions and the distribution of ^{76}Ge in the detectors imply that some
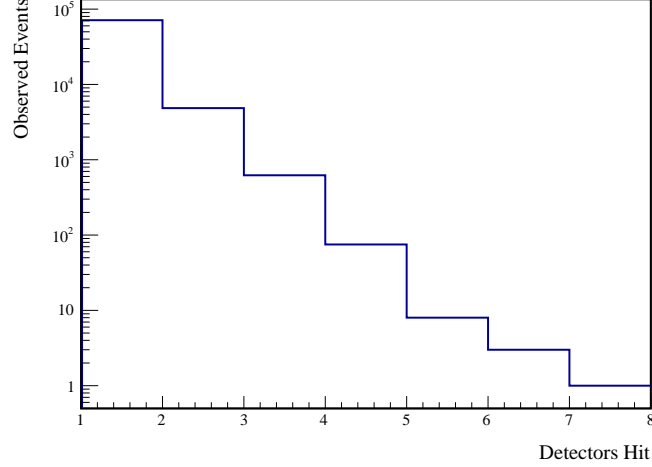
Figure 5.2: The measured multiplicities for events in datasets 1-6a. For multiplicity 1 events, only events with energy between 40 keV and 4 MeV were considered.

differences should be expected. Figure 5.4 indeed shows a slow reduction in the overall background rate over time. One possible explanation for this is that a significant quantity of ^{68}Ge exists in natural HPGe detectors as a result of cosmogenic activation, and has a half-life of 271 days, which is observable on the timescale of the MAJORANA DEMONSTRATOR's operation. ^{68}Ga is a β^+ emitter which is a part of the ^{68}Ge decay chain, which produces two 511 keV γs and has a high probability of producing multi-detector events.

5.1.2   Background Cut Evaluation

A second important check to ensure that the cuts applied to each $\beta\beta$ E.S. mode is to compare each cut efficiency to the expected background cut efficiency. Since the background model used for this analysis uses preliminary results, disagreement between the expected and measured cut efficiencies could indicate a difference between the background model and the measured backgrounds rather than a problem with the application of cuts. However, any major discrepencies could indicate a bug in the analysis. To perform this comparison, the
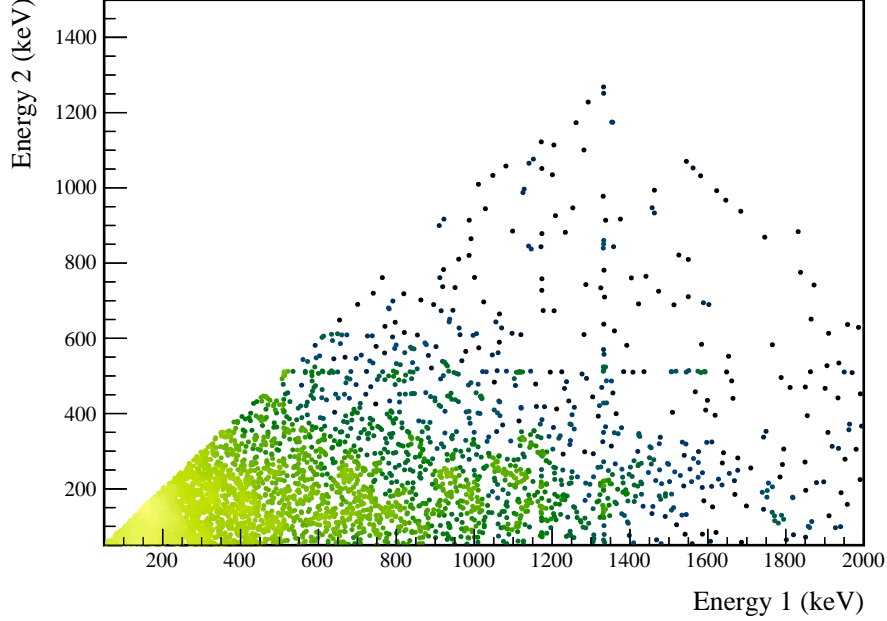
Figure 5.3: Measured energy spectrum of open multiplicity 2 events in datasets 1-6a.

cut efficiencies are measured both in terms of the total number of events cut, ϵ_{total} and the number of events that are uniquely cut, ϵ_{unique} (i.e. not cut by any of the others). Table 5.1 lists each cut for the $\beta\beta$ E.S. decay to the 0_1^+ state and the expected and measured cut efficiencies. The expected background cut efficiencies, $\langle\epsilon\rangle$ represent the fraction of simulated events cut, measured as an exposure-weighted average across all open datasets. The measured background cut efficiencies, $\hat{\epsilon}$ represent the measured fraction of events cut. Statistical uncertainties in the expected efficiencies are negligible compared to the uncertainties in the measured efficiencies, and are not included. The sacrifice is the number of events uniquely sacrificed by the cut. ΔDP is the expected improvement in discovery potential, defined in Appendix B, as a result of the cut. Figure 5.5 shows the effects of data cuts on multiplicity 2 events. Figure 5.6 shows the effects of cuts on events in the ROI in both measured and simulated data.

Cut Name	Cut Description		$\langle\epsilon_{total}\rangle$	$\hat{\epsilon}_{total}$	$\langle\epsilon_{unique}\rangle$	$\hat{\epsilon}_{unique}$	Sacrifice	ΔDP
Enriched Source		M1:	23.2 %	$27.2^{+3.8}_{-3.5}$ %	2.2 %	$2.0^{+1.5}_{-0.9}$ %	0.7 %	7%
Detector Cut	Any other detector: isEnr	M2:	42.7 %	$62.8^{+7.0}_{-7.6}$ %	4.4 %	$4.7^{+4.4}_{-2.3}$ %	2.1 %	
Coincident	No other detector: (((energy<40.6) || (energy>402.6 && energy<409.6) || (energy>506.8 && energy<512.4) || (energy>608. && energy<610.2) || (energy>1170.6 && energy<1175.) || (energy>1235.)) && isEnr) || (	M1:	29.6 %	$33.3^{+4.0}_{-3.8}$ %	4.4 %	$4.8^{+2.1}_{-1.5}$ %	3.9 %	7%
Energy Cut	((energy<83.) || (energy>228.2 && energy<350.6) || (energy>475.2 && energy<516.8) || (energy>566.6 && energy<613.4) || (energy>737.4)) && !isEnr)	M2:	37.5 %	48.8 ± 7.5 %	4.2 %	$2.3^{+3.6}_{-1.4}$ %	3.5 %	
Sum Energy Cut	Not: (sumE<870.) || (sumE>870.6 && sumE<877.6) || (sumE>878. && sumE<891.) || (sumE>891.2 && sumE<913.8) || (sumE>960.8 && sumE<972.) || (sumE>1066.8 && sumE<1072.6) || (sumE>1170.8 && sumE<1174.6) || (sumE>1330. && sumE<1333.6) || (sumE>1458.2 && sumE<1461.8) || (sumE>1761.8 && sumE<1765.8) || (sumE>1794.4)	M1:	75.0 %	$74.8^{+3.4}_{-3.7}$ %	44.5 %	$41.5^{+4.1}_{-4.0}$ %	31.8 %	20%
		M2:	75.6 %	$74.4^{+6.0}_{-7.2}$ %	33.0 %	$25.6^{+7.2}_{-6.0}$ %	32.1 %	
Combined Cuts		M1:	84.5 %	$84.4^{+2.8}_{-3.2}$ %	—	—	44.9 %	27%
		M2:	89.5 %	$95.3^{+2.3}_{-4.4}$ %	—		53.1 %	

Table 5.1: Table of detection efficiencies and uncertainties for $2\nu\beta\beta$ of ^{76}Ge to the 0^+_1 state of ^{76}Se.

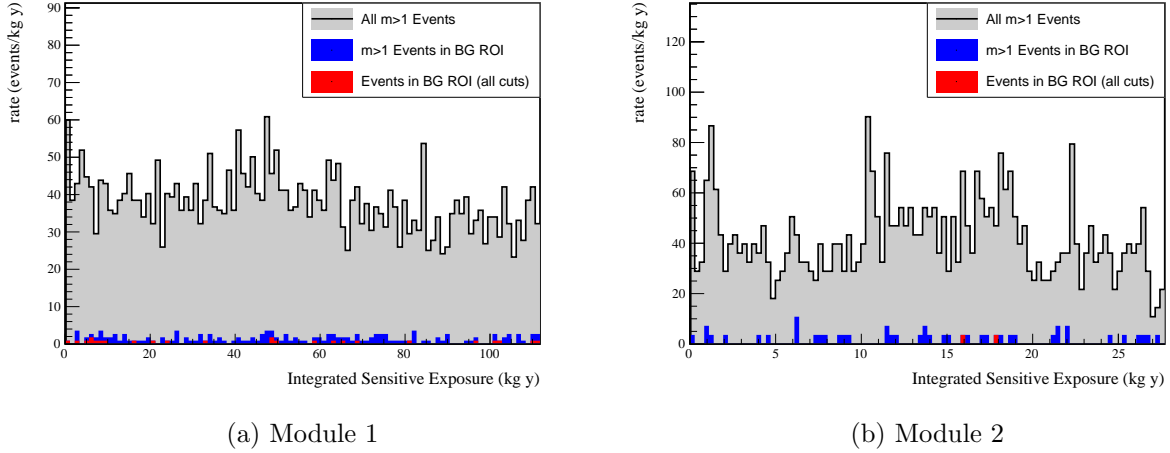(a) Module 1   (b) Module 2

Figure 5.4: Event rate with respect to sensitive exposure, or the detection efficiency of the $2\nu\beta\beta$ decay to the 0_1^+ excited state times the exposure. Integrated exposure is the total sensitive exposure prior to an event. The background rate is expected to be mostly flat, with differences discussed in Section 5.1.1.

5.2 Results

5.2.1 Statistical Methods

Neyman confidence intervals are computed for each peak in each $\beta\beta$ E.S. decay mode, and each module. For a given peak k, the expected number of signal counts is

$$\langle s_k \rangle = \ln 2 \frac{N_A}{m_{76}} \epsilon_k \frac{M_{iso}T_{live}}{T_{1/2}} \tag{5.1}$$

where M_{iso} is the total isotopic mass and T_{live} is the livetime ($M_{iso}T_{live}$ is the exposure and is calculated in Section 4.2.1 to be 13.356 ± 0.021 kg-y for module 1 and 7.872 ± 0.13 kg-y for module 2. ϵ_k is the total detection efficiency of the decay mode using peak k, and is calculated in Chapter 4, and can be found in Appendix D. $m_{76} = 0.0759214$ kg is the molar mass of ^{76}Ge, and $N_A = 6.02214076 \times 10^{23}$ is Avagadro's number. Fun fact: an Avagadro's number of avocados has approximately the volume of Mars. We will define the single count
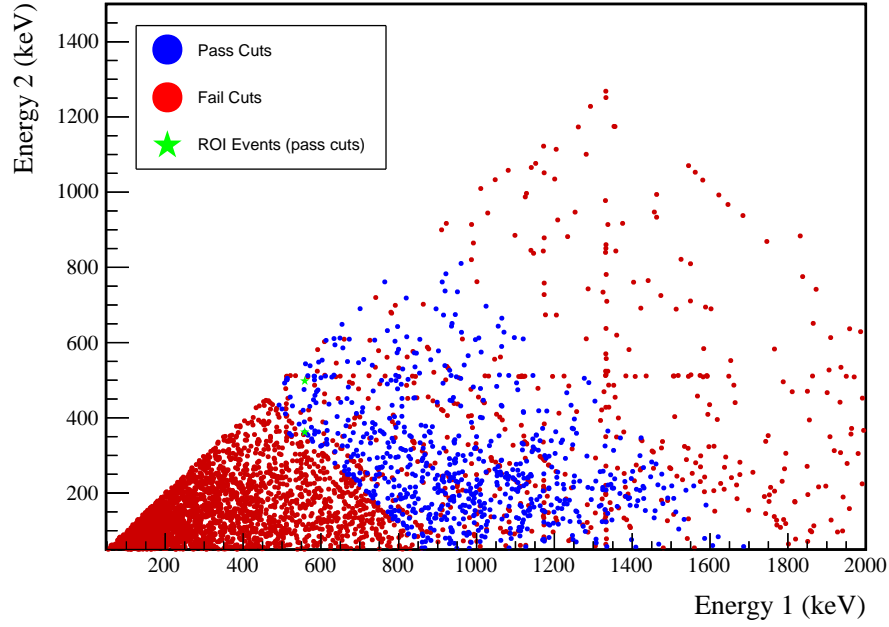
Figure 5.5: Energy spectrum of multiplicity 2 events. Red events are events that are cut. For blue events, at least one of the hits passes all cuts; however, the other hit may fail. For green events, one of the hits must both pass all cuts and place the event in the BG or ES ROI. Note that the green events include any events of multiplicity > 1; for higher multiplicity events, instead of showing the energy in the second detector, the sum of the energy in all other detectors is shown.
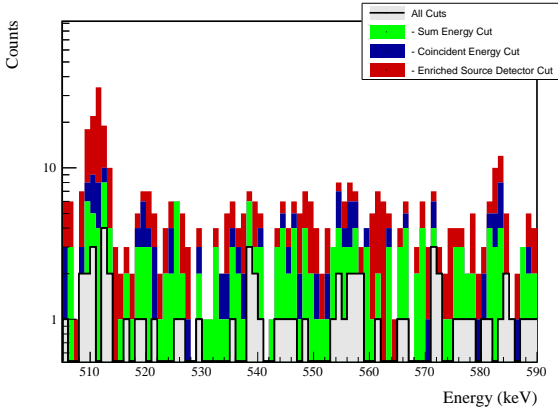
(a) Measured ROI Events
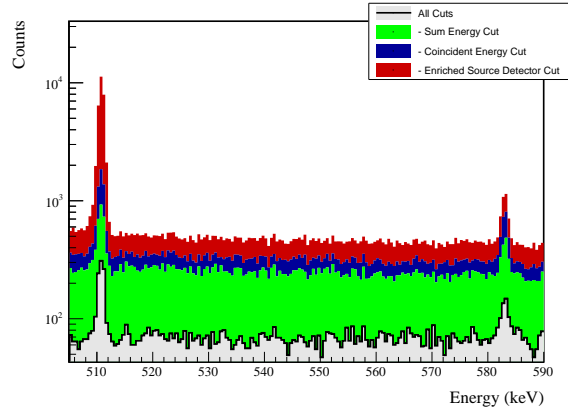
(b) Simulated ROI Events

Figure 5.6: Effect of cuts on all events in the BG and ES ROIs. Events are applied in sequence from top to bottom, meaning that if an event is cut by multiple cuts, it will be colored based on the first cut that applied. Both the simulated and measured event spectra are shown for comparison.

half-life to be

$$T_k^* = \ln 2 \frac{N_A}{m_{76}} \epsilon_k M_{iso} T_{live} \tag{5.2}$$

which is the decay half-life that would produce on average one count in signal ROI k.

Because of the nearly background free nature of this search, a likelihood construction is used that assumes Poisson statistics for the number of counts in the signal and background ROIs.

$$\mathcal{L}_k(T_{1/2}, T_k^*, b_k | n_k, m_k, \langle T_k^* \rangle, \sigma_{T^*,k}, \tau) = \frac{\mu_k^{n_k} e^{-\mu_k}}{n_k!} \cdot \frac{(b_k \tau)^{m_k} e^{-b_k/\tau}}{m_k!} \cdot \frac{1}{\sigma_{T^*,k} \sqrt{2\pi}} e^{-\frac{(T_k^* - \langle T_k^* \rangle)^2}{2\sigma_{T^*,k}^2}}$$

$$\mu_k = s_k + b_k = \frac{T_k^*}{T_{1/2}} + b_k$$

$$\tag{5.3}$$

$T_{1/2}$ represents the decay mode half-life and is the parameter of interest. T_k^* and b_k are nuisance parameters representing the measured single count halflife and expected backgrounds in the ES ROI, respectively. μ_k is the total expected number of counts, combining background and signal, in the ES ROI. n_k is the measured number of events in the ES ROI and is expected to be drawn from a Poisson distribution with mean μ_k. m_k is the measured number of events in the BG ROI and is expected to be drawn from a Poisson distribution with mean b_k/τ, where τ is the ratio between the number of expected background counts in the BG ROI to the number in the ES ROI. Note that since these events are multi-detector events, it is possible for multiple hits in the event to fall into one of the ROIs; however, we will choose a single hit to represent the whole event. In this case, any hit that falls into the ES ROI takes precedence over any hit that falls into the BG ROI, and if multiple hits fall into the ES ROI, one is chosen at random. This approach would produce a very small bump in an otherwise flat background at the ES ROI; this is accounted for in the calculation of τ. τ is usually determined based on the background simulation; however, in cases where the simulation statistics are limited after applying all cuts, a flat background is assumed and the ratio of the ES ROI width to the BG ROI width is used. $\langle T_k^* \rangle$ represents the expected value of T_k^* based on previous measurements of exposure and detection efficiency, which is

assumed to have Gaussian uncertainty:

$$\sigma_{T^*,k} = \langle T_k^* \rangle \sqrt{(\frac{\sigma_{\epsilon,k}}{\epsilon_k})^2 + (\frac{\sigma_{exposure}}{M_{iso}T_{live}})^2} \tag{5.4}$$

The implementation of Equation 5.3 is performed by the `TRolke` class in ROOT [117]. This likelihood function is used to compute a likelihood ratio

$$\text{LR}_k(T_{1/2}) = \frac{\sup_{T_k^*,b_k} \left(\mathcal{L}_k(T_{1/2}, T_k^*, b_k | n_k, m_k, \langle T_k^* \rangle, \sigma_{T^*,k}, \tau) \right)}{\sup_{T_{1/2},T_k^*,b_k} \left(\mathcal{L}_k(T_{1/2}, T_k^*, b_k | n_k, m_k, \langle T_k^* \rangle, \sigma_{T^*,k}, \tau) \right)} \tag{5.5}$$

The `TRolke` class analytically computes the supremum over T_k^* and b_k, returning the log-likelihood difference. The implementation is parameterized in terms of $\Gamma = \frac{1}{T_{1/2}}$, which is restricted to positive values; if the supremum of the function has a negative value of Γ, then the value at $\Gamma = 0$ is used instead. Since the likelihood ratio is expected to be χ^2-distributed, to construct a 90% confidence interval, we seek the values of $T_{1/2}$ corresponding to a log-likelihood ratio value of 2.7. In cases where the lower limit on γ is found to be < 0, a lower limit on $T_{1/2}$ is reported.

After constructing confidence intervals for each peak and module individually, a combined confidence interval is constructed for each $\beta\beta$ E.S. decay mode. A combined log-likelihood over all peak/module combinations k is defined by

$$\log \left(\mathcal{L}(T_{1/2}) \right) = \sum_{k=0}^{N} \sup_{T_k^*,b_k} \left(\log \left(\mathcal{L}_k(T_{1/2}, T_k^*, b_k | n_k, m_k, \langle T_k^* \rangle, \sigma_{T^*,k}, \tau) \right) \right) \tag{5.6}$$

This construction relies on the fact that the T_k^* and b_k values across each peak can be independantly maximized, enabling the continued use of the `TRolke` implementation. A combined likelihood ratio is constructed:

$$\log \left(\text{LR}(T_{1/2}) \right) = \log \left(\mathcal{L}(T_{1/2}) \right) - \sup_{T_{1/2}} \left(\log \left(\mathcal{L}(T_{1/2}) \right) \right) \tag{5.7}$$

and used to compute a confidence interval as above. Table 5.2 contains the limits constructed for each decay mode, peak and module. For all modes, a lower half-life limit is set.

Note that each decay mode is analyzed independently. The problem with this approach is that all decay modes have the 559 keV peak in common, meaning that the results will

be correlated. For this result, since all modes only have a lower limit on half-life set, this approach is not problematic since for any individual mode, we would take the supremum over all other half-lives, which would be at or near infinity, resulting in the same sets of equations used here. However, if the $\beta\beta$ E.S. to the 0_1^+ mode is discovered, it will become necessary to perform a full combined analysis.

The detection sensitivity is computed by constructing a toy Monte Carlo for each decay mode, assuming that each $T_{1/2}$ is infinite. For each sample i, a random n_i and m_i is drawn from a Poisson distribution with mean b_k and m_k. The confidence interval for a measurement with these values is computed. The median sensitivity is extracted by taking the median lower half-life limit over all samples. For the results in Table 5.2, 100001 samples were used.

5.2.2   *Limits and Sensitivities*

The limits and sensitivities for each peak and module individually, and the combination for each mode, are shown in Table 5.2. Figure 5.7 shows the event spectrum after all cuts have been applied with both ROIs highlighed.
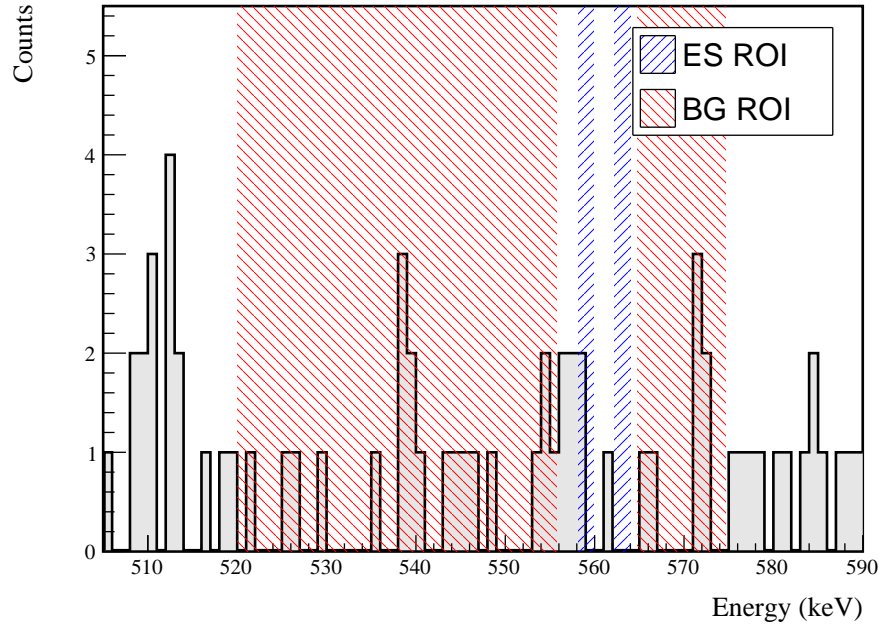
Figure 5.7: Events that pass all cuts for the $2\nu\beta\beta$ to 0_1^+ decay mode. The ES and BG ROIs are highlighted. Note that these ROIs undergo small variations from dataset to dataset, and the ROIs drawn here are averaged over all datasets. The energies shown in this spectrum are the energies of the hit that places the event in the ROI. A single event will only be placed once into an ROI; however, as drawn here, if multiple hits in a single event fall into an ROI, they will all be drawn.

Decay Mode	Peak	Module	n_{ROI}	m_{BG}	Expected ROI BGs	T^* ($\times 10^{23}$y)	$T_{1/2}$ ($\times 10^{23}$y) 90% Limit	$T_{1/2}$ ($\times 10^{23}$y) 90% Sensitivity
$0^+_{g.s.} \xrightarrow{2\nu\beta\beta} 0^+_1$	559 keV	M1	2	23	0.88	8.41 ± 0.60	> 1.9	> 3.2
		M2	0	2	0.09	2.10 ± 0.37	> 1.5	> 1.5
	563 keV	M1	0	23	0.97	8.42 ± 0.60	> 6.2	> 3.2
		M2	0	2	0.08	2.08 ± 0.37	> 1.5	> 1.5
	Combined						> 6.8	> 7.0
$0^+_{g.s.} \xrightarrow{2\nu\beta\beta} 2^+_1$	559 keV	M1	0	16	0.68	10.43 ± 1.04	> 7.7	> 7.7
		M2	0	1	0.04	2.66 ± 0.88	> 1.8	> 1.8
	Combined						> 9.6	> 5.3
$0^+_{g.s.} \xrightarrow{2\nu\beta\beta} 2^+_2$	559 keV	M1	2	38	1.46	7.24 ± 0.87	> 1.8	> 2.9
		M2	0	5	0.22	1.89 ± 0.85	> 1.2	> 1.2
	657 keV	M1	1	20	0.69	5.49 ± 0.70	> 1.8	> 4.0
		M2	0	3	0.10	1.50 ± 0.74	> 0.9	> 0.9
	1216 keV	M1	0	29	0.79	3.14 ± 0.84	> 2.2	> 1.1
		M2	0	4	0.14	0.77 ± 0.93	> 1.1	> 1.1
	Combined						> 5.7	> 5.3
$0^+_{g.s.} \xrightarrow{0\nu\beta\beta} 0^+_1$	559 keV	M1	0	2	0.09	11.47 ± 0.98	> 8.4	> 8.4
		M2	0	0	0.00	2.92 ± 0.56	> 2.1	> 2.1
	563 keV	M1	0	2	0.09	11.32 ± 0.96	> 8.3	> 8.3
		M2	0	0	0.00	2.86 ± 0.55	> 2.1	> 2.1
	Combined						> 21.1	> 21.1
$0^+_{g.s.} \xrightarrow{0\nu\beta\beta} 2^+_1$	559 keV	M1	0	0	0.00	12.04 ± 1.31	> 8.8	> 8.8
		M2	0	0	0.00	3.01 ± 1.02	> 2.0	> 2.0
	Combined						> 11.0	> 11.0
$0^+_{g.s.} \xrightarrow{0\nu\beta\beta} 2^+_2$	559 keV	M1	0	2	0.08	7.16 ± 0.95	> 5.2	> 5.2
		M2	0	0	0.00	1.81 ± 0.85	> 1.1	> 1.1
	657 keV	M1	0	7	0.27	7.00 ± 0.96	> 5.1	> 5.1
		M2	0	1	0.02	1.76 ± 0.90	> 1.0	> 1.0
	1216 keV	M1	0	0	0.00	3.23 ± 0.85	> 2.3	> 2.3
		M2	0	0	0.00	0.81 ± 0.95	> 0.2	> 0.2
	Combined						> 16.0	> 16.0

Table 5.2: Results for all decay modes.

Chapter 6

CONCLUSION

6.1 Summary of Results

The results presented in this dissertation represent the best limits to date for each ^{76}Ge $\beta\beta$ E.S. decay mode. Meaningful constraints are placed on the value of the $\beta\beta$ E.S. to the 0_1^+ nuclear matrix element. This chapter will place the results of this analysis in the context of previous results and theoretical predictions. It will also discuss the potential for future improvements on this result.

6.1.1 Comparison to GERDA Phase I result

GERDA phase I published the previous best results for all $2\nu\beta\beta$ decay modes in 2015, using 22.3 kg-y of exposure[57]. This result, using 21.3 kg-y of exposure has achieved a significantly higher sensitivity and limit. GERDA employed similar analysis techniques to this result, but the MAJORANA DEMONSTRATOR enjoys several advantages in performing searches in multi-site detectors. First, the GERDA liquid argon veto acts as shielding for γs that travel between HPGe detectors. A 600 keV γ has a mean free path through liquid argon of $\sim$9 cm, and the spacing between different GERDA strings is several cm, resulting in significantly lower detection efficiency compared to the MAJORANA DEMONSTRATOR. For the decay to the 0_1^+ state, GERDA had a detection efficiency of 0.989 %, while the MAJORANA DEMONSTRATOR had an efficiency of 1.71%, exposure-averaged between the two modules.

In addition, GERDA has a significantly higher background rate in the ROI: for the decay to the 0_1^+ state, GERDA expects 7.9 background counts while the MAJORANA DEMONSTRATOR expects 2.02 counts. One reason for this, is that the MAJORANA DEMONSTRATOR has significantly better resolution: the FWHM for a 583 keV coincident γ is 1.3 keV

Table 6.1: A comparison between the key parameters behind the results for MAJORANA DEMONSTRATOR and GERDA for each $2\nu\beta\beta$ to excited states mode. Backgrounds and efficiencies are combined across modules and peaks. Limits and sensitivities are at 90% Neyman confidence level.

$2\nu\beta\beta$ E.S. Decay Mode	MAJORANA (21.3 kg)				GERDA (22.3 kg-y)			
	Exp. BGs	Eff. (%)	Limit (10^{23} y)	Sensitivity (10^{23} y)	Exp. BGs	Eff. (%)	Limit (10^{23} y)	Sensitivity (10^{23} y)
$0^+_{g.s.} \xrightarrow{2\nu\beta\beta} 0^+_1$	2.02	1.71	> 6.8	> 7.0	7.9	0.919	> 3.7	> 1.9
$0^+_{g.s.} \xrightarrow{2\nu\beta\beta} 2^+_1$	0.72	1.06	> 9.6	> 5.3	2.4	0.389	> 1.6	> 1.3
$0^+_{g.s.} \xrightarrow{2\nu\beta\beta} 2^+_2$	3.40	1.64	> 5.6	> 5.3	8.7	0.686	> 2.3	> 1.4

for the MAJORANA DEMONSTRATOR, and 4.2 keV for GERDA. Electronic crosstalk in the GERDA detector array increases the FWHM from 3.8 keV to 4.2 keV. The LMFE boards (Section 2.2.1) and their proximity to the MAJORANA detectors provide low noise and minimal crosstalk (Section 4.3.4), and the charge trapping correction (Section 2.2.3) provides further improvements. As a result, the MAJORANA DEMONSTRATOR uses separate ROIs for the 559 and 563 keV γs that combine to a width of 3.3 keV, while GERDA uses a single 8.5 keV wide ROI. This explains most of the difference in background rates between the experiments; if GERDA had the same ROI, the expected background rate would reduce to 3.1 counts. Additionally, the dominant background for GERDA in this search comes from ^{42}K from the ^{42}Ar-^{42}K-^{42}Ca chain inside of the liquid argon shield (see Figure 6.1). Because this decay can emit γs from the interior of the detector array, it will produce multi-site events with high enough energies to pass the coincident energy cuts at a relatively high rate. This likely explains the remaining difference between the background rates.

Since publishing the phase I result[57], GERDA has implemented numerous improvements that may improve on the previous result[47]. GERDA phase II has since replaced
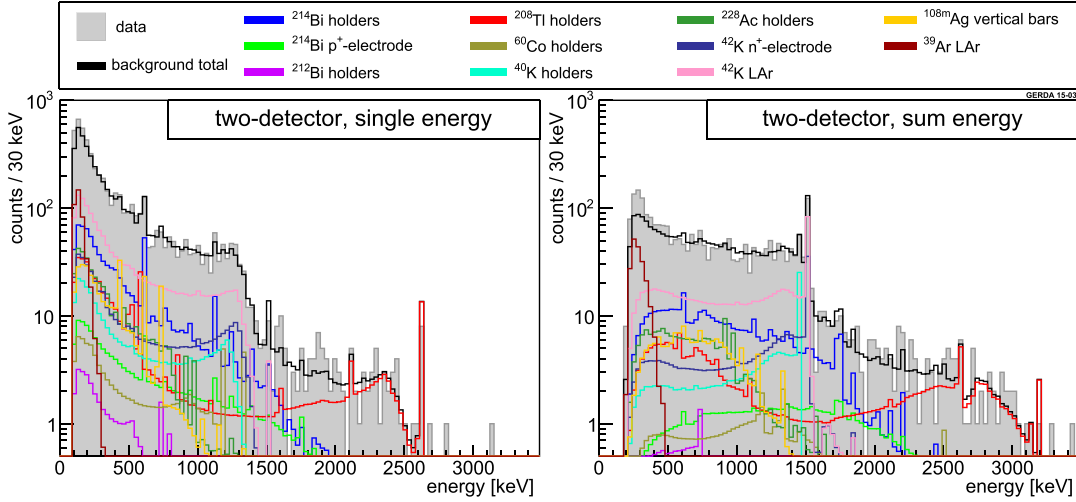
Figure 6.1: The measured GERDA single-hit and sum-energy spectra for high multiplicity events compared with the measured data. The dominant background in this spectrum originates from ^{42}K in the liquid argon shield. Taken from [57].

many coaxial HPGe detectors with BEGe detectors, which are smaller, resulting in a more granular array that will be more sensitive to multi-detector events. Additionally, the liquid argon shield has been instrumented, enabling it to act as an active shield, which may reduce backgrounds, and potentially could be used to detect γs from the excited state decays. ^{42}K backgrounds are expected to be reduced with the addition of protective shrouds around detectors. Finally, improvements to the signal electronics and corrections for detector crosstalk may be implemented to improve the energy resolution.

6.1.2 Comparison to Theoretical Predictions

Section 1.5.1 and table 1.2 presented various half-life calculations for the $2\nu\beta\beta$ to excited state decay modes and discussed some of the factors that lead to an uncertainty spanning orders of magnitude in half-life. Because of the large number of factors that affect these calculations, it is difficult to draw conclusions about the different models based on a comparison

to an experimental result. Nevertheless, we shall perform such a comparison: the 90% limit presented in this document rules out all predictions made with QRPA-based models for the $2\nu\beta\beta$ to 0_1^+ state (the largest prediction by Suhonen[57], calculated assuming a g_A factor of 1.27, is disfavored with a p-value of 0.08). For the $2\nu\beta\beta$ to 2_1^+ state the HFB prediction by Dhiman and Raina[63] is newly ruled out. The $2\nu\beta\beta$ to 2_2^+ state remains firmly out of reach of experiments. For the $0\nu\beta\beta$ decay modes, a meaningful comparison between experiment and nuclear theory calculations is not possible until the $0\nu\beta\beta$ to the ground state is observed. In addition, it is difficult to predict how an error in the prediction of any $2\nu\beta\beta$ to excited state half-life might correlate with an error in the $0\nu\beta\beta$ half-life predictions, for reasons discussed in Section 1.5. Improvements in some of the existing models presented in Table 1.2 and future models can use excited state results as an additional test. Ideally, they will agree with a measured result of the excited state decay half-lives, and predict similar values of the $0\nu\beta\beta$ nuclear matrix elements, with measurements across multiple isotopes. Table 6.2 shows the current status of searches for $2\nu\beta\beta$ to 0_1^+ states across multiple isotopes. For a more complete discussion, see Barabash's review [53].

6.2 The Future of $\beta\beta$ E.S. in ^{76}Ge

The MAJORANA DEMONSTRATOR has been continuously acquiring data since the April 18, 2018 cutoff used in this analysis, and will continue to do so until it has a projected $\sim$100 kg-y of exposure. In addition, much of the data-taking period remains to be unblinded, which increases the available exposure before the cutoff to $\sim$40 kg-y. This increase in exposure should increase the sensitivity to the $\beta\beta$ E.S. to the 0_1^+ state half-life above 10^{24} y, potentially enabling a test of the EFT prediction of $1.7 \cdot 10^{24}$ y[56].

6.2.1 Potential Improvements

In addition to gathering additional exposure, other improvements to this search are possible. In particular, the AvsE parameter, which is used to determine whether a waveform within a single detector is multi-site or single-site (see Section 2.2.5), may be useful. When a γ is

Table 6.2: Table of results and predictions for the half-life of $2\nu\beta\beta$ to 0_1^+ states across multiple isotopes. For the RQRPA results, half-lives were calculated within the references; for the IBM and EFT results, they were calculated using equation 1.30.

	Experiment	Theoretical $T_{1/2}^{2\nu\ E.S.}$ (y)		
Isotope	$T_{1/2}^{2\nu\ E.S.}$ (y)	RQRPA[61, 118]	IBM[55]	EFT[56]
^{48}Ca	$> 1.5 \cdot 10^{20}$ [119]	-	$2.0 \cdot 10^{23}$	-
^{76}Ge	$> 6.8 \cdot 10^{23}$	$(1.0 - 3.1) \cdot 10^{23}$	$7.1 \cdot 10^{24}$	$1.7 \cdot 10^{24}$
^{82}Se	$> 3.4 \cdot 10^{22}$ [120]	$(1.5 - 3.3) \cdot 10^{21}$	$4.1 \cdot 10^{23}$	$4.5 \cdot 10^{22}$
^{96}Zr	$> 3.1 \cdot 10^{20}$ [121]	$(2.4 - 3.8) \cdot 10^{21}$	$3.0 \cdot 10^{24}$	-
^{100}Mo	$6.7^{+0.5}_{-0.4} \cdot 10^{20}$ [53]	$(0.81 - 4.1) \cdot 10^{22}$	$5.7 \cdot 10^{21}$	$5.2 \cdot 10^{20}$
^{116}Cd	$> 2.0 \cdot 10^{21}$ [122]	$(1.6 - 3.3) \cdot 10^{24}$	$8.4 \cdot 10^{23}$	$1.8 \cdot 10^{23}$
^{130}Te	$> 2.5 \cdot 10^{23}$ [123]	$(7.2 - 16) \cdot 10^{23}$	$3.0 \cdot 10^{25}$	$2.8 \cdot 10^{25}$
^{136}Xe	$> 8.3 \cdot 10^{23}$ [124]	$(1.3 - 8.9) \cdot 10^{23}$	$3.0 \cdot 10^{25}$	-
^{150}Nd	$1.2^{+0.3}_{-0.2} \cdot 10^{20}$ [53]	-	$1.9 \cdot 10^{21}$	-
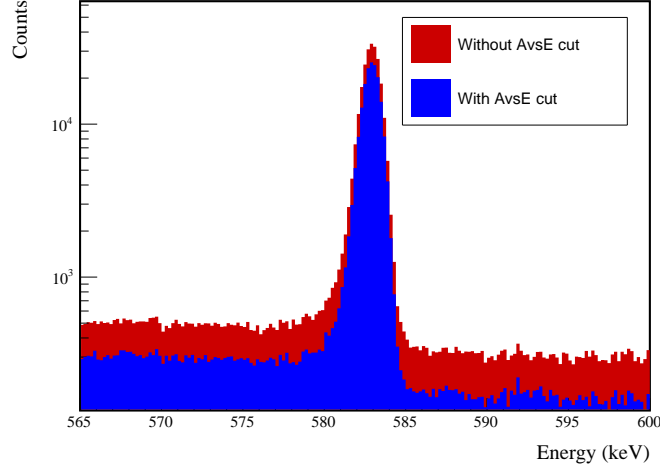
Figure 6.2: A 583 keV peak from a ^{228}Th calibration run using AvsE to select multi-site events (blue). The effect is to keep 75% of events in the peak while keeping only 41% of events in the continuum.

fully absorbed within a single detector, it will typically be detected as a multi-site event, while most Compton continuum events are single-site. For example, the 583 keV γ from the ^{228}Th spectrum is $\sim$75% multi-site, while the Compton continuum is only $\sim$41% multi-site, as shown in Figure 6.2. If the peak search were to only look at multi-site events, it would likely produce a small gain of up to $\sim$20% in sensitivity.

The coincident energy cut could also benefit from using AvsE. For decay modes with only a single γ (such as the 2_1^+ modes), the coincident detector in a true signal will have only a single site, from the $\beta\beta$-decay. On the other hand, for events with multiple γs, coincident events with energy above the Q-value of the decay will result from events involving the internal absorption of one of the γs; as a result, these events will be inherently multi-site. Using AvsE in this cut will be especially important for differentiating between 2_1^+ and 0_1^+ events since they both involve a 559 keV peak. This means that some method of differentiating between events involving one and two γs will be critical to differentiating
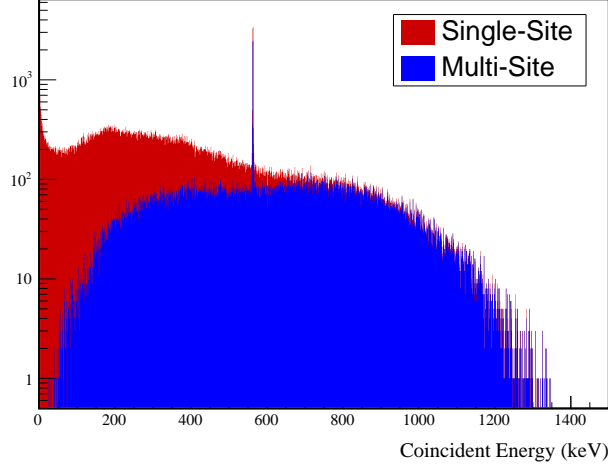
Figure 6.3: Simulated energy spectrum for hits in coincidence with a 559 or 563 keV γ from a $2\nu\beta\beta$ to 0_1^+ event. The dt-heuristic was applied to simulate the effect of an AvsE cut.

events in this peak, and AvsE may provide the best way of doing so. A simulation of the effect of AvsE on the coincident energy spectrum is shown in Figure 6.3. The reason AvsE is not currently used for this search is that it cannot be simulated reliably. The current method of simulating this parameter, called the dt-heuristic, is calibrated over an energy range close to 2039 keV, and has a relatively high error at the energies of interest for this analysis. Since this analysis relies heavily on uncertain simulations that would introduce significant systematic error, and since the improvements brought by using AvsE are expected to be small, this cut was not used for this analysis. However, further improvements to the dt-heuristic and development of pulse-shape simulations that can improve AvsE simulation may allow the implementation of this cut in the future.

6.2.2 Multi-Site Event Decomposition

In addition to distinguishing between single- and multi-site events, PPC HPGe detectors offer the possibility to decompose a multi-site waveform and measure the energies of the
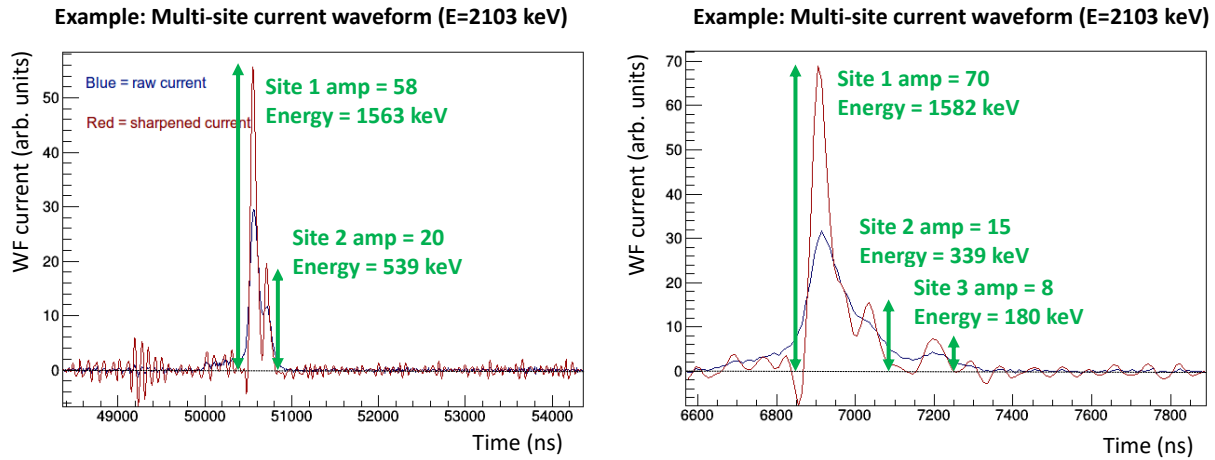
Figure 6.4: A Wiener deconvolution of two current waveforms with a Lorentzian deconvolution kernel. The current peaks can be identified and their amplitudes calibrated to measure energy. The waveforms were selected from the SEP and are expected to have a site with 1592 keV of energy.

component sites. Multi-site waveforms consist of multiple rises, as discussed in Section 2.2.5, and the current amplitude of each individual rise is proportional to the energy contained in the local charge cloud producing it. This proportionality is the reason the AvsE parameter works: for a single-site, the maximum current amplitude should be some fixed fraction of the total energy, while for multi-site waveforms, the current amplitude will be significantly less. Due to electronic noise, however, picking out individual components of waveforms and measuring the energy with each one is difficult. One method that has been demonstrated for doing this is to apply a Wiener deconvolution filter, which uses deconvolution with a known kernel function in order to sharpen the current peaks, combined with an optimal Wiener filter to prevent noise from blowing up. A proof of principle for this technique is shown in Figure 6.4.

To demonstrate the effectiveness of this technique, we can look at an inherently multi-site event such as a single-escape event. The single-escape peak produced by the ^{208}Tl
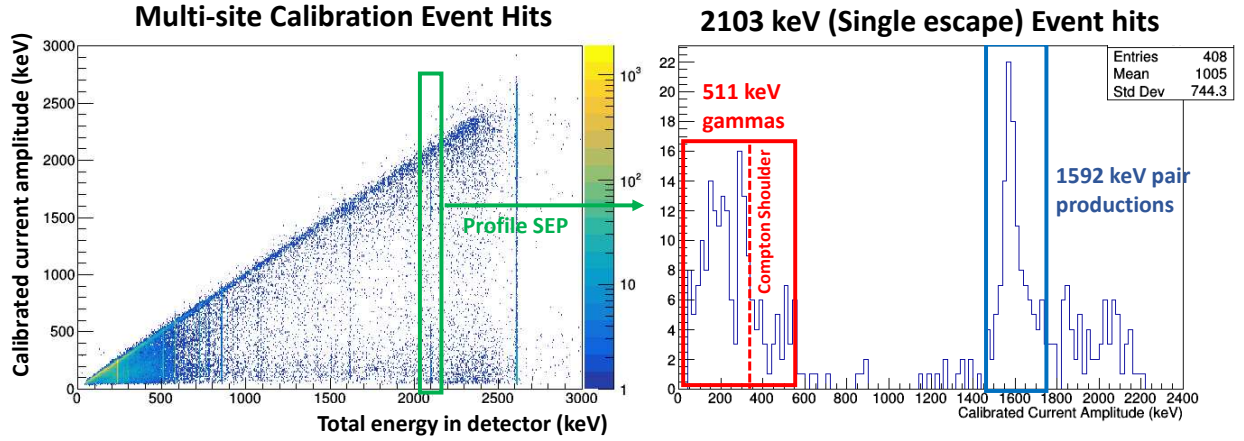
Figure 6.5: Left: A 2D spectrum showing the energy of individual sites in multi-site events from a ^{228}Th calibration run, vs the total energy of the event.

Right: A profile along the single escape peak (total energy 2103 keV). The expected features of a 1592 keV peak for the pair production site and a 511 keV Compton spectrum from the γ are observable.

2614 keV γ will consist of a 1592 keV pulse, produced by the site of the pair production, and additional sites that sum to 511 keV, produced by the annihilation γ. Figure 6.5 shows how these expected features can be extracted from SEP events in a MAJORANA DEMONSTRATOR calibration run. Using this technique, we are able to identify the 1592 keV site in 44% of SEP events, a number that could significantly improve with refinements to the algorithm.

Multi-site event decomposition would be useful in searching for $\beta\beta$ E.S. events because these events are inherently multi-site. The search presented here takes advantage of this by looking at multi-detector events; however, often the γ-rays in these events will not escape the source detector without losing at least some energy. In this case, the event would not be visible using this search's detection signature, but would be visible by looking for individual sites that sum to the full γ energy. Based on simulations, 60% of $2\nu\beta\beta$ to 0_1^+ events have the full energy of at least one of the two γs absorbed inside of Germanium detectors, which sets a much higher ceiling on the detection efficiency than the 2% used in this document. Using

the 44% of pair production sites tagged in SEP events as a proxy, it is imaginable that such a search could achieve a detection efficency of 20-25%, a ten-fold improvement over the current search. This would also increase the measured background rate significantly, by introducing single-detector multi-site backgrounds; furthermore, the poorer energy resolution for these events would necessitate a wider ROI. Even so, this could produce a large gain in sensitivity.

6.2.3   Searching for $\beta\beta$ E.S. with LEGEND

LEGEND-200 is preparing to begin operation in 2021, with lower backgrounds than the MAJORANA DEMONSTRATOR and GERDA and a target exposure of $\sim$1 t-y (Section 2.5). In spite of this high exposure, however, many challenges remain for LEGEND-200 to offer a significantly improved result in the search for $\beta\beta$ E.S.. LEGEND-200 will use the GERDA liquid argon shield, which carries disadvantages for a $\beta\beta$ E.S. search due to higher backgrounds and lower detection efficiencies. GERDA Phase II may find techniques to mitigate these disadvantages, and will likely publish a result soon. In addition, LEGEND-200 is using the inverted coaxial detector geometry, which increases the mass of each detector, but as a result reduces the granularity of the detector array. This will further reduce detection efficiency. Finally, once the $\beta\beta$ E.S. to the 0_1^+ decay is discovered, it will act as the largest background for the 2_1^+ decay, which will further limit sensitivity without finding a method to distinguish the two. For these reasons, LEGEND-200 may struggle to significantly improve upon the final MAJORANA DEMONSTRATOR results without implementing many of the improvements mentioned in the previous section.

If LEGEND-200 succeeds in these improvements and manages a measurement with $> 10\%$ detection efficiency that remains nearly background free, future measurements could feasibly have half-life sensitivities exceeding 10^{26} y. This would almost certainly observe the $\beta\beta$ E.S. to 0_1^+ decay mode (and if it didn't that would be an interesting result in its own right!). It would also begin to probe into the theoretical half-life predictions for the 2_1^+ decay mode, with potentially interesting results regarding a Bosonic component of neutrinos (Section 1.5.3, [71]). With the same improvements and lower backgrounds, LEGEND-1000 may probe half-

lives exceeding 10^{27} y, offering a strong possibility of observing $2\nu\beta\beta$ to the 2_1^+ excited state. Finally, under the optimistic scenario that LEGEND-200 discovers $0\nu\beta\beta$, LEGEND-1000 may begin a search for $0\nu\beta\beta$ to excited states, with implications toward understanding the underlying mechanism for $0\nu\beta\beta$ decay and the Majorana nature of neutrino mass.

BIBLIOGRAPHY

[1] E. Fermi. Versuch einer theorie der β-strahlen. i. *Zeitschrift für Physik*, 88(3):161–177, Mar 1934.

[2] Abraham. Pais. *Inward Bound*. Oxford University Press, 1 edition, Sept. 1988.

[3] C. L. Cowan, F. Reines, F. B. Harrison, H. W. Kruse, and A. D. McGuire. Detection of the free neutrino: a confirmation. *Science*, 124(3212):103–104, 1956.

[4] Raymond Davis Jr. Nobel lecture, December 2002.

[5] T. D. Lee and C. N. Yang. Question of parity conservation in weak interactions. *Phys. Rev.*, 104:254–258, Oct 1956.

[6] C. S. Wu, E. Ambler, R. W. Hayward, D. D. Hoppes, and R. P. Hudson. Experimental test of parity conservation in beta decay. *Phys. Rev.*, 105:1413–1415, Feb 1957.

[7] Richard L. Garwin, Leon M. Lederman, and Marcel Weinrich. Observations of the failure of conservation of parity and charge conjugation in meson decays: the magnetic moment of the free muon. *Phys. Rev.*, 105:1415–1417, Feb 1957.

[8] M. Goldhaber, L. Grodzins, and A. W. Sunyar. Helicity of neutrinos. *Phys. Rev.*, 109:1015–1017, Feb 1958.

[9] M. Tanabashi, K. Hagiwara, K. Hikasa, K. Nakamura, Y. Sumino, F. Takahashi, J. Tanaka, K. Agashe, G. Aielli, C. Amsler, M. Antonelli, D. M. Asner, H. Baer, Sw. Banerjee, R. M. Barnett, T. Basaglia, C. W. Bauer, J. J. Beatty, V. I. Belousov, J. Beringer, S. Bethke, A. Bettini, H. Bichsel, O. Biebel, K. M. Black, E. Blucher, O. Buchmuller, V. Burkert, M. A. Bychkov, R. N. Cahn, M. Carena, A. Ceccucci, A. Cerri, D. Chakraborty, M.-C. Chen, R. S. Chivukula, G. Cowan, O. Dahl, G. D'Ambrosio, T. Damour, D. de Florian, A. de Gouvêa, T. DeGrand, P. de Jong, G. Dissertori, B. A. Dobrescu, M. D'Onofrio, M. Doser, M. Drees, H. K. Dreiner, D. A. Dwyer, P. Eerola, S. Eidelman, J. Ellis, J. Erler, V. V. Ezhela, W. Fetscher, B. D. Fields, R. Firestone, B. Foster, A. Freitas, H. Gallagher, L. Garren, H.-J. Gerber, G. Gerbier, T. Gershon, Y. Gershtein, T. Gherghetta, A. A. Godizov, M. Goodman, C. Grab, A. V. Gritsan, C. Grojean, D. E. Groom, M. Grünewald, A. Gurtu, T. Gutsche, H. E. Haber, C. Hanhart, S. Hashimoto, Y. Hayato, K. G. Hayes,

A. Hebecker, S. Heinemeyer, B. Heltsley, J. J. Hernández-Rey, J. Hisano, A. Höcker, J. Holder, A. Holtkamp, T. Hyodo, K. D. Irwin, K. F. Johnson, M. Kado, M. Karliner, U. F. Katz, S. R. Klein, E. Klempt, R. V. Kowalewski, F. Krauss, M. Kreps, B. Krusche, Yu. V. Kuyanov, Y. Kwon, O. Lahav, J. Laiho, J. Lesgourgues, A. Liddle, Z. Ligeti, C.-J. Lin, C. Lippmann, T. M. Liss, L. Littenberg, K. S. Lugovsky, S. B. Lugovsky, A. Lusiani, Y. Makida, F. Maltoni, T. Mannel, A. V. Manohar, W. J. Marciano, A. D. Martin, A. Masoni, J. Matthews, U.-G. Meißner, D. Milstead, R. E. Mitchell, K. Mönig, P. Molaro, F. Moortgat, M. Moskovic, H. Murayama, M. Narain, P. Nason, S. Navas, M. Neubert, P. Nevski, Y. Nir, K. A. Olive, S. Pagan Griso, J. Parsons, C. Patrignani, J. A. Peacock, M. Pennington, S. T. Petcov, V. A. Petrov, E. Pianori, A. Piepke, A. Pomarol, A. Quadt, J. Rademacker, G. Raffelt, B. N. Ratcliff, P. Richardson, A. Ringwald, S. Roesler, S. Rolli, A. Romaniouk, L. J. Rosenberg, J. L. Rosner, G. Rybka, R. A. Ryutin, C. T. Sachrajda, Y. Sakai, G. P. Salam, S. Sarkar, F. Sauli, O. Schneider, K. Scholberg, A. J. Schwartz, D. Scott, V. Sharma, S. R. Sharpe, T. Shutt, M. Silari, T. Sjöstrand, P. Skands, T. Skwarnicki, J. G. Smith, G. F. Smoot, S. Spanier, H. Spieler, C. Spiering, A. Stahl, S. L. Stone, T. Sumiyoshi, M. J. Syphers, K. Terashi, J. Terning, U. Thoma, R. S. Thorne, L. Tiator, M. Titov, N. P. Tkachenko, N. A. Törnqvist, D. R. Tovey, G. Valencia, R. Van de Water, N. Varelas, G. Venanzoni, L. Verde, M. G. Vincter, P. Vogel, A. Vogt, S. P. Wakely, W. Walkowiak, C. W. Walter, D. Wands, D. R. Ward, M. O. Wascko, G. Weiglein, D. H. Weinberg, E. J. Weinberg, M. White, L. R. Wiencke, S. Willocq, C. G. Wohl, J. Womersley, C. L. Woody, R. L. Workman, W.-M. Yao, G. P. Zeller, O. V. Zenin, R.-Y. Zhu, S.-L. Zhu, F. Zimmermann, P. A. Zyla, J. Anderson, L. Fuller, V. S. Lugovsky, and P. Schaffner. Review of particle physics. *Phys. Rev. D*, 98:030001, Aug 2018.

[10] Sheldon L. Glashow. Partial-symmetries of weak interactions. *Nuclear Physics*, 22(4):579 – 588, 1961.

[11] Steven Weinberg. A model of leptons. *Phys. Rev. Lett.*, 19:1264–1266, Nov 1967.

[12] Abdus Salam. Weak and Electromagnetic Interactions. *Conf. Proc.*, C680519:367–377, 1968.

[13] F.J. Hasert, S. Kabe, W. Krenz, J. Von Krogh, D. Lanske, J. Morfin, K. Schultze, H. Weerts, G.H. Bertrand-Coremans, J. Sacton, W. Van Doninck, P. Vilain, U. Camerini, D.C. Cundy, R. Baldi, I. Danilchenko, W.F. Fry, D. Haidt, S. Natali, P. Musset, B. Osculati, R. Palmer, J.B.M. Pattison, D.H. Perkins, A. Pullia, A. Rousset, W. Venus, H. Wachsmuth, V. Brisson, B. Degrange, M. Haguenauer, L. Kluberg, U. Nguyen-Khac, P. Petiau, E. Belotti, S. Bonetti, D. Cavalli, C. Conta, E. Fiorini, M. Rollier, B. Aubert, D. Blum, L.M. Chounet, P. Heusse, A. Lagarrigue, A.M. Lutz, A. Orkin-Lecourtois, J.P. Vialle, F.W. Bullock, M.J. Esten, T.W. Jones, J. McKenzie, A.G. Michette, G. Myatt, and W.G. Scott. Observation of neutrino-like interactions

without muon or electron in the gargamelle neutrino experiment. *Physics Letters B*, 46(1):138 – 140, 1973.

[14] G. Arnison et al. Experimental Observation of Lepton Pairs of Invariant Mass Around 95-GeV/c**2 at the CERN SPS Collider. *Phys. Lett.*, B126:398–410, 1983. [,7.55(1983)].

[15] P. Bagnaia et al. Evidence for Z0 —¿ e+ e- at the CERN anti-p p Collider. *Phys. Lett.*, B129:130–140, 1983. [,7.69(1983)].

[16] ATLAS Collaboration. Observation of a new particle in the search for the standard model higgs boson with the atlas detector at the lhc. *Physics Letters B*, 716(1):1 – 29, 2012.

[17] CMS Collaboration. Observation of a new boson at a mass of 125 gev with the cms experiment at the lhc. *Physics Letters B*, 716(1):30 – 61, 2012.

[18] John N. Bahcall, Aldo M. Serenelli, and Sarbani Basu. New solar opacities, abundances, helioseismology, and neutrino fluxes. *The Astrophysical Journal*, 621(1):L85–L88, jan 2005.

[19] Bruce T. Cleveland, Timothy Daily, Jr. Raymond Davis, James R. Distel, Kenneth Lande, C. K. Lee, Paul S. Wildenhain, and Jack Ullman. Measurement of the solar electron neutrino flux with the homestake chlorine detector. *The Astrophysical Journal*, 496(1):505–526, mar 1998.

[20] J. N. Abdurashitov, V. N. Gavrin, S. V. Girin, V. V. Gorbachev, T. V. Ibragimova, A. V. Kalikhov, N. G. Khairnasov, T. V. Knodel, I. N. Mirmov, A. A. Shikhin, E. P. Veretenkin, V. M. Vermul, V. E. Yants, G. T. Zatsepin, T. J. Bowles, W. A. Teasdale, D. L. Wark, M. L. Cherry, J. S. Nico, B. T. Cleveland, R. Davis, K. Lande, P. S. Wildenhain, S. R. Elliott, and J. F. Wilkerson. Measurement of the solar neutrino capture rate with gallium metal. *Phys. Rev. C*, 60:055801, Oct 1999.

[21] B. Pontecorvo. Inverse beta processes and nonconservation of lepton charge. *Zhurnal Eksperimental'noĭ i Teoreticheskoĭ Fiziki*, 34:247, 1957.

[22] Ziro Maki, Masami Nakagawa, and Shoichi Sakata. Remarks on the unified model of elementary particles. *Prog. Theor. Phys.*, 28:870–880, 1962. [,34(1962)].

[23] V. Gribov and B. Pontecorvo. Neutrino astronomy and lepton charge. *Physics Letters B*, 28(7):493–496, Jan 1969.

[24] Y. Fukuda, T. Hayakawa, E. Ichihara, K. Inoue, K. Ishihara, H. Ishino, Y. Itow, T. Kajita, J. Kameda, S. Kasuga, K. Kobayashi, Y. Kobayashi, Y. Koshio, M. Miura, M. Nakahata, S. Nakayama, A. Okada, K. Okumura, N. Sakurai, M. Shiozawa, Y. Suzuki, Y. Takeuchi, Y. Totsuka, S. Yamada, M. Earl, A. Habig, E. Kearns, M. D. Messier, K. Scholberg, J. L. Stone, L. R. Sulak, C. W. Walter, M. Goldhaber, T. Barszczxak, D. Casper, W. Gajewski, P. G. Halverson, J. Hsu, W. R. Kropp, L. R. Price, F. Reines, M. Smy, H. W. Sobel, M. R. Vagins, K. S. Ganezer, W. E. Keig, R. W. Ellsworth, S. Tasaka, J. W. Flanagan, A. Kibayashi, J. G. Learned, S. Matsuno, V. J. Stenger, D. Takemori, T. Ishii, J. Kanzaki, T. Kobayashi, S. Mine, K. Nakamura, K. Nishikawa, Y. Oyama, A. Sakai, M. Sakuda, O. Sasaki, S. Echigo, M. Kohama, A. T. Suzuki, T. J. Haines, E. Blaufuss, B. K. Kim, R. Sanford, R. Svoboda, M. L. Chen, Z. Conner, J. A. Goodman, G. W. Sullivan, J. Hill, C. K. Jung, K. Martens, C. Mauger, C. McGrew, E. Sharkey, B. Viren, C. Yanagisawa, W. Doki, K. Miyano, H. Okazawa, C. Saji, M. Takahata, Y. Nagashima, M. Takita, T. Yamaguchi, M. Yoshida, S. B. Kim, M. Etoh, K. Fujita, A. Hasegawa, T. Hasegawa, S. Hatakeyama, T. Iwamoto, M. Koga, T. Maruyama, H. Ogawa, J. Shirai, A. Suzuki, F. Tsushima, M. Koshiba, M. Nemoto, K. Nishijima, T. Futagami, Y. Hayato, Y. Kanaya, K. Kaneyuki, Y. Watanabe, D. Kielczewska, R. A. Doyle, J. S. George, A. L. Stachyra, L. L. Wai, R. J. Wilkes, and K. K. Young. Evidence for oscillation of atmospheric neutrinos. *Phys. Rev. Lett.*, 81:1562–1567, Aug 1998.

[25] Q. R. Ahmad, R. C. Allen, T. C. Andersen, J. D.Anglin, J. C. Barton, E. W. Beier, M. Bercovitch, J. Bigu, S. D. Biller, R. A. Black, I. Blevis, R. J. Boardman, J. Boger, E. Bonvin, M. G. Boulay, M. G. Bowler, T. J. Bowles, S. J. Brice, M. C. Browne, T. V. Bullard, G. Bühler, J. Cameron, Y. D. Chan, H. H. Chen, M. Chen, X. Chen, B. T. Cleveland, E. T. H. Clifford, J. H. M. Cowan, D. F. Cowen, G. A. Cox, X. Dai, F. Dalnoki-Veress, W. F. Davidson, P. J. Doe, G. Doucas, M. R. Dragowsky, C. A. Duba, F. A. Duncan, M. Dunford, J. A. Dunmore, E. D. Earle, S. R. Elliott, H. C. Evans, G. T. Ewan, J. Farine, H. Fergani, A. P. Ferraris, R. J. Ford, J. A. Formaggio, M. M. Fowler, K. Frame, E. D. Frank, W. Frati, N. Gagnon, J. V. Germani, S. Gil, K. Graham, D. R. Grant, R. L. Hahn, A. L. Hallin, E. D. Hallman, A. S. Hamer, A. A. Hamian, W. B. Handler, R. U. Haq, C. K. Hargrove, P. J. Harvey, R. Hazama, K. M. Heeger, W. J. Heintzelman, J. Heise, R. L. Helmer, J. D. Hepburn, H. Heron, J. Hewett, A. Hime, M. Howe, J. G. Hykawy, M. C. P. Isaac, P. Jagam, N. A. Jelley, C. Jillings, G. Jonkmans, K. Kazkaz, P. T. Keener, J. R. Klein, A. B. Knox, R. J. Komar, R. Kouzes, T. Kutter, C. C. M. Kyba, J. Law, I. T. Lawson, M. Lay, H. W. Lee, K. T. Lesko, J. R. Leslie, I. Levine, W. Locke, S. Luoma, J. Lyon, S. Majerus, H. B. Mak, J. Maneira, J. Manor, A. D. Marino, N. McCauley, A. B. McDonald, D. S. McDonald, K. McFarlane, G. McGregor, R. Meijer Drees, C. Mifflin, G. G. Miller, G. Milton, B. A. Moffat, M. Moorhead, C. W. Nally, M. S. Neubauer, F. M. Newcomer, H. S. Ng, A. J. Noble, E. B. Norman, V. M. Novikov, M. O'Neill, C. E.

Okada, R. W. Ollerhead, M. Omori, J. L. Orrell, S. M. Oser, A. W. P. Poon, T. J. Radcliffe, A. Roberge, B. C. Robertson, R. G. H. Robertson, S. S. E. Rosendahl, J. K. Rowley, V. L. Rusu, E. Saettler, K. K. Schaffer, M. H. Schwendener, A. Schülke, H. Seifert, M. Shatkay, J. J. Simpson, C. J. Sims, D. Sinclair, P. Skensved, A. R. Smith, M. W. E. Smith, T. Spreitzer, N. Starinsky, T. D. Steiger, R. G. Stokstad, L. C. Stonehill, R. S. Storey, B. Sur, R. Tafirout, N. Tagg, N. W. Tanner, R. K. Taplin, M. Thorman, P. M. Thornewell, P. T. Trent, Y. I. Tserkovnyak, R. Van Berg, R. G. Van de Water, C. J. Virtue, C. E. Waltham, J.-X. Wang, D. L. Wark, N. West, J. B. Wilhelmy, J. F. Wilkerson, J. R. Wilson, P. Wittich, J. M. Wouters, and M. Yeh. Direct evidence for neutrino flavor transformation from neutral-current interactions in the sudbury neutrino observatory. *Phys. Rev. Lett.*, 89:011301, Jun 2002.

[26] K. Eguchi, S. Enomoto, K. Furuno, J. Goldman, H. Hanada, H. Ikeda, K. Ikeda, K. Inoue, K. Ishihara, W. Itoh, T. Iwamoto, T. Kawaguchi, T. Kawashima, H. Kinoshita, Y. Kishimoto, M. Koga, Y. Koseki, T. Maeda, T. Mitsui, M. Motoki, K. Nakajima, M. Nakajima, T. Nakajima, H. Ogawa, K. Owada, T. Sakabe, I. Shimizu, J. Shirai, F. Suekane, A. Suzuki, K. Tada, O. Tajima, T. Takayama, K. Tamae, H. Watanabe, J. Busenitz, Z. Djurcic, K. McKinny, D.-M. Mei, A. Piepke, E. Yakushev, B. E. Berger, Y. D. Chan, M. P. Decowski, D. A. Dwyer, S. J. Freedman, Y. Fu, B. K. Fujikawa, K. M. Heeger, K. T. Lesko, K.-B. Luk, H. Murayama, D. R. Nygren, C. E. Okada, A. W. P. Poon, H. M. Steiner, L. A. Winslow, G. A. Horton-Smith, R. D. McKeown, J. Ritter, B. Tipton, P. Vogel, C. E. Lane, T. Miletic, P. W. Gorham, G. Guillian, J. G. Learned, J. Maricic, S. Matsuno, S. Pakvasa, S. Dazeley, S. Hatakeyama, M. Murakami, R. C. Svoboda, B. D. Dieterle, M. DiMauro, J. Detwiler, G. Gratta, K. Ishii, N. Tolich, Y. Uchida, M. Batygov, W. Bugg, H. Cohn, Y. Efremenko, Y. Kamyshkov, A. Kozlov, Y. Nakamura, L. De Braeckeleer, C. R. Gould, H. J. Karwowski, D. M. Markoff, J. A. Messimore, K. Nakamura, R. M. Rohm, W. Tornow, A. R. Young, and Y.-F. Wang. First results from kamland: Evidence for reactor antineutrino disappearance. *Phys. Rev. Lett.*, 90:021802, Jan 2003.

[27] Carlo Giunti and Chung W. Kim. *Fundamentals of Neutrino Physics and Astrophysics*. Oxford University Press, 1 edition, May 2007.

[28] P. A. M. Dirac. The Quantum Theory of the Electron. *Proceedings of the Royal Society of London Series A*, 117(778):610–624, Feb 1928.

[29] Ettore Majorana. Teoria simmetrica dell'elettrone e del positrone. *Il Nuovo Cimento (1924-1942)*, 14(4):171, Sep 2008.

[30] A. D. Sakharov. Violation of CP Invariance, C Asymmetry, and Baryon Asymmetry of the Universe. *ZhETF Pisma Redaktsiiu*, 5:32, Jan 1967.

[31] Tommy Ohlsson and Shun Zhou. Renormalization group running of neutrino parameters. *Nature Communications*, 5(5153), 10 2014.

[32] Heinrich Päs and Werner Rodejohann. Neutrinoless double beta decay. *New Journal of Physics*, 17(11):115010, nov 2015.

[33] Pavel Fileviez Pérez. New paradigm for baryon and lepton number violation. *Physics Reports*, 597:1 – 30, 2015. New paradigm for baryon and lepton number violation.

[34] K. Abe, Y. Haga, Y. Hayato, M. Ikeda, K. Iyogi, J. Kameda, Y. Kishimoto, M. Miura, S. Moriyama, M. Nakahata, T. Nakajima, Y. Nakano, S. Nakayama, A. Orii, H. Sekiya, M. Shiozawa, A. Takeda, H. Tanaka, T. Tomura, R. A. Wendell, R. Akutsu, T. Irvine, T. Kajita, K. Kaneyuki, Y. Nishimura, E. Richard, K. Okumura, L. Labarga, P. Fernandez, J. Gustafson, C. Kachulis, E. Kearns, J. L. Raaf, J. L. Stone, L. R. Sulak, S. Berkman, C. M. Nantais, H. A. Tanaka, S. Tobayama, M. Goldhaber, W. R. Kropp, S. Mine, P. Weatherly, M. B. Smy, H. W. Sobel, V. Takhistov, K. S. Ganezer, B. L. Hartfiel, J. Hill, N. Hong, J. Y. Kim, I. T. Lim, R. G. Park, A. Himmel, Z. Li, E. O'Sullivan, K. Scholberg, C. W. Walter, T. Wongjirad, T. Ishizuka, S. Tasaka, J. S. Jang, J. G. Learned, S. Matsuno, S. N. Smith, M. Friend, T. Hasegawa, T. Ishida, T. Ishii, T. Kobayashi, T. Nakadaira, K. Nakamura, Y. Oyama, K. Sakashita, T. Sekiguchi, T. Tsukamoto, A. T. Suzuki, Y. Takeuchi, T. Yano, S. V. Cao, T. Hiraki, S. Hirota, K. Huang, T. Kikawa, A. Minamino, T. Nakaya, K. Suzuki, Y. Fukuda, K. Choi, Y. Itow, T. Suzuki, P. Mijakowski, K. Frankiewicz, J. Hignight, J. Imber, C. K. Jung, X. Li, J. L. Palomino, M. J. Wilking, C. Yanagisawa, D. Fukuda, H. Ishino, T. Kayano, A. Kibayashi, Y. Koshio, T. Mori, M. Sakuda, C. Xu, Y. Kuno, R. Tacik, S. B. Kim, H. Okazawa, Y. Choi, K. Nishijima, M. Koshiba, Y. Totsuka, Y. Suda, M. Yokoyama, C. Bronner, M. Hartz, K. Martens, Ll. Marti, Y. Suzuki, M. R. Vagins, J. F. Martin, A. Konaka, S. Chen, Y. Zhang, and R. J. Wilkes. Search for proton decay via $p \to e^+ \pi^0$ and $p \to \mu^+ \pi^0$ in 0.31 megaton·years exposure of the super-kamiokande water cherenkov detector. *Phys. Rev. D*, 95:012004, Jan 2017.

[35] Frank T. Avignone, Steven R. Elliott, and Jonathan Engel. Double beta decay, majorana neutrinos, and neutrino mass. *Rev. Mod. Phys.*, 80:481–516, Apr 2008.

[36] M. Goeppert-Mayer. Double beta-disintegration. *Phys. Rev.*, 48:512–516, Sep 1935.

[37] Mark G. Inghram and John H. Reynolds. Double beta-decay of te^{130}. *Phys. Rev.*, 78:822–823, Jun 1950.

[38] S. R. Elliott, A. A. Hahn, and M. K. Moe. Direct evidence for two-neutrino double-beta decay in ^{82}Se. *Phys. Rev. Lett.*, 59:2020–2023, Nov 1987.

[39] Ruben Saakyan. Two-neutrino double-beta decay. *Annual Review of Nuclear and Particle Science*, 63(1):503–529, 2013.

[40] Jonathan Engel and Javier Menéndez. Status and future of nuclear matrix elements for neutrinoless double-beta decay: a review. *Reports on Progress in Physics*, 80(4):046301, mar 2017.

[41] J. Kotila and F. Iachello. Phase-space factors for double-β decay. *Phys. Rev. C*, 85:034316, Mar 2012.

[42] Mihail Mirea, Tudor Pahomi, and Sabin Stoica. Values of the phase space factors involved in double beta decay. *Romanian Reports in Physics*, 67:872–889, 09 2015.

[43] Sabin Stoica and Mihail Mirea. Phase space factors for double-beta decays. *Frontiers in Physics*, 7:12, 2019.

[44] P. Gysbers, G. Hagen, J. D. Holt, G. R. Jansen, T. D. Morris, P. Navrátil, T. Papenbrock, S. Quaglioni, A. Schwenk, S. R. Stroberg, and K. A. Wendt. Discrepancy between experimental and theoretical β-decay rates resolved from first principles. *Nature Physics*, 15:1745–2481, May 2019.

[45] W. H. Furry. On transition probabilities in double beta-disintegration. *Phys. Rev.*, 56:1184–1193, Dec 1939.

[46] A. Gando, Y. Gando, T. Hachiya, A. Hayashi, S. Hayashida, H. Ikeda, K. Inoue, K. Ishidoshiro, Y. Karino, M. Koga, S. Matsuda, T. Mitsui, K. Nakamura, S. Obara, T. Oura, H. Ozaki, I. Shimizu, Y. Shirahata, J. Shirai, A. Suzuki, T. Takai, K. Tamae, Y. Teraoka, K. Ueshima, H. Watanabe, A. Kozlov, Y. Takemoto, S. Yoshida, K. Fushimi, T. I. Banks, B. E. Berger, B. K. Fujikawa, T. O'Donnell, L. A. Winslow, Y. Efremenko, H. J. Karwowski, D. M. Markoff, W. Tornow, J. A. Detwiler, S. Enomoto, and M. P. Decowski. Publisher's note: Search for majorana neutrinos near the inverted mass hierarchy region with kamland-zen [phys. rev. lett. 117, 082503 (2016)]. *Phys. Rev. Lett.*, 117:109903, Sep 2016.

[47] GERDA Collaboration, M. Agostini, A. M. Bakalyarov, M. Balata, I. Barabanov, L. Baudis, C. Bauer, E. Bellotti, S. Belogurov, S. T. Belyaev, G. Benato, A. Bettini, L. Bezrukov, T. Bode, D. Borowicz, V. Brudanin, R. Brugnera, A. Caldwell, C. Cattadori, A. Chernogorov, V. D'Andrea, E. V. Demidova, N. Di Marco, A. Domula, E. Doroshkevich, V. Egorov, R. Falkenstein, N. Frodyma, A. Gangapshev, A. Garfagnini, P. Grabmayr, V. Gurentsov, K. Gusev, J. Hakenmüller, A. Hegai, M. Heisel, S. Hemmer, R. Hiller, W. Hofmann, M. Hult, L. V. Inzhechik, L. Ioannucci, J. Janicskó Csáthy, J. Jochum, M. Junker, V. Kazalov, Y. Kermaïdic, T. Kihm,

I. V. Kirpichnikov, A. Kirsch, A. Kish, A. Klimenko, R. Kneißl, K. T. Knöpfle, O. Kochetov, V. N. Kornoukhov, V. V. Kuzminov, M. Laubenstein, A. Lazzaro, V. I. Lebedev, B. Lehnert, M. Lindner, I. Lippi, A. Lubashevskiy, B. Lubsandorzhiev, G. Lutter, C. Macolino, B. Majorovits, W. Maneschg, E. Medinaceli, M. Miloradovic, R. Mingazheva, M. Misiaszek, P. Moseev, I. Nemchenok, S. Nisi, K. Panas, L. Pandola, K. Pelczar, A. Pullia, C. Ransom, S. Riboldi, N. Rumyantseva, C. Sada, F. Salamida, M. Salathe, C. Schmitt, B. Schneider, S. Schönert, J. Schreiner, A-K. Schütz, O. Schulz, B. Schwingenheuer, O. Selivanenko, E. Shevchik, M. Shirchenko, H. Simgen, A. Smolnikov, L. Stanco, L. Vanhoefer, A. A. Vasenko, A. Veresnikova, K. von Sturm, V. Wagner, A. Wegmann, T. Wester, C. Wiesinger, M. Wojcik, E. Yanovich, I. Zhitnikov, S. V. Zhukov, D. Zinatulina, A. J. Zsigmond, K. Zuber, and G. Zuzel. Upgrade for phase ii of the gerda experiment. *The European Physical Journal C*, 78(5):388, May 2018.

[48] C. Alduino, F. Alessandria, K. Alfonso, E. Andreotti, C. Arnaboldi, F. T. Avignone, O. Azzolini, M. Balata, I. Bandac, T. I. Banks, G. Bari, M. Barucci, J. W. Beeman, F. Bellini, G. Benato, A. Bersani, D. Biare, M. Biassoni, F. Bragazzi, A. Branca, C. Brofferio, A. Bryant, A. Buccheri, C. Bucci, C. Bulfon, A. Camacho, A. Caminata, L. Canonica, X. G. Cao, S. Capelli, M. Capodiferro, L. Cappelli, L. Cardani, M. Cariello, P. Carniti, M. Carrettoni, N. Casali, L. Cassina, R. Cereseto, G. Ceruti, A. Chiarini, D. Chiesa, N. Chott, M. Clemenza, D. Conventi, S. Copello, C. Cosmelli, O. Cremonesi, C. Crescentini, R. J. Creswick, J. S. Cushman, A. D'Addabbo, D. D'Aguanno, I. Dafinei, V. Datskov, C. J. Davis, F. Del Corso, S. Dell'Oro, M. M. Deninno, S. Di Domizio, M. L. Di Vacri, L. Di Paolo, A. Drobizhev, L. Ejzak, R. Faccini, D. Q. Fang, M. Faverzani, E. Ferri, F. Ferroni, E. Fiorini, M. A. Franceschi, S. J. Freedman, B. K. Fujikawa, R. Gaigher, A. Giachero, L. Gironi, A. Giuliani, L. Gladstone, J. Goett, P. Gorla, C. Gotti, C. Guandalini, M. Guerzoni, T. D. Gutierrez, E. E. Haller, K. Han, E. V. Hansen, K. M. Heeger, R. Hennings-Yeomans, K. P. Hickerson, H. Z. Huang, M. Iannone, L. Ioannucci, R. Kadel, G. Keppel, L. Kogler, Yu. G. Kolomensky, A. Leder, C. Ligi, K. E. Lim, X. Liu, Y. G. Ma, C. Maiano, M. Maino, L. Marini, M. Martinez, C. Martinez Amaya, R. H. Maruyama, Y. Mei, N. Moggi, S. Morganti, P. J. Mosteiro, S. S. Nagorny, T. Napolitano, M. Nastasi, S. Nisi, C. Nones, E. B. Norman, V. Novati, A. Nucciotti, I. Nutini, T. O'Donnell, M. Olcese, E. Olivieri, F. Orio, D. Orlandi, J. L. Ouellet, C. E. Pagliarone, M. Pallavicini, V. Palmieri, L. Pattavina, M. Pavan, M. Pedretti, R. Pedrotta, A. Pelosi, G. Pessina, V. Pettinacci, G. Piperno, C. Pira, S. Pirro, S. Pozzi, E. Previtali, F. Reindl, F. Rimondi, L. Risegari, C. Rosenfeld, C. Rossi, C. Rusconi, M. Sakai, E. Sala, C. Salvioni, S. Sangiorgio, D. Santone, D. Schaeffer, B. Schmidt, J. Schmidt, N. D. Scielzo, V. Singh, M. Sisti, A. R. Smith, F. Stivanello, L. Taffarello, L. Tatananni, M. Tenconi, F. Terranova, M. Tessaro, C. Tomei, G. Ventura, M. Vignati, S. L. Wagaarachchi, J. Wallig, B. S. Wang, H. W. Wang, B. Welliver, J. Wilson, K. Wilson, L. A. Winslow, T. Wise, L. Zanotti, C. Zarra, G. Q. Zhang, B. X. Zhu, S. Zimmermann, and S. Zucchelli. First

results from cuore: A search for lepton number violation via $0\nu\beta\beta$ decay of ^{130}Te. *Phys. Rev. Lett.*, 120:132501, Mar 2018.

[49] J. Schechter and J. W. F. Valle. Neutrinoless double-β decay in su(2)×u(1) theories. *Phys. Rev. D*, 25:2951–2954, Jun 1982.

[50] Vincenzo Cirigliano, Wouter Dekens, Jordy de Vries, Michael L. Graesser, Emanuele Mereghetti, Saori Pastore, and Ubirajara van Kolck. New leading contribution to neutrinoless double-β decay. *Phys. Rev. Lett.*, 120:202001, May 2018.

[51] Stefano Dell'Oro, Simone Marcocci, and Francesco Vissani. New expectations and uncertainties on neutrinoless double beta decay. *Phys. Rev. D*, 90:033005, Aug 2014.

[52] V. Cirigliano, W. Dekens, J. de Vries, M. L. Graesser, and E. Mereghetti. A neutrinoless double beta decay master formula from effective field theory. *Journal of High Energy Physics*, 2018(12):97, Dec 2018.

[53] A. S. Barabash. Brief review of double beta decay experiments. In *Proceedings, 2nd International Conference on Particle Physics and Astrophysics (ICPPA 2016): Moscow, Russia, October 10-14, 2016*, 2017.

[54] J. Barea, J. Kotila, and F. Iachello. Nuclear matrix elements for double-β decay. *Phys. Rev. C*, 87:014315, Jan 2013.

[55] J. Barea, J. Kotila, and F. Iachello. $0\nu\beta\beta$ and $2\nu\beta\beta$ nuclear matrix elements in the interacting boson model with isospin restoration. *Phys. Rev. C*, 91:034304, Mar 2015.

[56] E. A. Coello Pérez, J. Menéndez, and A. Schwenk. Gamow-teller and double-β decays of heavy nuclei within an effective theory. *Phys. Rev. C*, 98:045501, Oct 2018.

[57] M Agostini et al. $2\nu\beta\beta$ decay of 76ge into excited states with GERDA phase i. *Journal of Physics G: Nuclear and Particle Physics*, 43(4):044001, sep 2015.

[58] O. Civitarese and J. Suhonen. Two-neutrino double-beta decay to excited one- and two-phonon states. *Nuclear Physics A*, 575(2):251 – 268, 1994.

[59] S. Stoica and I. Mihut. Nuclear structure calculations of two-neutrino double-beta decay transitions to excited final states. *Nuclear Physics A*, 602(2):197 – 210, 1996.

[60] M. Aunola and J. Suhonen. Systematic study of beta and double beta decay to excited final states. *Nuclear Physics A*, 602(2):133 – 166, 1996.

[61] J. Toivanen and J. Suhonen. Study of several double-beta-decaying nuclei using the renormalized proton-neutron quasiparticle random-phase approximation. *Phys. Rev. C*, 55:2314–2323, May 1997.

[62] W.C. Haxton and G.J. Stephenson. Double beta decay. *Progress in Particle and Nuclear Physics*, 12:409 – 479, 1984.

[63] S. K. Dhiman and P. K. Raina. Two-neutrino double-beta decay matrix elements for ground and excited states of ^{76}Ge and ^{82}Se nuclei. *Phys. Rev. C*, 50:R2660–R2663, Dec 1994.

[64] J. Schwieger, F. Šimkovic, Amand Faessler, and Wiesław A. Kamiński. Double β decay to excited states of several medium-heavy nuclei within the renormalized quasiparticle random phase approximation. *Phys. Rev. C*, 57:1738–1743, Apr 1998.

[65] C. M. Raduta and A. A. Raduta. Unified description of the double β decay to the first quadrupole phonon state in spherical and deformed nuclei. *Phys. Rev. C*, 76:044306, Oct 2007.

[66] S. Unlu. Quasi random phase approximation predictions on two-neutrino double beta decay half-lives to the first 2+state. *Chinese Physics Letters*, 31(4):042101, apr 2014.

[67] F. Šimkovic and A. Faessler. Distinguishing the O$\nu\beta\beta$-decay mechanisms. *Progress in Particle and Nuclear Physics*, 48:201–209, July 2002.

[68] Juhani Hyvärinen and Jouni Suhonen. Neutrinoless $\beta\beta$ decays to excited 0^+ states and the majorana-neutrino mass. *Phys. Rev. C*, 93:064306, Jun 2016.

[69] A.D. Dolgov and A.Yu. Smirnov. Possible violation of the spin-statistics relation for neutrinos: Cosmological and astrophysical consequences. *Physics Letters B*, 621(1):1 – 10, 2005.

[70] A.S. Barabash, A.D. Dolgov, R. Dvornický, F. Šimkovic, and A.Yu. Smirnov. Statistics of neutrinos and the double beta decay. *Nuclear Physics B*, 783(1):90 – 111, 2007.

[71] W. Tornow. Search for a bosonic component in the neutrino wave function. *Nuclear Physics A*, 844(1):57c – 62c, 2010. Proceedings of the 4th International Symposium on Symmetries in Subatomic Physics.

[72] N. Abgrall, E. Aguayo, F. T. Avignone, A. S. Barabash, F. E. Bertrand, M. Boswell, V. Brudanin, M. Busch, A. S. Caldwell, Y.-D. Chan, C. D. Christofferson, D. C. Combs,

J. A. Detwiler, P. J. Doe, Yu. Efremenko, V. Egorov, H. Ejiri, S. R. Elliott, J. Esterline, J. E. Fast, P. Finnerty, F. M. Fraenkle, A. Galindo-Uribarri, G. K. Giovanetti, J. Goett, M. P. Green, J. Gruszko, V. E. Guiseppe, K. Gusev, A. L. Hallin, R. Hazama, A. Hegai, R. Henning, E. W. Hoppe, S. Howard, M. A. Howe, K. J. Keeter, M. F. Kidd, A. Knecht, O. Kochetov, S. I. Konovalov, R. T. Kouzes, B. D. LaFerriere, J. Leon, L. E. Leviner, J. C. Loach, P. N. Luke, S. MacMullin, R. D. Martin, S. Mertens, L. Mizouni, M. Nomachi, J. L. Orrell, C. O'Shaughnessy, N. R. Overman, David Phillips, A. W. P. Poon, K. Pushkin, D. C. Radford, K. Rielage, R. G. H. Robertson, M. C. Ronquest, A. G. Schubert, B. Shanks, T. Shima, M. Shirchenko, K. J. Snavely, N. Snyder, D. Steele, J. Strain, A. M. Suriano, J. Thompson, V. Timkin, W. Tornow, R. L. Varner, S. Vasilyev, K. Vetter, K. Vorren, B. R. White, J. F. Wilkerson, T. Williams, W. Xu, E. Yakushev, A. R. Young, C.-H. Yu, and V. Yumatov. The MAJORANA DEMONSTRATOR neutrinoless double-beta decay experiment. *Advances in High Energy Physics*, 2014:365432, Aug 2014.

[73] M. Agostini, A. M. Bakalyarov, M. Balata, I. Barabanov, L. Baudis, C. Bauer, E. Bellotti, S. Belogurov, A. Bettini, L. Bezrukov, J. Biernat, T. Bode, D. Borowicz, V. Brudanin, R. Brugnera, A. Caldwell, C. Cattadori, A. Chernogorov, T. Comellato, V. D'Andrea, E. V. Demidova, N. Di Marco, A. Domula, E. Doroshkevich, V. Egorov, R. Falkenstein, A. Gangapshev, A. Garfagnini, P. Grabmayr, V. Gurentsov, K. Gusev, J. Hakenmüller, A. Hegai, M. Heisel, S. Hemmer, R. Hiller, W. Hofmann, M. Hult, L. V. Inzhechik, J. Janicskó Csáthy, J. Jochum, M. Junker, V. Kazalov, Y. Kermaidic, T. Kihm, I. V. Kirpichnikov, A. Kirsch, A. Kish, A. Klimenko, R. Kneißl, K. T. Knöpfle, O. Kochetov, V. N. Kornoukhov, V. V. Kuzminov, M. Laubenstein, A. Lazzaro, M. Lindner, I. Lippi, A. Lubashevskiy, B. Lubsandorzhiev, G. Lutter, C. Macolino, B. Majorovits, W. Maneschg, M. Miloradovic, R. Mingazheva, M. Misiaszek, P. Moseev, I. Nemchenok, K. Panas, L. Pandola, K. Pelczar, L. Pertoldi, A. Pullia, C. Ransom, S. Riboldi, N. Rumyantseva, C. Sada, F. Salamida, C. Schmitt, B. Schneider, S. Schönert, A-K. Schütz, O. Schulz, B. Schwingenheuer, O. Selivanenko, E. Shevchik, M. Shirchenko, H. Simgen, A. Smolnikov, L. Stanco, L. Vanhoefer, A. A. Vasenko, A. Veresnikova, K. von Sturm, V. Wagner, A. Wegmann, T. Wester, C. Wiesinger, M. Wojcik, E. Yanovich, I. Zhitnikov, S. V. Zhukov, D. Zinatulina, A. Zschocke, A. J. Zsigmond, K. Zuber, and G. Zuzel. Improved limit on neutrinoless double-β decay of ^{76}Ge from gerda phase ii. *Phys. Rev. Lett.*, 120:132503, Mar 2018.

[74] N. Abgrall, I. J. Arnquist, F. T. Avignone, A. S. Barabash, F. E. Bertrand, A. W. Bradley, V. Brudanin, M. Busch, M. Buuck, T. S. Caldwell, Y.-D. Chan, C. D. Christofferson, P.-H. Chu, C. Cuesta, J. A. Detwiler, C. Dunagan, Yu. Efremenko, H. Ejiri, S. R. Elliott, T. Gilliss, G. K. Giovanetti, J. Goett, M. P. Green, J. Gruszko, I. S. Guinn, V. E. Guiseppe, C. R. S. Haufe, R. Henning, E. W. Hoppe, S. Howard, M. A. Howe, B. R. Jasinski, K. J. Keeter, M. F. Kidd, S. I. Konovalov, R. T. Kouzes, A. M. Lopez, J. MacMullin, R. D. Martin, R. Massarczyk, S. J. Meijer, S. Mertens,

C. O'Shaughnessy, A. W. P. Poon, D. C. Radford, J. Rager, A. L. Reine, K. Rielage, R. G. H. Robertson, B. Shanks, M. Shirchenko, A. M. Suriano, D. Tedeschi, J. E. Trimble, R. L. Varner, S. Vasilyev, K. Vetter, K. Vorren, B. R. White, J. F. Wilkerson, C. Wiseman, W. Xu, E. Yakushev, C.-H. Yu, V. Yumatov, I. Zhitnikov, and B. X. Zhu. New limits on bosonic dark matter, solar axions, pauli exclusion principle violation, and electron decay from the majorana demonstrator. *Phys. Rev. Lett.*, 118:161801, Apr 2017.

[75] S. I. Alvis, I. J. Arnquist, F. T. Avignone, A. S. Barabash, C. J. Barton, F. E. Bertrand, V. Brudanin, M. Busch, M. Buuck, T. S. Caldwell, Y-D. Chan, C. D. Christofferson, P.-H. Chu, C. Cuesta, J. A. Detwiler, C. Dunagan, Yu. Efremenko, H. Ejiri, S. R. Elliott, T. Gilliss, G. K. Giovanetti, M. P. Green, J. Gruszko, I. S. Guinn, V. E. Guiseppe, C. R. Haufe, L. Hehn, R. Henning, E. W. Hoppe, M. A. Howe, S. I. Konovalov, R. T. Kouzes, A. M. Lopez, R. D. Martin, R. Massarczyk, S. J. Meijer, S. Mertens, J. Myslik, C. O'Shaughnessy, G. Othman, W. Pettus, A. W. P. Poon, D. C. Radford, J. Rager, A. L. Reine, K. Rielage, R. G. H. Robertson, N. W. Ruof, B. Shanks, M. Shirchenko, A. M. Suriano, D. Tedeschi, R. L. Varner, S. Vasilyev, K. Vorren, B. R. White, J. F. Wilkerson, C. Wiseman, W. Xu, E. Yakushev, C.-H. Yu, V. Yumatov, I. Zhitnikov, and B. X. Zhu. First limit on the direct detection of lightly ionizing particles for electric charge as low as $e/1000$ with the majorana demonstrator. *Phys. Rev. Lett.*, 120:211804, May 2018.

[76] S. I. Alvis, I. J. Arnquist, F. T. Avignone, A. S. Barabash, C. J. Barton, V. Basu, F. E. Bertrand, B. Bos, V. Brudanin, M. Busch, M. Buuck, T. S. Caldwell, Y-D. Chan, C. D. Christofferson, P.-H. Chu, C. Cuesta, J. A. Detwiler, Yu. Efremenko, H. Ejiri, S. R. Elliott, T. Gilliss, G. K. Giovanetti, M. P. Green, J. Gruszko, I. S. Guinn, V. E. Guiseppe, C. R. Haufe, R. J. Hegedus, L. Hehn, R. Henning, D. Hervas Aguilar, E. W. Hoppe, M. A. Howe, K. J. Keeter, M. F. Kidd, S. I. Konovalov, R. T. Kouzes, A. M. Lopez, R. D. Martin, R. Massarczyk, S. J. Meijer, S. Mertens, J. Myslik, G. Othman, W. Pettus, A. Piliounis, A. W. P. Poon, D. C. Radford, J. Rager, A. L. Reine, K. Rielage, N. W. Ruof, B. Shanks, M. Shirchenko, D. Tedeschi, R. L. Varner, S. Vasilyev, B. R. White, J. F. Wilkerson, C. Wiseman, W. Xu, E. Yakushev, C.-H. Yu, V. Yumatov, I. Zhitnikov, and B. X. Zhu. Search for trinucleon decay in the majorana demonstrator. *Phys. Rev. D*, 99:072004, Apr 2019.

[77] P. N. Luke, F. S. Goulding, N. W. Madden, and R. H. Pehl. Low capacitance large volume shaped-field germanium detector. *IEEE Transactions on Nuclear Science*, 36(1):926–930, Feb 1989.

[78] P S Barbeau, J I Collar, and O Tench. Large-mass ultralow noise germanium detectors: performance and applications in neutrino and astroparticle physics. *Journal of Cosmology and Astroparticle Physics*, 2007(09):009–009, sep 2007.

[79] N. Abgrall, I.J. Arnquist, F.T. Avignone III, A.S. Barabash, F.E. Bertrand, A.W. Bradley, V. Brudanin, M. Busch, M. Buuck, J. Caja, M. Caja, T.S. Caldwell, C.D. Christofferson, P.-H. Chu, C. Cuesta, J.A. Detwiler, C. Dunagan, D.T. Dunstan, Yu. Efremenko, H. Ejiri, S.R. Elliott, T. Gilliss, G.K. Giovanetti, J. Goett, M.P. Green, J. Gruszko, I.S. Guinn, V.E. Guiseppe, C.R.S. Haufe, R. Henning, E.W. Hoppe, B.R. Jasinski, M.F. Kidd, S.I. Konovalov, R.T. Kouzes, A.M. Lopez, J. Mac-Mullin, R.D. Martin, R. Massarczyk, S.J. Meijer, S. Mertens, J.H. Meyer, J. Myslik, C. O'Shaughnessy, A.W.P. Poon, D.C. Radford, J. Rager, A.L. Reine, J.A. Reising, K. Rielage, R.G.H. Robertson, B. Shanks, M. Shirchenko, A.M. Suriano, D. Tedeschi, L.M. Toth, J.E. Trimble, R.L. Varner, S. Vasilyev, K. Vetter, K. Vorren, B.R. White, J.F. Wilkerson, C. Wiseman, W. Xu, E. Yakushev, C.-H. Yu, V. Yumatov, I. Zhitnikov, and B.X. Zhu. The processing of enriched germanium for the majorana demonstrator and r&d for a next generation double-beta decay experiment. *Nuclear Instruments and Methods in Physics Research Section A: Accelerators, Spectrometers, Detectors and Associated Equipment*, 877:314 – 322, 2018.

[80] E.W. Hoppe, C.E. Aalseth, O.T. Farmer, T.W. Hossbach, M. Liezers, H.S. Miley, N.R. Overman, and J.H. Reeves. Reduction of radioactive backgrounds in electroformed copper for ultra-sensitive radiation detectors. *Nuclear Instruments and Methods in Physics Research Section A: Accelerators, Spectrometers, Detectors and Associated Equipment*, 764:116 – 121, 2014.

[81] N. Abgrall, I.J. Arnquist, F.T. Avignone, A.S. Barabash, F.E. Bertrand, A.W. Bradley, V. Brudanin, M. Busch, M. Buuck, D. Byram, A.S. Caldwell, Y-D. Chan, C.D. Christofferson, P.-H. Chu, C. Cuesta, J.A. Detwiler, P.J. Doe, C. Dunagan, Yu. Efremenko, H. Ejiri, S.R. Elliott, Z. Fu, A. Galindo-Uribarri, G.K. Giovanetti, J. Goett, M.P. Green, J. Gruszko, I.S. Guinn, V.E. Guiseppe, R. Henning, E.W. Hoppe, S. Howard, M.A. Howe, B.R. Jasinski, K.J. Keeter, M.F. Kidd, S.I. Konovalov, R.T. Kouzes, B.D. LaFerriere, J. Leon, A. Li, J. MacMullin, R.D. Martin, R. Massarczyk, S.J. Meijer, S. Mertens, J.L. Orrell, C. O'Shaughnessy, A.W.P. Poon, D.C. Radford, J. Rager, K. Rielage, R.G.H. Robertson, E. Romero-Romero, B. Shanks, M. Shirchenko, N. Snyder, A.M. Suriano, D. Tedeschi, A. Thompson, K.T. Ton, J.E. Trimble, R.L. Varner, S. Vasilyev, K. Vetter, K. Vorren, B.R. White, J.F. Wilkerson, C. Wiseman, W. Xu, E. Yakushev, C.-H. Yu, and V. Yumatov. High voltage testing for the majorana demonstrator. *Nuclear Instruments and Methods in Physics Research Section A: Accelerators, Spectrometers, Detectors and Associated Equipment*, 823:83 – 90, 2016.

[82] I. Guinn, N. Abgrall, I. J. Arnquist, F. T. Avignone, C. X. Baldenegro-Barrera, A. S. Barabash, F. E. Bertrand, A. W. Bradley, V. Brudanin, M. Busch, M. Buuck, D. Byram, A. S. Caldwell, Y-D. Chan, C. D. Christofferson, C. Cuesta, J. A. Detwiler,

Yu. Efremenko, H. Ejiri, S. R. Elliott, A. Galindo-Uribarri, T. Gilliss, G. K. Giovanetti, J. Goett, M. P. Green, J. Gruszko, V. E. Guiseppe, R. Henning, E. W. Hoppe, S. Howard, M. A. Howe, B. R. Jasinski, K. J. Keeter, M. F. Kidd, S. I. Konovalov, R. T. Kouzes, B. D. LaFerriere, J. Leon, J. MacMullin, R. D. Martin, S. J. Meijer, S. Mertens, J. L. Orrell, C. O'Shaughnessy, A. W. P. Poon, D. C. Radford, J. Rager, K. Rielage, R. G. H. Robertson, E. Romero-Romero, B. Shanks, M. Shirchenko, N. Snyder, A. M. Suriano, D. Tedeschi, J. E. Trimble, R. L. Varner, S. Vasilyev, K. Vetter, K. Vorren, B. R. White, J. F. Wilkerson, C. Wiseman, W. Xu, E. Yakushev, C.-H. Yu, V. Yumatov, and I. Zhitnikov. Low background signal readout electronics for the majorana demonstrator. *AIP Conference Proceedings*, 1672(1):030001, 2015.

[83] N. Abgrall, E. Aguayo, F.T. Avignone, A.S. Barabash, F.E. Bertrand, V. Brudanin, M. Busch, D. Byram, A.S. Caldwell, Y-D. Chan, C.D. Christofferson, D.C. Combs, C. Cuesta, J.A. Detwiler, P.J. Doe, Yu. Efremenko, V. Egorov, H. Ejiri, S.R. Elliott, J. Esterline, J.E. Fast, P. Finnerty, F.M. Fraenkle, A. Galindo-Uribarri, G.K. Giovanetti, J. Goett, M.P. Green, J. Gruszko, V.E. Guiseppe, K. Gusev, A.L. Hallin, R. Hazama, A. Hegai, R. Henning, E.W. Hoppe, S. Howard, M.A. Howe, K.J. Keeter, M.F. Kidd, O. Kochetov, S.I. Konovalov, R.T. Kouzes, B.D. LaFerriere, J. Diaz Leon, L.E. Leviner, J.C. Loach, J. MacMullin, R.D. Martin, S.J. Meijer, S. Mertens, M.L. Miller, L. Mizouni, M. Nomachi, J.L. Orrell, C. O'Shaughnessy, N.R. Overman, R. Petersburg, D.G. Phillips, A.W.P. Poon, K. Pushkin, D.C. Radford, J. Rager, K. Rielage, R.G.H. Robertson, E. Romero-Romero, M.C. Ronquest, B. Shanks, T. Shima, M. Shirchenko, K.J. Snavely, N. Snyder, A. Soin, A.M. Suriano, D. Tedeschi, J. Thompson, V. Timkin, W. Tornow, J.E. Trimble, R.L. Varner, S. Vasilyev, K. Vetter, K. Vorren, B.R. White, J.F. Wilkerson, C. Wiseman, W. Xu, E. Yakushev, A.R. Young, C.-H. Yu, V. Yumatov, and I. Zhitnikov. The majorana parts tracking database. *Nuclear Instruments and Methods in Physics Research Section A: Accelerators, Spectrometers, Detectors and Associated Equipment*, 779:52 – 62, 2015.

[84] N. Abgrall, I.J. Arnquist, F.T. Avignone, H.O. Back, A.S. Barabash, F.E. Bertrand, M. Boswell, A.W. Bradley, V. Brudanin, M. Busch, M. Buuck, D. Byram, A.S. Caldwell, Y.-D. Chan, C.D. Christofferson, P.-H. Chu, C. Cuesta, J.A. Detwiler, J.A. Dunmore, Yu. Efremenko, H. Ejiri, S.R. Elliott, P. Finnerty, A. Galindo-Uribarri, V.M. Gehman, T. Gilliss, G.K. Giovanetti, J. Goett, M.P. Green, J. Gruszko, I.S. Guinn, V.E. Guiseppe, R. Henning, E.W. Hoppe, S. Howard, M.A. Howe, B.R. Jasinski, R.A. Johnson, K.J. Keeter, M.F. Kidd, O. Kochetov, S.I. Konovalov, R.T. Kouzes, B.D. LaFerriere, J. Leon, J.C. Loach, J. MacMullin, S. MacMullin, R.D. Martin, R. Massarczyk, S. Meijer, S. Mertens, M.L. Miller, J.L. Orrell, C. O'Shaughnessy, N.R. Overman, A.W.P. Poon, K. Pushkin, D.C. Radford, J. Rager, K. Rielage, R.G.H. Robertson, E. Romero-Romero, M.C. Ronquest, A.G. Schubert, B. Shanks, M. Shirchenko, K.J. Snavely, N. Snyder, D. Steele, A.M. Suriano, D. Tedeschi, J.E. Trimble, R.L. Varner,

S. Vasilyev, K. Vetter, K. Vorren, B.R. White, J.F. Wilkerson, C. Wiseman, W. Xu, E. Yakushev, C.-H. Yu, V. Yumatov, and I. Zhitnikov. The majorana demonstrator radioassay program. *Nuclear Instruments and Methods in Physics Research Section A: Accelerators, Spectrometers, Detectors and Associated Equipment*, 828:22 – 36, 2016.

[85] J Heise. The sanford underground research facility at homestake. *Journal of Physics: Conference Series*, 606:012015, may 2015.

[86] C Wiseman. Muon veto analysis for the Majorana Demonstrator (internal). Technical report, University of South Carolina, 2016.

[87] N. Abgrall, E. Aguayo, F.T. Avignone, A.S. Barabash, F.E. Bertrand, A.W. Bradley, V. Brudanin, M. Busch, M. Buuck, D. Byram, A.S. Caldwell, Y-D. Chan, C.D. Christofferson, P.-H. Chu, C. Cuesta, J.A. Detwiler, C. Dunagan, Yu. Efremenko, H. Ejiri, S.R. Elliott, A. Galindo-Uribarri, T. Gilliss, G.K. Giovanetti, J. Goett, M.P. Green, J. Gruszko, I.S. Guinn, V.E. Guiseppe, R. Henning, E.W. Hoppe, S. Howard, M.A. Howe, B.R. Jasinski, K.J. Keeter, M.F. Kidd, S.I. Konovalov, R.T. Kouzes, B.D. LaFerriere, J. Leon, A.M. Lopez, J. MacMullin, R.D. Martin, R. Massarczyk, S.J. Meijer, S. Mertens, J.L. Orrell, C. O'Shaughnessy, N.R. Overman, A.W.P. Poon, D.C. Radford, J. Rager, K. Rielage, R.G.H. Robertson, E. Romero-Romero, M.C. Ronquest, C. Schmitt, B. Shanks, M. Shirchenko, N. Snyder, A.M. Suriano, D. Tedeschi, J.E. Trimble, R.L. Varner, S. Vasilyev, K. Vetter, K. Vorren, B.R. White, J.F. Wilkerson, C. Wiseman, W. Xu, E. Yakushev, C.-H. Yu, V. Yumatov, and I. Zhitnikov. Muon flux measurements at the davis campus of the sanford underground research facility with the majorana demonstrator veto system. *Astroparticle Physics*, 93:70 – 75, 2017.

[88] P. Barton, P. Luke, M. Amman, Y. Chan, J. Detwiler, J. Loach, R. Martin, A. Poon, C. Tindall, and K. Vetter. Low-noise low-mass front end electronics for low-background physics experiments using germanium detectors. In *2011 IEEE Nuclear Science Symposium Conference Record*, pages 1976–1979, Oct 2011.

[89] S. Zimmermann, J. T. Anderson, D. Doering, J. Joseph, C. Lionberger, T. Stezelberger, and H. Yaver. Implementation and performance of the electronics and computing system of the gamma ray energy tracking in-beam nuclear array (gretina). In *2011 IEEE Nuclear Science Symposium Conference Record*, pages 596–601, Oct 2011.

[90] V. Radeka. Trapezoidal filtering of signals from large germanium detectors at high rates. *IEEE Transactions on Nuclear Science*, 19(1):412–428, Feb 1972.

[91] Glenn F Knoll. *Radiation detection and measurement*. Wiley, New York, NY, 4 edition, 2010.

[92] P. Chu, B. Zhu, J. Detwiler, I. Guinn, T. Gillis, D. Radford, R. Varner, and S. Mertens. Unidoc of energy performance of MAJORANA DEMONSTRATOR. Technical Report 2017-12, Los Alamos National Laboratory, Mar 2017.

[93] N. Abgrall, I.J. Arnquist, F.T. Avignone III, A.S. Barabash, F.E. Bertrand, M. Boswell, A.W. Bradley, V. Brudanin, M. Busch, M. Buuck, T.S. Caldwell, C.D. Christofferson, P.-H. Chu, C. Cuesta, J.A. Detwiler, C. Dunagan, Yu. Efremenko, H. Ejiri, S.R. Elliott, Z. Fu, V.M. Gehman, T. Gilliss, G.K. Giovanetti, J. Goett, M.P. Green, J. Gruszko, I.S. Guinn, V.E. Guiseppe, C.R. Haufe, R. Henning, E.W. Hoppe, M.A. Howe, B.R. Jasinski, K.J. Keeter, M.F. Kidd, S.I. Konovalov, R.T. Kouzes, A.M. Lopez, J. MacMullin, R.D. Martin, R. Massarczyk, S.J. Meijer, S. Mertens, J.L. Orrell, C. O'Shaughnessy, A.W.P. Poon, D.C. Radford, J. Rager, A.L. Reine, K. Rielage, R.G.H. Robertson, B. Shanks, M. Shirchenko, A.M. Suriano, D. Tedeschi, J.E. Trimble, R.L. Varner, S. Vasilyev, K. Vetter, K. Vorren, B.R. White, J.F. Wilkerson, C. Wiseman, W. Xu, C.-H. Yu, V. Yumatov, I. Zhitnikov, and B.X. Zhu. The majorana demonstrator calibration system. *Nuclear Instruments and Methods in Physics Research Section A: Accelerators, Spectrometers, Detectors and Associated Equipment*, 872:16 – 22, 2017.

[94] S. I. Alvis, I. J. Arnquist, F. T. Avignone, A. S. Barabash, C. J. Barton, V. Basu, F. E. Bertrand, B. Bos, M. Buuck, T. S. Caldwell, Y-D. Chan, C. D. Christofferson, P.-H. Chu, C. Cuesta, J. A. Detwiler, H. Ejiri, S. R. Elliott, T. Gilliss, G. K. Giovanetti, M. P. Green, J. Gruszko, I. S. Guinn, V. E. Guiseppe, C. R. Haufe, R. J. Hegedus, L. Hehn, R. Henning, D. Hervas Aguilar, E. W. Hoppe, M. A. Howe, K. J. Keeter, M. F. Kidd, S. I. Konovalov, R. T. Kouzes, A. M. Lopez, R. D. Martin, R. Massarczyk, S. J. Meijer, S. Mertens, J. Myslik, G. Othman, W. Pettus, A. Piliounis, A. W. P. Poon, D. C. Radford, J. Rager, A. L. Reine, K. Rielage, N. W. Ruof, B. Shanks, M. Shirchenko, D. Tedeschi, R. L. Varner, S. Vasilyev, B. R. White, J. F. Wilkerson, C. Wiseman, W. Xu, E. Yakushev, C.-H. Yu, V. Yumatov, I. Zhitnikov, and B. X. Zhu. Multisite event discrimination for the majorana demonstrator. *Phys. Rev. C*, 99:065501, Jun 2019.

[95] I. Antcheva, M. Ballintijn, B. Bellenot, M. Biskup, R. Brun, N. Buncic, Ph. Canal, D. Casadei, O. Couet, V. Fine, L. Franco, G. Ganis, A. Gheata, D. Gonzalez Maline, M. Goto, J. Iwaszkiewicz, A. Kreshuk, D. Marcos Segura, R. Maunder, L. Moneta, A. Naumann, E. Offermann, V. Onuchin, S. Panacek, F. Rademakers, P. Russo, and M. Tadel. Root — a c++ framework for petabyte data storage, statistical analysis and visualization. *Computer Physics Communications*, 180(12):2499 – 2512, 2009. 40 YEARS OF CPC: A celebratory issue focused on quality software for high performance, grid and novel computing architectures.

[96] M. Frigo and S. G. Johnson. The design and implementation of fftw3. *Proceedings of the IEEE*, 93(2):216–231, Feb 2005.

[97] Leif Lonnblad. CLHEP: A project for designing a C++ class library for high-energy physics. *Comput. Phys. Commun.*, 84:307–316, 1994.

[98] S. Agostinelli, J. Allison, K. Amako, J. Apostolakis, H. Araujo, P. Arce, M. Asai, D. Axen, S. Banerjee, G. Barrand, F. Behner, L. Bellagamba, J. Boudreau, L. Broglia, A. Brunengo, H. Burkhardt, S. Chauvie, J. Chuma, R. Chytracek, G. Cooperman, G. Cosmo, P. Degtyarenko, A. Dell'Acqua, G. Depaola, D. Dietrich, R. Enami, A. Feliciello, C. Ferguson, H. Fesefeldt, G. Folger, F. Foppiano, A. Forti, S. Garelli, S. Giani, R. Giannitrapani, D. Gibin, J.J. Gómez Cadenas, I. González, G. Gracia Abril, G. Greeniaus, W. Greiner, V. Grichine, A. Grossheim, S. Guatelli, P. Gumplinger, R. Hamatsu, K. Hashimoto, H. Hasui, A. Heikkinen, A. Howard, V. Ivanchenko, A. Johnson, F.W. Jones, J. Kallenbach, N. Kanaya, M. Kawabata, Y. Kawabata, M. Kawaguti, S. Kelner, P. Kent, A. Kimura, T. Kodama, R. Kokoulin, M. Kossov, H. Kurashige, E. Lamanna, T. Lampén, V. Lara, V. Lefebure, F. Lei, M. Liendl, W. Lockman, F. Longo, S. Magni, M. Maire, E. Medernach, K. Minamimoto, P. Mora de Freitas, Y. Morita, K. Murakami, M. Nagamatu, R. Nartallo, P. Nieminen, T. Nishimura, K. Ohtsubo, M. Okamura, S. O'Neale, Y. Oohata, K. Paech, J. Perl, A. Pfeiffer, M.G. Pia, F. Ranjard, A. Rybin, S. Sadilov, E. Di Salvo, G. Santin, T. Sasaki, N. Savvas, Y. Sawada, S. Scherer, S. Sei, V. Sirotenko, D. Smith, N. Starkov, H. Stoecker, J. Sulkimo, M. Takahata, S. Tanaka, E. Tcherniaev, E. Safai Tehrani, M. Tropeano, P. Truscott, H. Uno, L. Urban, P. Urban, M. Verderi, A. Walkden, W. Wander, H. Weber, J.P. Wellisch, T. Wenaus, D.C. Williams, D. Wright, T. Yamada, H. Yoshida, and D. Zschiesche. Geant4—a simulation toolkit. *Nuclear Instruments and Methods in Physics Research Section A: Accelerators, Spectrometers, Detectors and Associated Equipment*, 506(3):250 – 303, 2003.

[99] M. A. Howe, G. A. Cox, P. J. Harvey, F. McGirt, K. Rielage, J. F. Wilkerson, and J. M. Wouters. Sudbury neutrino observatory neutral current detector acquisition software overview. *IEEE Transactions on Nuclear Science*, 51(3):878–883, June 2004.

[100] M. Agostini, J. A. Detwiler, P. Finnerty, K. Kröninger, D. Lenz, J. Liu, M. G. Marino, R. Martin, K. D. Nguyen, and L. Pandola. The MGDO software library for data analysis in Ge neutrinoless double-beta decay experiments. In *Journal of Physics Conference Series*, volume 375 of *Journal of Physics Conference Series*, page 042027, Jul 2012.

[101] M. Boswell, Y. Chan, J. A. Detwiler, P. Finnerty, R. Henning, V. M. Gehman, R. A. Johnson, D. V. Jordan, K. Kazkaz, M. Knapp, K. Kroninger, D. Lenz, L. Leviner, J. Liu, X. Liu, S. MacMullin, M. G. Marino, A. Mokhtarani, L. Pandola, A. G. Schubert, J. Schubert, C. Tomei, and O. Volynets. Mage-a geant4-based monte carlo application framework for low-background germanium experiments. *IEEE Transactions on Nuclear Science*, 58(3):1212–1220, June 2011.

[102] C. E. Aalseth, N. Abgrall, E. Aguayo, S. I. Alvis, M. Amman, I. J. Arnquist, F. T. Avignone, H. O. Back, A. S. Barabash, P. S. Barbeau, C. J. Barton, P. J. Barton, F. E. Bertrand, T. Bode, B. Bos, M. Boswell, A. W. Bradley, R. L. Brodzinski, V. Brudanin, M. Busch, M. Buuck, A. S. Caldwell, T. S. Caldwell, Y-D. Chan, C. D. Christofferson, P.-H. Chu, J. I. Collar, D. C. Combs, R. J. Cooper, C. Cuesta, J. A. Detwiler, P. J. Doe, J. A. Dunmore, Yu. Efremenko, H. Ejiri, S. R. Elliott, J. E. Fast, P. Finnerty, F. M. Fraenkle, Z. Fu, B. K. Fujikawa, E. Fuller, A. Galindo-Uribarri, V. M. Gehman, T. Gilliss, G. K. Giovanetti, J. Goett, M. P. Green, J. Gruszko, I. S. Guinn, V. E. Guiseppe, A. L. Hallin, C. R. Haufe, L. Hehn, R. Henning, E. W. Hoppe, T. W. Hossbach, M. A. Howe, B. R. Jasinski, R. A. Johnson, K. J. Keeter, J. D. Kephart, M. F. Kidd, A. Knecht, S. I. Konovalov, R. T. Kouzes, B. D. LaFerriere, J. Leon, K. T. Lesko, L. E. Leviner, J. C. Loach, A. M. Lopez, P. N. Luke, J. MacMullin, S. MacMullin, M. G. Marino, R. D. Martin, R. Massarczyk, A. B. McDonald, D.-M. Mei, S. J. Meijer, J. H. Merriman, S. Mertens, H. S. Miley, M. L. Miller, J. Myslik, J. L. Orrell, C. O'Shaughnessy, G. Othman, N. R. Overman, G. Perumpilly, W. Pettus, D. G. Phillips, A. W. P. Poon, K. Pushkin, D. C. Radford, J. Rager, J. H. Reeves, A. L. Reine, K. Rielage, R. G. H. Robertson, M. C. Ronquest, N. W. Ruof, A. G. Schubert, B. Shanks, M. Shirchenko, K. J. Snavely, N. Snyder, D. Steele, A. M. Suriano, D. Tedeschi, W. Tornow, J. E. Trimble, R. L. Varner, S. Vasilyev, K. Vetter, K. Vorren, B. R. White, J. F. Wilkerson, C. Wiseman, W. Xu, E. Yakushev, H. Yaver, A. R. Young, C. H. Yu, V. Yumatov, I. Zhitnikov, B. X. Zhu, and S. Zimmermann. Search for neutrinoless double-β decay in ^{76}Ge with the majorana demonstrator. *Phys. Rev. Lett.*, 120:132502, Mar 2018.

[103] S. I. Alvis et al. A Search for Neutrinoless Double-Beta Decay in ^{76}Ge with 26 kg-yr of Exposure from the MAJORANA DEMONSTRATOR. *Phys. Rev. Lett. (submitted)*, 2019.

[104] Gary J. Feldman and Robert D. Cousins. Unified approach to the classical statistical analysis of small signals. *Phys. Rev. D*, 57:3873–3889, Apr 1998.

[105] N. Abgrall, A. Abramov, N. Abrosimov, I. Abt, M. Agostini, M. Agartioglu, A. Ajjaq, S. I. Alvis, F. T. Avignone, X. Bai, M. Balata, I. Barabanov, A. S. Barabash, P. J. Barton, L. Baudis, L. Bezrukov, T. Bode, A. Bolozdynya, D. Borowicz, A. Boston, H. Boston, S. T. P. Boyd, R. Breier, V. Brudanin, R. Brugnera, M. Busch, M. Buuck, A. Caldwell, T. S. Caldwell, T. Camellato, M. Carpenter, C. Cattadori, J. Cederkäll, Y.-D. Chan, S. Chen, A. Chernogorov, C. D. Christofferson, P.-H. Chu, R. J. Cooper, C. Cuesta, E. V. Demidova, Z. Deng, M. Deniz, J. A. Detwiler, N. Di Marco, A. Domula, Q. Du, Yu. Efremenko, V. Egorov, S. R. Elliott, D. Fields, F. Fischer, A. Galindo-Uribarri, A. Gangapshev, A. Garfagnini, T. Gilliss, M. Giordano, G. K. Giovanetti, M. Gold, P. Golubev, C. Gooch, P. Grabmayr, M. P. Green, J. Gruszko, I. S. Guinn,

V. E. Guiseppe, V. Gurentsov, Y. Gurov, K. Gusev, J. Hakenmüeller, L. Harkness-Brennan, Z. R. Harvey, C. R. Haufe, L. Hauertmann, D. Heglund, L. Hehn, A. Heinz, R. Hiller, J. Hinton, R. Hodak, W. Hofmann, S. Howard, M. A. Howe, M. Hult, L. V. Inzhechik, J. Janicskó Csáthy, R. Janssens, M. Ješkovský, J. Jochum, H. T. Johansson, D. Judson, M. Junker, J. Kaizer, K. Kang, V. Kazalov, Y. Kermadic, F. Kiessling, A. Kirsch, A. Kish, A. Klimenko, K. T. Knöpfle, O. Kochetov, S. I. Konovalov, I. Kontul, V. N. Kornoukhov, T. Kraetzschmar, K. Kröninger, A. Kumar, V. V. Kuzminov, K. Lang, M. Laubenstein, A. Lazzaro, Y. L. Li, Y.-Y. Li, H. B. Li, S. T. Lin, M. Lindner, I. Lippi, S. K. Liu, X. Liu, J. Liu, D. Loomba, A. Lubashevskiy, B. Lubsandorzhiev, G. Lutter, H. Ma, B. Majorovits, F. Mamedov, R. D. Martin, R. Massarczyk, J. A. J. Matthews, N. McFadden, D.-M. Mei, H. Mei, S. J. Meijer, D. Mengoni, S. Mertens, W. Miller, M. Miloradovic, R. Mingazheva, M. Misiaszek, P. Moseev, J. Myslik, I. Nemchenok, T. Nilsson, P. Nolan, C. O'Shaughnessy, G. Othman, K. Panas, L. Pandola, L. Papp, K. Pelczar, D. Peterson, W. Pettus, A. W. P. Poon, P. P. Povinec, A. Pullia, X. C. Quintana, D. C. Radford, J. Rager, C. Ransom, F. Recchia, A. L. Reine, S. Riboldi, K. Rielage, S. Rozov, N. W. Rouf, E. Rukhadze, N. Rumyantseva, R. Saakyan, E. Sala, F. Salamida, V. Sandukovsky, G. Savard, S. Schönert, A.-K. Schütz, O. Schulz, M. Schuster, B. Schwingenheuer, O. Selivanenko, B. Sevda, B. Shanks, E. Shevchik, M. Shirchenko, F. Simkovic, L. Singh, V. Singh, M. Skorokhvatov, K. Smolek, A. Smolnikov, A. Sonay, M. Spavorova, I. Stekl, D. Stukov, D. Tedeschi, J. Thompson, T. Van Wechel, R. L. Varner, A. A. Vasenko, S. Vasilyev, A. Veresnikova, K. Vetter, K. von Sturm, K. Vorren, M. Wagner, G.-J. Wang, D. Waters, W.-Z. Wei, T. Wester, B. R. White, C. Wiesinger, J. F. Wilkerson, M. Willers, C. Wiseman, M. Wojcik, H. T. Wong, J. Wyenberg, W. Xu, E. Yakushev, G. Yang, C.-H. Yu, Q. Yue, V. Yumatov, J. Zeman, Z. Zeng, I. Zhitnikov, B. Zhu, D. Zinatulina, A. Zschocke, A. J. Zsigmond, K. Zuber, and G. Zuzel. The large enriched germanium experiment for neutrinoless double beta decay (legend). *AIP Conference Proceedings*, 1894(1):020027, 2017.

[106] Graham K. Giovanetti. *P-Type Point Contact Germanium Detectors and Their Application in Rare-Event Searches*. PhD thesis, University of North Carolina, 2015.

[107] M. Buuck. Background model fitting and transition layer modeling. Majorana Collaboration Meeting, Mar. 5-7 2018.

[108] O. A. Ponkratenko, V. I. Tretyak, and Yu. G. Zdesenko. Event generator decay4 for simulating double-beta processes and decays of radioactive nuclei. *Physics of Atomic Nuclei*, 63(7):1282–1287, Jul 2000.

[109] Balraj Singh. Nuclear data sheets update for a = 76. *Nuclear Data Sheets*, 74(1):63 – 164, 1995.

[110] Robley D. Evans. *The Atomic Nucleus*, chapter 6, page 240. International series in pure and applied physics. McGraw-Hill, New York, 1955.

[111] Micah Buuck. *A Comprehensive Radiogenic Background Model for the MAJORANA DEMONSTRATOR*. PhD thesis, University of Washington, 2019.

[112] Pavol Vojtyla. Fast computer simulations of background of low-level ge γ-spectrometers induced by ^{210}pb^{210}bi in shielding lead. *Nuclear Instruments and Methods in Physics Research Section B: Beam Interactions with Materials and Atoms*, 117(1):189 – 198, 1996.

[113] A Reine, T Caldwell, C Cuesta, I Guinn, and J Myslik. Run selection and data cleaning of ds5 (m1 and m2) (internal). Technical Report 2017-020, University of North Carolina at Chapel Hill, May 2018.

[114] F. James. MINUIT Function Minimization and Error Analysis: Reference Manual Version 94.1. Technical Report CERN-D506, CERN CN Division, Geneva, 1994.

[115] P. Chu, J. Detwiler, and I. Guinn. Energy systematic of MAJORANA DEMONSTRATOR. Technical Report 2017-021, Los Alamos National Laboratory, Oct 2017.

[116] H. Akaike. A new look at the statistical model identification. *IEEE Transactions on Automatic Control*, 19(6):716–723, December 1974.

[117] Wolfgang A. Rolke, Angel M. López, and Jan Conrad. Limits and confidence intervals in the presence of nuisance parameters. *Nuclear Instruments and Methods in Physics Research Section A: Accelerators, Spectrometers, Detectors and Associated Equipment*, 551(2):493 – 503, 2005.

[118] Pekka Pirinen and Jouni Suhonen. Systematic approach to β and $2\nu\beta\beta$ decays of mass $a = 100 - -136$ nuclei. *Phys. Rev. C*, 91:054309, May 2015.

[119] A. Bakalyarov, A. Balysh, A. S. Barabash, P. Beneš, Ch. Briançon, V. Brudanin, P. Čermák, V. Egorov, F. Hubert, Ph. Hubert, N. A. Korolev, V. N. Kosjakov, A. Kovalik, N. A. Lebedev, V. I. Lebedev, A. F. Novgorodov, N. I. Rukhadze, N. I. Štekl, V. V. Timkin, I. E. Veleshko, Ts. Vylov, and V. I. Umatov. Improved limits on β- and β-β- decays of 48ca. *Journal of Experimental and Theoretical Physics Letters*, 76(9):545–547, Nov 2002.

[120] J. W. Beeman, F. Bellini, P. Benetti, L. Cardani, N. Casali, D. Chiesa, M. Clemenza, I. Dafinei, S. Di Domizio, F. Ferroni, L. Gironi, A. Giuliani, C. Gotti, M. Laubenstein, M. Maino, S. Nagorny, S. Nisi, C. Nones, F. Orio, L. Pagnanini, L. Pattavina,

G. Pessina, G. Piperno, S. Pirro, E. Previtali, C. Rusconi, K. Schäffner, C. Tomei, and M. Vignati. Double-beta decay investigation with highly pure enriched ^{82}se for the lucifer experiment. *The European Physical Journal C*, 75(12):591, Dec 2015.

[121] S. W. Finch and W. Tornow. Search for two-neutrino double-β decay of ^{96}Zr to excited states of ^{96}Mo. *Phys. Rev. C*, 92:045501, Oct 2015.

[122] A. Piepke, M. Beck, J. Bockholt, D. Glatting, G. Heusser, H.V. Klapdor-Kleingrothaus, B. Maier, F. Petry, U. Schmidt-Rohr, H. Strecker, M. Völlinger, A.S. Barabash, V.I. Umatov, A. Müller, and J. Suhonen. Investigation of the $\beta\beta$ decay of 116cd into excited states of 116sn. *Nuclear Physics A*, 577(3):493 – 510, 1994.

[123] CUORE Collaboration, C. Alduino, K. Alfonso, D. R. Artusa, III Avignone, F. T., O. Azzolini, T. I. Banks, G. Bari, J. W. Beeman, and F. Bellini. Double-beta decay of ^{130}Te to the first 0^+ excited state of ^{130}Xe with CUORE-0. *arXiv e-prints*, page arXiv:1811.10363, Nov 2018.

[124] K. Asakura et al. Search for double-beta decay of ^{136}Xe to excited states of ^{136}Ba with the KamLAND-Zen experiment. *Nucl. Phys.*, A946:171–181, 2016.

[125] Simon Duane, A.D. Kennedy, Brian J. Pendleton, and Duncan Roweth. Hybrid monte carlo. *Physics Letters B*, 195(2):216 – 222, 1987.

[126] Radford M. Neal. MCMC using Hamiltonian dynamics. *arXiv e-prints*, page arXiv:1206.1901, Jun 2012.

[127] Mark Girolami and Ben Calderhead. Riemann manifold langevin and hamiltonian monte carlo methods. *Journal of the Royal Statistical Society: Series B (Statistical Methodology)*, 73(2):123–214, 2011.

[128] R. B. Oberer, C. A. Gunn, L. G. Chiang, R. E. Valiga, and J. A. Cantrell. Small-angle compton scattering to determine the depth of a radioactive source in matter. Technical Report RP 900000-0006, Oak Ridge Y-12 Plant (Y-12), Oak Ridge, TN, 4 2011.

[129] F. Alessandria, R. Ardito, D. R. Artusa, III Avignone, F. T., O. Azzolini, M. Balata, T. I. Banks, G. Bari, J. Beeman, F. Bellini, A. Bersani, M. Biassoni, T. Bloxham, C. Brofferio, C. Bucci, X. Z. Cai, L. Canonica, X. Cao, S. Capelli, L. Carbone, L. Cardani, M. Carrettoni, N. Casali, D. Chiesa, N. Chott, M. Clemenza, C. Cosmelli, O. Cremonesi, R. J. Creswick, I. Dafinei, A. Dally, V. Datskov, A. De Biasi, M. M. Deninno, S. Di Domizio, M. L. di Vacri, L. Ejzak, R. Faccini, D. Q. Fang, H. A. Farach, M. Faverzani, G. Fernandes, E. Ferri, F. Ferroni, E. Fiorini, M. A. Franceschi, S. J. Freedman, B. K. Fujikawa, A. Giachero, L. Gironi, A. Giuliani, J. Goett, P. Gorla,

C. Gotti, E. Guardincerri, T. D. Gutierrez, E. E. Haller, K. Han, K. M. Heeger, H. Z. Huang, R. Kadel, K. Kazkaz, G. Keppel, L. Kogler, Yu. G. Kolomensky, D. Lenz, Y. L. Li, C. Ligi, X. Liu, Y. G. Ma, C. Maiano, M. Maino, M. Martinez, R. H. Maruyama, Y. Mei, N. Moggi, S. Morganti, T. Napolitano, S. Newman, S. Nisi, C. Nones, E. B. Norman, A. Nucciotti, T. O'Donnell, F. Orio, D. Orlandi, J. L. Ouellet, M. Pallavicini, V. Palmieri, L. Pattavina, M. Pavan, M. Pedretti, G. Pessina, G. Piperno, S. Pirro, E. Previtali, V. Rampazzo, F. Rimondi, C. Rosenfeld, C. Rusconi, E. Sala, S. Sangiorgio, N. D. Scielzo, M. Sisti, A. R. Smith, F. Stivanello, L. Taffarello, M. Tenconi, W. D. Tian, C. Tomei, S. Trentalange, G. Ventura, M. Vignati, B. S. Wang, H. W. Wang, T. Wise, A. Woodcraft, L. Zanotti, C. Zarra, B. X. Zhu, and S. Zucchelli. Sensitivity and Discovery Potential of CUORE to Neutrinoless Double-Beta Decay. *arXiv e-prints*, page arXiv:1109.0494, Sep 2011.

Appendix A

PEAK SHAPE DESCRIPTION AND MEASUREMENT

A.1 Peak Shape Function and Parameters

A moneenergetic energy peak in the MAJORANA DEMONSTRATOR is typically modelled using the following peakshape function

$$
\begin{aligned}
\mathrm{PS}(E; A, \mu, \sigma, f_{tail}, \tau, h_{step}) = A\big((1 - f_{tail})\mathrm{Gaus}(E; \mu, \sigma) \\
+ f_{tail} \cdot \mathrm{ExGaus}(E; \mu, \sigma, \tau) \\
+ \frac{h_{step}}{2}\mathrm{erfc}(\frac{E - \mu}{\sqrt{2}\sigma})\big)
\end{aligned}
\tag{A.1}
$$

where A is the total area of the peak. The peak shape consists of a Gaussian component:

$$
\mathrm{Gaus}(E; \mu, \sigma) = \frac{1}{\sqrt{2\pi\sigma^2}}\exp(-\frac{(E - \mu)^2}{2\sigma^2})
\tag{A.2}
$$

and a low energy (LE) tail, defined as an exponentially modified Gaussian (exGaus) component:

$$
\mathrm{ExGaus}(E; \mu, \sigma, \tau) = \frac{1}{2|\tau|}\mathrm{erfc}(\mathrm{sgn}(\tau)\frac{(E - \mu) + \frac{\sigma^2}{\tau}}{\sqrt{2}\sigma})\exp(\frac{E - \mu}{\tau} + \frac{\sigma^2}{\tau^2})
\tag{A.3}
$$

σ represents the gaussian width, τ represents the length of the LE tail, and f_{tail} represents the fraction of the peak contained in the LE tail. Note that this formulation of the ExGaus function allows for negative values of τ, resulting in a high energy tail instead of a low energy tail. These three parameters combine to define the width of the peak, while μ represents the mean of the Gaussian component; note that the mean of the peak as a whole will be lower due to the LE tail. The LE tail originates from position dependant factors in the detectors that cause energy loss, including charge trapping and transition layers. Finally, the peak shape contains a step component, described by the complementary error function (erfc), where h_{step} defines the fraction of the peak amplitude that appears in the step. The
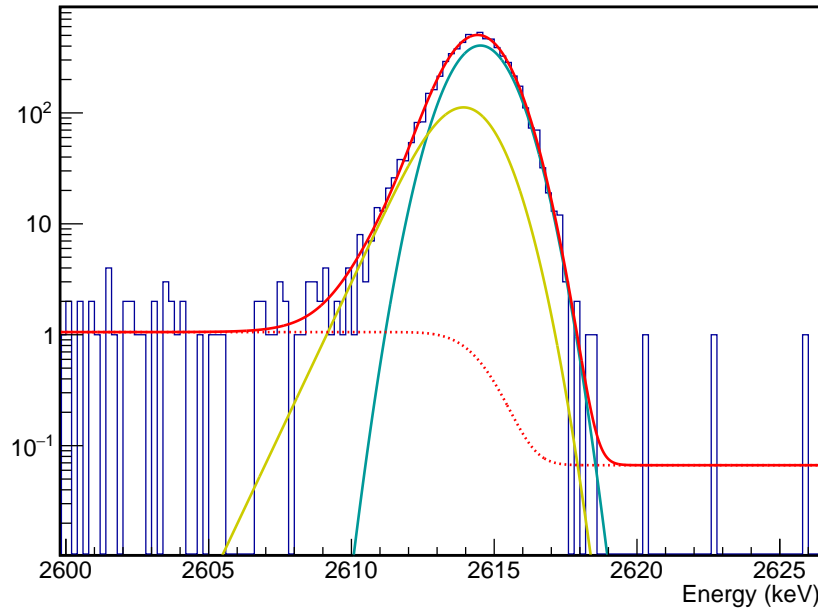
Figure A.1: A 2614 keV calibration peak fitted to the peakshape function described by equation A.1. The Gaussian component is shown in teal, the low energy tail in gold, the step in dashed red, and the combined peak shape in red.

step is caused by factors that cause enough energy loss to pull events entirely out of the peak, such as low angle scattering of a γ before entering a detector and detector transition layers. Events in the step component are not considered part of the full energy peak, and the step is primarily a factor for calibration events which must pass through the copper cryostat which is not true of events that originate in the detectors. For this reason, the step is not considered when optimizing the signal ROI. The peak shape function is shown in Figure A.1. This peak shape function can be optionally extended with the addition of a high energy tail

as follows:

$$\begin{aligned}
\text{PS}(E; A, \mu, \sigma, f_{LT}, \tau_{LT}, f_{HT}, \tau_{HT}, h_{step}) = A\big((1 - f_{LT} - f_{HT})\text{Gaus}(E; \mu, \sigma) \\
+ f_{LT} \cdot \text{ExGaus}(E; \mu, \sigma, \tau_{LT}) \\
+ f_{HT} \cdot \text{ExGaus}(E; \mu, \sigma, -\tau_{HT}) \\
+ \frac{h_{step}}{2}\text{erfc}(\frac{E - \mu}{\sqrt{2}\sigma}))
\end{aligned} \tag{A.4}$$

Typically, no high energy tail is used, meaning $f_{HT} = 0$. A high energy tail is necessary only if an abnormal peakshape appears. This can occur if the energy filter parameters are mis-set, or if peaks other than full energy γ peaks are being fit, as is the case in Section 4.2.4, where the single- and double-escape peaks are used.

A simultaneous fit of many peaks in a calibration spectrum is performed in order to define the peak shape parameters at all energies. The peak shape parameters are defined as independant functions of energies and several hyperparameters as follows

- A is independant of energy, since it depends on the relative intensities and the different detection efficiencies of each γ.

- μ is also independant of energy. μ is ostensibly linear with respect to energy; however, due to local and global energy nonlinearities, in order to avoid systematic errors in the other peak shape parameters, this parameter is treated as independant.

- σ is defined as follows

$$\sigma(E) = \sqrt{\sigma_0^2 + \sigma_1^2 E + \sigma_2^2 E^2} \tag{A.5}$$

σ_0 arises primarily from electronic noise. σ_1 arises primarily from the Fano factor F, and is ostensibly

$$\sigma_1^2 = (2.35)^2 F \epsilon E \tag{A.6}$$

where $F = 0.08$ and $\epsilon = 2.96$ eV is the electron-hole production energy. In actuality, other factors also contribute to σ_1, so it is measured to be larger than expected. σ_2

arises from a variety of systematic energy uncertainties, including charge trapping, gain drift and small errors in energy calculation.

- f_{tail} is defined to be constant with respect to energy.

- τ is defined as linear with respect to energy

$$\tau(E) = \tau_0 + \tau_1 \tag{A.7}$$

τ_1 arises primarily from charge trapping and transition layer events, each of which cause charge loss. τ_0, while expected to be zero, is necessary in order to obtain a strong fit result.

- h_{step} is defined as

$$h_{step}(E) = \frac{h_0}{E^2} + h_1 E^{-0.88} \tag{A.8}$$

The inverse square term arises from low angle scattering of γs as they approach the detector. The second power law term arises from transition layer events, and the power of -0.88 was empirically measured in simulations and data. This model is described in greater detail in Section A.4.

The fit result of a simultaneous fit of 18 peaks from a 6 hour long ^{228}Th calibration run is shown in Figure A.2.

A.2 Performing a Simultaneous Fit

Because of the large number of fit parameters ($\sim$35 parameters are used for weekly calibrations and $\sim$100 parameters are used with high statistics calibrations to perform more detailed characterizations of parameters), and because of the highly correlated nature of some of the parameters, the fit result is heavily dependant on the initial parameter guess. To ensure convergence on the global minimum of the negative log-likelihood in a timely manner, Hamiltonian Monte Carlo (HMC) is used[125][126]. HMC is a Markov Chain Monte Carlo
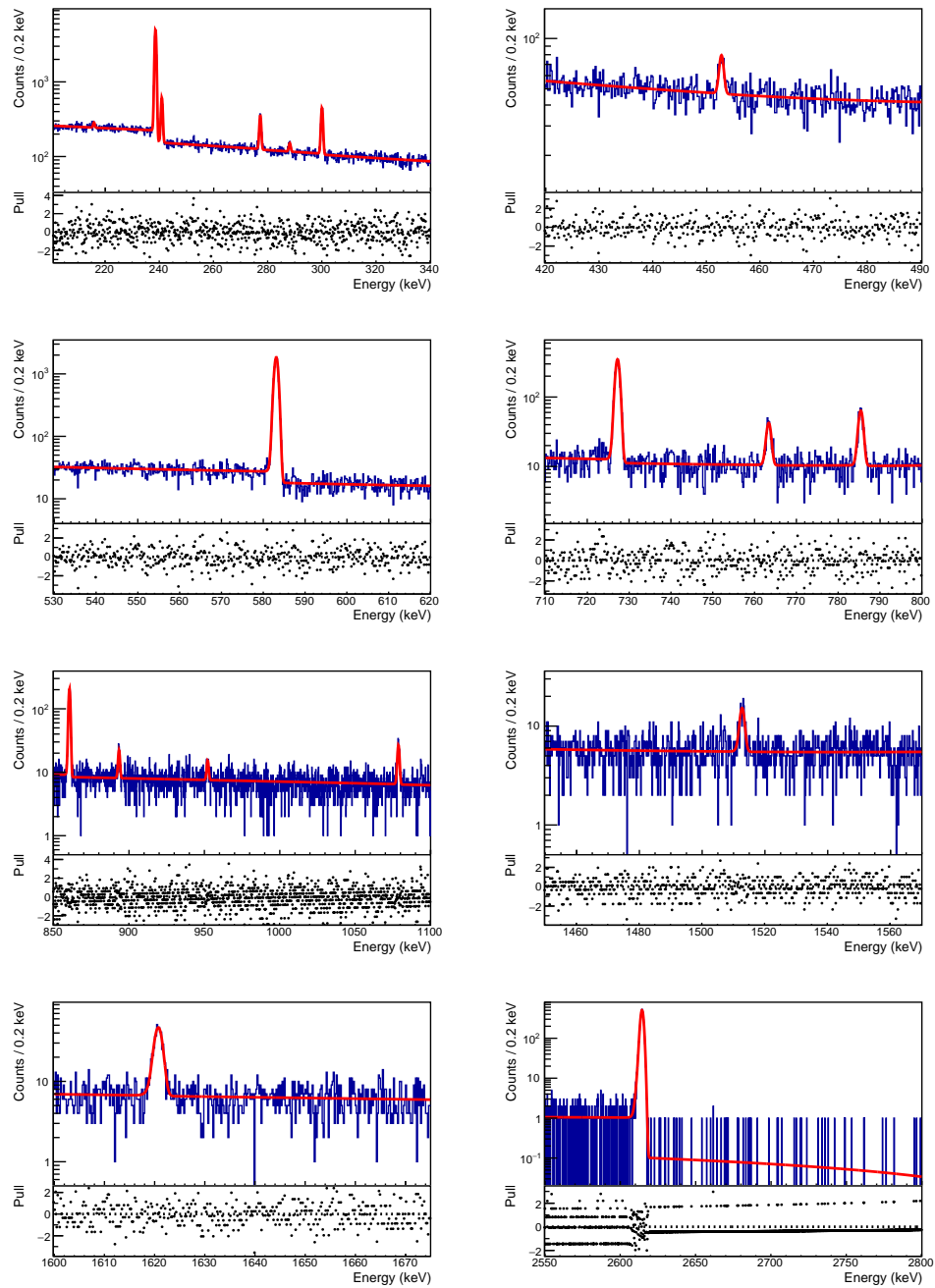
Figure A.2: A simultaneous fit of 18 peaks from a 6 hour long ^{228}Th calibration run)

(MCMC) technique that uses the parameter gradient of the negative log-likelihood in order to take large steps through the parameter space with a high acceptance rate. Several adaptations to the step sizes are applied, which prevent the algorithm used from exactly converging to the posterior described by the log-likelihood with a flat prior. First, the step size is increased by a factor of 1.1 after each successful step and decreased by a factor of 1.2 after each unsuccessful step. This adaptation asymptotically results in an acceptance rate of $\sim 2/3$, a target suggested by [126]. Second, the mass scale matrix is adapted to equal the diagonal elements of the Fisher information metric between each step. This adaptation is based on Riemann Manifold HMC[127], although it does not properly evolve the metric between steps and will therefore fail to converge exactly. The combination of these adaptations results in a quick and reliable convergence that approximates the posterior, and is very useful as a burn-in when fitting. The adaptations above are combined are run over 200 HMC steps, using the leapfrog algorithm with 50 leapfrog steps for each HMC step. In addition, the evaluation of the parameter gradient of the negative log-likelihood is performed analytically, which helps to speed up evaluation and ensure reliability.

After this HMC burn in is performed, the minimum negative log-likelihood sample is used as an initial parameter guess for a gradient descent fit. The Minuit fitting package is used to perform this fit[114]. Minuit evaluates for the parameters that maximize the likelihood and uses the Hessian matrix to obtain a covariance matrix. This result is used to obtain the values and errors of the calibration parameters.

A.3   Computing Auxiliary Parameters

In addition to the bare parameters used to describe this peakshape model, other auxiliary parameters are often useful to calculate when using this model to characterize detectors. Examples of such parameters include the values of the individual peakshape parameters for an arbitrary peak energy, and other parameters that can be derived from the peakshape function such as the peak centroid or full width at half max (FWHM). The peak centroid

is used for the first stage of calibration and the FWHM is used when optimizing the ROI for a peak. It is not ideal to numerically compute these parameters directly from the data, because such a measurement would be biased by the background or by the step component of the peakshape, which is not intrisic to the detectors. To do this, first we calculate the value of the detector-intrisic peak shape parameters (i.e. μ, σ, f_{LE}, τ_{LE}, f_{HE} and τ_{HE} at the desired energy using the functions used to describe each parameter. From here, derived parameters can be calculated; for example, the centroid is

$$\text{cen}(\mu, \sigma, f_{LE}, \tau_{LE}, f_{HE}, \tau_{HE}) = \mu - f_{LE} \cdot \tau_{LE} + f_{HE} \cdot \tau_{HE} \qquad (A.9)$$

and the FWHM is numerically calculated by finding the half max energies and taking the difference between them, assuming no background and no step. The uncertainties on these parameters is computed from the covariance matrix. For parameter θ:

$$\sigma_\theta^2 = \sum_{i=0}^{N} \sum_{j=0}^{N} \frac{\partial \theta}{\partial p_i} \Sigma_{i,j} \frac{\partial \theta}{\partial p_j} \qquad (A.10)$$

where p_i are the set of model parameters.

A.4   The Step Height Model

The dependancy of the step height on energy is described by

$$h_{step}(E) = \frac{h_0}{E^2} + h_1 E^{-h_2} \qquad (A.11)$$

The inverse square component arises from low angle scattering of γs as they approach the detectors. This inverse square dependence can be analytically derived by taking the Compton scattering differential cross section in the limit as scattering angle approaches 0[128]. h_0 increases linearly with the thickness of shielding between the source and the detector. As a result, the model parameters measured are valid only for γs from the calibration source; peaks generated by other sources may have different steps, and peaks generated from a source internal to the detector would be expected to measure $h_0 = 0$.
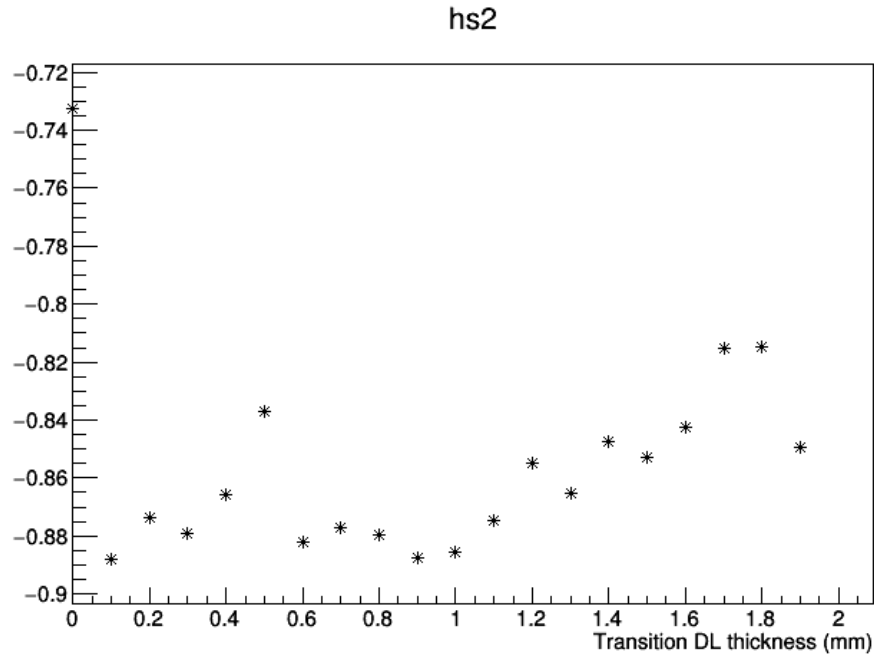
Figure A.3: Values of h_2 from the step height model measured using a simultaneous peak fit for simulations of the ^{228}Th calibration source using different transition layer thicknesses.

The second power law term arises from the transition layer of the detectors. Because of this model is nonlinear, floating the power parameter results in unreliable fitting for the standard 90-minute calibration runs, so h_2 is empirically measured using both data and simulations to be -0.88. Many simulations of the ^{228}Th calibration source were run using the dead layer model described in equation 3.1, and the thickness of the transition layer varied between 0 and 2 mm. For each simulation, a simultaneous fit of many peaks was performed, floating all of the step height parameters. The values of h_2 measured are shown in Figure A.3, and have a stable value of -0.88 for dead layer thickness of < 1 mm. Typical dead layer thicknesses for detectors are ~ 0.5 mm. To measure this parameter from data, many peaks in a long calibration run were used. A fit was then performed for each detector, floating h_2 and fixing h_0. The value of h_0 is fixed to a value extracted from a fit of a calibration simulation that does not include the dead layer. The values of h_2 were measured from simultaneous fits of the
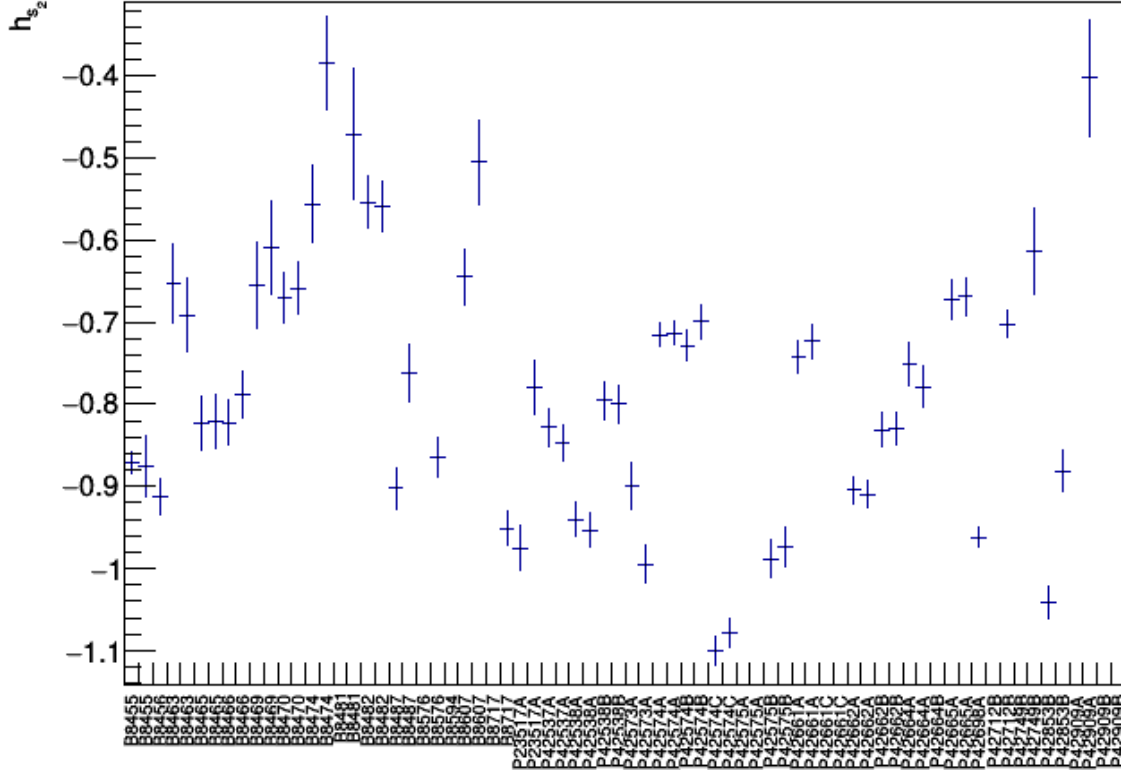
Figure A.4: Values of h_2 from the step height model measured using a simultaneous peak fit of the measured ^{228}Th calibration spectrum. h_0 was fixed to values measured from simulations.

spectrum measured for each detector in a long calibration run, and are shown in Figure A.4. The measured values have large systematic uncertainties that are not accounted for in the fits, but the mean is consistent with the value of -0.88 measured using the simulations.

A.5 GAT Implementation

Implementations of the peak shape function, the parameter gradient of the peak shape function, the CDF of the peak shape function, and functions calculating various auxillary parameters such as the FWHM, centroid and standard deviation are included in `GATPeakShapeUtil.hh`.

Implementation of an energy range with a single peak on top of a quadratic background, along with tools for fitting this energy region are included in `GATPeakShape.hh`. Implementation of an energy region with multiple peaks included, with the peakshape parameters determined by functions of energy and various hyperparameters are included in `GATMultiPeakRegion.hh`. Implementation of the multi peak fitter, which manages many `GATMultiPeakRegion`s and the various parameter functions and hyperparameters, as well as many tools for computing auxiliary parameters at various energies, are included in `GATMultiPeakFitter.hh`. Implementation of a combined likelihood function to be used for simultaneous fitting is included in `GATGlobalFitFCN.hh`. Implementation of the HMC algorithm described in Section A.2 is contained in `GATHybridMonteCarlo.hh`.

Appendix B

SENSITIVITY AND DISCOVERY POTENTIAL

When performing rare event searches in the presence of backgrounds, it is often useful to select regions of interest and data cleaning cuts that optimize the experimental sensitivity. Median n-σ count sensitivity, $\hat{S}(\overline{B}, n_\sigma)$ is defined as the median upper limit of an n-σ confidence interval on the number of observed signal counts, assuming the presence of no signal and backgrounds sampled from a distribution based on measured background level $\overline{B}$. A similar quantity, n-σ discovery sensitivity, is defined as the true strength of a signal that would produce a discovery with significance n-σ 50% of the time. Unlike median sensitivity, discovery sensitivity accounts for the distribution in the number of counts that would be seen based on the true rate. For this reason, discovery sensitivity is a slightly more useful quantity when projecting or optimizing an experiment's sensitivity, even though median (or mean) sensitivity is the quantity that is usually reported. For the purpose of this appendix, we will focus on discovery sensitivity.

The sensitivity of the experiment to the total rate of the process being searched for is

$$\hat{\Gamma}(\overline{B}, \epsilon, n_\sigma) \propto \frac{\hat{S}(\overline{B}, n_\sigma)}{\epsilon} \tag{B.1}$$

where ϵ is the total detection efficiency of the signal being sought. Optimizing event selection for a search requires balancing the tradeoff between reducing backgrounds, which will decrease $\hat{S}(\overline{B})$, and improving signal detection efficiency.

When optimizing a search, it is useful to use certain approximations when calculating sensitivity. In the high background limit, a common approximation is to assume the backgrounds measured will have a gaussian distribution with standard deviation of $\sqrt{\overline{B}}$. In this

case, the discovery (and median) sensitivity will be

$$\hat{S}(\overline{B}, n_\sigma) = n_\sigma * \sqrt{\overline{B}} \tag{B.2}$$

This approximation fails, however, in the low background limit, where a better approximation is that the background will instead be sampled from a Poisson distribution with mean counts $\overline{B}$. Because the Poisson distribution is a PDF over a discrete variable, the resultent sensitivity will have step-like properties and must be solved for using a toy Monte Carlo, properties that are not ideal for performing sensitivity optimizations. For this reason, when computing the sensitivity we instead use the analytic continuation of the CDF of the poisson distribution, which is the lower incomplete gamma function

$$\gamma(s, x) = \frac{1}{\Gamma(s)} \int_0^x t^{s-1} e^{-t} dt \tag{B.3}$$

In this case, we can find the sensitivity, by first numerically solving for the number of counts required for an n-sigma discovery, $\hat{N}$, with expected backgrounds $\overline{B}$, where

$$\gamma(\hat{N} + 1, \overline{B}) = \text{erfc}(\frac{n_\sigma}{\sqrt{2}}) \tag{B.4}$$

To get the median sensitivity, we then numerically solve

$$\gamma(\hat{N} + 1, \overline{B} + \hat{S}) = 0.5 \tag{B.5}$$

We define the function found by solving these equations to be the discovery potential[129],

$$\hat{S}(\overline{B}, n_\sigma) = \text{DP}(\overline{B}, n_\sigma) \tag{B.6}$$

For the purposes of this dissertation, we always use the 3-sigma discovery potential

$$\text{DP}(\overline{B}) = \text{DP}(\overline{B}, 3) \tag{B.7}$$

Figure B.1 shows a comparison of the gaussian approximation for sensitivity to the discovery potential. This function is implemented in `GATPeakShapeUtils.hh` as `GATPeakShapeFunction::DiscoveryLimit`.
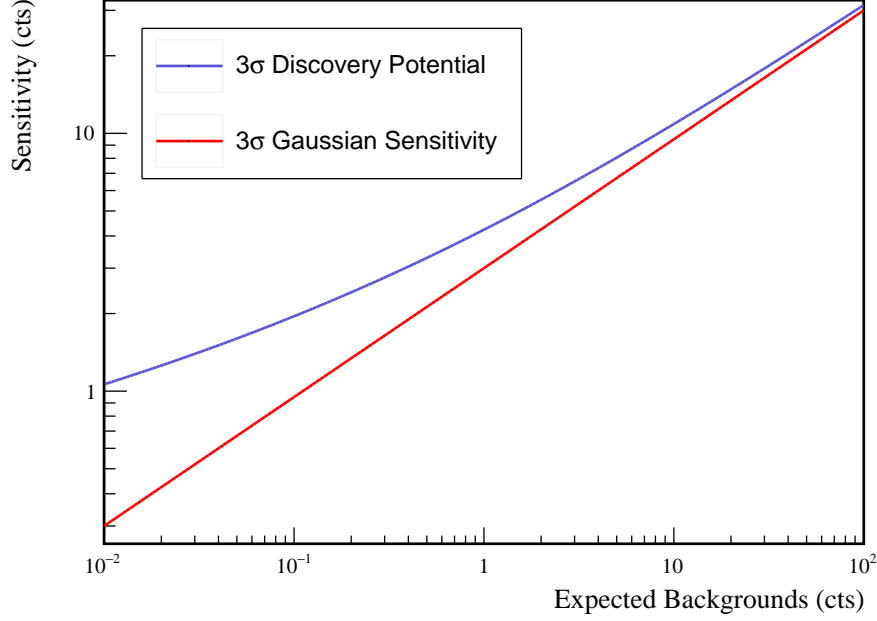
Figure B.1: A comparison of the Gaussian approximation for sensitivity and the discovery potential as a function of expected background level. Note that in the high background limit, both formulations for sensitivity converge, as expected.

Next, we want to figure out how we will use these quantities to optimize our data selection. To determine whether it is worth adding a cut or modifying a cut, consider the efficiency and expected background counts before and after applying the cut (ϵ_i, $\overline{B}_i$ and ϵ_f, $\overline{B}_f$, respectively). A cut represents an improvement if

$$\frac{\hat{S}(\overline{B}_f)}{\epsilon_f} < \frac{\hat{S}(\overline{B}_i)}{\epsilon_i} \tag{B.8}$$

Rearranging this, we get

$$\frac{\Delta \hat{S}(\overline{B})}{\hat{S}(\overline{B}_i)} < \frac{\Delta \epsilon}{\epsilon_i} \tag{B.9}$$

If we assume that a small number of events are cut, we can Taylor expand:

$$\frac{\partial \hat{S}}{\partial \overline{B}} \frac{\Delta \overline{B}}{\hat{S}(\overline{B})} < \frac{\Delta \epsilon}{\epsilon} \tag{B.10}$$

$$\frac{\partial \log\left(\hat{S}\right)}{\partial \log\left(\overline{B}\right)} > \frac{\text{False Positive Rate}}{\text{True Positive Rate}} \tag{B.11}$$

Looking at figure B.1, we see that in the high background limit, using the Gaussian sensitivity approximation we will draw the same conclusion about whether or not a cut is worth applying regardless of the absolute background level. A cut is worth applying as long as the true positive rate of the cut is twice the true negative rate. On the other hand, in the low background limit, this is not the case; instead, as we approach zero background, we will be less aggressive in cutting events. For this reason, experiments approaching the background free limit will use wider regions of interest in peak searches.

Appendix C

THE Majorana Demonstrator EVENT BUILDER

The primary purpose of the Majorana Demonstrator's event builder is to convert raw data files produced by ORCA into built files to be used in the next stages of analysis. Built files use the .root file format, which is compatible with the root analysis framework. Data is stored in these files as data objects from the Majorana Gerda Data Objects (MGDO) library. The data is stored as events, which contain multiple waveforms and associated digitizer data such as energy and time that take place close together. The event builder is responsible for combining individual data packets into events. In addition, the event builder performs many basic data quality checks, or garbage checks.

C.1 Built File Contents

A built file is a ROOT file, which is written and read by the ROOT analysis framework. ROOT files offer several advantages for storing large quantities of data: they enable relatively simple interfacing with C++libraries, they are robust under schema evolution, and they handle data compression automatically. Data is stored primarily in TTrees, which are buffers containing a large number of same-class C++objects. The contents of the MJD built files will be described in this section.

MGTree: A TTree containing Germanium detector data. The tree has the following two branches:

  run contains MJTRun objects which hold basic run data such as run number and start and stop times.

event contains MGTEvent objects, which contain the individual waveforms and associated digitizer data and data about the event as a whole.

MGGarbageTree: A TTree containing Germanium detector data that has failed data quality checks. The tree has the following three branches:

run contains MJTRun objects which hold basic run data such as run number and start and stop times.

event contains MGTEvent objects, which contain the individual waveforms and associated digitizer data and data about the event as a whole.

garbageCode is a 32-bit mask encoding which garbage checks failed. The meaning of each bit is in section C.3.2

VetoTree: A TTree containing veto data from the CaenV830Scaler card and Caen792Nqdc cards. The tree has the following 4 branches:

run contains MJTRun objects which hold basic run data such as run number and start and stop times.

vetoEvent contains MGTBasicEvent objects, which detector data from one scaler data packet and several Nqdc data packets.

mVeto contains the event multiplicity, which is the number of QDC channels above threshold.

vetoBits contains a 32-bit mask encoding the results of several checks described in section C.3.3

headerXML: A string of the XML header from the ORCA file. This contains information about the run configuration and is formatted as an XML plist.

ChannelMap: A MJTChannelMap object, compiling information from the tables in the MajoranaModel ORCA object, which describe which detector, pulser, and array position corresponds to each channel. This is useful for obtaining information about each channel, such as detector name and position. The channel map uses a table structure with one row for each Germanium detector.

ChannelSettings: A MJTChannelSettings object. This contains information about the settings for each card. These settings are stored as a tree, with a node hierarchy of card name→ crate → card → setting name → channel.

builderInfo: A string containing information about how the file was built. It contains the command used to build the file and information about the version of MJOR and its dependancies.

C.2   Code Structure

MJOR is based on OrcaRoot, an object-oriented C++library designed to process an ORCA data stream into a ROOT data structure, typically a TTree. OrcaRoot reads out one data packet at a time using either the ORFileReader or ORSocketReader classes. A data processor manager (class ORDataProcManager) passes each data packet to data processor classes (inheriting from ORDataProcessor). MJOR contains data processors for the various data readout cards used by the MAJORANA DEMONSTRATOR and data processors for combining data into events and writing events to TTrees. The majorcaroot executable is used to setup the data loaders that will be used for an ORCA datastream. This section will describe the majorcaroot executable and the various data processor classes.

C.2.1   majorcaroot

majorcaroot is the executable used to run the event builder. The command line options are described in section C.2.4. majorcaroot process each file twice. On the first pass, only the

ORRunTimesCalculator is used, which only processes the run stop packet in order to find the end time of the run, as recorded by ORCA, and the total number of data packets in the run. After this, the run is processed again, with the processors handling the detector data.

When processing the data the second time, the data processor MOHeaderProcessor is used. MOHeaderProcessor inherits from ORHeaderProcessor, which reads the XML header from the ORCA datastream. MOHeaderProcessor also edits the XML header, if certain command line options are used. For example, the run type can be changed or a special channel map can be added.

C.2.2 Germanium digitizer processors

The event builder is represented by the class class MOEventBuilder, which is the data processor responsible for building Germanium detector events. The data loader is represented by the class MOEventDataLoader and daughter classes MOGretina4MDataLoader, MOGretina4DataLoader, and MOSIS3302DataLoader, which are data processors responsible for reading the waveforms and digitizer data out of the data stream. A flow diagram of the Germanium data loader and event builder is shown in figure C.1.

At the start of the ORCA datastream, the event builder allocates the data structures described in the following paragraphs. It creates the branches in MGTree and MGGarbageTree, as described in section C.1. It also fills channel map with the contents of the tables in the MajoranaModel section of the XML header, and the channel settings with the contents of the hardware dictionary produced by OrcaRoot. Finally, it fills the MJTRun, using the stop time and packet number found by the ORRunTimesCalculator. If either the datastream is not an ORCA file or the file contains no run stop packet, the stop time and packet number are set to zero.

When a digitized waveform is read from the ORCA datastream, the data loader class requests an empty event from MOEventBuilder, which will be popped from a buffer of used, empty events called the used event buffer. If the used event buffer is empty, a new event is allocated instead. The purpose of the used event buffer is to recycle the waveform objects
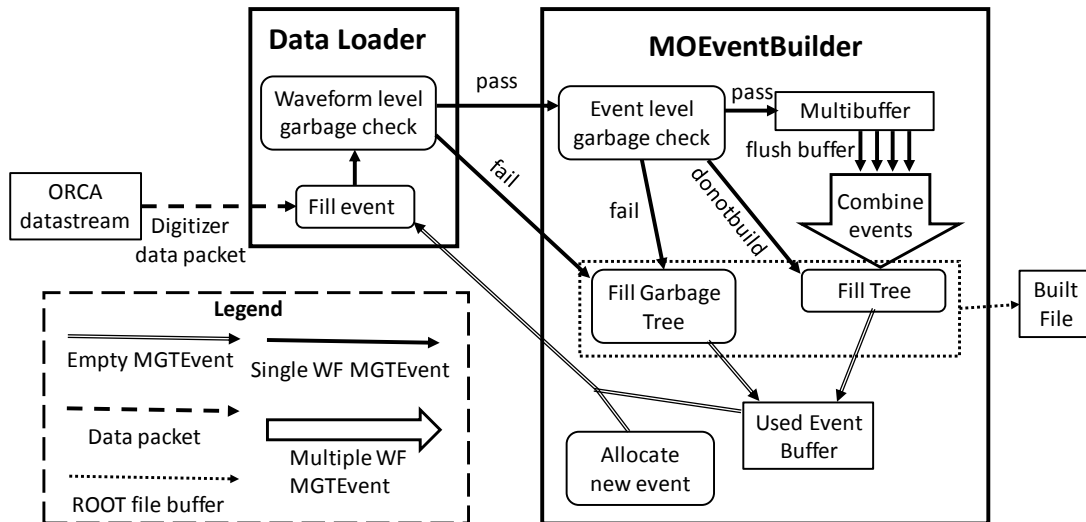
Figure C.1: Data flow diagram for building Germanium events as described in section C.2.2. The logic for flushing the buffer is layed out in figure C.2

and avoid repeatedly allocating and deallocating large arrays. The data loader class fills the empty event with a single MGTWaveform and MGTGretina4DigitizerData object, filled using the data packet from ORCA. The data loader then performs waveform level garbage checks for data corruption that can be detected within a single data packet. The event is then passed to the event builder.

The event builder does one of three things with the new event. If the event was flagged as garbage, it is immediately recorded into MGGarbageTree, cleared, and recycled into the used event buffer. If the event builder is run in donotbuild mode, the event is immediately recorded into MGTree, cleared, and recycled into the used event buffer. Otherwise, the event is placed into the multibuffer, a C++standard library map from a channel number to a C++standard library vector of single-waveform events. The multi-buffer structure is used because data packets from within a single channel are time-ordered, but packets across multiple channels are not. Thus, this structure does not require sorting events by timestamp and it makes timestamp-based garbage checks much simpler to implement. Before being

added to the multibuffer, event-level garbage checks are performed, which require comparing multiple waveforms and digitizer data. If these checks fail, the event is not recorded into the multi-buffer, but instead is immediately written to the garbage tree, cleared, and recycled into the used event buffer. Otherwise, the event is placed into the buffer for its channel and the event builder checks whether or not to flush the oldest event from the multi-buffer.

The event buffer has two possible conditions for flushing the buffer. First, if all channels have at least two events, the buffer will flush. This condition is chosen because once every buffer has at least one event, no more waveforms should appear with a timestamp earlier than any waveforms presently in the buffer. In order to ensure that the event builder can continue to make event level garbage checks, it is important that each buffer is left with at least one event, so the condition is two events in each channel instead of one. The second condition for flushing the buffer is when the buffer has too many events or uses too much memory. The exact condition can be changed by selecting the correct command line option. The default option is to flush when 10000 events are in the multi-buffer. This second condition should only be needed if one channel has a significantly lower data rate than the others, causing the multibuffer to fill up. The buffer is flushed by merging any events within the time window into a single built event. Events are merged by moving the waveform and digitizer data into the built event. The merged event is then cleared and recycled into the used event buffer. If an event is merged with a timestamp later than the latest timestamp in the event, the event window is expanded and any waveforms in the new window are merged into the event. After the built event has been filled, event parameters such as the oldest timestamp and total energy of the event are set. Finally, the event is written to MGTree, cleared, and recycled into the used event buffer.

This scheme for flushing the multibuffer can lead to misbuilt events under two conditions. First, if the data rate is very high in at least one channel and very low in another, the high rate channels can trigger the second condition and flush an event with a timestamp later than a waveform in the low rate channel that has not yet been read into the buffer. In this case, the low rate channel waveform will be written into the garbage tree. The data rates in
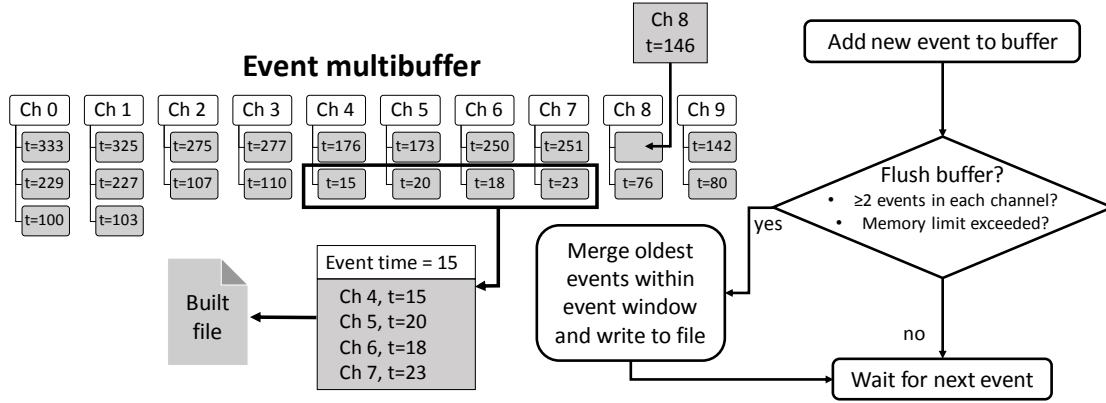
Figure C.2: Diagram of multibuffer structure and logic for flushing events from buffer, as desribed in section C.2.2.

MJD's collaboration runs are not high enough to trigger this under ordinary circumstances. If this does become a problem, it can be reduced by increasing the threshold for flushing the buffer due to memory or event count. The second cause of misbuilt events is when the data rate is high enough in enough channels that the sliding event window expands multiple times and includes a waveform from a channel that has already appeared in the event. Ordinary data rates in MJD calibration runs are not high enough to cause this to occur. This can be made less likely by reducing the event window, which defaults to 10 μs

Once the entire ORCA datastream has been read by the event builder, any events remaining in the multibuffer are merged and written to MGTree. Finally, MGTree, MGGarbage-Tree, and the channel map and settings are written to the built file.

C.2.3   Veto processors

The data processors MOCaen792NqdcDataLoader and MOCaenV830DataLoader are used to read data from the QDC and scaler cards, respectively. The class MOVetoDataLoader combines the data from both of these processors into MGTBasicEvents and writes these events into VetoTree. A dataflow diagram for the veto loader is shown in figure C.3. The
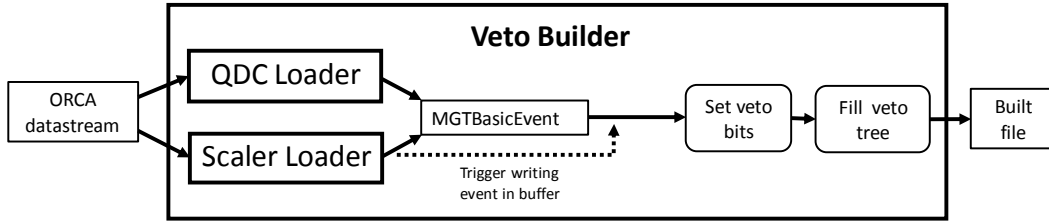
Figure C.3: Data flow diagram for building Germanium events as described in section C.2.3.

expected ordering of data packets in the ORCA data stream for a veto event is a scaler data packet followed immediately by a QDC packet for each QDC card. No other data packets are expected between any of these. The veto loader is written with the expectation that data packets appear in this order.

At the start of the ORCA datastream, VetoTree is initialized and its branches are created as described in section C.1. The MJTRun is filled, using the ORRunTimesCalculator as described in the previous section. A single MGTBasicEvent is allocated to act as a buffer for the veto data.

Whenever a scaler data packet is read by the ORCA datastream, the data is stored by the MOCaenV830DataLoader class. The data from only a single scaler packet is stored at any given time, and should always consist of the most recently read scaler packet. When a QDC data packet is read, the data from each channel is put into its own MJTVetoDetectorData object along with the currently stored scaler data. Each detector data is placed into the MGTBasicEvent buffer. Every time a scaler data packet is read, the MOVetoDataLoader class writes the event buffer to VetoTree and clears the event. In this way, each QDC packet is associated with the most recent scaler packet, as expected for the ordering of data packets described at the start of this section. Before writing the event, several basic data checks, described in section C.3.3, are performed and the vetoBits bitmask is set.

At the end of the ORCA datastream, the remaining data is written to VetoTree, and VetoTree is written to the built file.

C.2.4   majorcaroot usage and options

majorcaroot can be called either on a set of raw ORCA files or on a port of a socket. The correct usage is `majorcaroot [options] [input file(s)/socket host:port]`. The possible options are:

-h, –help : print a usage message and exit

-v, –verbosity [verbosity] : set the severity/verbosity for the logger. Choices are: debug, trace, routine, warning, error, and fatal.

-t, –eventwindow [time] : set the windowing time for the event building. Format is [number][unit] (no space). Unit choices are s, ms, us, ns. If not specified, majorcaroot uses "10us".

-x, –disablevalidatexml : do not validate the XML plist in the ORCA file header. ORXmlPlist will generate a warning. Use when not online.

-e, –nevents [num] : Only process until nevents are in the output tree.

-s, –sis : use SIS3302 data loader.

-g, –gret : use Gretina4 data loader.

-G, –gretM : use Gretina4M data loader.
By default, majorcaroot will look into XML header to check which data loader to use.

–veto [on/off/qdconly/donotbuild] : force veto loader on or off. Default is to turn on if both Caen 792 Nqdc and Caen V830 scaler data are found. Use qdconly if scaler card is not in use but qdc card is. donotbuild will write veto events whenever a qdc data packet is encountered, meaning events only will contain data from a single qdc packet.

-n –nomca : do not use data builder for ORTEC 927 MCA even if MCA data exists.

-i, –mangleChannelIDsForGELATIO [num] : subtract the [num] from all crate-card-channel IDs (dangerous; for GELATIO users).

-C, –disablecollectgarbage : do not throw away bad events into MGGarbageTree.

-f, –fixheaderbools : fix booleans in XML header that have been stored incorrectly by ORCA. This is only necessary for older versions of ORCA.

-r, –setrunbits [bits] : Set run type bits to the given value. Can be given in decimal or hexidecimal with prefix 0x.

–forcerunbitson [bits] : Turn on all bits set to 1 and ignore bits set to zero. Can be used in combination with –forcerunbitsoff.

–forcerunbitsoff [bits] : Turn off all bits set to 1 and ignore bits set to zero. Can be used in combination with –forcerunbitson

–setspecialchanmap [name of file : Set the special channel map to the contents of a file.

-D, –donotbuild : push events to the output tree for each digitizer record: do no time sorting or event clustering.

-E, –doubleencoding : use double encoding instead of short. This results in a larger file size.

-I, –ignoreenabled : do not check for bad channels. Do not flush buffer when all enabled channels have events. This is for debugging purposes only.

-N, –limbufevents [num] : flush buffer when it contains more than [num] events.

-T, –limbuftime [time : flush buffer when it contains events older than [time] relative to incoming events.

-M, –limbufmem [MB] : flush buffer when it grows larger than [MB] megabytes ([MB] should be an int).

-P, –limbufmempct [pct] : flush buffer when it grows larger than [pct] percent of the system memory (integer between 1 and 100).

Default limbuf method is equivalent to –limbufevents 10000.

C.2.5 majorcaroot_checker

The majorcaroot_checker program checks a single built file to ensure that they are built correctly. The correct usage is `majorcaroot_checker [built file]`. majorcaroot_checker accepts no options; instead, it reads the builderInfo string from the built file in order to determine which options to use. majorcaroot_checker is not guaranteed to correctly check files that originated with majorcaroot from a different version of MJOR.

majorcaroot_checker begins by looping through each of the TTrees in the file and performing several checks on each event. A list is allocated with size equal to the total number of data packets in the run in order to count the number of properly built events in each data packet. If an event fails checks performed on it, then it is not added to this list.

In MGTree, each event is checked to ensure that it is in order by time and that each waveform falls in the correct time window. The event is also checked to ensure that each channel does not have multiple waveforms. Finally, each waveform is checked to ensure that all MGTWaveform data members were filled and do not contain corrupt data.

In MGGarbageTree, specific checks are not performed on waveforms since any problems are assumed to be related to the reason the waveform is in MGGarbageTree to begin with. If the garbageCode indicates a corrupt data header or bad timestamp and the event occurred in the middle of a run, a warning is emitted, since these types of garbage events are common

at the start and end of runs, but not in the middle. After scanning through the tree, majorcaroot_checker outputs a list of each unique set of garbage bits in the tree, and how many times they occurred.

In VetoTree, each veto event is checked to ensure that all data members are filled correctly. After scanning through the tree, majorcaroot_checker outputs a list of each unique set of veto bits in the tree, and how many times they occurred.

After scanning each tree, the checker rescans the original ORCA file, assuming that the original file has the same relative path as when majorcaroot was first run. The checker scans using the MOOrcaFileFilter data processor. This processor takes the list of built data packets that was filled while scanning each tree as an input. For each data packet that is not found in the list or has the wrong number of entries (e.g. if a gretina data packet has 8 entries, but only 7 were found in MGTree with the correct index), the raw data record is written into a new ORCA binary file. Furthermore, a count of the number of data packets from each type of card in the file is given.

C.3   Bit Definitions

This section contains the definitions of garbage bits, run bits, and veto bits. These bits are stored as 32-bit masks, with each bit representing some condition. Multiple bits may be set at once. The bits are listed in tables from least significant bit to most significant bit, with double lines breaking up hexadecimal digits. The bits are defined in MGDO in the header file Majorana/MJTypes.hh, along with some basic commands for manipulating them.

C.3.1   Run bits

The run bits are contained in the XML header of the ORCA file and are read into the run branch of each tree. These bits are set during ORCA run configuration, however options exist to change these bits in the built file.

bit	name	description
0	Maintenance	This is already defined. It is tied to the operations in ORCA and is used when the operator is making changes, etc. to the configuration
1	bb-decay	Selected for "good" data taking.
2	Calibration-Prototype	Set if calibration source present on Prototype.
3	Calibration-Module 1	Set if calibration source present on Module 1.
4	Calibration-Module 2	Set if calibration source present on Module 2.
5	Co60	Set for use of Cobalt-60 source.
6	Th228	Set for use of Th-228 source.
7	Partial shield	Set if part of poly shield is not present.
8	Prototype offline	Set if Prototype is offline.
9	Module 1 offline	Set if Module 1 is offline.
10	Module 2 offline	Set if Module 2 is offline.
11	Radon purge offline	Set if radon purge is offline or abnormal.
12	Machine shop	Set if work ongoing in machine shop.
13	Disruptive work	Set if work in Detector Room might be disruptive to data taking
14	Blank Monolith (East side)	Set if blank monolith is in east shield spot.
15	Blank Monolith (South side)	Set if blank monolith is in south shield spot.

C.3.2   Garbage bits

The garbage bits are encoded in the MGGarbageTree branch "garbageCode." Each entry in MGGarbageTree should have an event with a single waveform/digitizer data and a non-zero garbage code. The first three bits are specific to the Gretina4M card/firmware and will not be thrown for others. The remaining bits will be thrown for any card/firmware.

bit	name	description
0	BadHeader1	The first word of a Gretina4M data packet is not 0xAAAAAAAA
1	BadHeader2	The second word of a Gretina4M data packet is not 0x000000D#, where # is any hexidecimal digit
2	BadHeader3	The energy and timestamp in the Gretina packet header are both zero
3	TooOld	Waveform has a timestamp older than an event that has already be written. This may indicate that the memory limits are too stringent.
4	InvalidCard	Waveform comes from a card that is not being read out by ORCA
5	InvalidChannel	Waveform comes from a channel that is not enabled
6	TSOutOfOrder	Waveforms within a single channel should be time ordered. If a waveform comes after a waveform in the same channel with a later timestamp, set this bit.
7	RepeatWF	Two consecutive waveforms within a single channel have identical waveforms
8	NWaveforms	Event contains no waveforms. This case represents an exception to garbage events having one waveform
9	AllZero	Waveform has all zero entries

C.3.3   Veto bits

Veto bits are assigned to each veto event in VetoTree. The veto bits represent differences in veto events from the expected configuration. Events that are tagged are not separated from normal events, meaning that the veto bits can be set to zero.

bit	name	description
0	MissingChannels	<32 veto data objects exist in the event.
1	ExtraChannels	>32 veto data objects exist in the event.
2	ScalerOnly	Event has no QDC data. The event should contain a single veto-data with only have time and scaler-related fields set.
3	BadTimeStamp	Timestamp is 0xFFFF FFFF FFFF FFFF.
4	QDCOutOfSequence	Event does not have the expected Scaler-QDC-QDC sequence. This is set if fQDCIndex - fScalerIndex is not 1 or 2.
5	DuplicateChannel	A QDC channel appears multiple times in a single event.
6	HWCountMismatch	Event count on scaler changes from event count of QDC. This is only set for the event where the mismatch occurs.

Appendix D

DETAILED RESULTS FOR ALL DECAY MODES

The main document concerned itself primarily with the $2\nu\beta\beta$ of ^{76}Ge to the 0_1^+ excited state. However, results are presented for all decay modes and energy peaks. This appendix will present figures and tables detailing the simulations, cuts, efficiencies and results for each decay mode and peak.

D.1 $2\nu\beta\beta$ to 0_1^+

Note that both the 559 and 563 keV peaks will be shown together since they use the same sets of cuts.
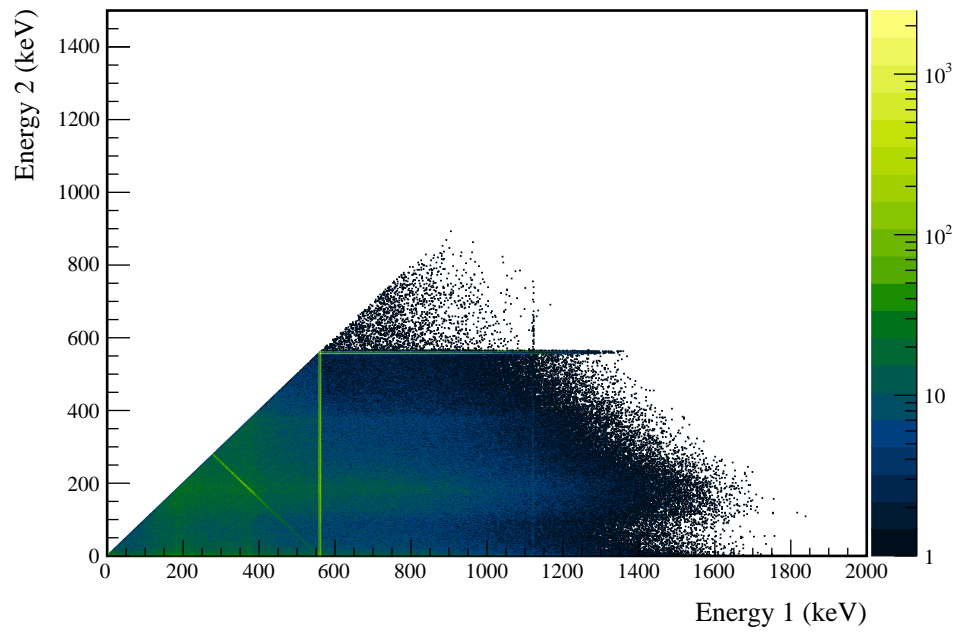
Figure D.1: Simulated multiplicity 2 energy spectrum of the $2\nu\beta\beta$ to 0_1^+ decay mode

Table D.1: Table of energy estimation uncertainties for the 559 and 563 keV peaks.

DS	E_{peak} (keV)	σ_{fit} (keV)	σ_{drift} (keV)	σ (keV)	$f_{t,fit}$	τ_{fit} (keV)	$\delta_{\mu,fit}$ (keV)	$\delta_{\mu,NL}$ (keV)	$\delta_{\mu,drift}$ (keV)	$\delta_{\mu,xtalk}$ (keV)	$\delta_{\mu,peak}$ (keV)	δ_{μ} (keV)	FWHM (keV)	$\delta_{fwhm,fit}$ (keV)	$\delta_{fwhm,drift}$ (keV)	$\delta_{fwhm,xtalk}$ (keV)	δ_{FWHM} (keV)	δ_{α}	$E_{ROI,1}$ (keV)	$E_{ROI,2}$ (keV)	ϵ_{ROI}	$\sigma_{\epsilon_{ROI}}$
DS1	559.101	0.460	0.063	0.464	0.230	0.515	0.001	0.104	0.002	0.012	0.005	0.105	1.152	0.001	0.039	0.011	0.040	0.035	558.199	559.847	0.871	0.015
DS2	559.101	0.461	0.055	0.464	0.249	0.515	0.002	0.067	0.004	0.012	0.005	0.068	1.158	0.001	0.107	0.011	0.108	0.093	558.186	559.845	0.874	0.031
DS3	559.101	0.470	0.066	0.474	0.224	0.505	0.001	0.026	0.024	0.012	0.005	0.038	1.174	0.001	0.073	0.011	0.074	0.063	558.187	559.863	0.879	0.021
DS4	559.101	0.455	0.077	0.461	0.108	0.445	0.002	0.076	0.010	0.012	0.005	0.078	1.111	0.001	0.106	0.011	0.107	0.096	558.283	559.856	0.888	0.032
DS5a	559.101	0.560	0.085	0.567	0.106	0.855	0.002	0.079	0.005	0.012	0.005	0.080	1.367	0.002	0.055	0.011	0.056	0.041	558.098	560.022	0.875	0.014
DS5b	559.101	0.469	0.074	0.475	0.158	0.491	0.001	0.020	0.011	0.012	0.005	0.026	1.157	0.001	0.125	0.011	0.125	0.108	558.229	559.872	0.885	0.036
DS5c	559.101	0.460	0.085	0.468	0.174	0.489	0.001	0.037	0.030	0.012	0.005	0.050	1.145	0.001	0.162	0.011	0.162	0.142	558.231	559.860	0.883	0.046
DS6a	559.101	0.456	0.044	0.458	0.191	0.463	0.001	0.069	0.025	0.012	0.005	0.075	1.123	0.000	0.041	0.011	0.042	0.038	558.241	559.841	0.881	0.014
DS1	563.178	0.461	0.064	0.466	0.230	0.518	0.001	0.104	0.002	0.012	0.005	0.105	1.156	0.001	0.039	0.011	0.040	0.035	562.273	563.927	0.871	0.015
DS2	563.178	0.463	0.055	0.466	0.249	0.517	0.002	0.067	0.004	0.012	0.005	0.068	1.162	0.001	0.107	0.011	0.108	0.093	562.259	563.924	0.874	0.030
DS3	563.178	0.471	0.066	0.476	0.224	0.508	0.001	0.026	0.024	0.012	0.005	0.038	1.179	0.001	0.073	0.011	0.074	0.063	562.261	563.943	0.879	0.021
DS4	563.178	0.457	0.077	0.463	0.108	0.447	0.002	0.076	0.010	0.012	0.005	0.078	1.115	0.001	0.106	0.011	0.107	0.096	562.357	563.935	0.888	0.032
DS5a	563.178	0.562	0.086	0.569	0.106	0.858	0.002	0.079	0.006	0.012	0.005	0.080	1.372	0.002	0.055	0.011	0.056	0.041	562.172	564.103	0.875	0.014
DS5b	563.178	0.471	0.074	0.477	0.158	0.494	0.001	0.020	0.011	0.012	0.005	0.026	1.162	0.001	0.125	0.011	0.125	0.108	562.303	563.952	0.885	0.035
DS5c	563.178	0.462	0.086	0.470	0.174	0.492	0.001	0.037	0.030	0.012	0.005	0.050	1.149	0.001	0.162	0.011	0.162	0.141	562.305	563.939	0.883	0.046
DS6a	563.178	0.457	0.044	0.459	0.191	0.465	0.001	0.069	0.026	0.012	0.005	0.075	1.127	0.000	0.041	0.011	0.042	0.038	562.315	563.921	0.881	0.013

(a) Simulated BG Sum Energy Spectrum
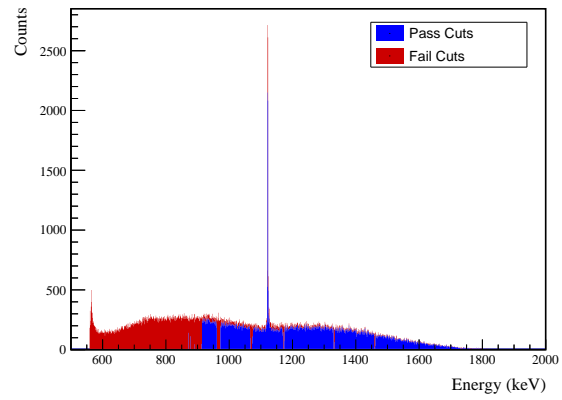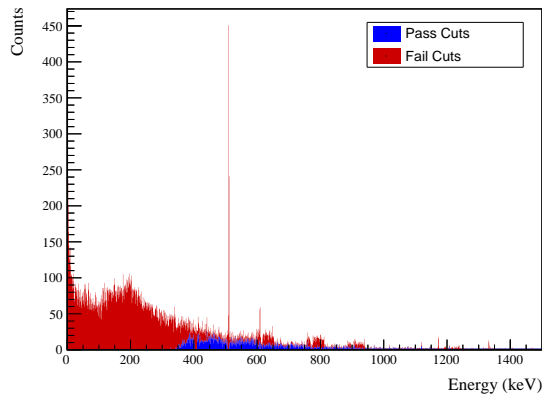
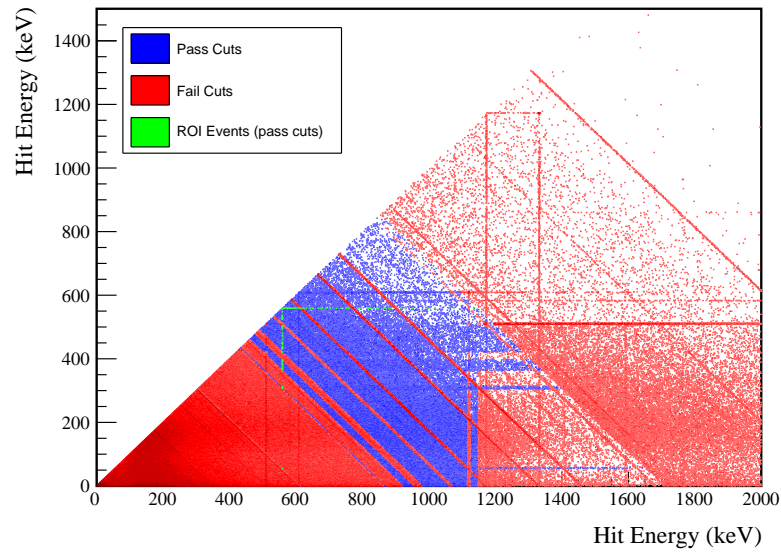(b) Simulated ES Sum Energy Spectrum

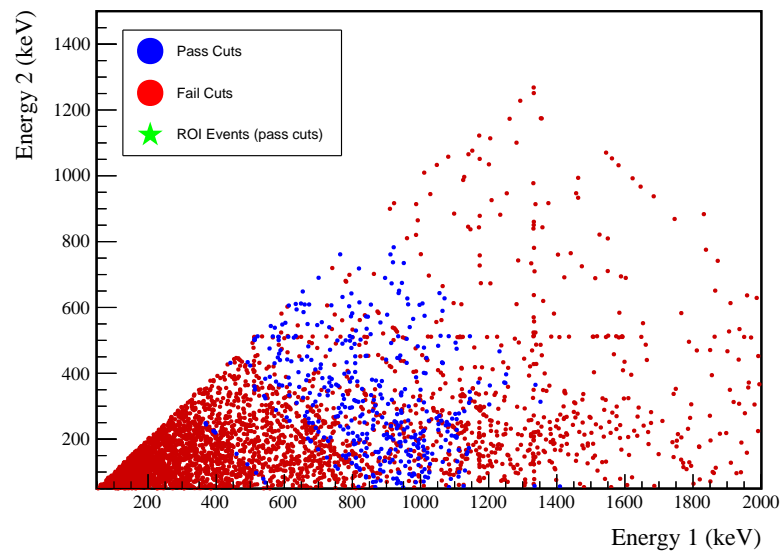(c) Simulated BG Coincident Energy Spectrum
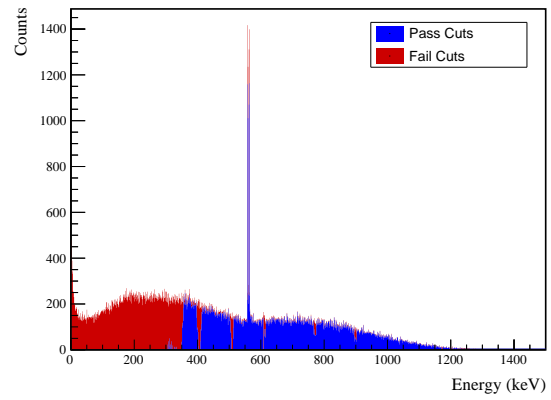
(d) Simulated ES Coincident Energy Spectrum

Figure D.2: Sum energy and coincident energy spectra for the 559 and 563 keV peaks.
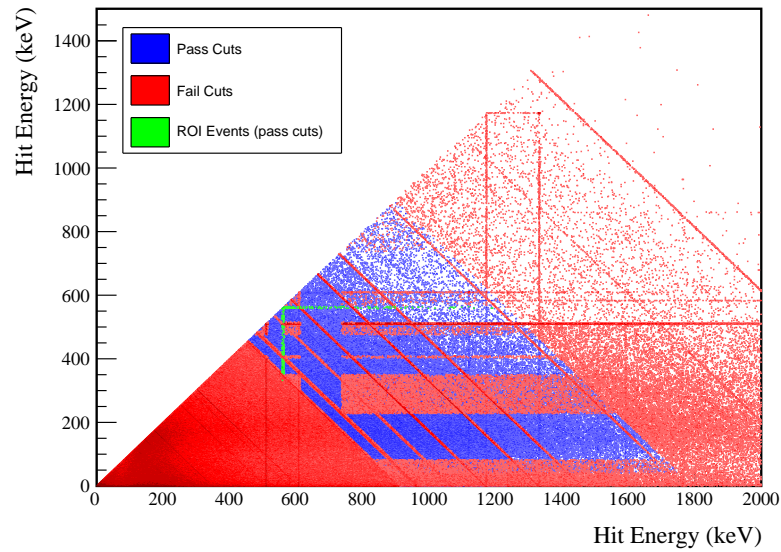
(a) Simulation
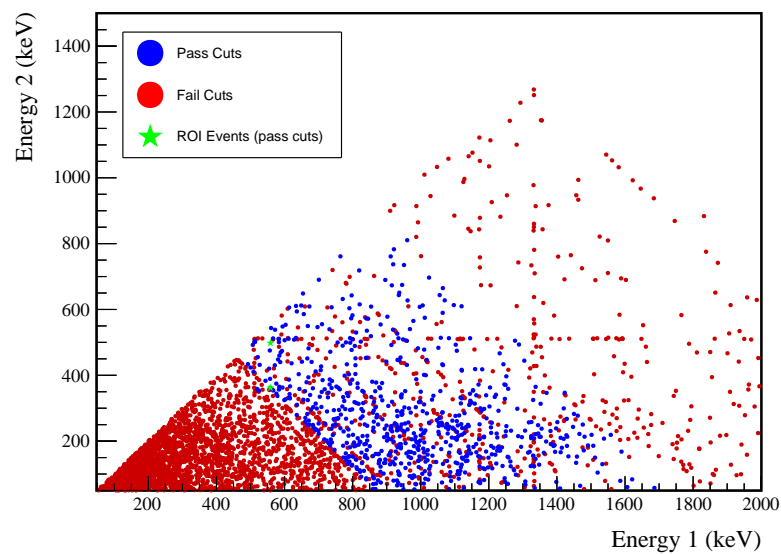
(b) Data

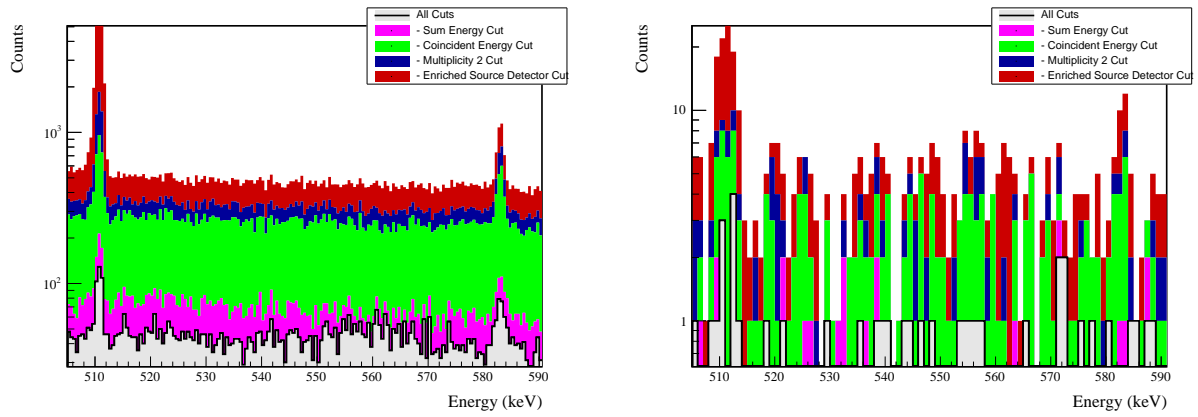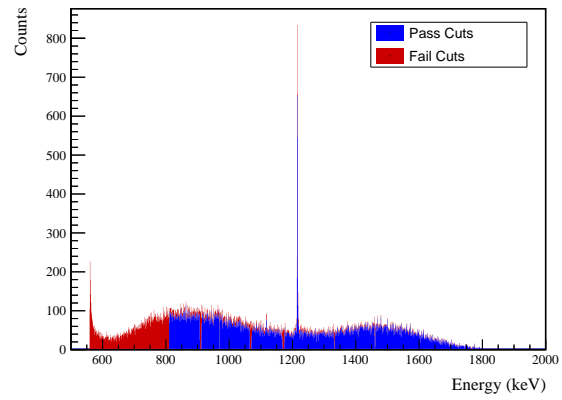Figure D.3: Simulated and measured multiplicity 2 energy spectrum with sum and coincident energy cuts included for the 559 and 563 keV peaks.

(a) Effect of all cuts on ROI

Source	Module 1 efficiency	Module 2 efficiency
Multi-Detector with Full Energy γ	$5.9 \pm 0.2\%$	$3.2 \pm 0.5\%$
Region of Interest	$87.9 \pm 1.4\%$	$87.9 \pm 1.4\%$
Dead Layer	$74.5 \pm 4.3\%$	$65.7 \pm 6.0\%$
Detector Dead Times	$97.5 \pm 1.2\%$	$98.1 \pm 0.9\%$
Enriched Source Detector Cut	$96.8 \pm\ <0.1\%$	$89.4 \pm\ <0.1\%$
Coincident Energy Cut	$88.5 \pm 0.5\%$	$84.4 \pm 0.5\%$
Sum Energy Cut	$60.2 \pm 0.5\%$	$54.0 \pm 0.5\%$
Final Efficiency	$2.29 \pm 0.16\%$	$0.97 \pm 0.17\%$

(b) Table of efficiencies

Figure D.4: Plot showing effect of cuts applied sequentially on ROI peak and table of detection efficiencies for the 559 and 563 keV peaks.
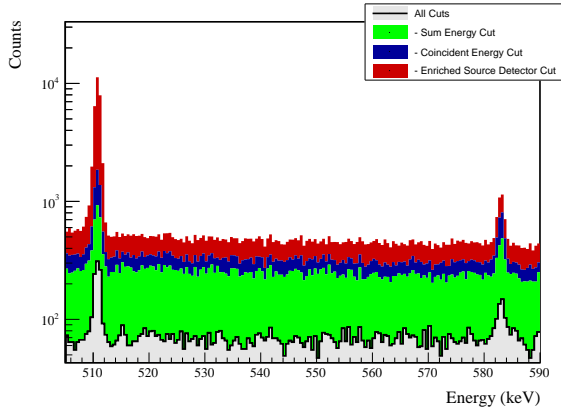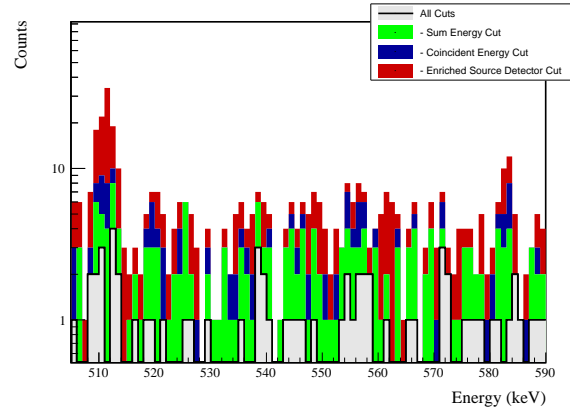
(a) Simulated BG Cuts
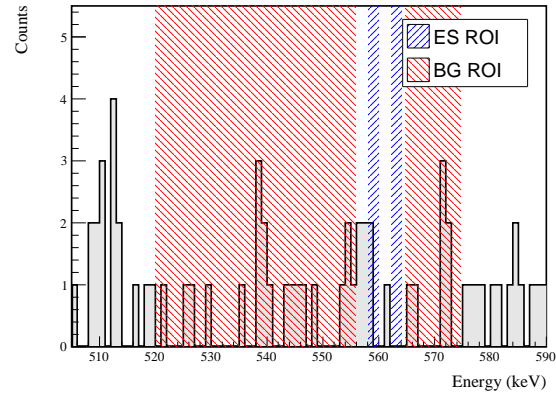
(b) Data Cuts

(c) Data ROIs

Figure D.5: Effect of all cuts applied to measured and simulated background data.

| Cut Name	Cut Description		$\langle\epsilon_{total}\rangle$	$\hat{\epsilon}_{total}$	$\langle\epsilon_{unique}\rangle$	$\hat{\epsilon}_{unique}$	Sacrifice	ΔDP
Enriched Source		M1:	23.2 %	$27.2^{+3.8}_{-3.5}$ %	2.2 %	$2.0^{+1.5}_{-0.9}$ %	0.7 %	7%
Detector Cut	Any other detector: isEnr	M2:	42.7 %	$62.8^{+7.0}_{-7.6}$ %	4.4 %	$4.7^{+4.4}_{-2.3}$ %	2.1 %	
Coincident	No other detector: (((energy<40.6) || (energy>402.6 && energy<506.8 && energy<512.4) || (energy>608. && energy>610.2) || (energy>1170.6 && energy<1175.) || (energy>1235.)) && isEnr) || (	M1:	29.6 %	$33.3^{+4.0}_{-3.8}$ %	4.4 %	$4.8^{+2.1}_{-1.5}$ %	3.9 %	7%
Energy Cut	((energy<83.) || (energy>228.2 && energy<350.6) || (energy>475.2 && energy<516.8) || (energy>566.6 && energy<613.4) || (energy>737.4)) && !isEnr)	M2:	37.5 %	48.8 ± 7.5 %	4.2 %	$2.3^{+3.6}_{-1.4}$ %	3.5 %	
Sum Energy Cut	Not: (sumE<870.) || (sumE>870.6 && sumE<877.6) || (sumE>878. && sumE<891.) || (sumE>891.2 && sumE<913.8) || (sumE>960.8 && sumE<972.) || (sumE>1066.8 && sumE<1072.6) || (sumE>1170.8 && sumE<1174.6) || (sumE>1330. && sumE<1333.6) || (sumE>1458.2 && sumE<1461.8) || (sumE>1761.8 && sumE<1765.8) || (sumE>1794.4)	M1:	75.0 %	$74.8^{+3.4}_{-3.7}$ %	44.5 %	$41.5^{+4.1}_{-4.0}$ %	31.8 %	20%
		M2:	75.6 %	$74.4^{+6.0}_{-7.2}$ %	33.0 %	$25.6^{+7.2}_{-6.0}$ %	32.1 %	
Combined Cuts		M1:	84.5 %	$84.4^{+2.8}_{-3.2}$ %	–	–	44.9 %	27%
		M2:	89.5 %	$95.3^{+2.3}_{-4.4}$ %	–	–	53.1 %	

Table D.2: Table of cut descriptions and efficiencies for simulated backgrounds and measured data for the 559 and 563 keV peaks.

D.2 $2\nu\beta\beta$ **to** 2_1^+
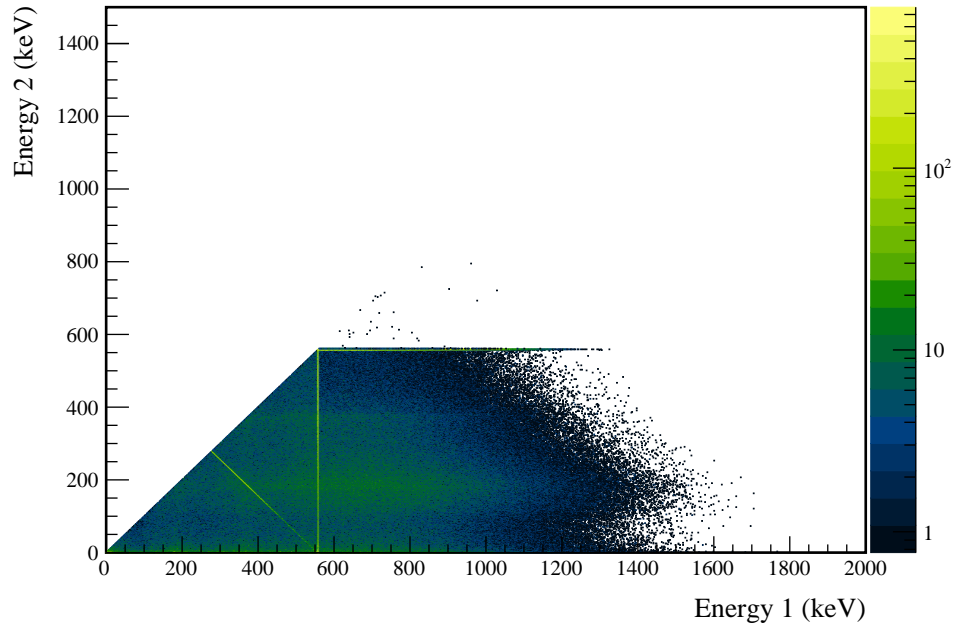
Figure D.6: Simulated multiplicity 2 energy spectrum of the $2\nu\beta\beta$ to 2_1^+ decay mode

Table D.3: Table of energy estimation uncertainties for the 559 keV peak.

DS	E_{peak} (keV)	σ_{fit} (keV)	σ_{drift} (keV)	σ (keV)	$f_{t,fit}$	τ_{fit} (keV)	$\delta_{\mu,fit}$ (keV)	$\delta_{\mu,NL}$ (keV)	$\delta_{\mu,drift}$ (keV)	$\delta_{\mu,xtalk}$ (keV)	$\delta_{\mu,peak}$ (keV)	δ_{μ} (keV)	FWHM (keV)	$\delta_{fwhm,fit}$ (keV)	$\delta_{fwhm,drift}$ (keV)	$\delta_{fwhm,xtalk}$ (keV)	δ_{FWHM} (keV)	δ_{α}	$E_{ROI,1}$ (keV)	$E_{ROI,2}$ (keV)	ϵ_{ROI}	$\sigma_{\epsilon_{ROI}}$
DS1	559.101	0.460	0.063	0.464	0.230	0.515	0.001	0.104	0.002	0.012	0.005	0.105	1.152	0.001	0.039	0.011	0.040	0.035	558.183	559.860	0.877	0.015
DS2	559.101	0.461	0.055	0.464	0.249	0.515	0.002	0.067	0.004	0.012	0.005	0.068	1.158	0.001	0.107	0.011	0.108	0.093	558.169	559.858	0.880	0.030
DS3	559.101	0.470	0.066	0.474	0.224	0.505	0.001	0.026	0.024	0.012	0.005	0.038	1.174	0.001	0.073	0.011	0.074	0.063	558.170	559.876	0.885	0.020
DS4	559.101	0.455	0.077	0.461	0.108	0.445	0.002	0.076	0.010	0.012	0.005	0.078	1.111	0.001	0.106	0.011	0.107	0.096	558.269	559.869	0.893	0.031
DS5a	559.101	0.560	0.085	0.567	0.106	0.855	0.002	0.079	0.005	0.012	0.005	0.080	1.367	0.002	0.055	0.011	0.056	0.041	558.081	560.038	0.881	0.014
DS5b	559.101	0.469	0.074	0.475	0.158	0.491	0.001	0.020	0.011	0.012	0.005	0.026	1.157	0.001	0.125	0.011	0.125	0.108	558.214	559.886	0.891	0.035
DS5c	559.101	0.460	0.085	0.468	0.174	0.489	0.001	0.037	0.030	0.012	0.005	0.050	1.145	0.001	0.162	0.011	0.162	0.142	558.216	559.873	0.888	0.045
DS6a	559.101	0.456	0.044	0.458	0.191	0.463	0.001	0.069	0.025	0.012	0.005	0.075	1.123	0.000	0.041	0.011	0.042	0.038	558.226	559.854	0.886	0.013

Cut Name	Cut Description		$\langle \epsilon_{total} \rangle$	$\hat{\epsilon}_{total}$	$\langle \epsilon_{unique} \rangle$	$\hat{\epsilon}_{unique}$	Sacrifice	ΔDP
Enriched Source Detector Cut	Any other detector: isEnr	M1:	23.2 %	$26.5^{+3.8}_{-3.5}$ %	4.5 %	$4.1^{+2.0}_{-1.3}$ %	1.7 %	18%
		M2:	42.7 %	$62.8^{+7.0}_{-7.6}$ %	8.7 %	$11.6^{+5.8}_{-4.0}$ %	4.1 %	
Multiplicity 2 Cut	m==2	M1:	15.4 %	$16.3^{+3.3}_{-2.8}$ %	0.7 %	$0.0^{+0.7}_{-0.0}$ %	0.0 %	2%
		M2:	11.7 %	$16.3^{+6.4}_{-4.9}$ %	0.7 %	$0.0^{+2.3}_{-0.0}$ %	0.0 %	
Coincident Energy Cut	No other detector: (((energy<53.8) || (energy>59.4 && energy<303.8) || (energy>314.4 && energy<362.4) || (energy>398.6 && energy<421.) || (energy>506.2 && energy<512.2) || (energy>1116.4 && energy<1124.2) || (energy>1147.8)) && isEnr)	M1:	59.2 %	55.8 ± 4.1 %	3.8 %	$4.8^{+2.1}_{-1.5}$ %	0.3 %	12%
		M2:	44.9 %	$30.2^{+7.4}_{-6.5}$ %	3.5 %	$0.0^{+2.3}_{-0.0}$ %	0.3 %	
Sum Energy Cut	Not: (sumE<612.8) || (sumE>618.4 && sumE<862.6) || (sumE>873.4 && sumE<921.) || (sumE>957.4 && sumE<979.6) || (sumE>1064.8 && sumE<1070.8) || (sumE>1171.6 && sumE<1174.6) || (sumE>1330. && sumE<1333.6) || (sumE>1457. && sumE<1462.4) || (sumE>1675.2 && sumE<1684.8) || (sumE>1706.4)	M1:	74.9 %	$74.8^{+3.4}_{-3.7}$ %	6.3 %	$5.4^{+2.2}_{-1.6}$ %	1.2 %	17%
		M2:	75.6 %	$76.7^{+5.8}_{-7.0}$ %	4.3 %	$2.3^{+3.6}_{-1.4}$ %	1.2 %	
Combined Cuts		M1:	89.9 %	$89.1^{+2.3}_{-2.8}$ %	—	—	30.9 %	79%
		M2:	93.0 %	$97.7^{+1.4}_{-3.6}$ %	—	—	34.0 %	

Table D.4: Table of cut descriptions and efficiencies for simulated backgrounds and measured data for the 559 keV peak.
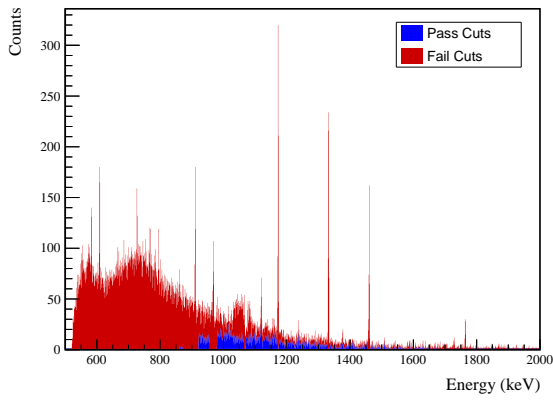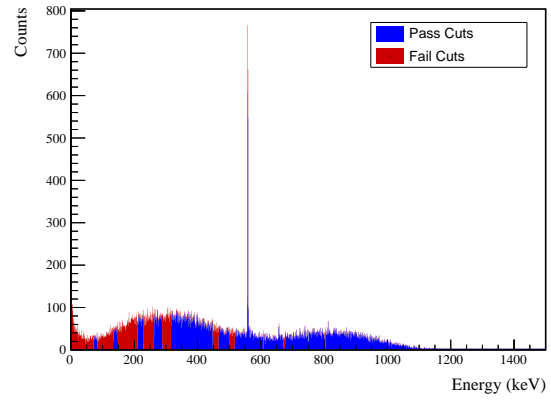
(a) Simulated BG Sum Energy Spectrum
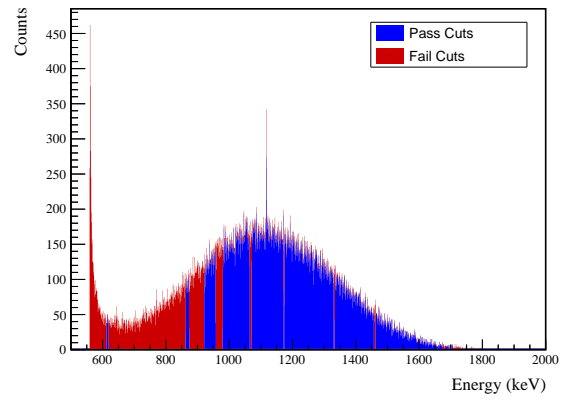
(b) Simulated ES Sum Energy Spectrum
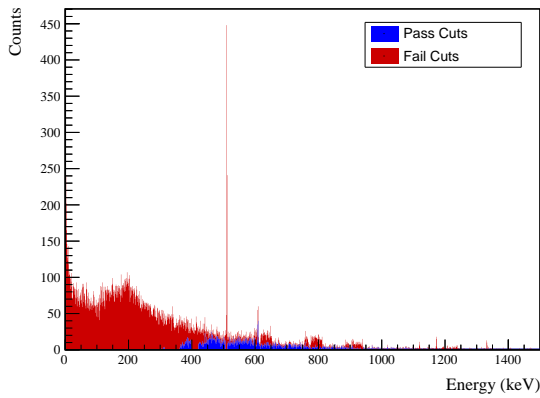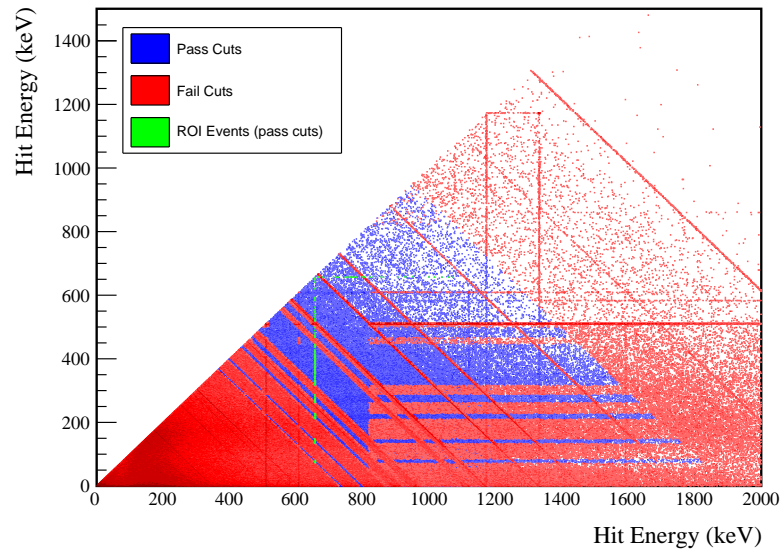

(c) Simulated BG Coincident Energy Spectrum
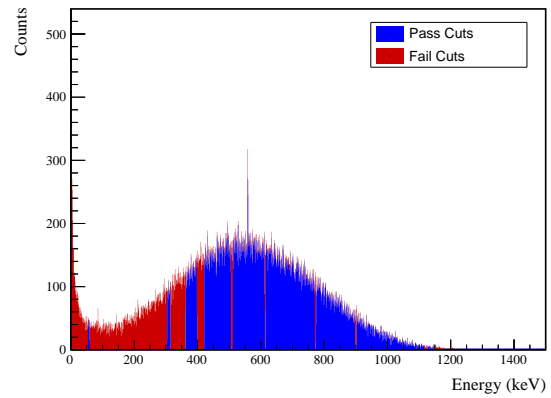
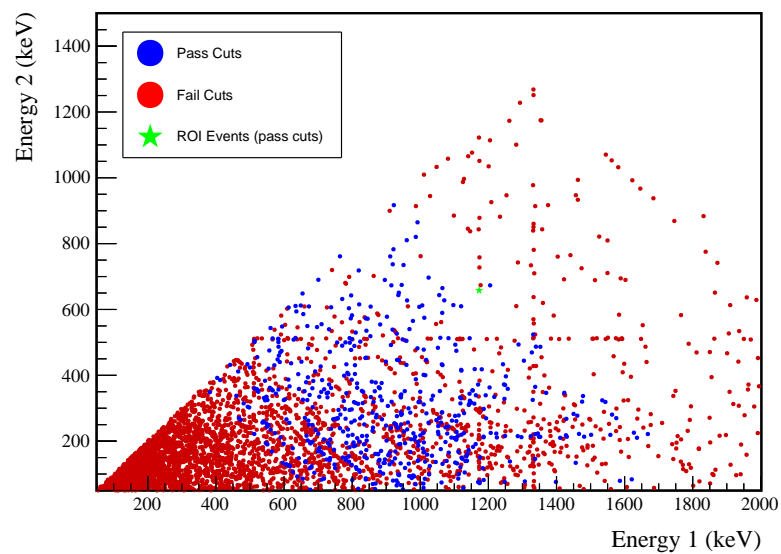
(d) Simulated ES Coincident Energy Spectrum

Figure D.7: Sum energy and coincident energy spectra for the 559 keV peak.

(a) Simulation

(b) Data

Figure D.8: Simulated and measured multiplicity 2 energy spectrum with sum and coincident energy cuts included for the 559 keV peak.
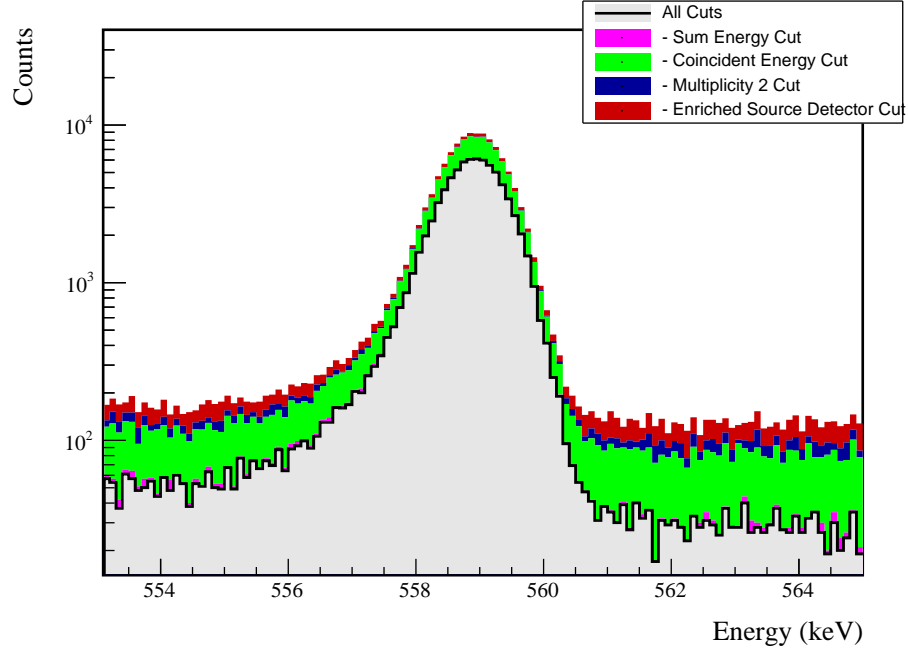
(a) Effect of all cuts on ROI

Source	Module 1 efficiency	Module 2 efficiency
Multi-Detector with Full Energy γ	$3.0 \pm 0.2\%$	$1.5 \pm 0.5\%$
Region of Interest	$88.4 \pm 2.0\%$	$88.4 \pm 2.0\%$
Dead Layer	$71.4 \pm 4.9\%$	$62.8 \pm 6.5\%$
Detector Dead Times	$97.5 \pm 1.2\%$	$98.0 \pm 0.9\%$
Enriched Source Detector Cut	$97.3 \pm\ <0.1\%$	$93.2 \pm\ <0.1\%$
Multiplicity 2 Cut	$99.5 \pm\ <0.1\%$	$99.7 \pm\ <0.1\%$
Coincident Energy Cut	$73.1 \pm 0.5\%$	$74.0 \pm 0.5\%$
Sum Energy Cut	$71.4 \pm 0.5\%$	$70.5 \pm 0.5\%$
Final Efficiency	$1.42 \pm 0.14\%$	$0.61 \pm 0.20\%$

(b) Table of efficiencies

Figure D.9: Plot showing effect of cuts applied sequentially on ROI peak and table of detection efficiencies for the 559 keV peak.

(a) Simulated BG Cuts

(b) Data Cuts
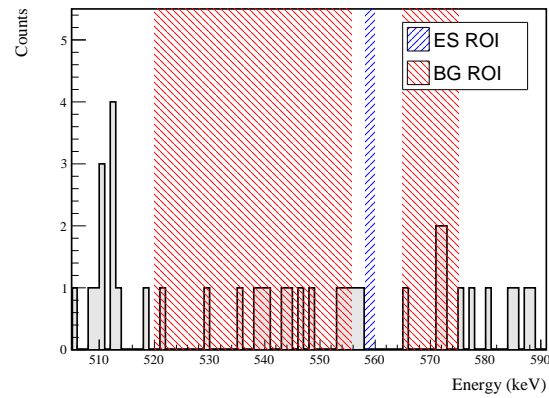
(c) Data ROIs

Figure D.10: Effect of all cuts applied to measured and simulated background data.

D.3 $2\nu\beta\beta$ **to** 2_2^+
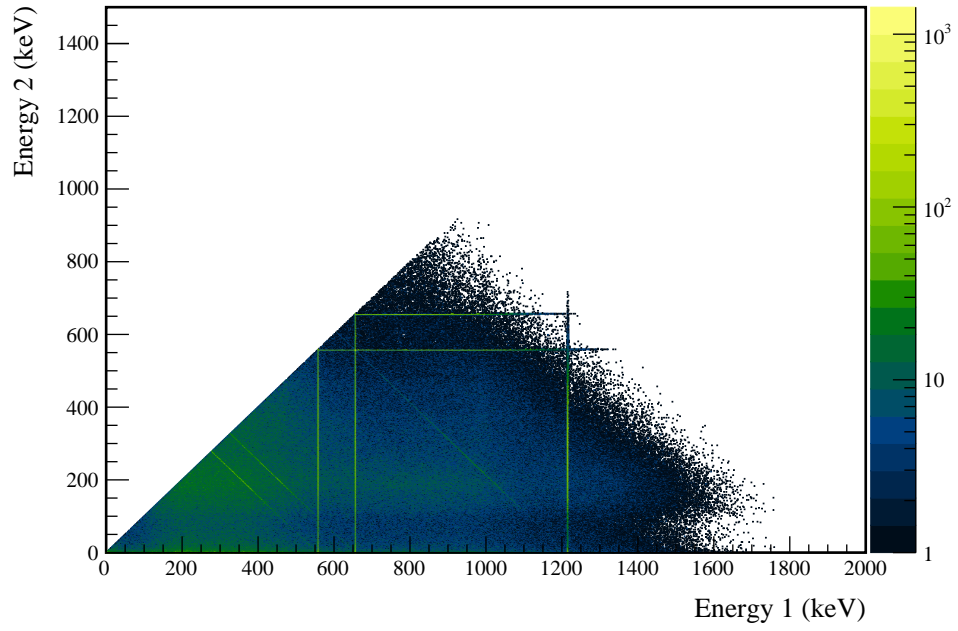
Figure D.11: Simulated multiplicity 2 energy spectrum of the $2\nu\beta\beta$ to 2_2^+ decay mode

D.3.1 559 keV peak

Table D.5: Table of energy estimation uncertainties for the 559 keV peak.

DS	E_{peak} (keV)	σ_{fit} (keV)	σ_{drift} (keV)	σ (keV)	$f_{t,fit}$	τ_{fit} (keV)	$\delta_{\mu,fit}$ (keV)	$\delta_{\mu,NL}$ (keV)	$\delta_{\mu,drift}$ (keV)	$\delta_{\mu,xtalk}$ (keV)	$\delta_{\mu,peak}$ (keV)	δ_μ (keV)	FWHM (keV)	$\delta_{fwhm,fit}$ (keV)	$\delta_{fwhm,drift}$ (keV)	$\delta_{fwhm,xtalk}$ (keV)	δ_{FWHM} (keV)	δ_α	$E_{ROI,1}$ (keV)	$E_{ROI,2}$ (keV)	ϵ_{ROI}	$\sigma_{\epsilon_{ROI}}$
DS1	559.101	0.460	0.063	0.464	0.230	0.515	0.001	0.104	0.002	0.012	0.005	0.105	1.152	0.001	0.039	0.011	0.040	0.035	558.218	559.832	0.864	0.016
DS2	559.101	0.461	0.055	0.464	0.249	0.515	0.002	0.067	0.004	0.012	0.005	0.068	1.158	0.001	0.107	0.011	0.108	0.093	558.206	559.830	0.867	0.032
DS3	559.101	0.470	0.066	0.474	0.224	0.505	0.001	0.026	0.024	0.012	0.005	0.038	1.174	0.001	0.073	0.011	0.074	0.063	558.206	559.847	0.872	0.021
DS4	559.101	0.455	0.077	0.461	0.108	0.445	0.002	0.076	0.010	0.012	0.005	0.078	1.111	0.001	0.106	0.011	0.107	0.096	558.299	559.841	0.881	0.033
DS5a	559.101	0.560	0.085	0.567	0.106	0.855	0.002	0.079	0.005	0.012	0.005	0.080	1.367	0.002	0.055	0.011	0.056	0.041	558.119	560.004	0.868	0.015
DS5b	559.101	0.469	0.074	0.475	0.158	0.491	0.001	0.020	0.011	0.012	0.005	0.026	1.157	0.001	0.125	0.011	0.125	0.108	558.247	559.857	0.878	0.037
DS5c	559.101	0.460	0.085	0.468	0.174	0.489	0.001	0.037	0.030	0.012	0.005	0.050	1.145	0.001	0.162	0.011	0.162	0.142	558.249	559.844	0.876	0.048
DS6a	559.101	0.456	0.044	0.458	0.191	0.463	0.001	0.069	0.025	0.012	0.005	0.075	1.123	0.000	0.041	0.011	0.042	0.038	558.259	559.826	0.874	0.014

Cut Name	Cut Description	M	$\langle\epsilon_{total}\rangle$	$\hat{\epsilon}_{total}$	$\langle\epsilon_{unique}\rangle$	$\hat{\epsilon}_{unique}$	Sacrifice	ΔDP
Enriched Source		M1:	23.2 %	$26.5^{+3.8}_{-3.5}$ %	6.1 %	$6.1^{+2.3}_{-1.7}$ %	1.7 %	10%
Detector Cut	Any other detector: isEnr	M2:	42.7 %	$62.8^{+7.0}_{-7.6}$ %	11.8 %	$18.6^{+6.6}_{-5.2}$ %	5.2 %	
Coincident	No other detector: (((energy<41.) || (energy>349.6 && energy<352.8) || (energy>506.8 && energy<512.2) || (energy>608.4 && energy<612.6) || (energy>1307.4))	M1:	28.8 %	$34.0^{+4.0}_{-3.8}$ %	5.3 %	$5.4^{+2.2}_{-1.6}$ %	4.7 %	3%
Energy Cut	&& isEnr) || (((energy<42.) || (energy>120.2 && energy<514.2) || (energy>507.6 && energy<255.8 && energy>850.2)) && !isEnr)	M2:	35.6 %	48.8 ± 7.5 %	5.0 %	$7.0^{+4.9}_{-3.0}$ %	4.3 %	
Sum Energy Cut	Not: (sumE<810.2) || (sumE>907.2 && sumE<912.4) || (sumE>968. && sumE<969.2) || (sumE>1064.8 && sumE<1070.) || (sumE>1168.6 && sumE<1174.6) || (sumE>1330.4 && sumE<1333.4) || (sumE>1459.4 && sumE<1461.8) || (sumE>1761.8 && sumE<1766.) || (sumE>1906.)	M1:	61.1 %	$59.9^{+4.0}_{-4.1}$ %	34.7 %	$31.3^{+3.9}_{-3.7}$ %	16.3 %	18%
		M2:	61.8 %	$53.5^{+7.4}_{-7.6}$ %	25.8 %	$16.3^{+6.4}_{-4.9}$ %	16.8 %	
Combined Cuts		M1:	74.4 %	$74.1^{+3.4}_{-3.8}$ %	—	—	28.6 %	30%
		M2:	82.2 %	$88.4^{+4.0}_{-5.8}$ %	—	—	37.3 %	

Table D.6: Table of cut descriptions and efficiencies for simulated backgrounds and measured data for the 559 keV peak.
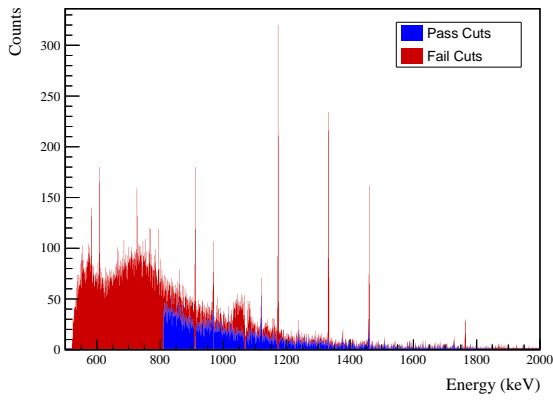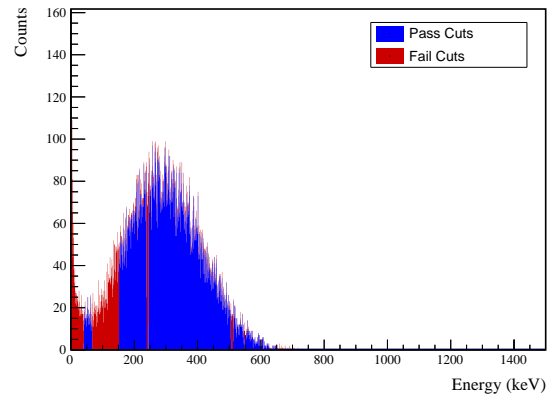
(a) Simulated BG Sum Energy Spectrum

(b) Simulated ES Sum Energy Spectrum
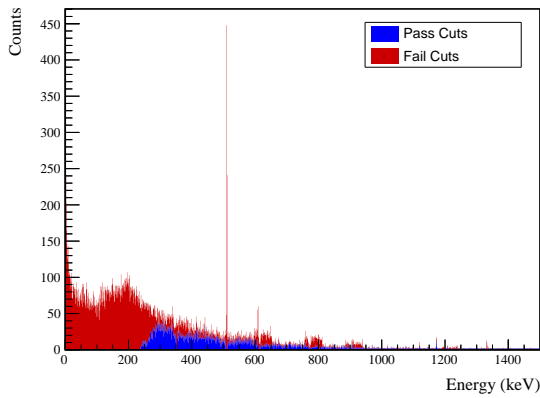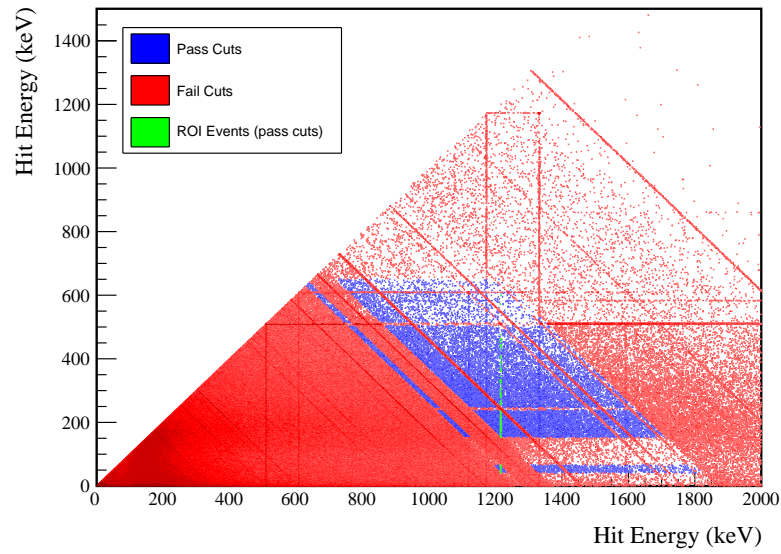

(c) Simulated BG Coincident Energy Spectrum
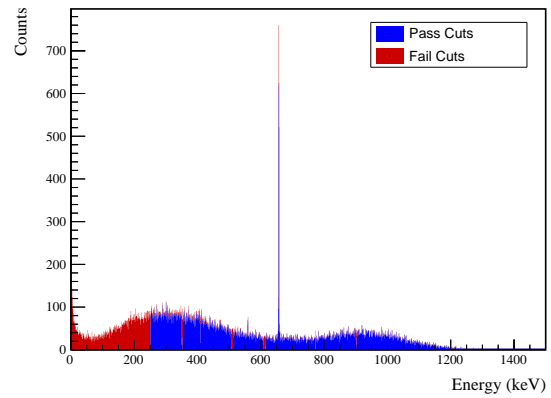
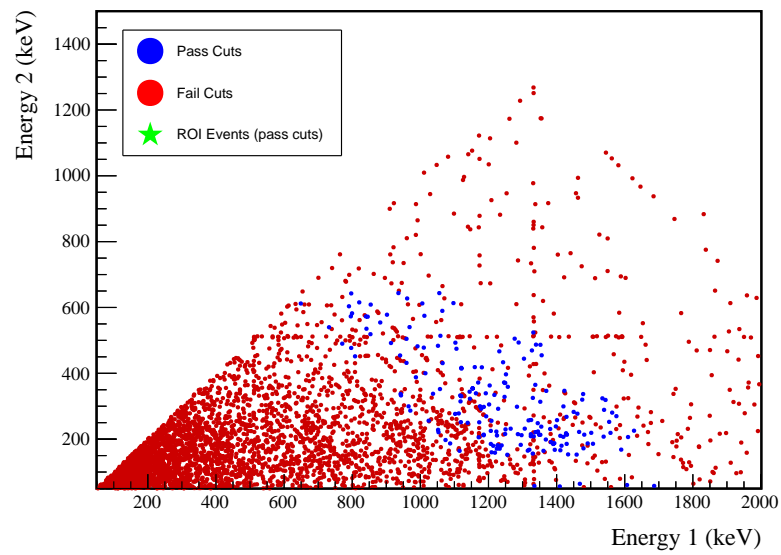(d) Simulated ES Coincident Energy Spectrum

Figure D.12: Sum energy and coincident energy spectra for the 559 keV peak.
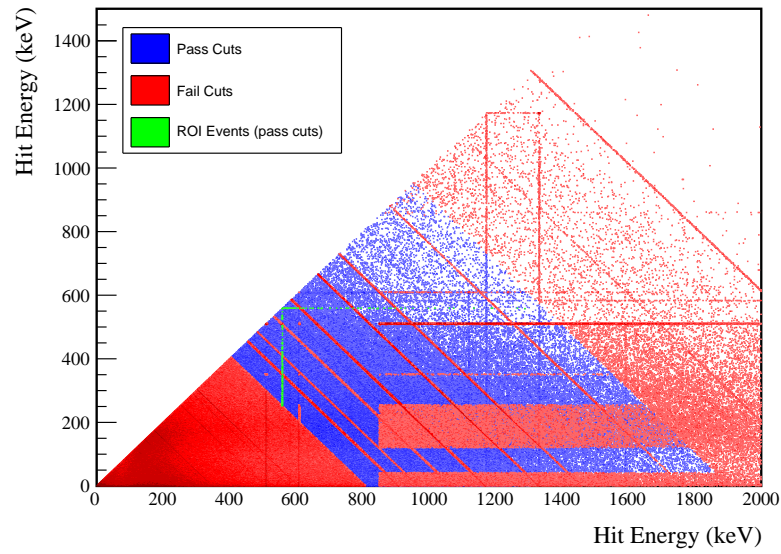
(a) Simulation
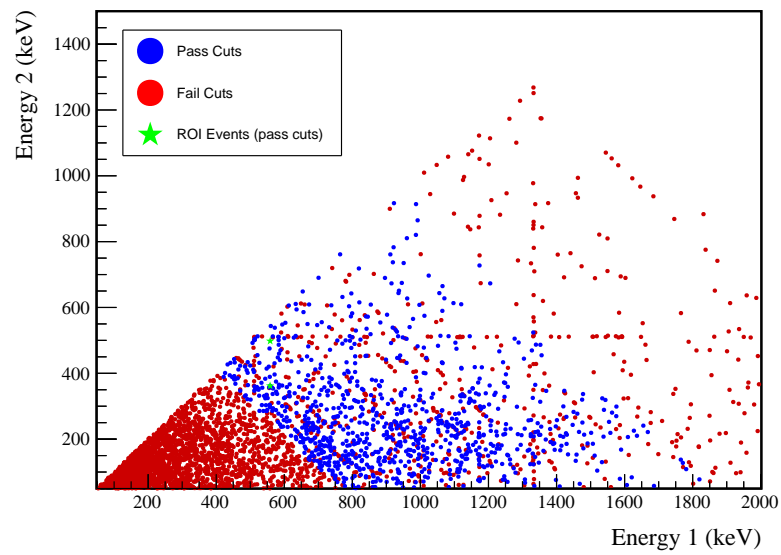
(b) Data

Figure D.13: Simulated and measured multiplicity 2 energy spectrum with sum and coincident energy cuts included for the 559 keV peak.
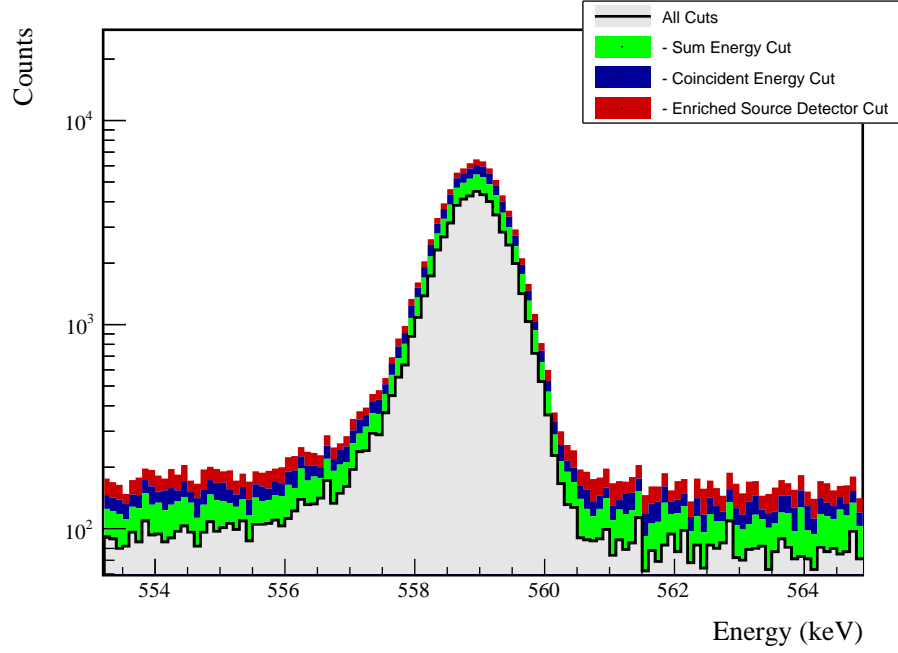
(a) Effect of all cuts on ROI

Source	Module 1 efficiency	Module 2 efficiency
Multi-Detector with Full Energy γ	$2.0 \pm 0.2\%$	$1.1 \pm 0.5\%$
Region of Interest	$87.1 \pm 2.1\%$	$87.1 \pm 2.1\%$
Dead Layer	$75.3 \pm 4.2\%$	$67.3 \pm 5.7\%$
Detector Dead Times	$97.6 \pm 1.1\%$	$98.2 \pm 0.9\%$
Enriched Source Detector Cut	$96.5 \pm\ <0.1\%$	$89.0 \pm\ <0.1\%$
Coincident Energy Cut	$89.7 \pm 0.5\%$	$85.9 \pm 0.5\%$
Sum Energy Cut	$78.3 \pm 0.5\%$	$73.3 \pm 0.5\%$
Final Efficiency	$0.99 \pm 0.12\%$	$0.44 \pm 0.20\%$

(b) Table of efficiencies

Figure D.14: Plot showing effect of cuts applied sequentially on ROI peak and table of detection efficiencies for the 559 keV peak.
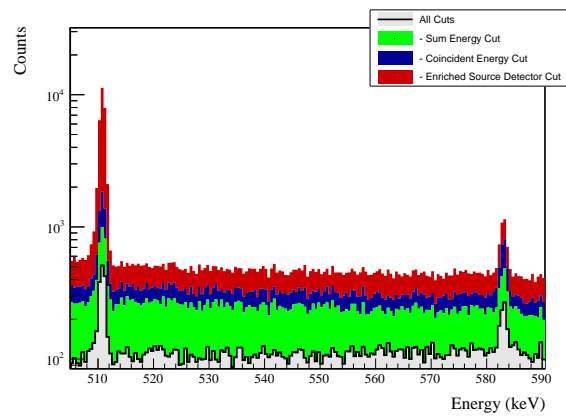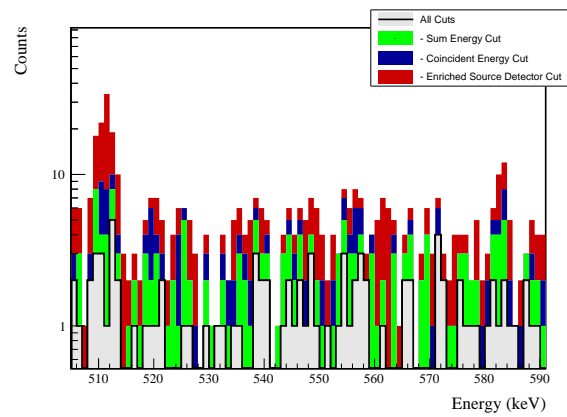
(a) Simulated BG Cuts

(b) Data Cuts
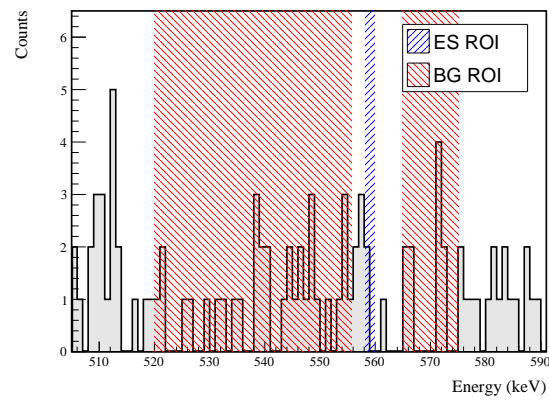
(c) Data ROIs

Figure D.15: Effect of all cuts applied to measured and simulated background data.

D.3.2 657 keV peak
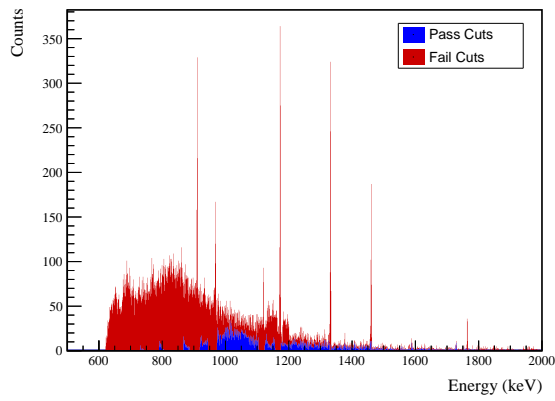
(a) Simulated BG Sum Energy Spectrum
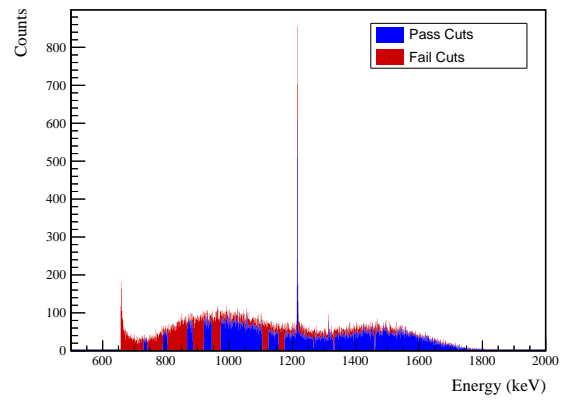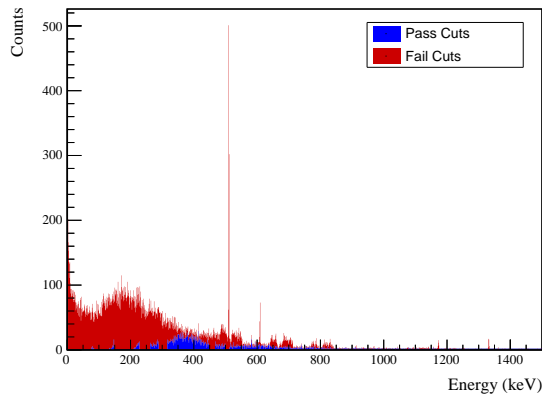
(b) Simulated ES Sum Energy Spectrum

(c) Simulated BG Coincident Energy Spectrum

(d) Simulated ES Coincident Energy Spectrum

Figure D.16: Sum energy and coincident energy spectra for the 657 keV peak.

Table D.7: Table of energy estimation uncertainties for the 657 keV peak.

DS	E_{peak} (keV)	σ_{fit} (keV)	σ_{drift} (keV)	σ (keV)	$f_{t,fit}$	τ_{fit} (keV)	$\delta_{\mu,fit}$ (keV)	$\delta_{\mu,NL}$ (keV)	$\delta_{\mu,drift}$ (keV)	$\delta_{\mu,xtalk}$ (keV)	$\delta_{\mu,peak}$ (keV)	δ_μ (keV)	FWHM (keV)	$\delta_{fwhm,fit}$ (keV)	$\delta_{fwhm,drift}$ (keV)	$\delta_{fwhm,xtalk}$ (keV)	δ_{FWHM} (keV)	δ_α	$E_{ROI,1}$ (keV)	$E_{ROI,2}$ (keV)	ϵ_{ROI}	$\sigma_{\epsilon_{ROI}}$
DS1	657.041	0.500	0.074	0.505	0.230	0.579	0.002	0.104	0.003	0.012	0.005	0.105	1.256	0.001	0.039	0.011	0.040	0.032	656.051	657.858	0.873	0.013
DS2	657.041	0.502	0.064	0.506	0.249	0.580	0.002	0.067	0.005	0.012	0.005	0.068	1.263	0.001	0.107	0.011	0.108	0.085	656.035	657.856	0.875	0.028
DS3	657.041	0.510	0.078	0.516	0.224	0.568	0.002	0.026	0.028	0.012	0.005	0.040	1.278	0.001	0.073	0.011	0.074	0.058	656.039	657.874	0.879	0.019
DS4	657.041	0.493	0.090	0.501	0.108	0.490	0.002	0.076	0.012	0.012	0.005	0.078	1.207	0.001	0.106	0.011	0.107	0.088	656.147	657.865	0.890	0.029
DS5a	657.041	0.606	0.100	0.614	0.106	0.924	0.002	0.079	0.006	0.012	0.005	0.080	1.481	0.002	0.055	0.011	0.056	0.038	655.948	658.045	0.878	0.013
DS5b	657.041	0.509	0.087	0.517	0.158	0.562	0.001	0.020	0.013	0.012	0.005	0.027	1.259	0.001	0.125	0.011	0.125	0.100	656.086	657.884	0.886	0.032
DS5c	657.041	0.500	0.100	0.510	0.174	0.555	0.002	0.037	0.035	0.012	0.005	0.053	1.247	0.001	0.162	0.011	0.162	0.130	656.087	657.872	0.883	0.042
DS6a	657.041	0.495	0.051	0.497	0.191	0.524	0.001	0.069	0.030	0.012	0.005	0.076	1.221	0.001	0.041	0.011	0.042	0.035	656.099	657.850	0.882	0.012

(a) Simulation

(b) Data

Figure D.17: Simulated and measured multiplicity 2 energy spectrum with sum and coincident energy cuts included for the 657 keV peak.
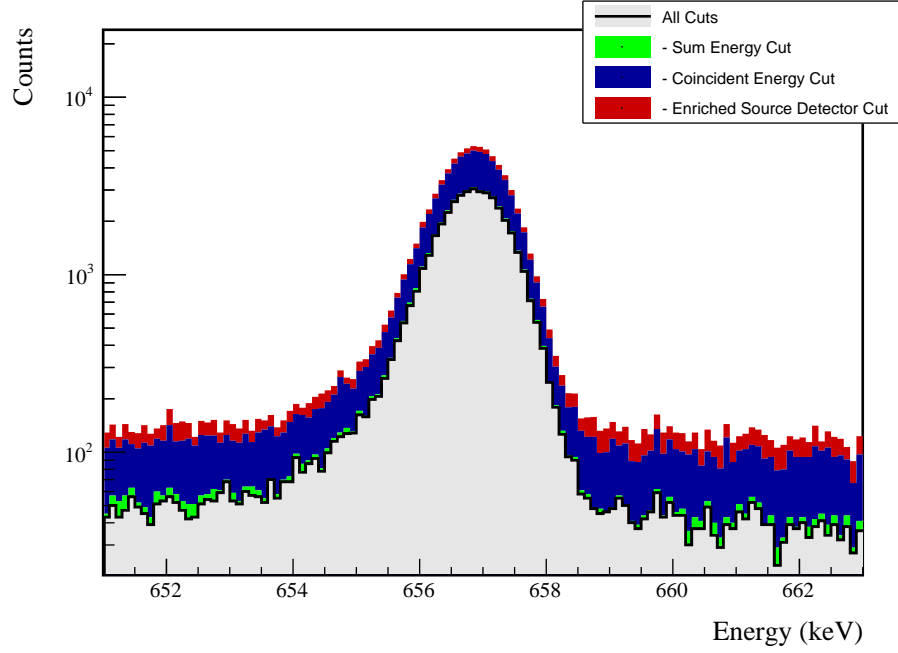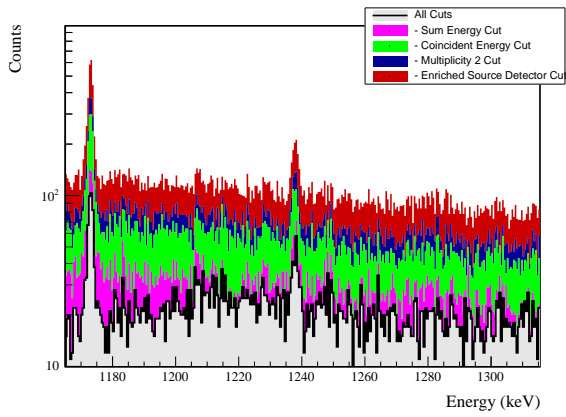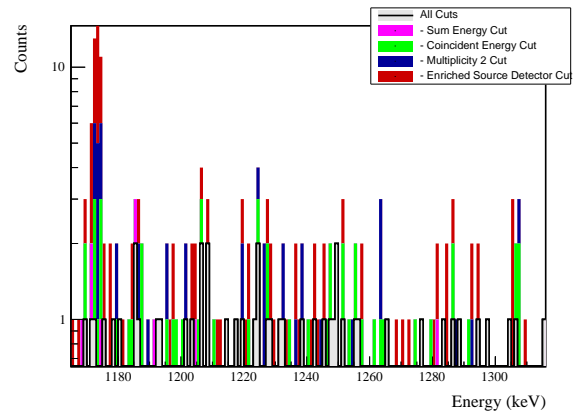
(a) Effect of all cuts on ROI

Source	Module 1 efficiency	Module 2 efficiency
Multi-Detector with Full Energy γ	$1.8 \pm 0.2\%$	$1.0 \pm 0.5\%$
Region of Interest	$88.0 \pm 1.8\%$	$88.0 \pm 1.8\%$
Dead Layer	$75.6 \pm 4.1\%$	$66.9 \pm 5.8\%$
Detector Dead Times	$97.8 \pm 1.0\%$	$98.2 \pm 0.8\%$
Enriched Source Detector Cut	$96.6 \pm\ <0.1\%$	$88.6 \pm\ <0.1\%$
Coincident Energy Cut	$62.2 \pm 0.5\%$	$65.6 \pm 0.5\%$
Sum Energy Cut	$73.7 \pm 0.5\%$	$68.9 \pm 0.5\%$
Final Efficiency	$0.75 \pm 0.10\%$	$0.35 \pm 0.17\%$

(b) Table of efficiencies

Figure D.18: Plot showing effect of cuts applied sequentially on ROI peak and table of detection efficiencies for the 657 keV peak.
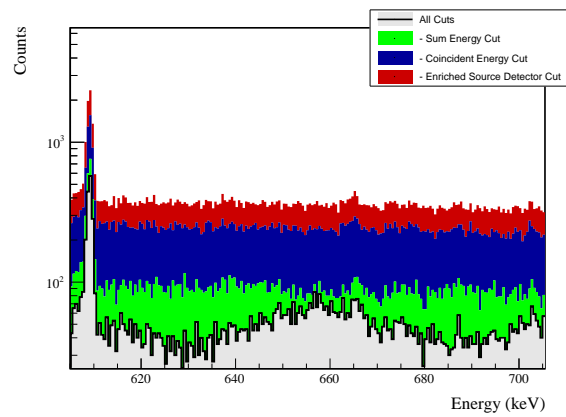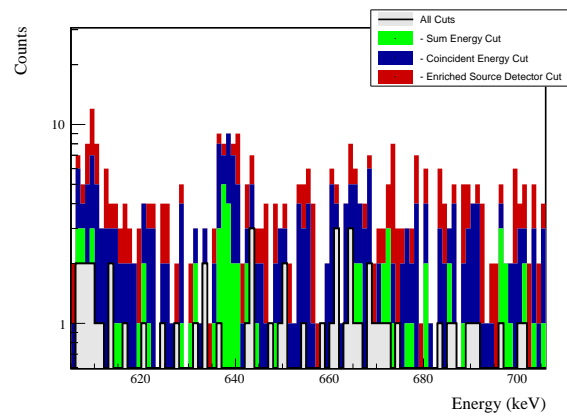
(a) Simulated BG Cuts
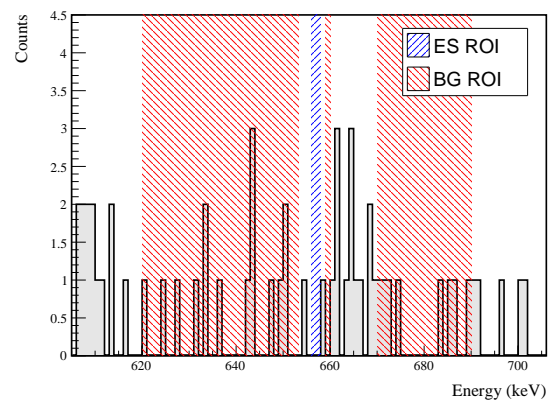
(b) Data Cuts

(c) Data ROIs

Figure D.19: Effect of all cuts applied to measured and simulated background data.

Cut Name	Cut Description		$\langle\epsilon_{total}\rangle$	$\hat{\epsilon}_{total}$	$\langle\epsilon_{unique}\rangle$	$\hat{\epsilon}_{unique}$	Sacrifice	ΔDP
Enriched Source	`Any other detector: isEnr`	M1:	23.9 %	$25.2^{+3.9}_{-3.5}$ %	7.2 %	$7.4^{+2.6}_{-2.0}$ %	1.7 %	21%
		M2:	43.7 %	$60.4^{+6.8}_{-7.2}$ %	13.5 %	$14.6^{+5.8}_{-4.4}$ %	5.5 %	
Detector Cut	`No other detector: ( ((energy>71.8) || (energy>84.4`							
	`&& energy<133.4) || (energy>148.4 && energy<209.8) ||`							
	`(energy>228.4 && energy<262.) || (energy>288.4 &&`							
Coincident	`energy<316.2) || (energy>447.4 && energy<467.2) ||`	M1:	54.0 %	51.9 ± 4.3 %	16.7 %	$17.0^{+3.5}_{-3.0}$ %	13.6 %	17%
	`(energy>499.6 && energy<512.8) || (energy>607.6 &&`							
Energy Cut	`energy<610.4) || (energy>1165.8 && energy<1175.6) ||`	M2:	47.6 %	$37.5^{+7.2}_{-6.7}$ %	13.1 %	$10.4^{+5.2}_{-3.6}$ %	8.0 %	
	`(energy>1187.6)) && isEnr ) || ( ((energy<55.2) ||`							
	`(energy>503.6 && energy<516.4) || (energy>820.)) &&`							
	`!isEnr )`							
	`Not:     (sumE<729.)  || (sumE>741.8 && sumE<790.4)`							
	`|| (sumE<805.4 && sumE<867.)  || (sumE>885.6 &&`							
	`sumE<919.8) || (sumE>945.  && sumE<973.2) ||`							
Sum Energy Cut	`(sumE>1104.4 && sumE<1123.8) || (sumE>1156.4 &&`	M1:	60.9 %	$57.0^{+4.2}_{-4.3}$ %	14.3 %	$15.6^{+3.4}_{-2.9}$ %	1.4 %	29%
	`sumE<1174.8) || (sumE>1328.8 && sumE<1333.6) ||`	M2:	60.3 %	$64.6^{+6.5}_{-7.1}$ %	9.7 %	$8.3^{+4.9}_{-3.2}$ %	1.4 %	
	`(sumE>1458.8 && sumE<1461.8) || (sumE>1762.4 &&`							
	`sumE<1766.)  || (sumE>1897.4)`							
Combined Cuts		M1:	86.5 %	$85.2^{+2.8}_{-3.3}$ %	—	—	42.0 %	34%
		M2:	89.9 %	$93.8^{+2.7}_{-4.5}$ %	—	—	45.2 %	

Table D.8: Table of cut descriptions and efficiencies for simulated backgrounds and measured data for the 657 keV peak.

D.3.3 1216 keV peak
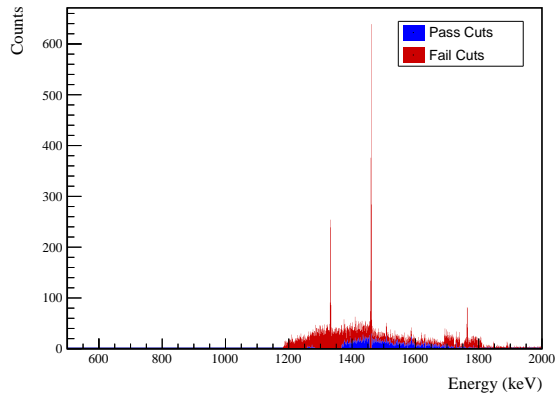
(a) Simulated BG Sum Energy Spectrum
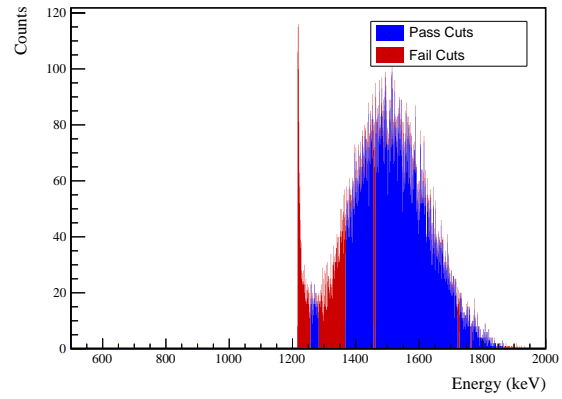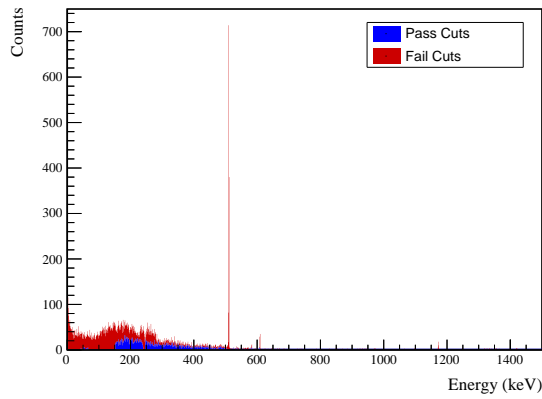
(b) Simulated ES Sum Energy Spectrum

(c) Simulated BG Coincident Energy Spectrum

(d) Simulated ES Coincident Energy Spectrum

Figure D.20: Sum energy and coincident energy spectra for the 1216 keV peak.

229

Table D.9: Table of energy estimation uncertainties for the 1216 keV peak.

DS	E_{peak} (keV)	σ_{fit} (keV)	σ_{drift} (keV)	σ (keV)	$f_{t,fit}$	τ_{fit} (keV)	$\delta_{\mu,fit}$ (keV)	$\delta_{\mu,NL}$ (keV)	$\delta_{\mu,drift}$ (keV)	$\delta_{\mu,xtalk}$ (keV)	$\delta_{\mu,peak}$ (keV)	δ_μ (keV)	FWHM (keV)	$\delta_{fwhm,fit}$ (keV)	$\delta_{fwhm,drift}$ (keV)	$\delta_{fwhm,xtalk}$ (keV)	δ_{FWHM} (keV)	δ_α	$E_{ROI,1}$ (keV)	$E_{ROI,2}$ (keV)	ϵ_{ROI}	$\sigma_{\epsilon_{ROI}}$
DS1	1216.104	0.705	0.137	0.718	0.230	0.945	0.003	0.104	0.005	0.012	0.020	0.107	1.787	0.001	0.039	0.011	0.040	0.023	1214.691	1217.262	0.868	0.008
DS2	1216.104	0.710	0.119	0.720	0.249	0.951	0.003	0.067	0.008	0.012	0.020	0.072	1.803	0.001	0.107	0.011	0.108	0.060	1214.663	1217.262	0.867	0.019
DS3	1216.104	0.715	0.144	0.729	0.224	0.925	0.003	0.026	0.051	0.012	0.020	0.062	1.812	0.001	0.073	0.011	0.074	0.041	1214.679	1217.281	0.872	0.013
DS4	1216.104	0.697	0.167	0.717	0.108	0.746	0.003	0.076	0.022	0.012	0.020	0.083	1.726	0.001	0.106	0.011	0.107	0.062	1214.829	1217.278	0.889	0.021
DS5a	1216.104	0.838	0.185	0.859	0.106	1.316	0.004	0.079	0.012	0.012	0.020	0.083	2.070	0.002	0.055	0.011	0.056	0.027	1214.581	1217.504	0.877	0.009
DS5b	1216.104	0.716	0.161	0.734	0.158	0.963	0.002	0.020	0.024	0.012	0.020	0.039	1.791	0.001	0.125	0.011	0.125	0.070	1214.743	1217.299	0.878	0.023
DS5c	1216.104	0.703	0.185	0.727	0.174	0.932	0.003	0.037	0.066	0.012	0.020	0.079	1.783	0.001	0.162	0.011	0.162	0.091	1214.738	1217.287	0.876	0.030
DS6a	1216.104	0.693	0.095	0.700	0.191	0.873	0.002	0.069	0.055	0.012	0.020	0.092	1.723	0.001	0.041	0.011	0.042	0.025	1214.771	1217.241	0.875	0.009

(a) Simulation

(b) Data

Figure D.21: Simulated and measured multiplicity 2 energy spectrum with sum and coincident energy cuts included for the 1216 keV peak.
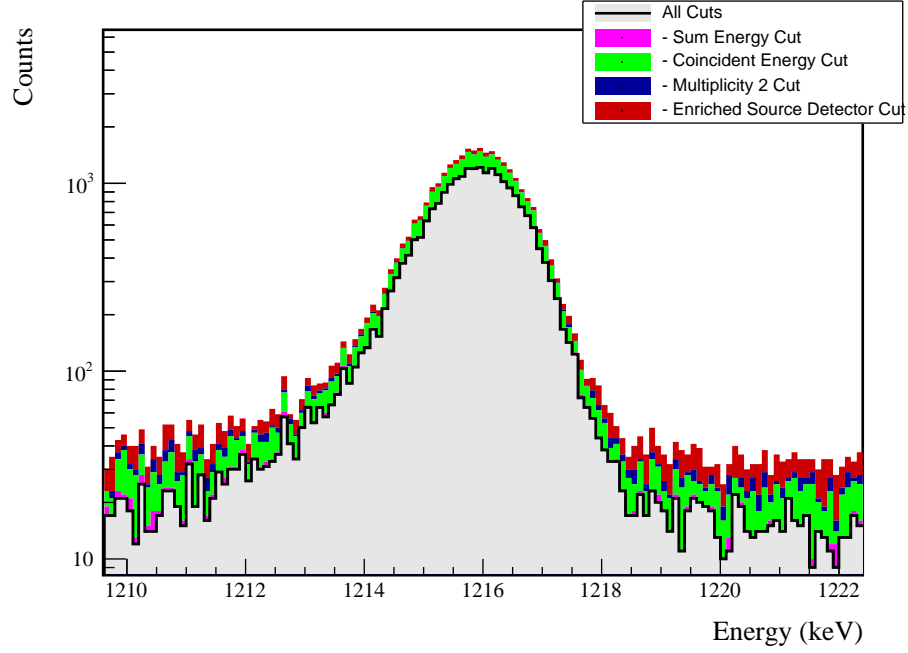
(a) Effect of all cuts on ROI

Source	Module 1 efficiency	Module 2 efficiency
Multi-Detector with Full Energy γ	$0.8 \pm 0.2\%$	$0.4 \pm 0.5\%$
Region of Interest	$87.5 \pm 1.3\%$	$87.5 \pm 1.3\%$
Dead Layer	$73.9 \pm 4.4\%$	$63.6 \pm 6.4\%$
Detector Dead Times	$97.5 \pm 1.1\%$	$98.1 \pm 0.9\%$
Enriched Source Detector Cut	$97.0 \pm\ <0.1\%$	$92.5 \pm\ <0.1\%$
Multiplicity 2 Cut	$99.6 \pm\ <0.1\%$	$99.8 \pm\ <0.1\%$
Coincident Energy Cut	$83.5 \pm 0.5\%$	$84.2 \pm 0.5\%$
Sum Energy Cut	$82.9 \pm 0.5\%$	$82.4 \pm 0.5\%$
Final Efficiency	$0.43 \pm 0.11\%$	$0.18 \pm 0.22\%$

(b) Table of efficiencies

Figure D.22: Plot showing effect of cuts applied sequentially on ROI peak and table of detection efficiencies for the 1216 keV peak.

(a) Simulated BG Cuts
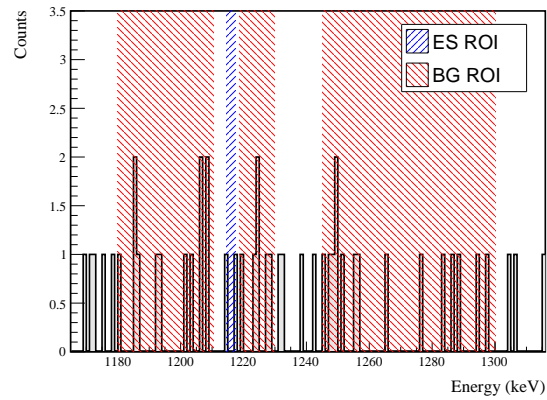
(b) Data Cuts

(c) Data ROIs

Figure D.23: Effect of all cuts applied to measured and simulated background data.

| Cut Name	Cut Description		$\langle \epsilon_{total} \rangle$	$\hat{\epsilon}_{total}$	$\langle \epsilon_{unique} \rangle$	$\hat{\epsilon}_{unique}$	Sacrifice	ΔDP
Enriched Source Detector Cut	`Any other detector: isEnr`	M1:	26.9 %	$16.9^{+4.5}_{-3.7}$ %	15.1 %	$8.4^{+3.6}_{-2.6}$ %	2.4 %	23%
		M2:	43.9 %	$61.9^{+9.8}_{-10.9}$ %	25.8 %	$28.6^{+10.7}_{-8.7}$ %	5.8 %	
Multiplicity 2 Cut	`m==2`	M1:	15.3 %	$16.9^{+4.5}_{-3.7}$ %	4.0 %	$3.6^{+2.7}_{-1.6}$ %	0.1 %	5%
		M2:	11.9 %	$9.5^{+8.4}_{-4.7}$ %	3.2 %	$0.0^{+4.5}_{--0.0}$ %	0.0 %	
Coincident Energy Cut	`No other detector: ( ((energy<40.8) || (energy>66.6 && energy<152.2) || (energy>239.6 && energy<245.8) || (energy>505.2 && energy<512.6) || (energy>608.8 && energy<610.) || (energy>650.8)) && isEnr )`	M1:	34.1 %	$38.6^{+5.4}_{-5.2}$ %	10.8 %	$8.4^{+3.6}_{-2.6}$ %	0.3 %	14%
		M2:	25.9 %	$14.3^{+9.3}_{-6.0}$ %	9.3 %	$4.8^{+7.0}_{-2.9}$ %	0.3 %	
Sum Energy Cut	`Not: (sumE<1257.) || (sumE>1283. && sumE<1367.4) || (sumE>1455.2 && sumE<1462.) || (sumE>1721.8 && sumE<1728.6) || (sumE>1762. && sumE<1766.) || (sumE>1845.6 && sumE<1851.2) || (sumE>1866.6)`	M1:	40.9 %	$38.6^{+5.4}_{-5.2}$ %	10.5 %	$4.8^{+2.9}_{-1.9}$ %	0.5 %	12%
		M2:	35.9 %	$42.9^{+10.9}_{-10.2}$ %	6.0 %	$0.0^{+4.5}_{--0.0}$ %	0.5 %	
Combined Cuts		M1:	77.1 %	$65.1^{+5.0}_{-5.4}$ %	—	—	20.1 %	44%
		M2:	79.8 %	$81.0^{+7.1}_{-9.9}$ %	—	—	23.8 %	

Table D.10: Table of cut descriptions and efficiencies for simulated backgrounds and measured data for the 1216 keV peak.

D.4 $0\nu\beta\beta$ **to** 0_1^+

Note that both the 559 and 563 keV peaks will be shown together since they use the same sets of cuts.
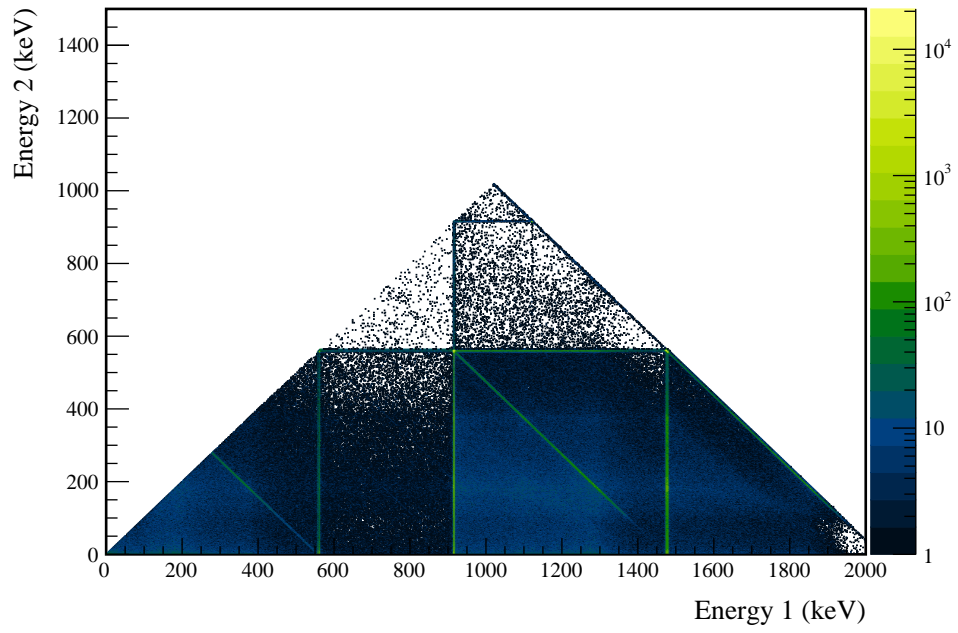
Figure D.24: Simulated multiplicity 2 energy spectrum of the $0\nu\beta\beta$ to 0_1^+ decay mode

Table D.11: Table of energy estimation uncertainties for the 559 and 563 keV peaks.

| DS	E_{peak} (keV)	σ_{fit} (keV)	σ_{drift} (keV)	σ (keV)	$f_{t,fit}$	τ_{fit} (keV)	$\delta_{\mu,fit}$ (keV)	$\delta_{\mu,NL}$ (keV)	$\delta_{\mu,drift}$ (keV)	$\delta_{\mu,xtalk}$ (keV)	$\delta_{\mu,peak}$ (keV)	δ_μ (keV)	FWHM (keV)	$\delta_{fwhm,fit}$ (keV)	$\delta_{fwhm,drift}$ (keV)	$\delta_{fwhm,xtalk}$ (keV)	δ_{FWHM} (keV)	δ_α	$E_{ROI,1}$ (keV)	$E_{ROI,2}$ (keV)	ϵ_{ROI}	$\sigma_{\epsilon_{ROI}}$
DS1	559.101	0.460	0.063	0.464	0.230	0.515	0.001	0.104	0.002	0.012	0.005	0.105	1.152	0.001	0.039	0.011	0.040	0.035	558.083	559.935	0.907	0.012
DS2	559.101	0.461	0.055	0.464	0.249	0.515	0.002	0.067	0.004	0.012	0.005	0.068	1.158	0.001	0.107	0.011	0.108	0.093	558.066	559.934	0.910	0.025
DS3	559.101	0.470	0.066	0.474	0.224	0.505	0.001	0.026	0.024	0.012	0.005	0.038	1.174	0.001	0.073	0.011	0.074	0.063	558.071	559.953	0.914	0.017
DS4	559.101	0.455	0.077	0.461	0.108	0.445	0.002	0.076	0.010	0.012	0.005	0.078	1.111	0.001	0.106	0.011	0.107	0.096	558.186	559.943	0.922	0.026
DS5a	559.101	0.560	0.085	0.567	0.106	0.855	0.002	0.079	0.005	0.012	0.005	0.080	1.367	0.002	0.055	0.011	0.056	0.041	557.975	560.129	0.910	0.012
DS5b	559.101	0.469	0.074	0.475	0.158	0.491	0.001	0.020	0.011	0.012	0.005	0.026	1.157	0.001	0.125	0.011	0.125	0.108	558.122	559.962	0.919	0.029
DS5c	559.101	0.460	0.085	0.468	0.174	0.489	0.001	0.037	0.030	0.012	0.005	0.050	1.145	0.001	0.162	0.011	0.162	0.142	558.123	559.948	0.917	0.037
DS6a	559.101	0.456	0.044	0.458	0.191	0.463	0.001	0.069	0.025	0.012	0.005	0.075	1.123	0.000	0.041	0.011	0.042	0.038	558.134	559.928	0.916	0.011
DS1	563.178	0.461	0.064	0.466	0.230	0.518	0.001	0.104	0.002	0.012	0.005	0.105	1.156	0.001	0.039	0.011	0.040	0.035	562.156	564.015	0.907	0.012
DS2	563.178	0.463	0.055	0.466	0.249	0.517	0.002	0.067	0.004	0.012	0.005	0.068	1.162	0.001	0.107	0.011	0.108	0.093	562.139	564.014	0.910	0.025
DS3	563.178	0.471	0.066	0.476	0.224	0.508	0.001	0.026	0.024	0.012	0.005	0.038	1.179	0.001	0.073	0.011	0.074	0.063	562.144	564.033	0.914	0.017
DS4	563.178	0.457	0.077	0.463	0.108	0.447	0.002	0.076	0.010	0.012	0.005	0.078	1.115	0.001	0.106	0.011	0.107	0.096	562.260	564.023	0.922	0.026
DS5a	563.178	0.562	0.086	0.569	0.106	0.858	0.002	0.079	0.006	0.012	0.005	0.080	1.372	0.002	0.055	0.011	0.056	0.041	562.048	564.210	0.910	0.011
DS5b	563.178	0.471	0.074	0.477	0.158	0.494	0.001	0.020	0.011	0.012	0.005	0.026	1.162	0.001	0.125	0.011	0.125	0.108	562.196	564.042	0.919	0.029
DS5c	563.178	0.462	0.086	0.470	0.174	0.492	0.001	0.037	0.030	0.012	0.005	0.050	1.149	0.001	0.162	0.011	0.162	0.141	562.197	564.028	0.917	0.037
DS6a	563.178	0.457	0.044	0.459	0.191	0.465	0.001	0.069	0.026	0.012	0.005	0.075	1.127	0.000	0.041	0.011	0.042	0.038	562.208	564.008	0.915	0.011

| Cut Name	Cut Description		$\langle\epsilon_{total}\rangle$	$\hat{\epsilon}_{total}$	$\langle\epsilon_{unique}\rangle$	$\hat{\epsilon}_{unique}$	Sacrifice	ΔDP
Enriched Source		M1:	23.2 %	$27.2^{+3.8}_{-3.5}$ %	0.5 %	$0.7^{+1.1}_{-0.4}$ %	1.3 %	13%
Detector Cut	Any other detector: isEnr	M2:	42.7 %	$62.8^{+7.0}_{-7.6}$ %	0.9 %	$7.0^{+4.9}_{-3.0}$ %	3.0 %	
Coincident	No other detector: (((energy<53.) ‖ (energy>469.6 && energy<525.2) ‖ (energy>587.8 && energy<853.2) ‖ (energy>1074.6 && energy<1079.2) ‖ (energy>1117.2 && energy<1121.8) ‖ (energy>1170.6 && energy<1175.) ‖ (energy>1331. && energy<1334.) ‖ (energy>1483.)) && isEnr) ‖ (((energy<44.8) ‖ (energy>508. && energy<522.6) ‖ (energy>1385.6)) && !isEnr)	M1:	28.8 %	$32.0^{+4.0}_{-3.7}$ %	0.8 %	$1.4^{+1.3}_{-0.7}$ %	4.5 %	9%
Energy Cut		M2:	26.9 %	$23.3^{+7.0}_{-5.8}$ %	0.5 %	$7.0^{+4.9}_{-3.0}$ %	2.9 %	
Sum Energy Cut	Not: (sumE<1472.) ‖ (sumE>1761.8 && sumE<1765.8) ‖ (sumE>2042.6)	M1:	97.1 %	$96.6^{+1.2}_{-1.8}$ %	50.9 %	49.0 ± 4.1 %	12.3 %	243%
		M2:	97.6 %	$86.0^{+4.5}_{-6.1}$ %	38.0 %	$27.9^{+7.3}_{-6.3}$ %	15.3 %	
Combined Cuts		M1:	98.4 %	$98.6^{+0.7}_{-1.3}$ %	–	–	26.5 %	298%
		M2:	99.1 %	$100.0^{+0.0}_{-2.3}$ %	–	–	35.9 %	

Table D.12: Table of cut descriptions and efficiencies for simulated backgrounds and measured data for the 559 and 563 keV peaks.
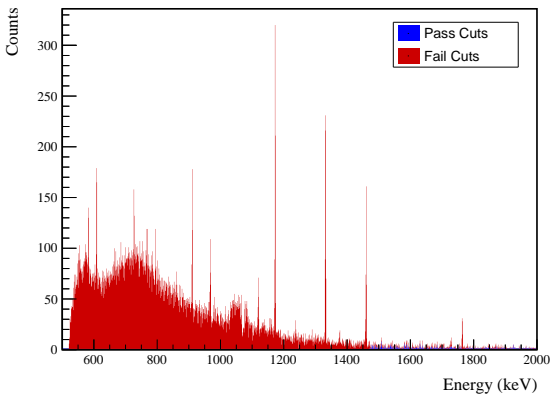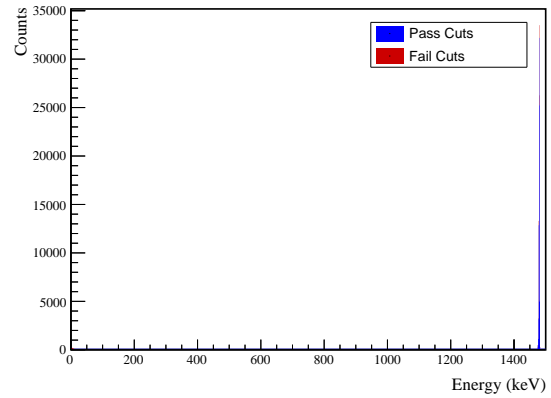
(a) Simulated BG Sum Energy Spectrum
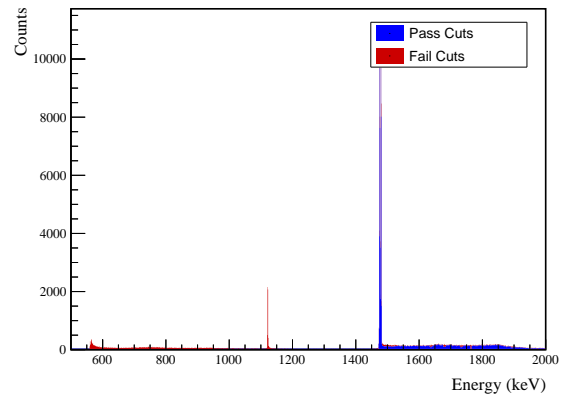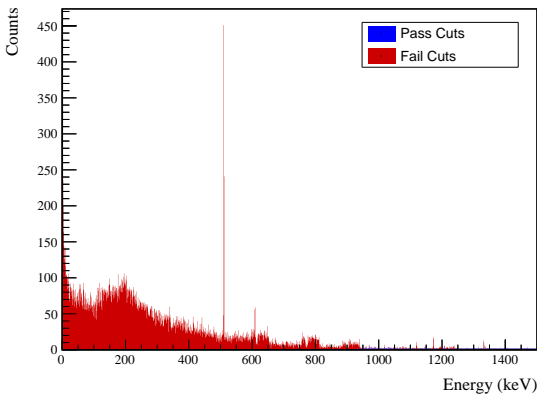
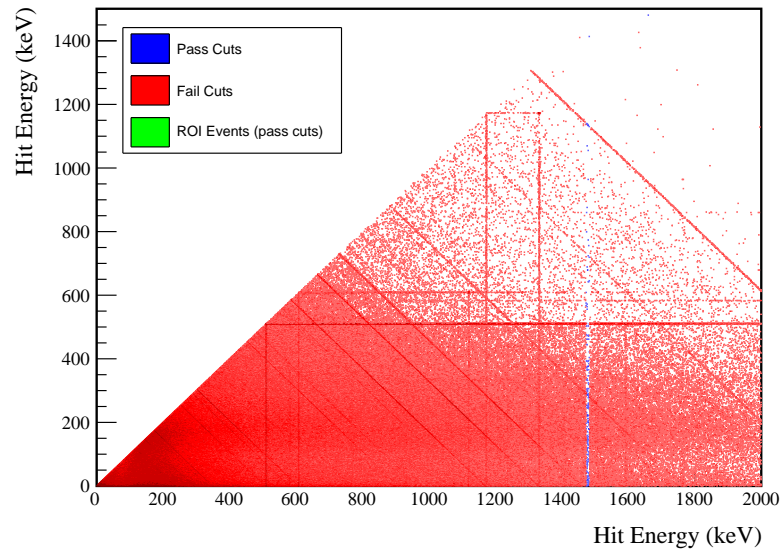(b) Simulated ES Sum Energy Spectrum
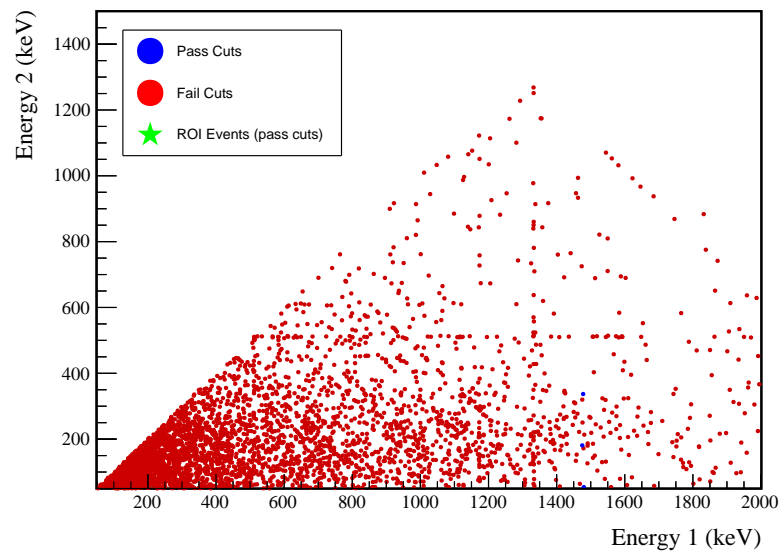

(c) Simulated BG Coincident Energy Spectrum
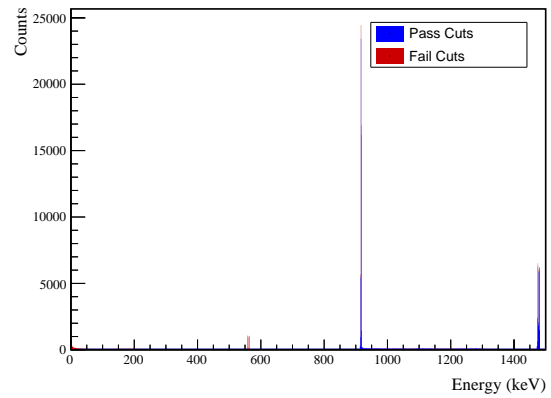
(d) Simulated ES Coincident Energy Spectrum

Figure D.25: Sum energy and coincident energy spectra for the 559 and 563 keV peaks.
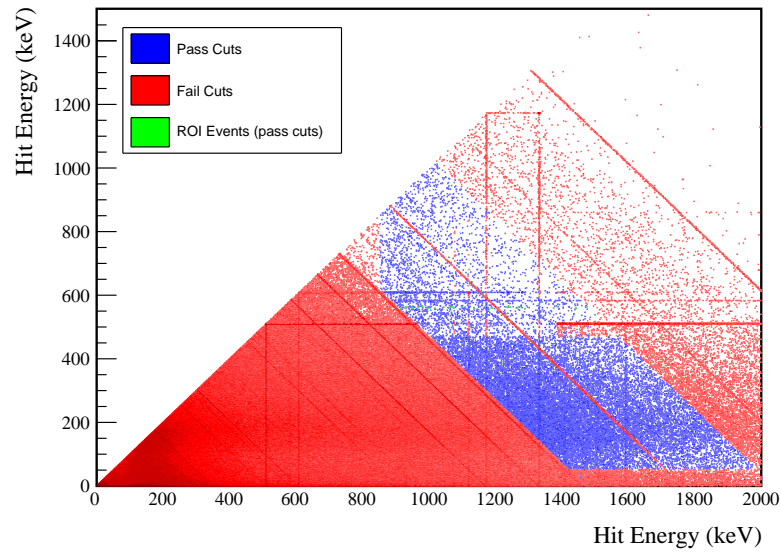
(a) Simulation
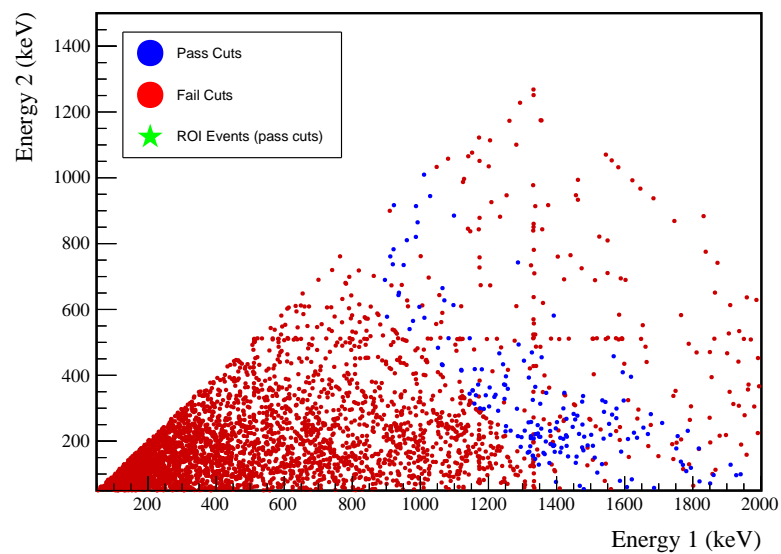
(b) Data

Figure D.26: Simulated and measured multiplicity 2 energy spectrum with sum and coincident energy cuts included for the 559 and 563 keV peaks.
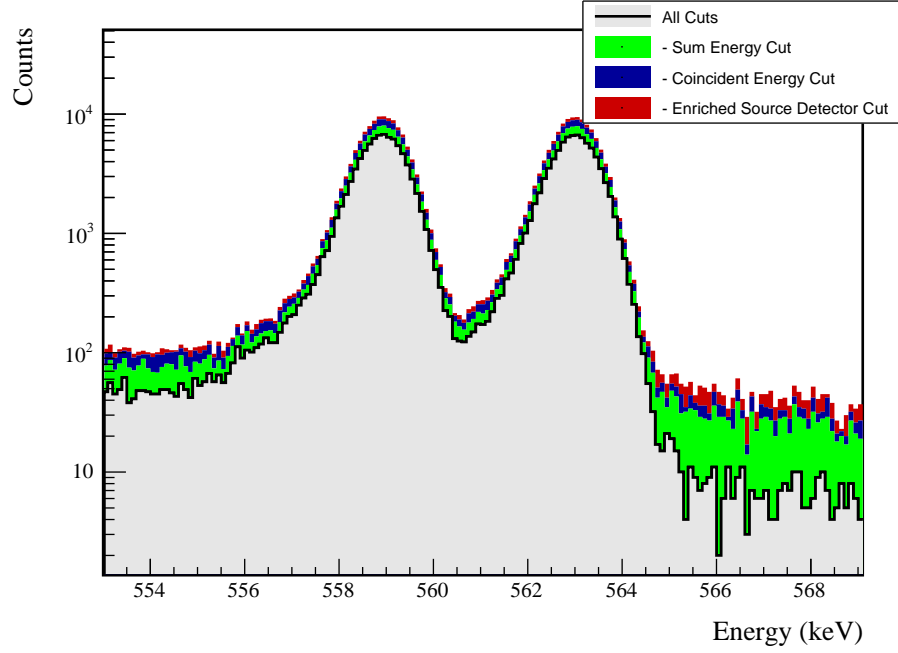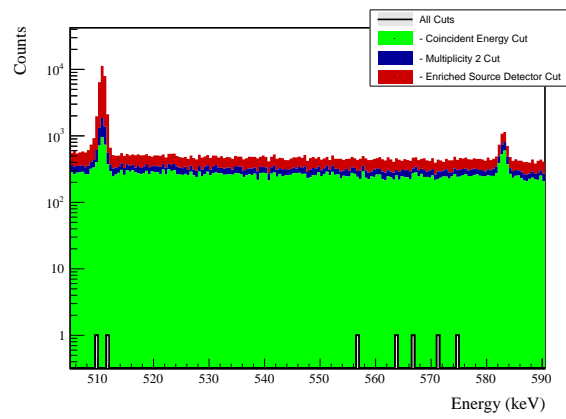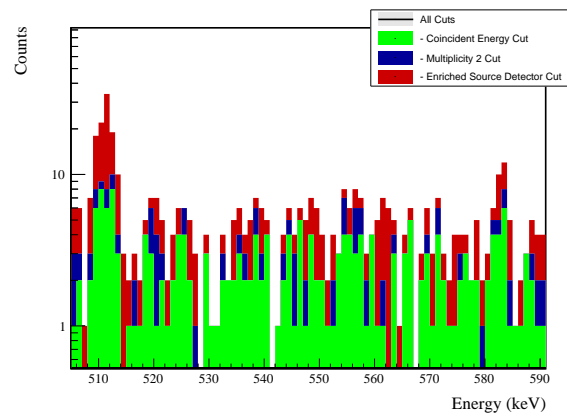
(a) Effect of all cuts on ROI

Source	Module 1 efficiency	Module 2 efficiency
Multi-Detector with Full Energy γ	$5.8 \pm 0.2\%$	$3.1 \pm 0.5\%$
Region of Interest	$91.3 \pm 1.1\%$	$91.3 \pm 1.1\%$
Dead Layer	$69.3 \pm 5.2\%$	$60.7 \pm 6.9\%$
Detector Dead Times	$97.6 \pm 1.1\%$	$98.1 \pm 0.9\%$
Enriched Source Detector Cut	$97.0 \pm\ <0.1\%$	$90.2 \pm\ <0.1\%$
Coincident Energy Cut	$88.2 \pm 0.3\%$	$87.4 \pm 0.3\%$
Sum Energy Cut	$79.6 \pm 0.3\%$	$70.9 \pm 0.3\%$
Final Efficiency	$3.10 \pm 0.26\%$	$1.34 \pm 0.26\%$

(b) Table of efficiencies

Figure D.27: Plot showing effect of cuts applied sequentially on ROI peak and table of detection efficiencies for the 559 and 563 keV peaks.
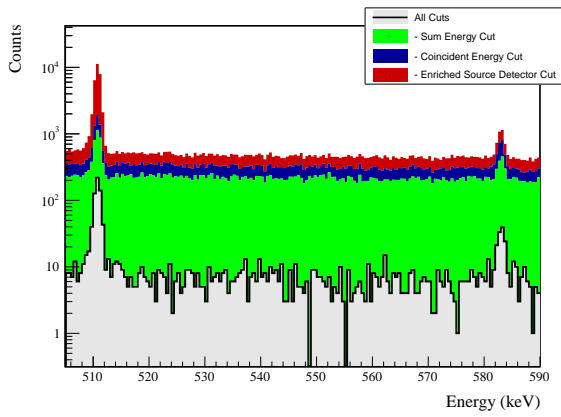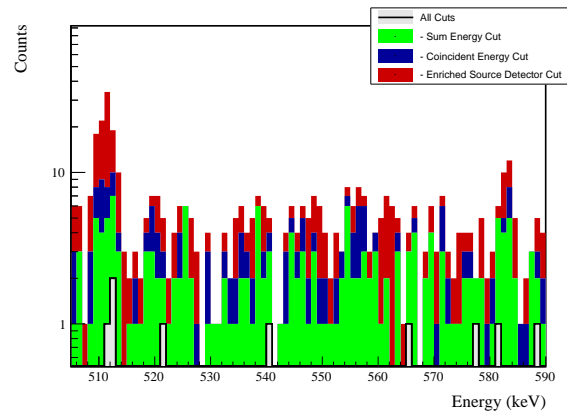
(a) Simulated BG Cuts

(b) Data Cuts
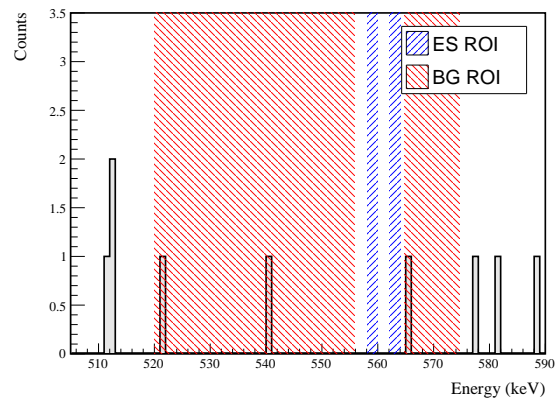
(c) Data ROIs

Figure D.28: Effect of all cuts applied to measured and simulated background data.
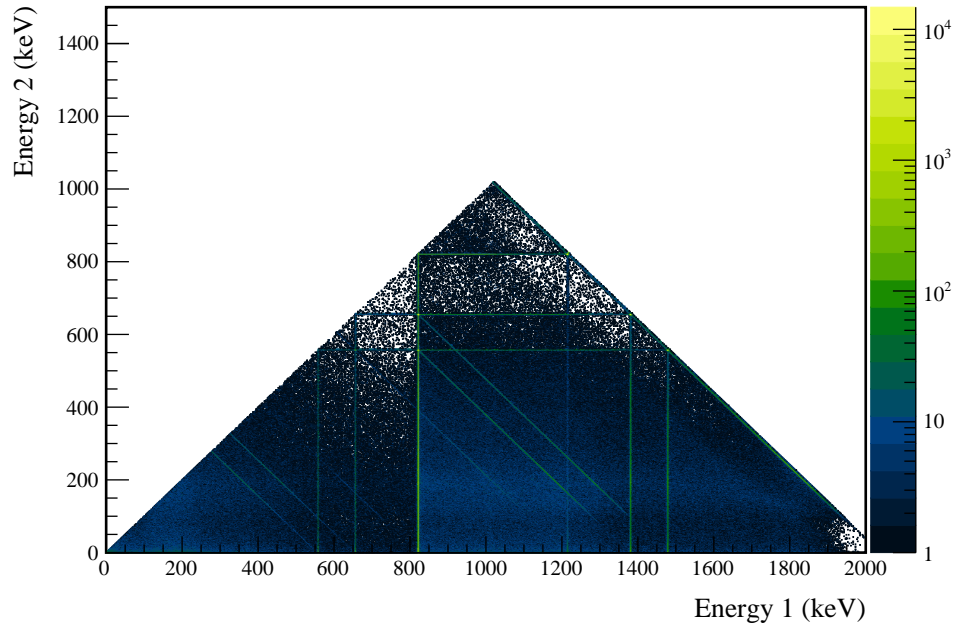
D.5 $0\nu\beta\beta$ ***to*** 2_1^+
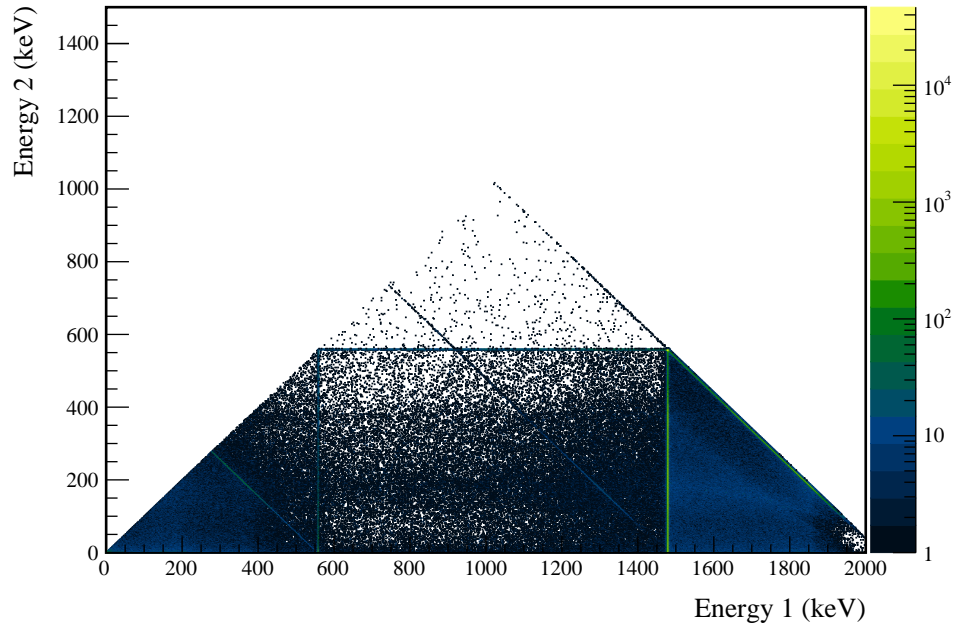
Figure D.29: Simulated multiplicity 2 energy spectrum of the $0\nu\beta\beta$ to 2_1^+ decay mode

Table D.13: Table of energy estimation uncertainties for the 559 keV peak.

DS	E_{peak} (keV)	σ_{fit} (keV)	σ_{drift} (keV)	σ (keV)	$f_{t,fit}$	τ_{fit} (keV)	$\delta_{\mu,fit}$ (keV)	$\delta_{\mu,NL}$ (keV)	$\delta_{\mu,drift}$ (keV)	$\delta_{\mu,xtalk}$ (keV)	$\delta_{\mu,peak}$ (keV)	δ_{μ} (keV)	FWHM (keV)	$\delta_{fwhm,fit}$ (keV)	$\delta_{fwhm,drift}$ (keV)	$\delta_{fwhm,xtalk}$ (keV)	δ_{FWHM} (keV)	δ_{α}	$E_{ROI,1}$ (keV)	$E_{ROI,2}$ (keV)	ϵ_{ROI}	$\sigma_{\epsilon_{ROI}}$
DS1	559.101	0.460	0.063	0.464	0.230	0.515	0.001	0.104	0.002	0.012	0.005	0.105	1.152	0.001	0.039	0.011	0.040	0.035	558.052	559.959	0.915	0.011
DS2	559.101	0.461	0.055	0.464	0.249	0.515	0.002	0.067	0.004	0.012	0.005	0.068	1.158	0.001	0.107	0.011	0.108	0.093	558.035	559.957	0.917	0.023
DS3	559.101	0.470	0.066	0.474	0.224	0.505	0.001	0.026	0.024	0.012	0.005	0.038	1.174	0.001	0.073	0.011	0.074	0.063	558.039	559.977	0.921	0.016
DS4	559.101	0.455	0.077	0.461	0.108	0.445	0.002	0.076	0.010	0.012	0.005	0.078	1.111	0.001	0.106	0.011	0.107	0.096	558.161	559.966	0.929	0.024
DS5a	559.101	0.560	0.085	0.567	0.106	0.855	0.002	0.079	0.005	0.012	0.005	0.080	1.367	0.002	0.055	0.011	0.056	0.041	557.942	560.158	0.918	0.011
DS5b	559.101	0.469	0.074	0.475	0.158	0.491	0.001	0.020	0.011	0.012	0.005	0.026	1.157	0.001	0.125	0.011	0.125	0.108	558.094	559.986	0.927	0.027
DS5c	559.101	0.460	0.085	0.468	0.174	0.489	0.001	0.037	0.030	0.012	0.005	0.050	1.145	0.001	0.162	0.011	0.162	0.142	558.095	559.972	0.924	0.035
DS6a	559.101	0.456	0.044	0.458	0.191	0.463	0.001	0.069	0.025	0.012	0.005	0.075	1.123	0.000	0.041	0.011	0.042	0.038	558.106	559.951	0.923	0.010

Cut Name	Cut Description		$\langle\epsilon_{total}\rangle$	$\hat{\epsilon}_{total}$	$\langle\epsilon_{unique}\rangle$	$\hat{\epsilon}_{unique}$	Sacrifice	ΔDP
Enriched Source		M1:	23.2 %	$26.5^{+3.8}_{-3.5}$ %	0.0 %	$0.0^{+0.7}_{-0.0}$ %	2.1 %	-2%
Detector Cut	Any other detector: isEnr	M2:	42.7 %	$62.8^{+7.0}_{-7.6}$ %	0.0 %	$0.0^{+2.3}_{--0.0}$ %	4.5 %	
Multiplicity 2		M1:	15.4 %	$16.3^{+3.3}_{-2.8}$ %	0.0 %	$0.0^{+0.7}_{-0.0}$ %	0.0 %	0%
Cut	m==2	M2:	11.7 %	$16.3^{+6.4}_{-4.9}$ %	0.0 %	$0.0^{+2.3}_{--0.0}$ %	0.0 %	
Coincident		M1:	100.0 %	$100.0^{+-0.0}_{-0.7}$ %	62.7 %	$59.9^{+4.0}_{-4.1}$ %	19.0 %	808%
Energy Cut	Any other detector: energy>1472.4 && energy<1483.3	M2:	100.0 %	$100.0^{+-0.0}_{-2.3}$ %	47.8 %	$27.9^{+7.3}_{-6.3}$ %	20.5 %	
Combined Cuts		M1:	100.0 %	$100.0^{+-0.0}_{-0.7}$ %	—	—	22.9 %	994%
		M2:	100.0 %	$100.0^{+-0.0}_{-2.3}$ %			27.9 %	

Table D.14: Table of cut descriptions and efficiencies for simulated backgrounds and measured data for the 559 keV peak.
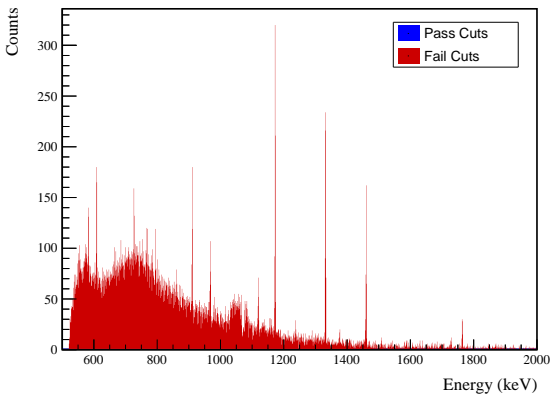
(a) Simulated BG Sum Energy Spectrum
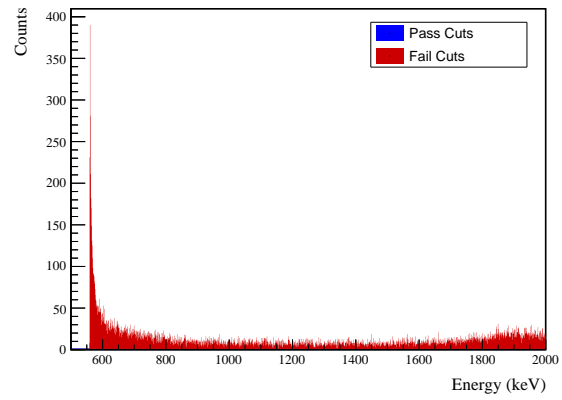
(b) Simulated ES Sum Energy Spectrum
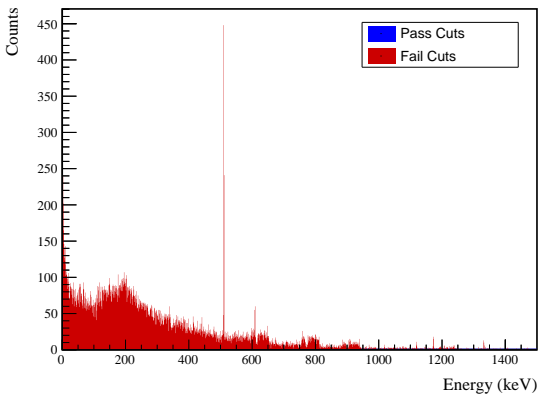
(c) Simulated BG Coincident Energy Spectrum

(d) Simulated ES Coincident Energy Spectrum

Figure D.30: Sum energy and coincident energy spectra for the 559 keV peak.

(a) Simulation

(b) Data

Figure D.31: Simulated and measured multiplicity 2 energy spectrum with sum and coincident energy cuts included for the 559 keV peak.
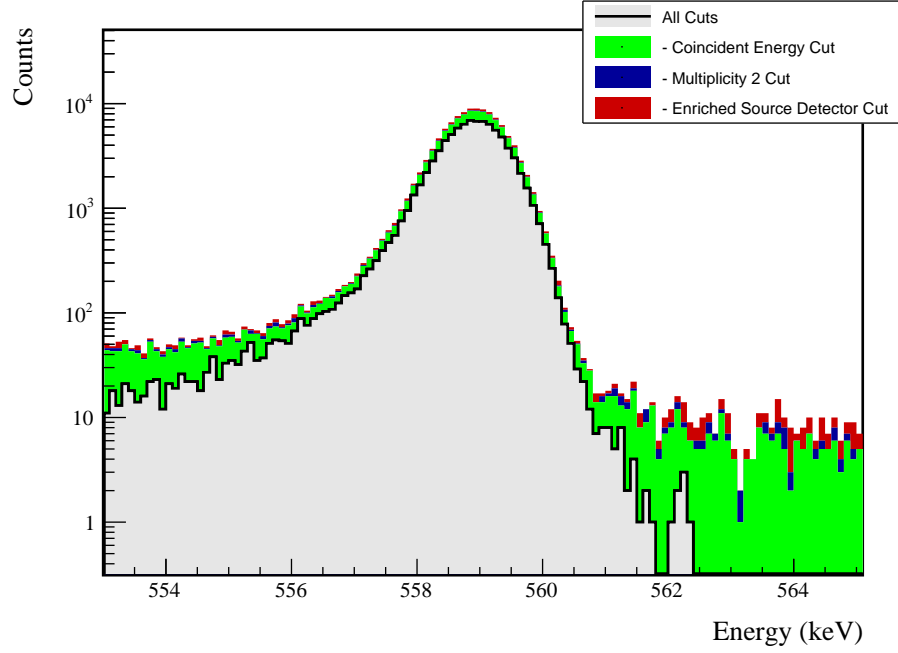
(a) Effect of all cuts on ROI

Source	Module 1 efficiency	Module 2 efficiency
Multi-Detector with Full Energy γ	$3.0 \pm 0.2\%$	$1.5 \pm 0.5\%$
Region of Interest	$92.1 \pm 1.5\%$	$92.1 \pm 1.5\%$
Dead Layer	$67.8 \pm 5.5\%$	$59.3 \pm 7.1\%$
Detector Dead Times	$97.5 \pm 1.1\%$	$98.0 \pm 0.9\%$
Enriched Source Detector Cut	$97.4 \pm\ <0.1\%$	$93.4 \pm\ <0.1\%$
Multiplicity 2 Cut	$98.6 \pm\ <0.1\%$	$99.2 \pm\ <0.1\%$
Coincident Energy Cut	$79.1 \pm 0.3\%$	$76.7 \pm 0.3\%$
Final Efficiency	$1.64 \pm 0.18\%$	$0.70 \pm 0.24\%$

(b) Table of efficiencies

Figure D.32: Plot showing effect of cuts applied sequentially on ROI peak and table of detection efficiencies for the 559 keV peak.

(a) Simulated BG Cuts

(b) Data Cuts
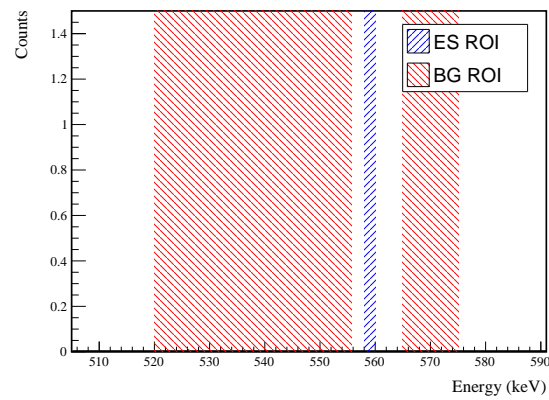
(c) Data ROIs

Figure D.33: Effect of all cuts applied to measured and simulated background data.

D.6 $0\nu\beta\beta$ **to** 2_2^+

Figure D.34: Simulated multiplicity 2 energy spectrum of the $0\nu\beta\beta$ to 2_2^+ decay mode

D.6.1   559 keV peak

Table D.15: Table of energy estimation uncertainties for the 559 keV peak.

| DS	E_{peak} (keV)	σ_{fit} (keV)	σ_{drift} (keV)	σ (keV)	$f_{t,fit}$	τ_{fit} (keV)	$\delta_{\mu,fit}$ (keV)	$\delta_{\mu,NL}$ (keV)	$\delta_{\mu,drift}$ (keV)	$\delta_{\mu,xtalk}$ (keV)	$\delta_{\mu,peak}$ (keV)	δ_{μ} (keV)	FWHM (keV)	$\delta_{fwhm,fit}$ (keV)	$\delta_{fwhm,drift}$ (keV)	$\delta_{fwhm,xtalk}$ (keV)	δ_{FWHM} (keV)	δ_{α}	$E_{ROI,1}$ (keV)	$E_{ROI,2}$ (keV)	ϵ_{ROI}	$\sigma_{\epsilon_{ROI}}$
DS1	559.101	0.460	0.063	0.464	0.230	0.515	0.001	0.104	0.002	0.012	0.005	0.105	1.152	0.001	0.039	0.011	0.040	0.035	558.084	559.935	0.907	0.012
DS2	559.101	0.461	0.055	0.464	0.249	0.515	0.002	0.067	0.004	0.012	0.005	0.068	1.158	0.001	0.107	0.011	0.108	0.093	558.067	559.933	0.909	0.025
DS3	559.101	0.470	0.066	0.474	0.224	0.505	0.001	0.026	0.024	0.012	0.005	0.038	1.174	0.001	0.073	0.011	0.074	0.063	558.072	559.952	0.913	0.017
DS4	559.101	0.455	0.077	0.461	0.108	0.445	0.002	0.076	0.010	0.012	0.005	0.078	1.111	0.001	0.106	0.011	0.107	0.096	558.187	559.942	0.922	0.026
DS5a	559.101	0.560	0.085	0.567	0.106	0.855	0.002	0.079	0.005	0.012	0.005	0.080	1.367	0.002	0.055	0.011	0.056	0.041	557.976	560.128	0.910	0.012
DS5b	559.101	0.469	0.074	0.475	0.158	0.491	0.001	0.020	0.011	0.012	0.005	0.026	1.157	0.001	0.125	0.011	0.125	0.108	558.123	559.962	0.919	0.029
DS5c	559.101	0.460	0.085	0.468	0.174	0.489	0.001	0.037	0.030	0.012	0.005	0.050	1.145	0.001	0.162	0.011	0.162	0.142	558.124	559.948	0.917	0.037
DS6a	559.101	0.456	0.044	0.458	0.191	0.463	0.001	0.069	0.025	0.012	0.005	0.075	1.123	0.000	0.041	0.011	0.042	0.038	558.135	559.927	0.915	0.011

Cut Name	Cut Description		$\langle\epsilon_{total}\rangle$	$\hat{\epsilon}_{total}$	$\langle\epsilon_{unique}\rangle$	$\hat{\epsilon}_{unique}$	Sacrifice	ΔDP
Enriched Source	Any other detector: isEnr	M1:	23.2 %	$26.5^{+3.8}_{-3.5}$ %	0.5 %	$0.7^{+1.1}_{-0.4}$ %	1.4 %	10%
Detector Cut		M2:	42.7 %	$62.8^{+7.0}_{-7.6}$ %	0.9 %	$7.0^{+4.9}_{-3.0}$ %	3.3 %	
Coincident	No other detector: (((energy<65.6) || (energy>504.4 && energy<516.4) || (energy>591.4 && energy<637.8) || (energy>841.8 && energy<868.6) || (energy>1074.6 && energy<1078.4) || (energy>1170.6 && energy<1175.) || (energy>1205. && energy<1208.) || (energy>1331. && energy<1334.) || (energy>1482.6)) && isEnr) || ((energy<44.8) || (energy>507.8 && energy<524.6) || (energy>1375.4)) && !isEnr)	M1:	25.2 %	$29.9^{+3.9}_{-3.6}$ %	0.6 %	$2.0^{+1.5}_{-0.9}$ %	3.1 %	5%
Energy Cut		M2:	24.4 %	$25.6^{+7.2}_{-6.0}$ %	0.4 %	$7.0^{+4.9}_{-3.0}$ %	1.8 %	
Sum Energy Cut	Not: (sumE<1214.) || (sumE>1216.2 && sumE<1377.6) || (sumE>1383.6 && sumE<1495.8) || (sumE>1761.8 && sumE<1765.8) || (sumE>2041.6)	M1:	97.1 %	$95.9^{+1.3}_{-2.0}$ %	54.4 %	51.7 ± 4.1 %	18.3 %	192%
		M2:	97.6 %	$86.0^{+4.5}_{-6.1}$ %	40.3 %	$25.6^{+7.2}_{-6.0}$ %	20.4 %	
Combined Cuts		M1:	98.3 %	$98.6^{+0.7}_{-1.3}$ %	—	—	31.5 %	226%
		M2:	99.0 %	$100.0^{+-0.0}_{-2.3}$ %	—	—	40.6 %	

Table D.16: Table of cut descriptions and efficiencies for simulated backgrounds and measured data for the 559 keV peak.
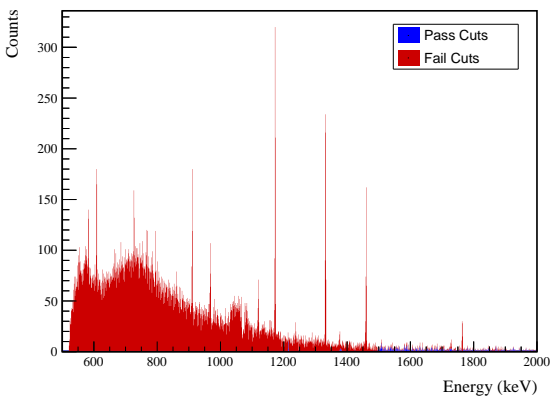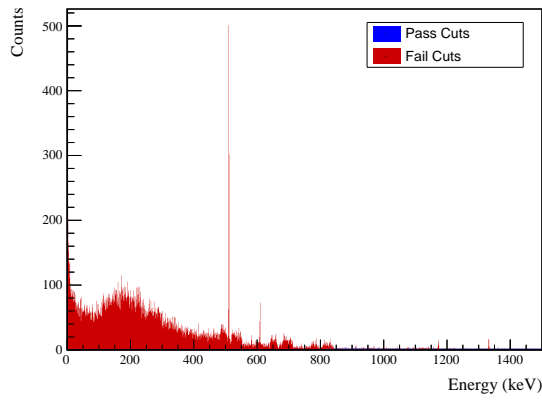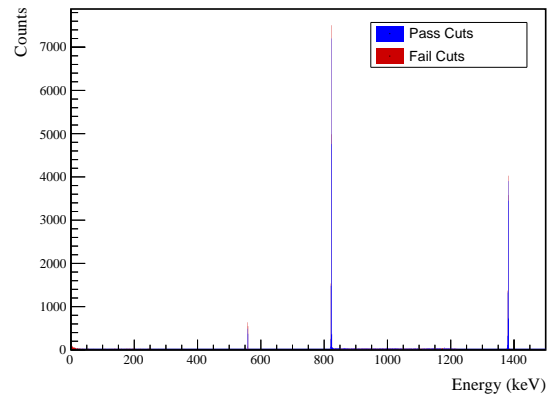
(a) Simulated BG Sum Energy Spectrum
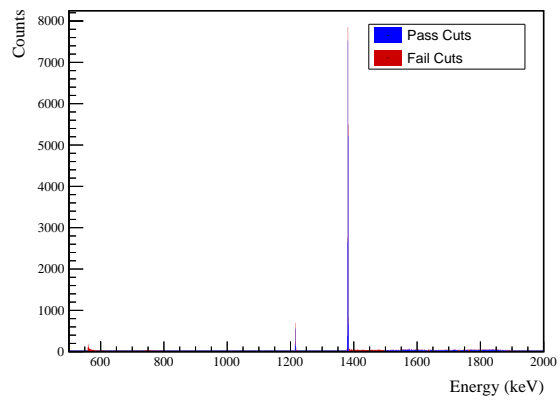
(b) Simulated ES Sum Energy Spectrum
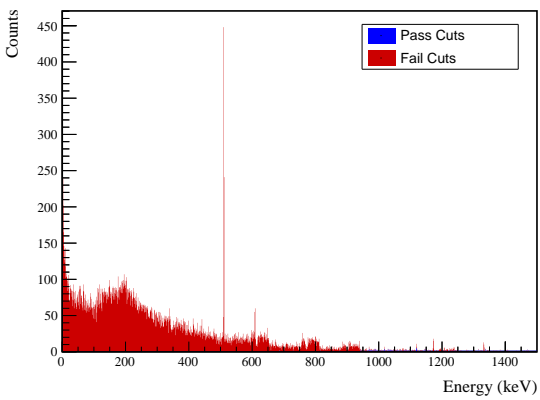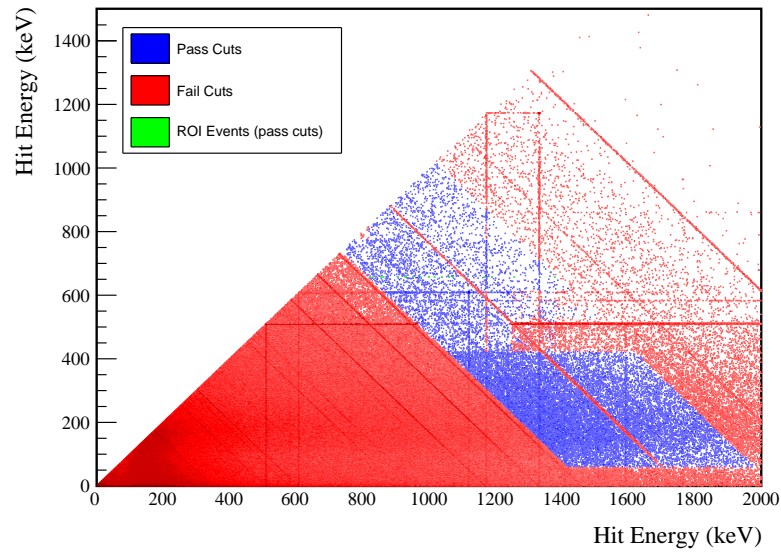
(c) Simulated BG Coincident Energy Spectrum
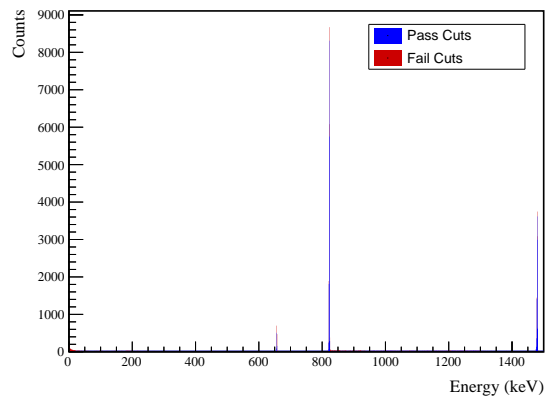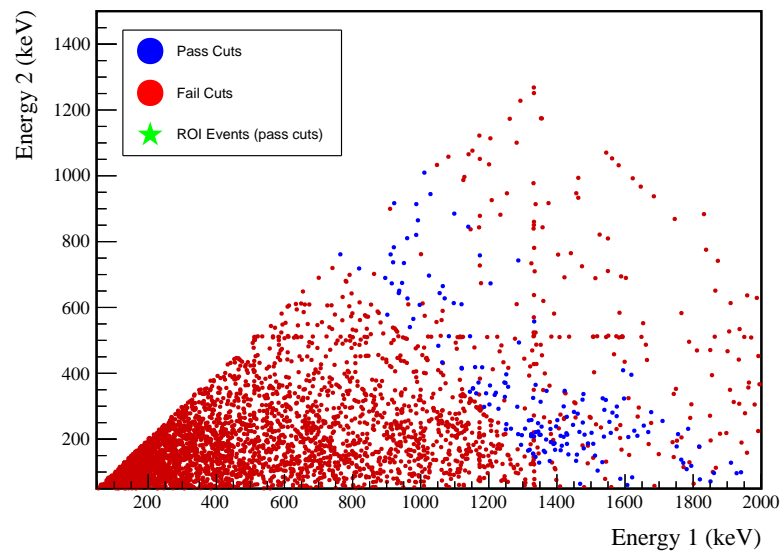
(d) Simulated ES Coincident Energy Spectrum

Figure D.35: Sum energy and coincident energy spectra for the 559 keV peak.
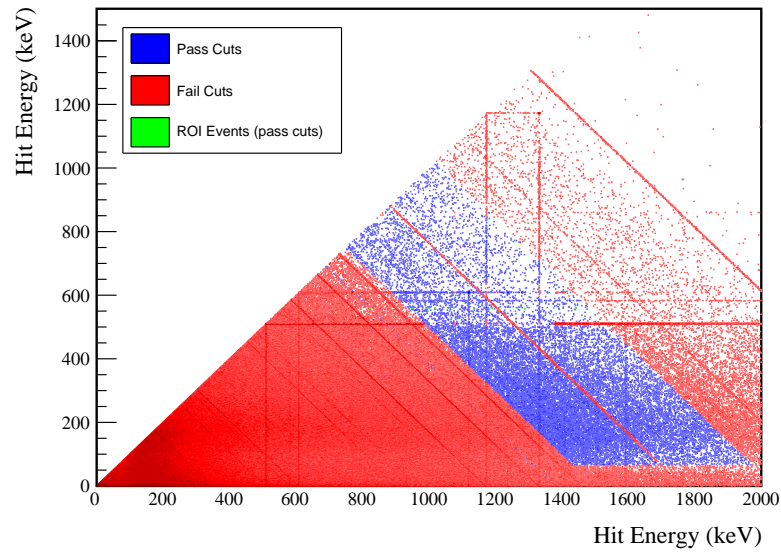
(a) Simulation
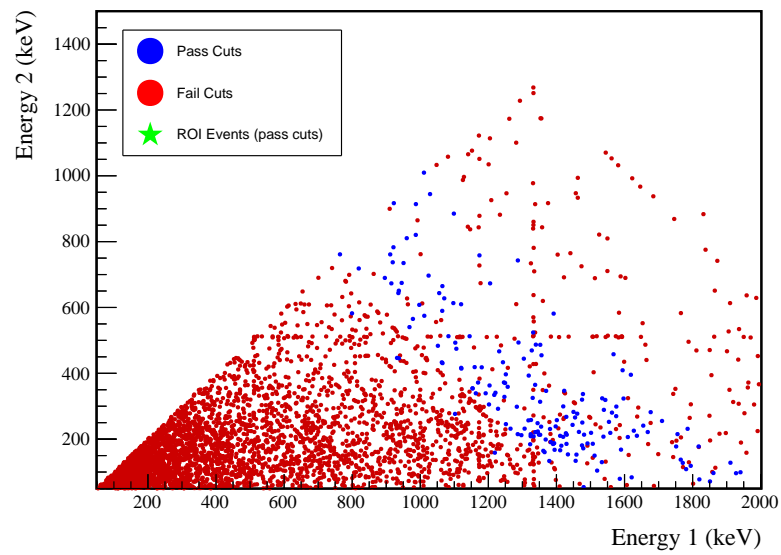
(b) Data

Figure D.36: Simulated and measured multiplicity 2 energy spectrum with sum and coincident energy cuts included for the 559 keV peak.
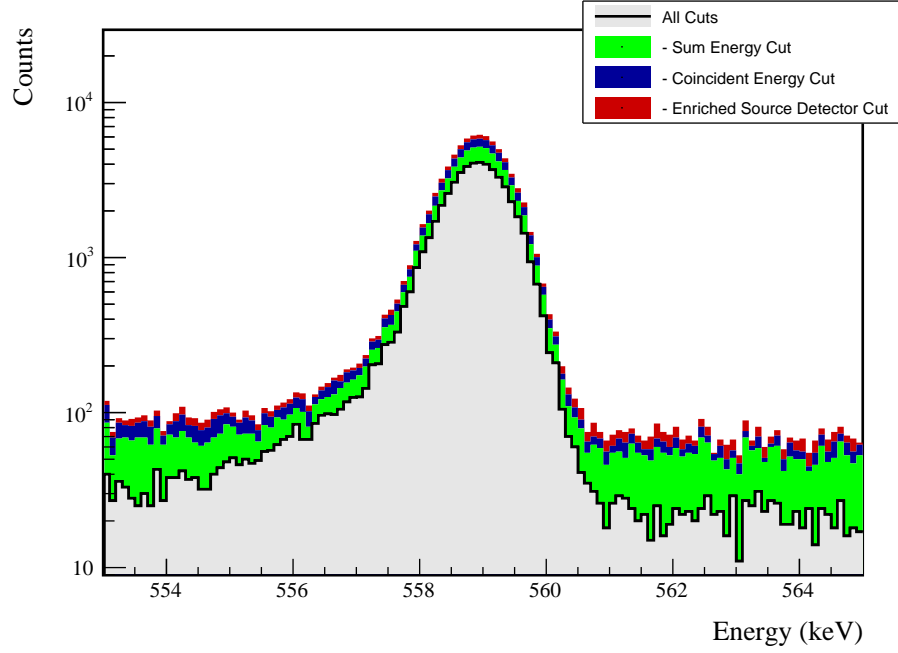
(a) Effect of all cuts on ROI

Source	Module 1 efficiency	Module 2 efficiency
Multi-Detector with Full Energy γ	$1.9 \pm 0.2\%$	$1.0 \pm 0.5\%$
Region of Interest	$91.3 \pm 1.6\%$	$91.3 \pm 1.6\%$
Dead Layer	$68.5 \pm 5.4\%$	$60.3 \pm 7.0\%$
Detector Dead Times	$97.6 \pm 1.1\%$	$98.1 \pm 0.9\%$
Enriched Source Detector Cut	$96.8 \pm\ <0.1\%$	$89.6 \pm\ <0.1\%$
Coincident Energy Cut	$89.5 \pm 0.3\%$	$88.6 \pm 0.3\%$
Sum Energy Cut	$73.2 \pm 0.3\%$	$65.3 \pm 0.3\%$
Final Efficiency	$0.98 \pm 0.13\%$	$0.42 \pm 0.20\%$

(b) Table of efficiencies

Figure D.37: Plot showing effect of cuts applied sequentially on ROI peak and table of detection efficiencies for the 559 keV peak.
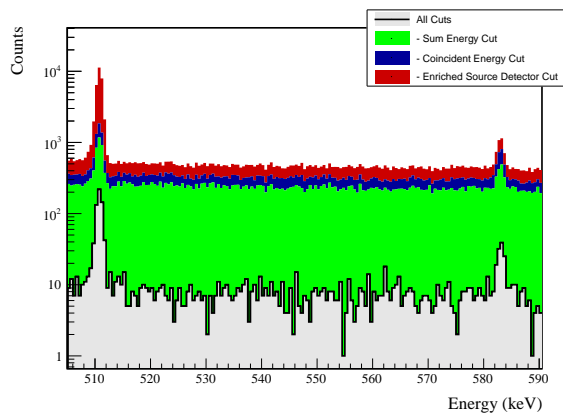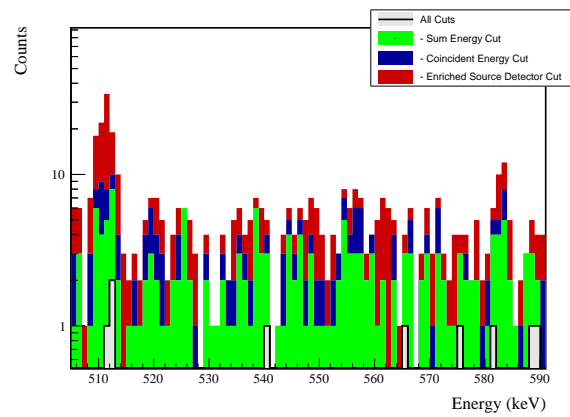
(a) Simulated BG Cuts

(b) Data Cuts
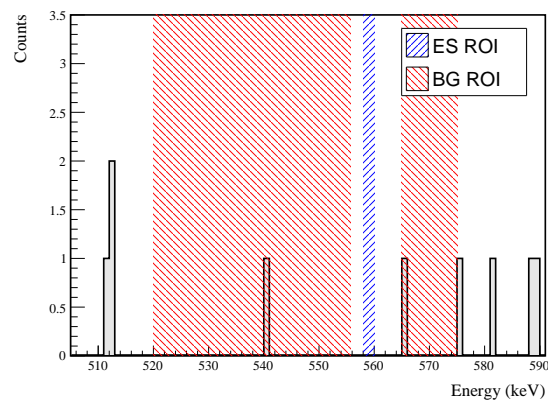
(c) Data ROIs

Figure D.38: Effect of all cuts applied to measured and simulated background data.

D.6.2 657 keV peak
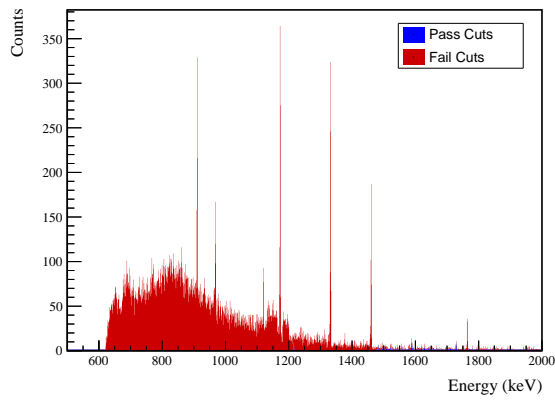
(a) Simulated BG Sum Energy Spectrum
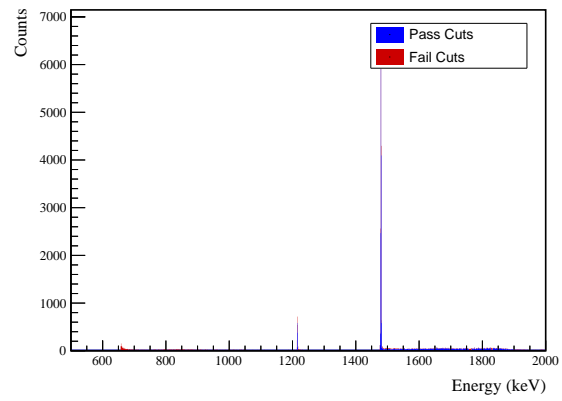
(b) Simulated ES Sum Energy Spectrum

(c) Simulated BG Coincident Energy Spectrum

(d) Simulated ES Coincident Energy Spectrum

Figure D.39: Sum energy and coincident energy spectra for the 657 keV peak.

Table D.17: Table of energy estimation uncertainties for the 657 keV peak.

| DS	E_{peak} (keV)	σ_{fit} (keV)	σ_{drift} (keV)	σ (keV)	$f_{t,fit}$	τ_{fit} (keV)	$\delta_{\mu,fit}$ (keV)	$\delta_{\mu,NL}$ (keV)	$\delta_{\mu,drift}$ (keV)	$\delta_{\mu,xtalk}$ (keV)	$\delta_{\mu,peak}$ (keV)	δ_μ (keV)	FWHM (keV)	$\delta_{fwhm,fit}$ (keV)	$\delta_{fwhm,drift}$ (keV)	$\delta_{fwhm,xtalk}$ (keV)	δ_{FWHM} (keV)	δ_α	$E_{ROI,1}$ (keV)	$E_{ROI,2}$ (keV)	ϵ_{ROI}	$\sigma_{\epsilon ROI}$
DS1	657.041	0.500	0.074	0.505	0.230	0.579	0.002	0.104	0.003	0.012	0.005	0.105	1.256	0.001	0.039	0.011	0.040	0.032	656.019	657.882	0.883	0.013
DS2	657.041	0.502	0.064	0.506	0.249	0.580	0.002	0.067	0.005	0.012	0.005	0.068	1.263	0.001	0.107	0.011	0.108	0.085	656.002	657.881	0.885	0.026
DS3	657.041	0.510	0.078	0.516	0.224	0.568	0.002	0.026	0.028	0.012	0.005	0.040	1.278	0.001	0.073	0.011	0.074	0.058	656.007	657.899	0.889	0.018
DS4	657.041	0.493	0.090	0.501	0.108	0.490	0.002	0.076	0.012	0.012	0.005	0.078	1.207	0.001	0.106	0.011	0.107	0.088	656.120	657.890	0.899	0.028
DS5a	657.041	0.606	0.100	0.614	0.106	0.924	0.002	0.079	0.006	0.012	0.005	0.080	1.481	0.002	0.055	0.011	0.056	0.038	655.915	658.075	0.887	0.012
DS5b	657.041	0.509	0.087	0.517	0.158	0.562	0.001	0.020	0.013	0.012	0.005	0.027	1.259	0.001	0.125	0.011	0.125	0.100	656.056	657.909	0.895	0.031
DS5c	657.041	0.500	0.100	0.510	0.174	0.555	0.002	0.037	0.035	0.012	0.005	0.053	1.247	0.001	0.162	0.011	0.162	0.130	656.057	657.896	0.893	0.040
DS6a	657.041	0.495	0.051	0.497	0.191	0.524	0.001	0.069	0.030	0.012	0.005	0.076	1.221	0.001	0.041	0.011	0.042	0.035	656.070	657.874	0.891	0.012

(a) Simulation

(b) Data

Figure D.40: Simulated and measured multiplicity 2 energy spectrum with sum and coincident energy cuts included for the 657 keV peak.
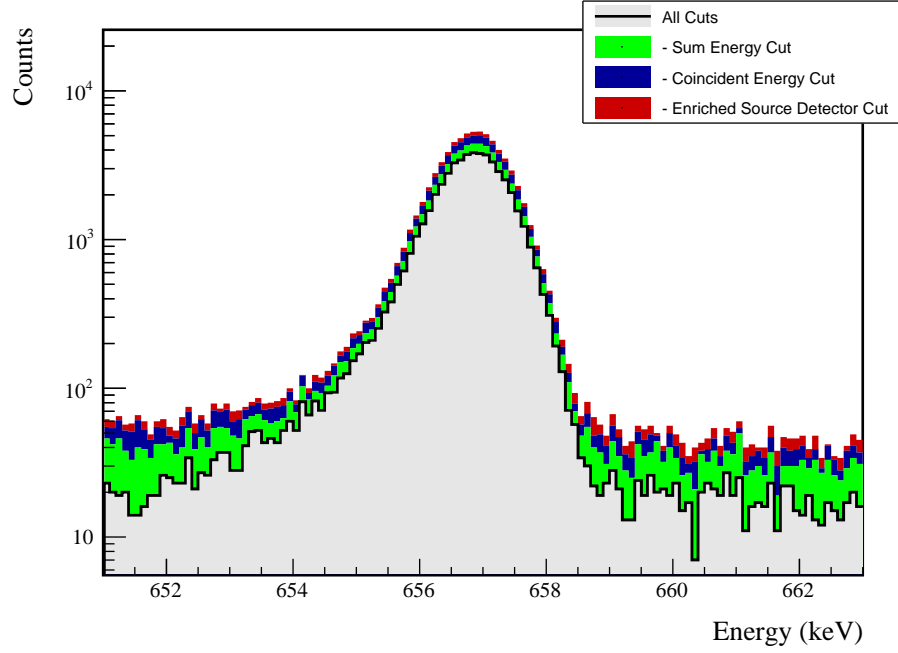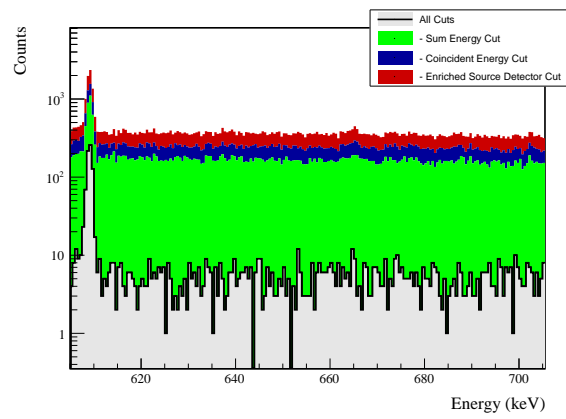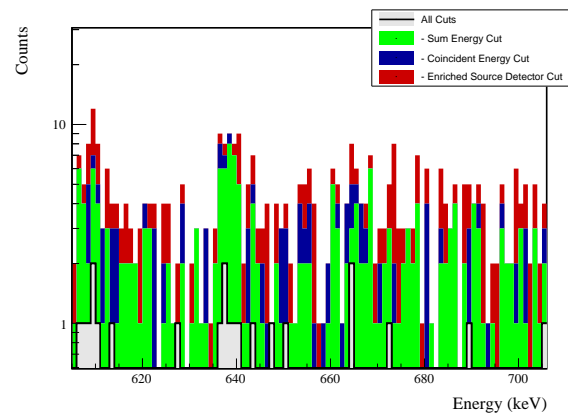
(a) Effect of all cuts on ROI

Source	Module 1 efficiency	Module 2 efficiency
Multi-Detector with Full Energy γ	$1.8 \pm 0.2\%$	$1.0 \pm 0.5\%$
Region of Interest	$89.0 \pm 1.7\%$	$89.0 \pm 1.7\%$
Dead Layer	$69.6 \pm 5.2\%$	$61.1 \pm 6.8\%$
Detector Dead Times	$97.6 \pm 1.1\%$	$98.1 \pm 0.9\%$
Enriched Source Detector Cut	$96.8 \pm\ < 0.1\%$	$89.4 \pm\ < 0.1\%$
Coincident Energy Cut	$88.4 \pm 0.3\%$	$87.1 \pm 0.3\%$
Sum Energy Cut	$80.9 \pm 0.3\%$	$72.9 \pm 0.3\%$
Final Efficiency	$0.95 \pm 0.13\%$	$0.41 \pm 0.21\%$

(b) Table of efficiencies

Figure D.41: Plot showing effect of cuts applied sequentially on ROI peak and table of detection efficiencies for the 657 keV peak.

(a) Simulated BG Cuts
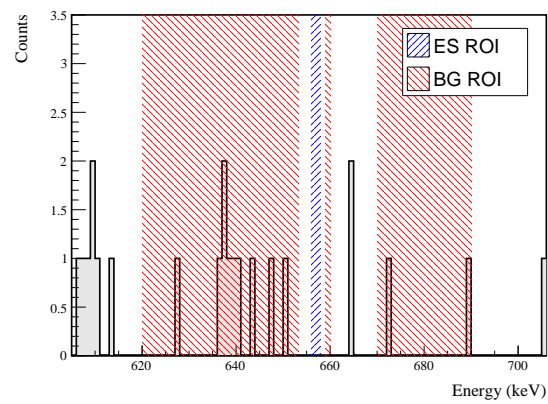
(b) Data Cuts

(c) Data ROIs

Figure D.42: Effect of all cuts applied to measured and simulated background data.

Cut Name	Cut Description		$\langle \epsilon_{total} \rangle$	$\hat{\epsilon}_{total}$	$\langle \epsilon_{unique} \rangle$	$\hat{\epsilon}_{unique}$	Sacrifice	ΔDP
Enriched Source	Any other detector: `isEnr`	M1:	23.9 %	$25.2^{+3.9}_{-3.5}$ %	0.6 %	$3.7^{+2.0}_{-1.3}$ %	1.4 %	12%
Detector Cut		M2:	43.7 %	$60.4^{+6.8}_{-7.2}$ %	1.2 %	$4.2^{+3.9}_{-2.1}$ %	3.7 %	
Coincident	No other detector: `(((energy<59.) || (energy>422.6 && energy<529.4) || (energy>562.4 && energy<616.6) || (energy>776.8 && energy<818.8) || (energy>1169.6 && energy<1333.2) || (energy>1308. && energy<1175.) || (energy>1384.8)) && isEnr) || (((energy<52.2) || (energy>1248.)) && energy>491.6 && energy<554.8) && !isEnr)`	M1:	30.4 %	$25.2^{+3.9}_{-3.5}$ %	0.8 %	$2.2^{+1.7}_{-1.0}$ %	4.9 %	7%
Energy Cut		M2:	29.1 %	$16.7^{+6.0}_{-4.7}$ %	0.6 %	$2.1^{+3.2}_{-1.3}$ %	3.2 %	
Sum Energy Cut	Not: `(sumE<1214.8) || (sumE>1216.8 && sumE<1475.2) || (sumE>1757.6 && sumE<1766.) || (sumE>2042.6)`	M1:	96.9 %	$88.9^{+2.4}_{-3.0}$ %	49.8 %	48.9 ± 4.3 %	11.6 %	207%
		M2:	97.0 %	$91.7^{+3.2}_{-4.9}$ %	36.9 %	$27.1^{+6.8}_{-5.9}$ %	13.6 %	
Combined Cuts		M1:	98.5 %	$94.8^{+1.6}_{-2.3}$ %	—	—	25.7 %	255%
		M2:	99.0 %	$97.9^{+1.3}_{-3.2}$ %	—	—	34.9 %	

Table D.18: Table of cut descriptions and efficiencies for simulated backgrounds and measured data for the 657 keV peak.
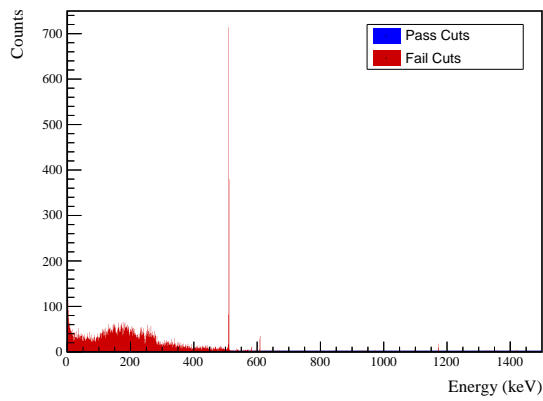
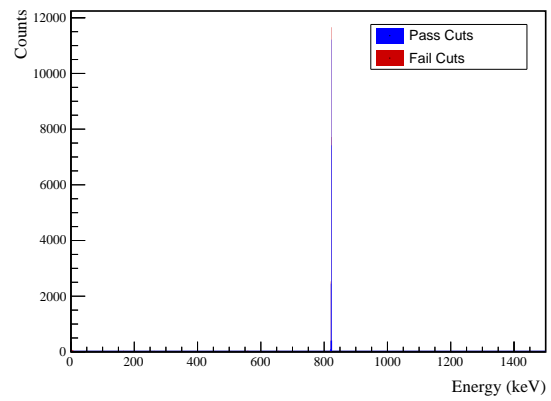## D.6.3 1216 keV peak
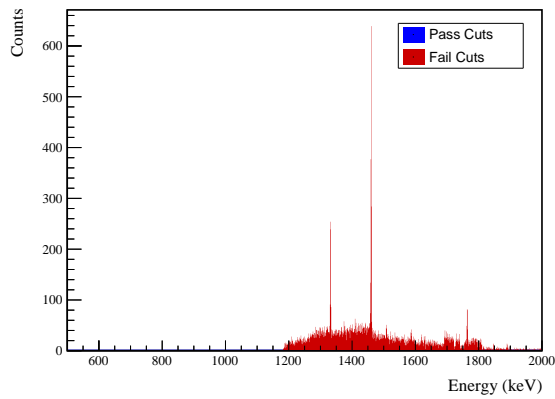
(a) Simulated BG Sum Energy Spectrum
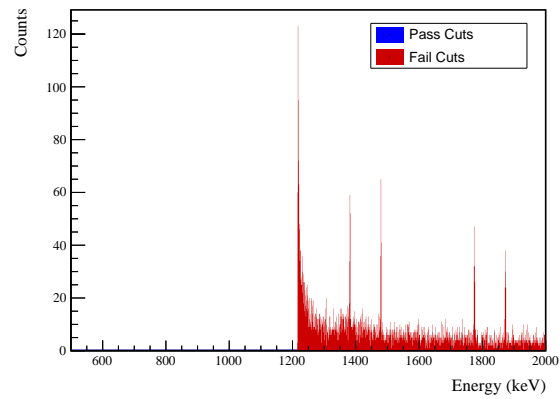
(b) Simulated ES Sum Energy Spectrum

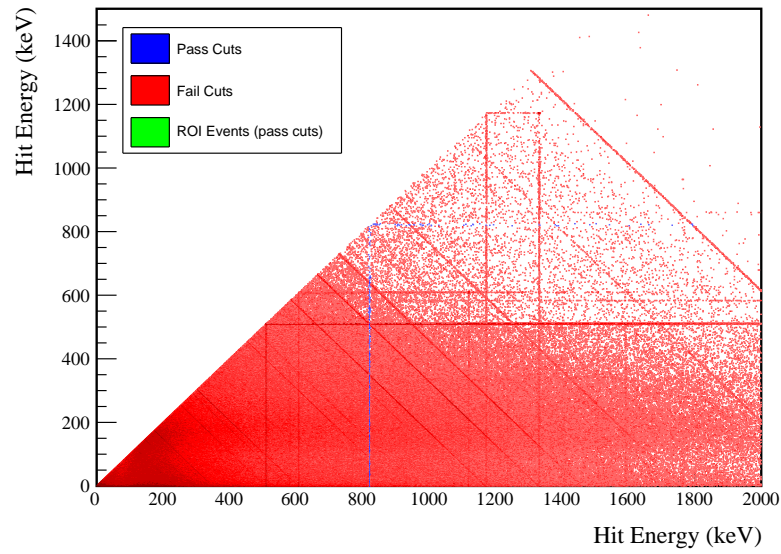(c) Simulated BG Coincident Energy Spectrum

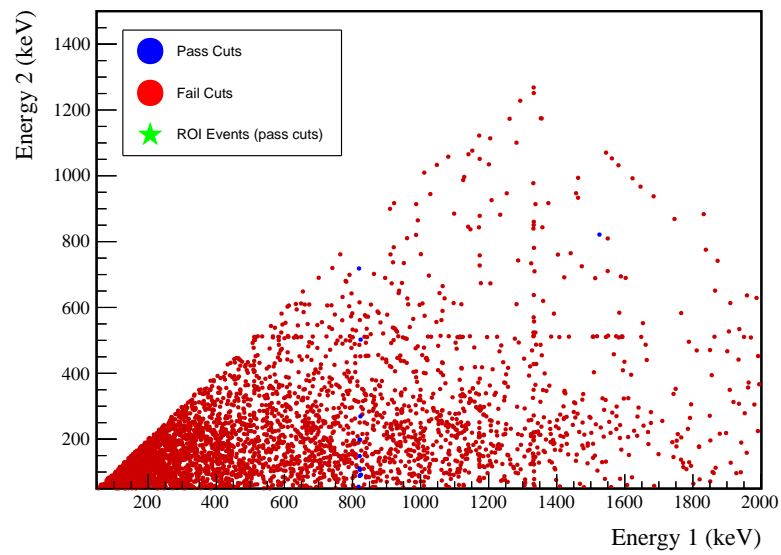

(d) Simulated ES Coincident Energy Spectrum

Figure D.43: Sum energy and coincident energy spectra for the 1216 keV peak.

Table D.19: Table of energy estimation uncertainties for the 1216 keV peak.

| DS	E_{peak} (keV)	σ_{fit} (keV)	σ_{drift} (keV)	σ (keV)	$f_{t,fit}$	τ_{fit} (keV)	$\delta_{\mu,fit}$ (keV)	$\delta_{\mu,NL}$ (keV)	$\delta_{\mu,drift}$ (keV)	$\delta_{\mu,xtalk}$ (keV)	$\delta_{\mu,peak}$ (keV)	δ_{μ} (keV)	FWHM (keV)	$\delta_{fwhm,fit}$ (keV)	$\delta_{fwhm,drift}$ (keV)	$\delta_{fwhm,xtalk}$ (keV)	δ_{FWHM} (keV)	δ_{α}	$E_{ROI,1}$ (keV)	$E_{ROI,2}$ (keV)	ϵ_{ROI}	$\sigma_{\epsilon_{ROI}}$
DS1	1216.104	0.705	0.137	0.718	0.230	0.945	0.003	0.104	0.005	0.012	0.020	0.107	1.787	0.001	0.039	0.011	0.040	0.023	1214.426	1217.449	0.914	0.006
DS2	1216.104	0.710	0.119	0.720	0.249	0.951	0.003	0.067	0.008	0.012	0.020	0.072	1.803	0.001	0.107	0.011	0.108	0.060	1214.387	1217.449	0.914	0.014
DS3	1216.104	0.715	0.144	0.729	0.224	0.925	0.003	0.026	0.051	0.012	0.020	0.062	1.812	0.001	0.073	0.011	0.074	0.041	1214.416	1217.470	0.917	0.010
DS4	1216.104	0.697	0.167	0.717	0.108	0.746	0.003	0.076	0.022	0.012	0.020	0.083	1.726	0.001	0.106	0.011	0.107	0.062	1214.621	1217.461	0.932	0.015
DS5a	1216.104	0.838	0.185	0.859	0.106	1.316	0.004	0.079	0.012	0.012	0.020	0.083	2.070	0.002	0.055	0.011	0.056	0.027	1214.323	1217.722	0.921	0.007
DS5b	1216.104	0.716	0.161	0.734	0.158	0.963	0.002	0.020	0.024	0.012	0.020	0.039	1.791	0.001	0.125	0.011	0.125	0.070	1214.506	1217.487	0.922	0.017
DS5c	1216.104	0.703	0.185	0.727	0.174	0.932	0.003	0.037	0.066	0.012	0.020	0.079	1.783	0.001	0.162	0.011	0.162	0.091	1214.497	1217.474	0.921	0.022
DS6a	1216.104	0.693	0.095	0.700	0.191	0.873	0.002	0.069	0.055	0.012	0.020	0.092	1.723	0.001	0.041	0.011	0.042	0.025	1214.535	1217.422	0.920	0.006

(a) Simulation

(b) Data

Figure D.44: Simulated and measured multiplicity 2 energy spectrum with sum and coincident energy cuts included for the 1216 keV peak.
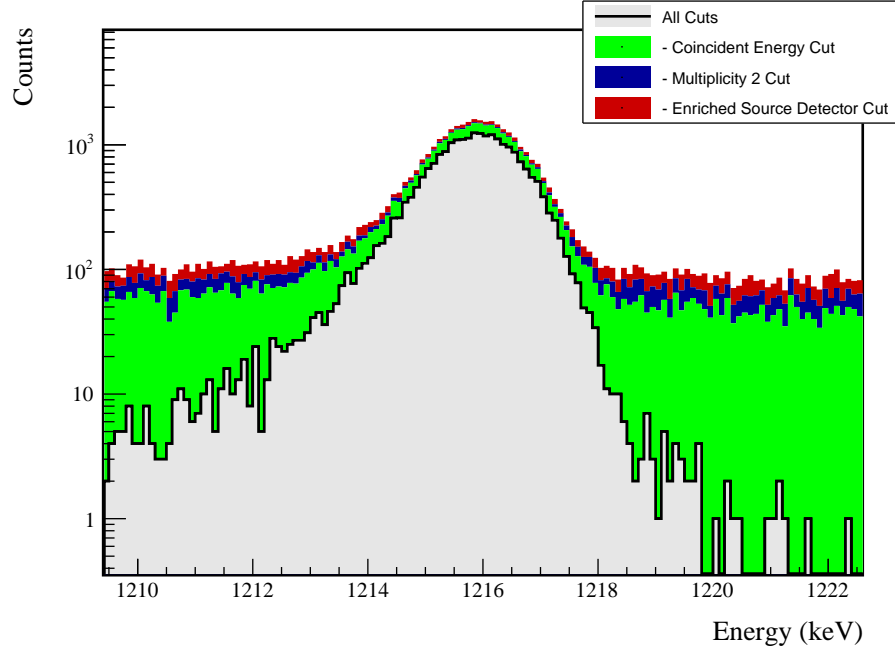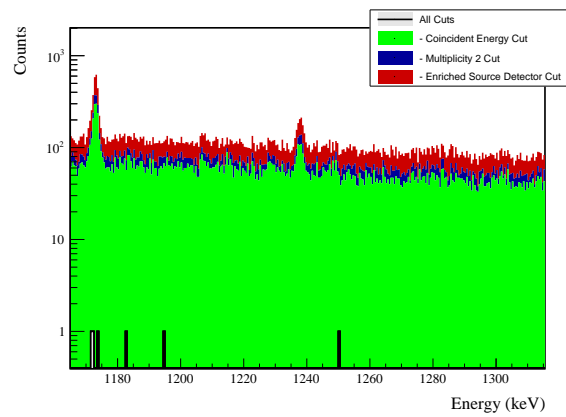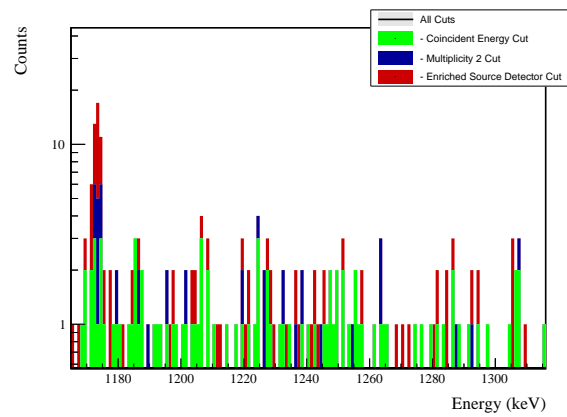
(a) Effect of all cuts on ROI

| Source	Module 1 efficiency	Module 2 efficiency
Multi-Detector with Full Energy γ	$0.8 \pm 0.2\%$	$0.4 \pm 0.5\%$
Region of Interest	$92.0 \pm 0.9\%$	$92.0 \pm 0.9\%$
Dead Layer	$68.8 \pm 5.3\%$	$61.2 \pm 6.8\%$
Detector Dead Times	$97.5 \pm 1.1\%$	$98.0 \pm 0.9\%$
Enriched Source Detector Cut	$96.1 \pm\ <0.1\%$	$90.8 \pm\ <0.1\%$
Multiplicity 2 Cut	$97.3 \pm\ <0.1\%$	$98.2 \pm\ <0.1\%$
Coincident Energy Cut	$76.9 \pm 0.3\%$	$75.7 \pm 0.3\%$
Final Efficiency	$0.44 \pm 0.12\%$	$0.19 \pm 0.22\%$

(b) Table of efficiencies

Figure D.45: Plot showing effect of cuts applied sequentially on ROI peak and table of detection efficiencies for the 1216 keV peak.

(a) Simulated BG Cuts
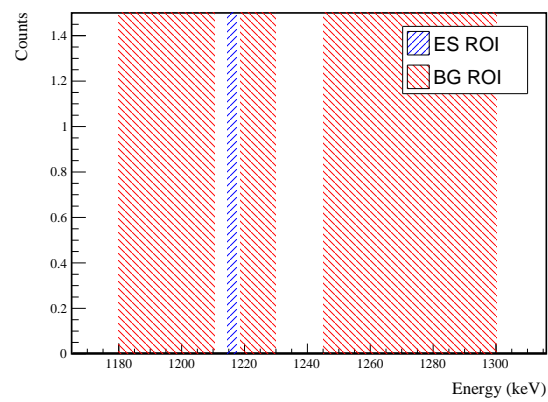
(b) Data Cuts

(c) Data ROIs

Figure D.46: Effect of all cuts applied to measured and simulated background data.

Cut Name	Cut Description		$\langle\epsilon_{total}\rangle$	$\hat{\epsilon}_{total}$	$\langle\epsilon_{unique}\rangle$	$\hat{\epsilon}_{unique}$	Sacrifice	ΔDP
Enriched Source Detector Cut	Any other detector: `isEnr`	M1:	26.9 %	$16.9^{+4.5}_{-3.7}$ %	0.0 %	$0.0^{+1.2}_{-0.0}$ %	2.0 %	-2%
		M2:	43.9 %	$61.9^{+9.8}_{-10.9}$ %	0.0 %	$0.0^{+4.5}_{-0.0}$ %	4.3 %	
Multiplicity 2 Cut	`m==2`	M1:	15.3 %	$16.9^{+4.5}_{-3.7}$ %	0.0 %	$0.0^{+1.2}_{-0.0}$ %	0.0 %	0%
		M2:	11.9 %	$9.5^{+8.4}_{-4.7}$ %	0.0 %	$0.0^{+4.5}_{-0.0}$ %	0.0 %	
Coincident Energy Cut	Any other detector: `energy>817.7 && energy<825.4`	M1:	100.0 %	$100.0^{+0.0}_{-1.2}$ %	59.6 %	$68.7^{+4.8}_{-5.3}$ %	18.7 %	555%
		M2:	100.0 %	$100.0^{+-0.0}_{-4.5}$ %	46.6 %	$33.3^{+10.8}_{-9.3}$ %	17.9 %	
Combined Cuts		M1:	100.0 %	$100.0^{+0.0}_{-1.2}$ %	–	–	25.2 %	669%
		M2:	100.0 %	$100.0^{+-0.0}_{-4.5}$ %	–	–	28.7 %	

Table D.20: Table of cut descriptions and efficiencies for simulated backgrounds and measured data for the 1216 keV peak.